Diss. ETH No. 21020

The Role of Heterogeneous Nucleation in Polar Stratospheric Cloud Formation: Microphysical Modeling

A dissertation submitted to
ETH ZURICH

for the degree of
Doctor of Sciences

presented by
INES ENGEL
Dipl. Landschaftsökologin
Westfälische Wilhelms-Universität Münster, Germany
born 08 October 1983
citizen of Germany

accepted on the recommendation of
Prof. Dr. Thomas Peter, examiner
Dr. Michael C. Pitts, co-examiner
Dr. Marc von Hobe, co-examiner

2013

Contents

Abstract

The Antarctic ozone hole is one of the most outstanding examples of atmospheric impact caused by human activities. Shortly after its discovery in 1985, anthropogenic halogen compounds were identified as responsible ozone depleting substances. The surface necessary for heterogeneous reactions activating chlorine species is provided by cold stratospheric aerosols and by polar stratospheric clouds (PSCs), which form in the lower stratosphere above the winter poles at very low temperatures. They are composed either of supercooled ternary $HNO_3/H_2O/H_2SO_4$ solution (STS) droplets, ice particles or solid hydrates, most likely nitric acid trihydrate (NAT). Ice and NAT particles can grow to sizes large enough to sediment. The resulting vertical redistribution of water (dehydration) and nitric acid (denitrification) is irreversible and changes the chemical composition of the stratosphere. Denitrification sustains the ozone depleting process to persist longer by delaying the deactivation of chlorine radicals back into reservoir species. Even though the above mentioned types of PSC particles have been identified and observed in the stratosphere, major aspects of PSC formation processes remain uncertain. The nucleation of NAT particles is probably least well understood and therefore often poorly represented in global models. This limits the ability to accurately predict the future evolution of the ozone layer recovery and impacts of stratospheric processes on climate.

The introduction of the Cloud-Aerosol Lidar and Infrared Pathfinder Satellite Observations (CALIPSO) satellite, which was launched in 2006, led to a hitherto unknown wealth of PSC observations in number and detail, collected from both hemispheres. The spaceborne Cloud-Aerosol Lidar with Orthogonal Polarization (CALIOP) onboard CALIPSO provides data of parallel and perpendicular backscattering, which has been interpreted in terms of PSC composition classes. Utilizing CALIOP remote data together with aircraft and balloon in situ measurements, major uncertainties in PSC formation have been addressed within the research project RECONCILE, short for "reconciliation of essential process parameters for an enhanced predictability of Arctic stratospheric ozone loss and its climate interactions". During the Arctic winter 2009/2010, a field campaign employing the high altitude research aircraft M55-Geophysica and various balloon soundings were conducted and complemented by laboratory experiments, microphysical and chemical transport modeling assimilations. This concerted action greatly expanded the accessibility to and understanding of PSC observations.

The activities in the 2009/2010 winter unveiled some surprising findings. Patchy, but extensive fields of NAT particles were frequently observed by CALIOP in December, when minimum temperatures were 3 K above the frost point anywhere inside the polar vortex, and 6 K too warm to enable homogeneous ice formation. This finding changes the previous understanding of NAT formation, which was thought to be governed by ice-assisted nucleation. It calls for a heterogeneous nucleation process of

NAT on preexisting solid particles, which is supported by measurements indicating that more than half of the stratospheric aerosol particles inside the Arctic vortex contain non-volatile residues. These residues may be coagulated meteoritic smoke particles, as has been suggested before. This idea is corroborated by this thesis through extensive trajectory and microphysical box model calculations with the Zurich Optical and Microphysical box Model (ZOMM). Heterogeneous NAT nucleation has been implemented by immersion freezing on nanometer sized dust particles. The model suggests that their nucleation efficiency is characterized by active sites, which implies that only a minor fraction of the dust particles are effective nuclei. Only the implementation of heterogeneous NAT nucleation may reconcile the model results with the CALIOP observations in December 2009. Moreover, in explaining these observations, the active-site hypothesis is clearly superior to alternative descriptions such as constant rates of NAT nucleation per volume of air.

In addition to the early NAT occurrence, later large areas of synoptic-scale ice PSCs dominated the winter and, furthermore, revealed unprecedented evidence of water redistribution in the Arctic stratosphere. A unique snapshot of water vapor repartitioning into ice particles was measured under extremely cold Arctic conditions with temperatures as low as 183 K. Balloon-borne, aircraft, and satellite measurements provide the picture that synoptic-scale ice PSCs and concurrent reductions and enhancements in water vapor are tightly linked with the observed de- and rehydration signatures, respectively. Motivated by the new findings about the heterogeneous nature of NAT nucleation and the exceptionally large ice coverage in January 2010, this thesis also questions the exclusively homogeneous nature of ice formation in the Arctic stratosphere. Observations cannot be explained merely by homogeneous ice nucleation but require heterogeneous ice nucleation on ice nuclei, e.g. meteoritic particles or preexisting NAT particles. In addition, obtaining model agreement with ice number densities inferred from the observations requires the presence of small-scale temperature fluctuations, with wavelengths unresolved by the trajectories based on numerical weather prediction models. Whereas the effect of small-scale temperature fluctuations on tropospheric ice clouds is already known, this work presents their relevance also for the stratosphere and calls for a better representation of accurate vertical wind speeds in models.

In summary, this thesis revisits the microphysics of PSCs with particular focus on heterogeneous nucleation pathways. Conclusive laboratory studies, which would prove that meteoritic dust contains suitable and efficient heterogeneous nuclei, or that other solid nuclei of so far unknown origin be suitable, are still missing. Vice versa, by means of comprehensive modeling studies, this work contributes substantially to a better understanding of PSC formation and leaves little doubt about the importance of heterogeneous processes.

Zusammenfassung

Das Ozonloch über der Antarktis gehört zu den gravierendsten vom Menschen verursachten Veränderungen der Erdatmosphäre. Bereits kurz nach der Entdeckung des Ozonlochs im Jahr 1985 wurden anthropogene Fluorchlorkohlenwasserstoffe als bedeutendste Quelle ozonschädlicher Chlorverbindungen identifiziert. Die Aktivierung von Chlorverbindungen, die für einen Großteil der Ozonzerstörung verantwortlich sind, findet auf den Oberflächen kalter, stratosphärischer Aerosole sowie polarer Stratosphärenwolken statt. PSCs (engl. Polar Stratospheric Clouds) können sich bei extrem kalten Temperaturen bilden, wie sie in der unteren Stratosphäre über den Winterpolen vorherrschen. Sie setzen sich aus unterkühlten, ternären $HNO_3/H_2O/H_2SO_4$-Lösungstropfen, Wassereis oder Kristallen der Salpetersäure zusammen, sogenannten NAT-Partikeln (engl. Nitric Acid Trihydrate). Die Sedimentation heranwachsender PSC-Teilchen kann eine irreversible Umverteilung des stratosphärischen Wassers (Dehydrierung) und der Salpetersäure (Denitrifizierung) hervorrufen. Die dadurch veränderte Zusammensetzung der stratosphärischen Gasphase begünstigt zusätzlich die Ozonzerstörung, da das Fehlen von Stickoxiden eine Deaktivierung des Chlors verhindert. Obwohl die Hauptbestandteile von PSCs bekannt sind und bereits in der Stratosphäre nachgewiesen werden konnten, bleiben viele Fragen bezüglich der Entstehungsmechanismen unbeantwortet. Der Bildungsprozess von NAT-Partikeln birgt vermutlich die größten Unsicherheiten und ist in globalen Modellen häufig nur sehr vereinfacht repräsentiert. Dadurch sind Vorhersagen über die zukünftige Entwicklung der Ozonschicht und die Auswirkungen stratosphärischer Prozesse auf das Klima nur eingeschränkt möglich.

Der Start des Satelliten CALIPSO im Jahr 2006 führte zu einer bisher nicht vorhanden Fülle und Qualität an PSC-Beobachtungen in beiden Hemisphären. Das an Bord befindliche polarisationsempfindliche Lidar CALIOP liefert hochaufgelöste, vertikale Profile des atmosphärischen Aerosols. Das stratosphärische Rückstreuverhältnis wird dahingehend interpretiert, PSCs anhand ihrer Zusammensetzung zu klassifizieren. Diese Daten werden in Kombination mit in-situ Flugzeug- und Ballonmessungen im Rahmen des Forschungsprojektes RECONCILE ausgewertet. Das Projekt hat sich die Beantwortung noch offener Fragen im Zusammenhang mit dem polaren Ozonabbau sowie die Verbesserung der Vorhersagen in Bezug auf die Entwicklung der Ozonschicht unter Berücksichtigung des Klimawandels zum Ziel gesetzt. Während des arktischen Winters 2009/2010 wurden hierzu eine Feldmesskampange durchgeführt, die den Einsatz des Forschungsflugzeugs M55-Geophysica und eine Vielzahl unterschiedlicher Ballonsondierungen beinhaltete. Die aufeinander abgestimmten Aktivitäten, in Kombination mit Laborexperimenten sowie mikrophysikalischen und chemischen Modellstudien, haben die Verfügbarkeit sowie das Verständnis von PSC-Beobachtungen bedeutend erweitert.

Der Winter 2009/2010 brachte einige unerwartete Forschungsergebnisse hervor. Während die Temperaturen im Dezember noch 3 K über dem Frostpunkt und damit 6 K zu warm für homogenes Gefrieren von Wasser waren, beobachtete CALIOP bereits das Vorkommen beträchtlicher Gebiete an NAT-Partikeln. Diese Erkenntnis verändert die bis dahin vorherrschende Ansicht zur Entstehung von NAT, die das Vorhandensein von Eis voraussetzt. Ein eisfreier, heterogener Gefrierprozess von NAT muss in Erwägung gezogen werden und wird durch Messungen gestützt. Diese zeigen, dass mehr als die Hälfte aller stratosphärischen Aerosole nicht flüchtige Bestandteile enthalten, die aus koagulierten meteoritischen Staubpartikeln bestehen könnten. Im Rahmen der vorliegenden Arbeit konnte diese Theorie über Trajektorien gestützte mikrophysikalische Boxmodellierung bekräftigt werden. Das dafür verwendete Modell wurde um einen heterogenen Gefrierprozess für NAT erweitert, der die Effektivität heterogener Gefrierkeime über deren Oberflächenbeschaffenheit definiert und nur wenige Keime als effektiv hervorhebt. Es hat sich gezeigt, dass Modellergebnisse und Beobachtungen nur dann in Übereinstimmung zu bringen sind, wenn das heterogene Gefrieren von NAT bei Temperaturen über dem Frostpunkt möglich ist. Weiterhin führt die Annahme unterschiedlich effizienter Keime zu besseren Modellergebnissen als eine konstanten Bildungsrate.

Zusätzlich zu dem beschriebenen unerwartet frühen Auftreten von NAT-Partikeln unterschied sich der Winter 2009/2010 gegenüber anderen Jahren durch das großflächige Vorkommen von Eiswolken. Darüber hinaus gelang eine für die Arktis bis heute einmalige Beobachtung stratosphärischer Dehydrierung. Bei Temperaturen um 183 K wurde eine Reduktion des Wassers in der Gasphase bei gleichzeitigem Nachweis von Eiskristallen beobachtet. Messungen unterschiedlichster Instrumente zeigen, dass das Auftreten synoptischer Eiswolken und die darauf folgenden Beobachtungen de- und rehydrierter Luftschichten im Zusammenhang stehen. Motiviert durch die neuen Erkenntnisse der NAT-Entstehung und das großflächige Vorkommen von Eis-PSCs, hinterfragt diese Arbeit auch das alleinige homogene Gefrieren von Wasser in der arktischen Stratosphäre. Es konnte gezeigt werden, dass sich auch die Beobachtungen der Eis-PSCs nur über einen zusätzlichen Gefrierprozess auf bereits vorhanden Oberflächen, beispielsweise von meteoritischem Material oder NAT-Partikeln, erklären lassen. Kleinskalige Temperaturfluktuationen sind eine weitere Voraussetzung dafür, dass Modellergebnisse und Beobachtungen in der Eisphase übereinstimmen. Während der Effekt kleinskaliger Temperaturfluktuationen auf troposphärische Eiswolken bekannt ist, wird innerhalb dieser Arbeit die stratosphärische Relevanz aufgezeigt. Trajektorien, die auf numerischen Wettervorhersagemodellen basieren, lösen Fluktuationen häufig nicht zufriedenstellend auf. Eine verbesserte Darstellung vertikaler Windgeschwindigkeiten wäre daher wünschenswert.

Zusammenfassend wurde im Rahmen dieser Arbeit die Mikrophysik von PSCs behandelt und mit dem Fokus auf heterogene Bildungsmechanismen neu überdacht. Bis heute fehlen schlüssige Laborstudien, die die Gefriereffizienz meteoritischer Partikel bestätigt. Dennoch trägt diese Arbeit substantiell zu einem besseren Verständnis der PSC-Bildungsmechanismen bei und lässt anhand von Modellstudien wenig Zweifel an der Wichtigkeit heterogener Gefrierprozesse.

Chapter 1

Introduction

The stratosphere extends from the tropopause up to an altitude of roughly 50 km. A typical stratospheric temperature profile in the mid-latitudes is characterized by temperatures increasing with altitude with coldest values just above the tropopause. Air enters the stratosphere from the troposphere primarily in the tropics by slow uplift, which is radiatively driven. This process freezes out most of the water at the tropopause and makes it sediment back to the troposphere in the form of small ice crystals. Therefore, stratospheric air is extremely dry. The vertical thermal structure of the stratosphere is a result of absorption of solar ultraviolet (UV) radiation by ozone (O_3), one of the most important constituents in the stratosphere. About 90 % of the atmospheric ozone is located between 15 to 30 km altitude in the so called ozone layer. The stratospheric ozone layer reduces harmful UV radiation penetrating down to the earth's surface and thus protects the biosphere, e.g. humans against skin cancer.

An overview of stratospheric ozone chemistry and the key role of polar stratospheric clouds (PSCs) in the polar ozone destruction cycle will be given in Sect. 1.1 and Sect. 1.2. Motivation and outline of this thesis are formulated in Sect. 1.3.

1.1 Stratospheric ozone chemistry

Formation and destruction of ozone was first described by Chapman (1930) and is known as the Chapman cycle:

$$O_2 + h\nu \rightarrow 2\,O \tag{1.1}$$

$$O + O_2 + M \rightarrow O_3 + M \tag{1.2}$$

$$O_3 + h\nu \rightarrow O + O_2 \tag{1.3}$$

$$O + O_3 \rightarrow 2\,O_2 \tag{1.4}$$

The main source of stratospheric ozone is photochemical in situ formation and hence peak values of up to 12 ppm are observed in the tropics, where incident solar radiation is largest. At wavelengths $\lambda < 242$ nm, molecular oxygen (O_2) is decomposed into two oxygen atoms (1.1) which rapidly react with other oxygen molecules to form ozone (1.2). M denotes a collision partner, not changed by the reaction, but required to simultaneously conserve momentum and energy. Harmful UV-B solar radiation is absorbed during the photodissociation reaction (1.3). The cycle between O and O_3 occurs

rapidly and O flips back and forth many times between (1.2) and (1.3). Therefore the sum of O and O_3 is commonly referred to as odd oxygen. Only the destruction of ozone by reacting with atomic oxygen (1.4) provides a net sink of odd oxygen and balances the ozone production in a pure oxygen chemistry, but can as sole ozone destruction channel not explain observed stratospheric ozone abundances. Rather, the stratospheric ozone production is largely balanced by catalytic cycles as additional ozone sinks:

$$XO + O \rightarrow X + O_2 \tag{1.5}$$
$$X + O_3 \rightarrow XO + O_2 \tag{1.6}$$
$$\text{Net}: \quad O + O_3 \rightarrow 2\,O_2$$
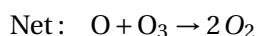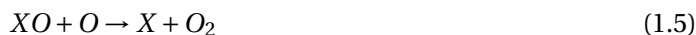
The net reaction of (1.5) and (1.6) is equal to (1.4). Reactive nitrogen (NO_x), chlorine (ClO_x) and hydrogen (HO_x) compounds are important catalysts (X), which are involved but not used up in these cycles. Their relative importance is depending on altitude. The NO_x cycle (Crutzen, 1970) dominates ozone loss between 25 and 40 km, whereas the ClO_x cycle (Molina and Rowland, 1974) dominates ozone destruction rates at around 40 km.

Photochemical formation and destruction of ozone in catalytic cycles govern the ozone distribution in the stratosphere. Additionally, transport of ozone from low to high latitudes is especially important in the lower stratosphere where the influence of photochemical processes gets smaller and ozone has a lifetime of several months. The Brewer-Dobson circulation, a large-scale mean meridional circulation pattern in the stratosphere, transports ozone from the tropics to the poles. The circulation is driven by planetary wave activities, oriented towards the winter pole and more strongly so in the northern hemisphere because of the stronger wave perturbations there. Although photochemical production rates and therefore peak values of ozone are highest in the tropics, the total ozone column is larger in mid and high latitudes, caused by dynamics (Müller, 2012, and references therein).

1.2   Polar stratospheric ozone depletion

Observational evidence for changes in the polar ozone layer were first published by Farman et al. (1985). They reported decreasing ozone levels in the Antarctic spring from ground based spectrophotometer measurements. Stolarski et al. (1986) confirmed the decline of total ozone by a reevaluation of ozone data seen by satellites, which had missed to detect this development earlier because of dismissed data, and for the first time described an "ozone hole" of large extent. The potential danger for the ozone layer of anthropogenic halogen emissions was first made by Molina and Rowland (1974), and also Farman et al. (1985) hinted in this direction, although it was clear that the Molina and Rowland cycle would not be able to explain the ozone hole. Human manufactured chlorine and bromine containing substances without natural sources, foremost chlorofluorocarbons (CFCs), were widely used in refrigerators, as propellants in aerosol cans and fire extinguishers at that time. They have been identified as major cause of the observed stratospheric ozone decline and are therefore named ozone depleting substances (ODSs). Although emitted in the troposphere, they eventually enter the strato-

sphere due to their long lifetimes of several decades. The most common CFCs are CFC-11 ($CFCl_3$) and CFC-12 (CF_2Cl_2). At high altitudes, UV radiation ($\lambda < 336$ nm) dissociates e.g. CFC-11

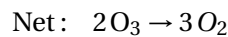$$CFCl_3 + h\nu \rightarrow CFCl_2 + Cl \tag{1.7}$$

and the released chlorine atom can serve as X in the catalytic cycles (1.5) and (1.6) that lead to the destruction of ozone. A response of the ozone layer above mid-latitudes can be attributed to the theory of Molina and Rowland (1974) but it neither explains ozone levels as low as observed above the Antarctic nor the seasonal occurrence in early spring. First, Solomon et al. (1986) pointed out that heterogeneous reactions on PSC surfaces might play a role in the polar ozone destruction. The stratosphere is essentially cloud free and only under extreme conditions as they occur above the poles in winter, clouds can form. Strong westerly winds encircle the winter poles and isolate the air within the jet stream from the mid-latitude stratosphere. Due to missing sunlight, temperatures decrease considerably within the so called polar vortex and enable even the small amounts of water and nitric acid to condense onto the preexisting stratospheric H_2SO_4-H_2O droplets, diluting them and possibly letting them freeze. In particular, the surface reaction

$$ClONO_2 + HCl \rightarrow Cl_2 + HNO_3 \tag{1.8}$$

activates chlorine reservoir species, so that molecular chlorine forms. At the same time, deactivation of chlorine into its reservoir chlorine nitrate ($ClONO_2$) via the NO_x cycle is hindered by denitrification. Denitrification describes the permanent removal of NO_y from the polar stratosphere by sedimentation of nitric acid HNO_3 containing PSC particles. Hence, chlorine remains in its active form. As soon as the first sunlight has sufficient intensity at the poles, molecular chlorine photodissociates in the near-UV and visible

$$Cl_2 + h\nu \rightarrow 2\,Cl \tag{1.9}$$

and efficient ozone destruction via the catalytic cycle of the ClO dimer follows (Molina and Molina, 1987):

$$2(Cl + O_3 \rightarrow ClO + O_2) \tag{1.10}$$

$$ClO + ClO + M \rightarrow Cl_2O_2 + M \tag{1.11}$$

$$Cl_2O_2 + h\nu \rightarrow 2\,Cl + O_2 \tag{1.12}$$

$$\text{Net}: \quad 2\,O_3 \rightarrow 3\,O_2$$

Even though bromine (Br) is about 160 times less abundant, bromine atoms are about 60 times more efficient in terms of their ozone destruction potential than chlorine in the stratosphere. Therefore, a second cycle depending on BrO concentrations is of similar importance as the ClO dimer cycle with the same net result, namely the destruction of two ozone molecules. Lowest ozone concentrations occur annually in early spring when the sun rises. In contrast to the catalytic cycle described by (1.5) and (1.6), which requires shortwave radiation to produce atomic oxygen, the sunlight found at the poles is sufficient to obtain large enough ClO abundances to efficiently destroy ozone. Figure 1.1a shows the Antarctic ozone hole on 26 September 2010 with chemical ozone losses larger than 100 DU compared to unperturbed times. Ozone depletion in the Arctic is less pronounced and much more variable from year to year than in the Antarctic. The Arctic polar vortex is generally warmer and less stable. Larger
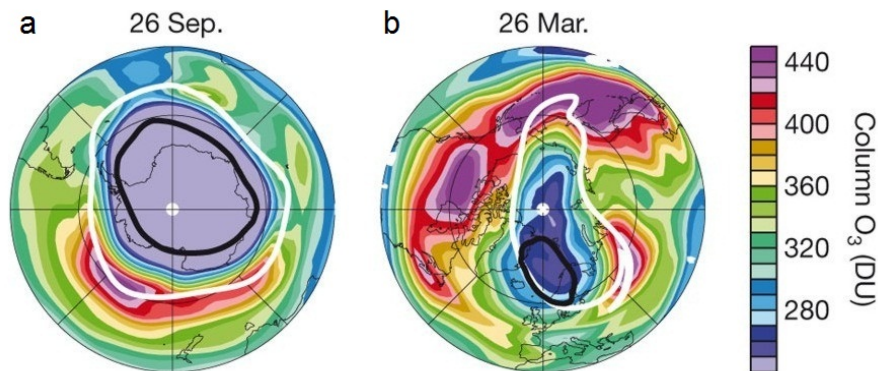
Figure 1.1: Ozone Monitoring Instrument (OMI) total ozone column in Dobson units (DU) in the (a) Antarctic on 26 September 2010 and (b) Arctic on 26 March 2011. Scaled potential vorticity (PV) contours of $1.4 \times 10^{-4}\,\mathrm{s}^{-1}$ (in vorticity units) are overlaid in white indicating the vortex edge. Black contour lines show temperature threshold for chlorine activation (196.5 K at 460 K isentropic surface). Figure taken from Manney et al. (2011).

land-ocean contrasts in the northern hemisphere generating atmospheric waves weaken the vortex and as a consequence, warm air masses from lower latitudes may mix into the polar vortex (Solomon, 2004). Recently, unusually long-lasting cold conditions led to an Arctic vortex, which persisted long enough to reach levels of chemical ozone destruction justifying the term Arctic ozone hole (Manney et al., 2011). Ozone concentrations as low as seen on 26 March 2011 in Fig. 1.1b have been unprecedented in the Arctic.

To protect the atmospheric ozone layer, the "Montreal Protocol on substances that deplete the ozone layer" was signed in 1987 and entered into force on 1 January 1989. It aims at reducing the production of ODSs and hence their atmospheric abundances. In the meantime, the protocol has undergone several revisions and it achieved universal ratification. Its success can be seen in passing peak values of mid-latitude stratospheric halogen loadings in the 1990s and in studies like "The world avoided" by Newman et al. (2009) demonstrating the future evolution of the ozone layer without the provisions of the Montreal Protocol. However, atmospheric halogen source gas levels drop only slowly due to their long lifetimes and residues not yet released to the atmosphere. The global ozone layer is expected to recover to values prior than 1980 in the year 2049 (Eyring et al., 2010), whereas the Antarctic ozone hole may recover from ODS emissions only in 2065 (WMO, 2011).

1.3   Motivation and outline

A complete and comprehensive knowledge of processes affecting stratospheric ozone is required to predict the future evolution of the ozone layer reliably. Although ODSs have been identified and their emissions are restricted by the Montreal Protocol, atmospheric ODS abundances are still high and lead to regular extensive ozone losses above the poles in both hemispheres. Principles of the ozone hole are well understood, but Arctic variability challenges our current knowledge. Due to short term changes in vortex evolution and temperature, a complete understanding of polar heterogeneous

chemistry and PSC microphysics is required to explain observed ozone losses. Models are still lacking accurate parameterizations and are therefore not able to capture this complexity (e.g. Rex et al., 2003; Lowe and MacKenzie, 2008). Deepening our understanding of atmospheric processes becomes even more important in consideration of climate change. Increasing greenhouse gas emissions causing global warming in the troposphere are associated with altering dynamics and cooling of the stratosphere (IPCC, 2007). While this development is expected to lead to faster ozone recovery over the mid-latitudes, at high latitudes this might increase the occurrence frequency of PSCs and cold Arctic winters with record ozone losses as in 2011 might become more likely.

The scope of this thesis is to advance knowledge about PSC formation. Until now, the composition of major liquid and solid PSC particles has been identified and different nucleation pathways explored. However, recent satellite observations on high spatial and temporal scales reveal that we are far from a complete understanding. Chapter 2 recapitulates the scientific background and previous knowledge about PSCs. It includes an overview about PSC measuring techniques and common classification schemes based on optical measurements. Within this thesis, microphysical processes were studied using data from the Arctic field campaign RECONCILE, which is described in Chpt. 3. New insights into heterogeneous formation of nitric acid trihydrate (NAT) and synoptic-scale ice clouds are presented in Chpt. 4 and 5, respectively. Unprecedented observations of vertical redistribution of stratospheric water (see Chpt. 6) and a subsequent microphysical modeling study (see Chpt. 7) are shown. A final discussion and an outlook given in Chpt. 8 complete the thesis.

Chapter 2

Scientific background

In the previous chapter, stratospheric ozone and the role of PSCs in the springtime depletion of polar ozone were introduced. The present chapter focuses on details of PSCs. PSC microphysics are described below, covering their composition and formation pathways. Additionally, instruments applied for PSC measurements within this thesis are presented. For a better understanding of the underlying optical techniques, the basic concept of light scattering by particles will be briefly introduced. Different approaches for PSC classifications have been developed during the past decades which will be discussed at the end of this chapter.

2.1 Polar stratospheric clouds

First reports about colorful PSC observations above the Scandinavian mountains go back to the late nineteenth century (Stanford and Davis, 1974). Their brilliant iridescence reminded of the shimmer of mother-of-pearl and over several decades, those clouds posed a riddle. They appeared in great height not being affected by the surface weather and motionless despite stormy winds at he ground (Dieterichs, 1950). In the middle of the last century, more and more details became known. Hesstvedt (1962) developed a two dimensional cloud model which summarized the state of the art knowledge. The mean height was confined to about 24 km. Stratospheric temperatures above the winter pole were known to be as low as - 80 °C and therefore close to ice saturation even though stratospheric air is extremely dry. At such low temperatures, a cooling connected to an adiabatic updraft of air is sufficient to freeze ice particles. Orographically induced mountain waves penetrate into the stratosphere, generating a quasi-stationary cold pool and explaining the motionlessness of the clouds. The connected rapid cooling results into almost monodisperse, micrometer-sized particle distributions which cause the colorful cloud appearance in the twilight sky by the particles' forward diffraction of sunlight (Peter and Grooß, 2012). With the satellite-borne sun photometer SAM II, McCormick et al. (1982) provided a first global picture of PSC occurrence and pointed out that PSCs are much more prevalent in the Antarctic than in the Arctic. The discovery of the Antarctic ozone hole by Farman et al. (1985) and the linkage to PSCs as key player in the ozone destruction cycle (Solomon et al., 1986) shifted the interest in PSCs from that of a scientific curiosity to a major field of research facing significant environmental impacts. Henceforth, intensive field work, laboratory studies and process related research was stimulated, which is briefly reviewed in the following sections.

2.1.1   The stratospheric aerosol layer

The global stratospheric aerosol layer is located in the lower stratosphere between the tropopause and about 30 km altitude, named after Junge et al. (1961) the "Junge layer". Aerosols within this layer are mostly small liquid droplets with sub-micrometer size and number densities up to $10\,\mathrm{cm}^{-3}$. Sulfuric acid (H_2SO_4) and water (H_2O) are the main constituent of those droplets, which are supercooled with respect to solid sulfuric acid hydrates. Therefore, the background aerosol particles are also termed supercooled binary solution (SBS $\equiv$ H_2SO_4-H_2O) droplets. At temperatures of 230 K and in thermodynamic equilibrium, the percentage of H_2SO_4 accounts for roughly 80 wt% within the droplet. H_2SO_4 is produced primarily by oxidation of sulfur dioxide (SO_2). Volcanic eruptions are the major source of SO_2 together with transport of tropospheric carbonyl sulfide (OCS) across the tropical tropopause (Brühl et al., 2012).

2.1.2   Composition and formation of polar stratospheric clouds

PSCs are composed of three major substances: water (H_2O), sulfuric acid (H_2SO_4) and nitric acid (HNO_3) that occur in the stratosphere with mixing ratios of about 5 ppmv, 0.2 ppbv and 10 ppbv, respectively, under volcanically quiescent conditions. This corresponds to about 160 tons per day of sulfur influx across the tropical tropopause, or 650 tons per day of aqueous sulfuric acid (SPARC, 2006). In addition, 20 to 100 tons per day of meteoritic material enter the stratosphere from above (Cziczo et al., 2001), constituting 3 to 15 wt% of the stratospheric aerosol. The meteoritic material is spread all over the globe and funneled into the polar winter stratospheres by the Brewer-Dobson circulation, leading to about 50 % of the total background aerosol droplets having a meteoritic core. These numbers are in agreement with Curtius et al. (2005) and supported by similar measurements performed within RECONCILE (von Hobe et al., 2012).

Airborne and ground-based lidar data gave evidence for the existence of solid and liquid PSC particles (e.g. Browell et al., 1990; Toon et al., 1990). Until now, many different particle types have been suggested and discussed but only the existence of ice, nitric acid trihydrate particles (NAT $\equiv$ $HNO_3\cdot$ $3\,H_2O$) and droplets of supercooled ternary solution (STS $\equiv$ HNO_3-H_2SO_4-H_2O) have been confirmed unequivocally, and that of nitric acid dihydrate particles (NAD $\equiv$ $HNO_3\cdot 2\,H_2O$) is thought to be likely. The following section is along the work of Lowe and MacKenzie (2008) and Peter and Grooß (2012).

The growth of liquid particles by uptake of HNO_3 into STS droplets with decreasing temperature was first shown by Zhang et al. (1993) and Molina et al. (1993). Whereas those authors believed that an uptake of HNO_3 leads most likely to the crystallization of NAT, Carslaw et al. (1994) demonstrated that results of his thermodynamic modeling study fitted aircraft measurements by Dye et al. (1992) best when assuming a supercooled solution. Figure 2.1a shows total particle volume observations obtained during a flight north of Stavanger versus simulations of liquid aerosol compositions. With decreasing temperature, H_2SO_4 concentration within the background aerosols decreases slowly whereas droplets start to take up HNO_3 (Fig. 2.1b). During this time period, the particle growth is moderate. At around 192 K, HNO_3 concentrations are as large as those of H_2SO_4 and the volume increases much stronger. This temperature is sometimes called T_{dew}, referring to the dew point of HNO_3, or T_{STS}, highlighting a significant increase in particle volume on the transition from aqueous sulfuric acid aerosols to liquid
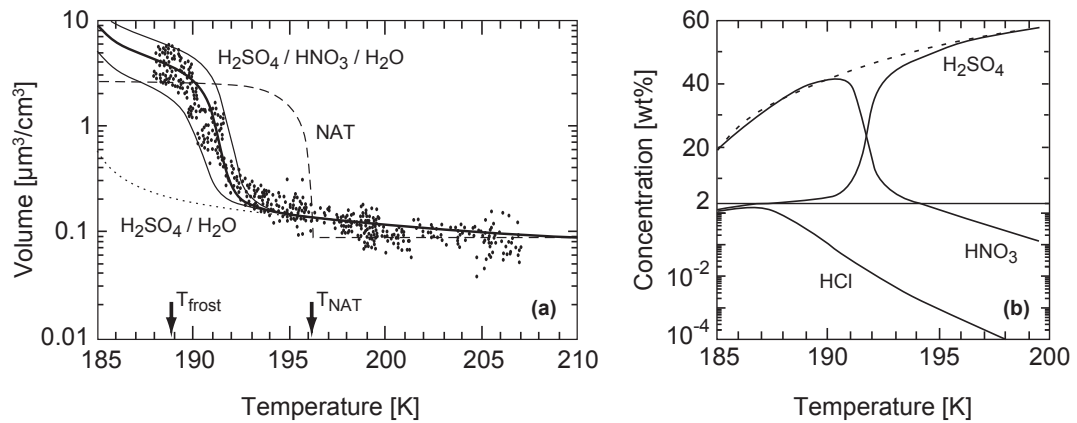
Figure 2.1: Volumes and concentrations of supercooled ternary solution (STS $\equiv$ HNO$_3$-H$_2$SO$_4$-H$_2$O) droplets as function of temperature. (a) Symbols: Arctic measurements by Dye et al. (1992) on 24 January 1989. Lines: model calculations of the volumes of various types of stratospheric particles in thermodynamic equilibrium with the gas phase: dotted line = supercooled binary solution (SBS $\equiv$ H$_2$SO$_4$-H$_2$O); dashed line = nitric acid trihydrate particles (NAT $\equiv$ HNO$_3$· 3 H$_2$O) (Hanson and Mauersberger, 1988); thick solid line = STS. Calculated volumes assume 5 ppmv H$_2$O and 10 ppbv total HNO$_3$ at 55 hPa, i.e. about 19 km altitude. Thin solid lines correspond to 5 ppbv and 15 ppbv HNO$_3$. (b) Weight fractions in STS droplets corresponding to thick solid line in (a). Solid curves: H$_2$SO$_4$, HNO$_3$, HCl (remaining fraction to balance 100 wt% is H$_2$O) according to Carslaw et al. (1994). Dotted line corresponds to H$_2$SO$_4$ in binary H$_2$SO$_4$-H$_2$O droplets. Figure and caption taken from Peter and Grooß (2012).

STS particles. The observations lie within a range of plausible total HNO$_3$ mixing ratios between 5 to 15 ppbv. Fully developed STS droplets can grow to sizes of around 0.3 µm radius (Carslaw et al., 1994). The assumption of pure H$_2$O uptake by the particles does not agree with the measurements. Particle volumes of SBS remain too small even at lowest temperatures.

Laboratory studies by Hanson and Mauersberger (1988) have shown that NAT is thermodynamically the most stable solid hydrate under stratospheric conditions. The authors performed accurate vapor pressure measurements and their parameterization is implemented in most state-of-the-art microphysical models. The equilibrium temperature of NAT (T_{NAT}) lies well above the ice frost point (T_{frost}). It corresponds to 196 K at 55 hPa assuming 5 ppmv H$_2$O and 10 ppbv total HNO$_3$. Observational evidence for the existence of NAT have been provided by balloon-borne measurements of Voigt et al. (2000), who measured a stoichiometric ratio of 3:1 between H$_2$O and HNO$_3$ at temperatures above T_{frost}. However, the assumption of NAT formation taking place without a nucleation barrier at temperatures as low as T_{NAT} could not be confirmed. On the one hand expected particle volumes resulting from spontaneous NAT nucleation at T_{NAT} and subsequent growth do not agree with the observed particle growth by Dye et al. (1992) as shown in Fig. 2.1a, on the other hand homogeneous nucleation of NAT at temperatures above T_{frost} has been clearly ruled out by laboratory bulk experiments (Koop et al., 1995; Knopf et al., 2002). Therefore, HNO$_3$ vapor deposition on ice surfaces was the only well characterized pathway of NAT formation, which was supported by laboratory evidence till now. Bier-

mann et al. (1998) and Middlebrook et al. (1996) proposed the possibility of NAT coated ice and Luo et al. (2003b) corroborated this idea by microphysical modeling. Downstream of mountain waves, high NAT supersaturations allow for the development of high number density NAT clouds on ice surfaces (number densities in the order of 10^{-1} cm^{-3}). Those clouds can act as "mother clouds" and individual NAT particles falling out of these clouds in low number densities can grow to large sizes of up to 10 μm (Fueglistaler et al., 2002). The exclusivity of NAT formation on ice particles has been doubted by several scientists in the past decade (e.g. Pagan et al., 2004; Larsen et al., 2004; Voigt et al., 2005). However, unambiguous observational proof for a heterogeneous nucleation pathway of NAT at temperatures above T_{frost} was missing so far.

Ice PSCs can exist only at temperatures below T_{frost} which corresponds to 189 K under the same conditions as in Fig. 2.1 (55 hPa, 5 ppmv). Temperatures within the Antarctic vortex drop below T_{frost} almost every year on large-scale, whereas synoptic-scale temperatures in the Arctic are rarely lower than this threshold. Localized cold pools generated by orographic mountain waves are typical spots for the occurrence of ice PSCs in the northern hemisphere. Homogeneous ice nucleation from liquid STS droplets can be expressed as a function of water activity and pressure (Koop et al., 2000) and requires a supercooling of $T \lesssim T_{\text{frost}}$ - 3 K (e.g. Koop et al., 1998). Number densities of ice clouds are very much dependent on the cooling rate of the air parcel (Hoyle et al., 2005). Synoptic-scale ice PSCs with number densities of 10^{-3} to 10^{-1} cm^{-3} can grow to larger sizes. The entire background aerosol of 10 cm^{-3} can freeze in wave events with high cooling rates and ice particle radii remain smaller than about 2 μm.

Other acid hydrates at cold stratospheric temperatures have been discussed in the past. Sulfuric acid tetrahydrate (SAT ≡ $H_2SO_4 \cdot 4\,H_2O$) and nitric acid dihydrate particles (NAD ≡ $HNO_3 \cdot 2\,H_2O$) are only two out of the "stratospheric particle zoo" (Koop et al., 1997). However, the different HNO_3 and H_2SO_4 hydrates will not be examined further in this thesis, because convincing observational evidence for their existence and their implication in PSC formation is missing. Figure 2.2 illustrates the conventional understanding of PSC formation summarizing particle types and pathways whose existence is strongly supported by observations and laboratory studies.

2.2 Light scattering of atmospheric particles

Scattering and absorption by air molecules, aerosol particles, cloud droplets, or ice crystals attenuate radiation on its way through the atmosphere. The Beer-Lambert law describes the exponential reduction in light intensity through a certain medium (here: the atmosphere) by scattering and absorption as

$$I = I_0 \cdot e^{-l \cdot k_{\text{ext}}}, \tag{2.1}$$

where I_0 is the intensity of the incident beam and I is the attenuated intensity at any length (l) into the medium. The so called extinction coefficient k_{ext} is the sum of the scattering and absorption coefficients with units of inverse length:

$$k_{\text{ext}} = k_{\text{scat}} + k_{\text{abs}}. \tag{2.2}$$

Light is scattered by molecules and particles in specific directions. The scattered light intensity at a particular scattering angle (θ) relative to the incident light beam is defined by the particle's scattering
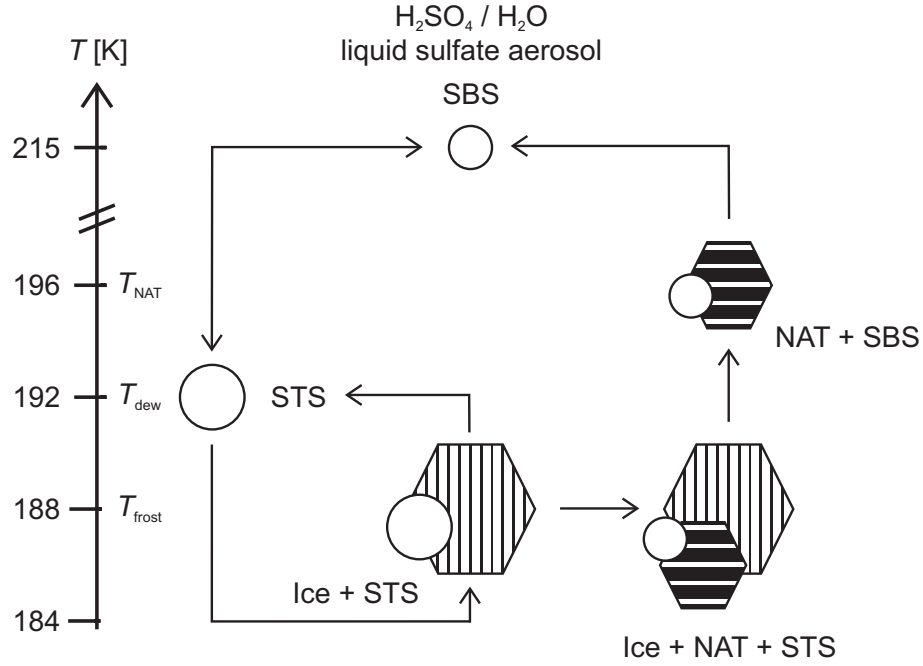
Figure 2.2: Potential PSC formation pathways as discussed within Sect. 2.1.2 including supercooled binary solution (SBS $\equiv$ H$_2$SO$_4$-H$_2$O), supercooled ternary solution (STS $\equiv$ HNO$_3$-H$_2$SO$_4$-H$_2$O), nitric acid trihydrate particles (NAT $\equiv$ HNO$_3 \cdot$ 3 H$_2$O), and ice particles. Simplified after Koop et al. (1997).

phase function (Marshall et al., 1995), which has units of per Steradian (sr^{-1}). As the particle increases in size, the forward-scattering becomes the dominant direction.

Scattering and absorption characteristics depend on compositions, sizes and shapes of atmospheric particles and also on the wavelength (λ) of the incident light. The particles composition is reflected by the refractive index (m), which describes the propagation of radiation through the particle with respect to the surrounding medium; m can be further separated into a real and an imaginary part representing nonabsorbing and absorbing components of the particle, respectively. The distinction between real and imaginary part becomes important when studying atmospheric aerosol particles with large fractions of soot and carbon. The absorbing component of stratospheric aerosol particles at common laser wavelengths is not significant and will be neglected.

The dimensionless Mie parameter is defined as the relation between the particle's radius (r) and λ:

$$x = \frac{2\pi r}{\lambda}. \tag{2.3}$$

On the basis of x, scattering of spherical particles can be divided into three categories (Seinfeld and Pandis, 2006):

- $x \ll 1$: Rayleigh scattering

  Rayleigh scattering describes the scattering of spherical particles which are small compared to the corresponding wavelength. Therefore, Rayleigh scattering is often referred to as molecular scattering and the scattering intensity is proportional to $1/\lambda^4$. Hence, shorter wavelengths scatter more efficiently than longer wavelengths. This relationship explains the blue color of the sky. At sunset, the blue component is partly scattered out and only redder components are left on the line of sight.
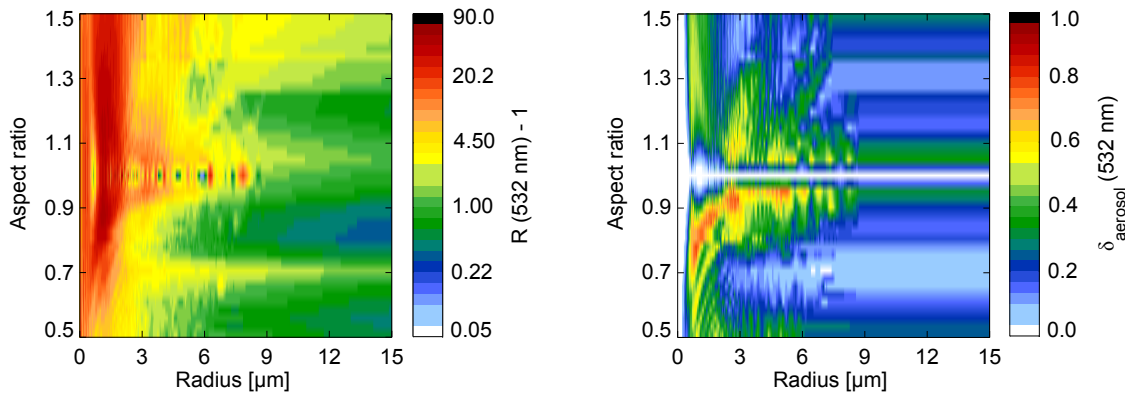
Figure 2.3: T-Matrix calculations for wavelength $\lambda = 532\,\text{nm}$ at 80 hPa, 190 K and 1 ppmv H_2O frozen as ice. Color-coded representations of (a) aerosol backscatter ratio ($R-1$) and (b) aerosol depolarization (δ_{aerosol}) as a function of particle radius and aspect ratio. Courtesy of Beiping Luo.

- $x \simeq 1$: Mie scattering

  Mie theory can serve as the basis of a computational procedure to calculate the scattering and absorption of light by any sphere as a function of wavelength. In 1908, Gustav Mie established the theory by solving the Maxwell equations (Mie, 1908). It is valid for spherical particles with sizes the same order of magnitude as the wavelength of the incident light. Further details can be found in the literature (e.g. Bohren and Huffman, 2004).

- $x \gg 1$: Geometric scattering

  Particles much larger than λ can be determined on the basis of the geometrical optics. However, this regime will not be discussed here.

However, particle shapes of ice and NAT crystals in PSCs deviate from spheres and need a different treatment in backscatter and extinction calculations. The transition-matrix method (T-matrix method) (see e.g. Waterman, 1971; Mishchenko et al., 2010, and references therein) provides solutions of the Maxwell equations as the Mie theory does, but assumes aspherical particles being similar to spheroids. It can be considered as an extension of the Mie theory which is computationally efficient owing to its matrix notation. Although the method is limited to rotationally symmetric particle shapes, one can model a wide variety of prolate and oblate shapes by changing the particle's aspect ratio. The effect of a change in the length-to-diameter ratio from 0.5 (prolate) to 1.5 (oblate) is shown in Fig. 2.3 with an aspect ratio of 1 equal to a sphere.

2.2.1 Main optical properties

The total volume backscatter coefficient (β) can be formulated as

$$\beta(\lambda) = \beta_{\text{mol}}(\lambda) + \beta_{\text{aerosol}}(\lambda) \tag{2.4}$$

and is normally expressed in units of $\text{km}^{-1}\text{sr}^{-1}$. β is composed of the individual backscatter coefficients by molecules (β_{mol}) and aerosols (β_{aerosol}), which can be further separated into contributions

of parallel (β_{para}) and perpendicular (β_{perp}) backscatter. In perfect (180°) backscatter, spherical particles do not change the polarization plane of originally polarized light, whereas aspherical particles change the polarization of the light and a scattering component perpendicular to the original polarization plane is detectable. Therefore, irregular shaped particles can be characterized and distinguished from droplets by high values of depolarization (δ), defined as the ratio between the parallel to the perpendicular component:

$$\delta(\lambda) = \frac{\beta_{\mathrm{perp}}(\lambda)}{\beta_{\mathrm{para}}(\lambda)}. \tag{2.5}$$

δ includes contributions from aerosols and molecules, but it can also be defined separately as either molecular (δ_{mol}) or aerosol depolarization ($\delta_{\mathrm{aerosol}}$). The pure molecular depolarization is assumed to be 0.0036 (Cairo et al., 1999). $\delta_{\mathrm{aerosol}}$ refers only to aerosols and yields useful information for cloud particle characterization.

The ratio of the total to the molecular backscatter coefficient is another direct index for the presence of aerosols and is termed backscatter ratio (R):

$$R(\lambda) = \frac{\beta_{\mathrm{mol}}(\lambda) + \beta_{\mathrm{aerosol}}(\lambda)}{\beta_{\mathrm{mol}}(\lambda)}. \tag{2.6}$$

Similarly, the aerosol backscatter ratio is equal to $R - 1$. The use of two different wavelengths open up the possibility to calculate the color index (CI):

$$CI = \frac{R(\lambda_1) - 1}{R(\lambda_2) - 1}. \tag{2.7}$$

Information about particle sizes can be obtained from the CI by assuming the particle's size distribution, shapes and refractive indices. The range of CI varies from 1 for very small (sub-micron) particles up to around $(\lambda_1/\lambda_2)^4$ for large (a few micrometers) particles (Rosen and Kjome, 1991). Above this limit, Mie oscillations inhibit distinct radii information.

2.3 Instrumentation

Light detection and ranging (lidar) systems are optical remote sensing technologies to observe the vertical structure of clouds and aerosols in the atmosphere. Pulsed laser beams are commonly used to determine the backscatter of particles as a function of time. With CALIPSO, a spaceborne lidar will be presented in detail. Profiles obtained from the backscatter sonde COBALD are similar to those generated from lidar systems and introduced within this section as well.

2.3.1 CALIPSO satellite

The Cloud-Aerosol Lidar and Infrared Pathfinder Satellite Observations (CALIPSO) satellite was launched on 28 April 2006 and retrieves global data since June 2006. CALIPSO is part of the NASA Afternoon Constellation (A-Train), which currently includes the satellites Aqua, CloudSat, PARASOL, and Aura besides CALIPSO. The naming originates in the equator crossing time of the satellites shortly after noon at about 1:30 pm. The satellites closely follow each other along the same track describing a sun-synchronous polar orbit at an altitude of 705 km. Due to an orbit inclination of 98.2°, the globally
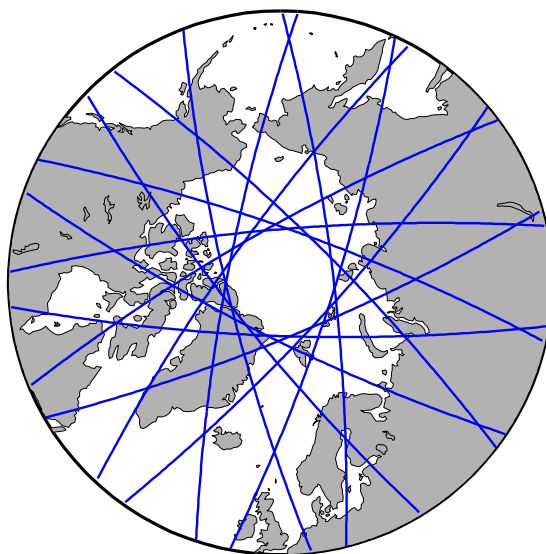
Figure 2.4: Typical CALIPSO measurement coverage above the Arctic. The orbit tracks are colored in blue and span 24 hours on 01 January 2010.

covered area ranges from 82° N to 82° S and each satellite completes 14.5 orbits per day with a repeat rate of 16 days (Stephens et al., 2002). Figure 2.4 gives an impression of the high polar coverage of A-Train overpasses within 24 hours.

The satellites obtain nearly simultaneous measurements of aerosols, clouds, trace gases, temperature, relative humidity, and radiative fluxes to study the earth's atmosphere and improve our understanding of weather and climate. The CALIPSO mission within the A-Train was developed to provide global profiling measurements of cloud and aerosol distribution and properties. The Cloud-Aerosol Lidar with Orthogonal Polarization (CALIOP) is the primary instruments aboard CALIPSO. CALIOP is the first spaceborne lidar comprising polarization, which was designed for aerosol and cloud measurements. Vertical profiles of elastic backscatter are acquired from a near nadir-viewing geometry during both, day and night. The Nd:YAG laser operates at two different wavelengths, 532 and 1064 nm, including a differentiation between parallel and perpendicular polarization at 532 nm. Profile data of total attenuated backscatter coefficients in units of $km^{-1}sr^{-1}$ are reported in the Level 1 data product and will be transmitted at different averaging resolutions. Since CALIPSO's primary focus are tropospheric processes, data provided for lower altitudes are transmitted at a higher resolution than within the altitude range relevant for PSC occurrence. Samples between 8.2 and 20.2 km are downlinked with a horizontal resolution of 1 km and a vertical spacing of 60 m. Moving up to 30.1 km, the horizontal resolution decreases to 1.67 km with 180 m vertical distance (Winker et al., 2003, 2007). However, CALIPSO's extensive polar coverage, as already seen in Fig. 2.4, turns the satellite to an ideal tool for PSC studies. More details about the PSC detection algorithm are given in Sect. 2.4.

2.3.2 COBALD backscatter sonde

The Compact Optical Backscatter Aerosol Detector (COBALD) has been engineered at ETH as a follow up development of the backscatter sonde by Rosen and Kjome (1991). It is designed to complement the payload of operational weather balloons and with approximately 500 g total weight, it is much lighter than its parent and not subject to aviation safety limitations. The operation scheme of COBALD is illustrated in a simplified way in Fig. 2.5. COBALD has two LEDs, each with approximately 250 mW optical power, at wavelengths of 455 and 870 nm. Backscattered light is detected with a frequency of typically 1 Hz. The detector is placed between the two LEDs with the optical axes aligned in parallel. Overlap between the emission's and the detector's reception fields of view is established at distances larger than 0.5 m in front of the instrument. Since the detected light decreases with the square of the scattering region distance, a range of up to 5 m is probed by the sonde. The viewing geometry of COBALD is such that backscatter is detected over an angular distribution of $\theta = 174° \ldots 180°$. So far, the instrument is designed for applications during night time only as solar radiation saturates the photodetector (Brabec, 2011).

The data analysis of Rosen and Kjome (1991) is followed to separate the individual contributions from molecules and aerosols to the measured backscatter signal. Molecular number densities can be derived from temperature and pressure recorded simultaneously by the hosting radiosonde. R (455 nm) is normalized to minimum values of 1.05 in clean air. The profile at 870 nm is adjusted such that the combination of both wavelengths as CI do not fall below a minimum value of five. A CI of less than five would imply an unrealistically high number density of small particles at the aerosol backscatter level commonly encountered (personal communication of Frank Wienhold).

The usage of the Wyoming backscatter sonde varied from observations of volcanic aerosol (Rosen et al., 1992) over cirrus (Beyerle et al., 2001) to polar stratospheric clouds (Larsen et al., 2004). COBALD has already been applied in different field studies (e.g. Bukowiecki et al., 2011; Brabec et al., 2012) as well.
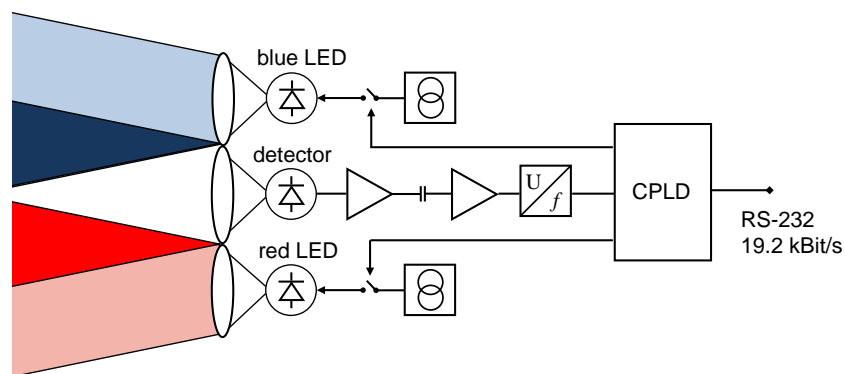

Figure 2.5: Operation scheme of COBALD. The blue and red LED emit light whose backscatter is recorded by the detector. The simplified electronics displayed is explained in the text (courtesy of Frank Wienhold).

2.3.3   Backscatter measurement intercomparison

During the RECONCILE campaign, described in detail within Chpt. 3, the opportunity was taken to obtain several COBALD measurements simultaneously to particle backscatter measurements by CALIOP and the elastic backscatter lidar in Ny-Ålesund.

A comparison between COBALD and CALIOP is shown in Fig. 2.6a. COBALD measurements were transformed to 532 nm using the Ångström law. Both measurements took place on 17 January 2010. The balloon sounding was timed in a way that COBALD reached an altitude of 20 km at the satellite's overpass time. Therefore, the agreement between the two vertical backscatter profiles is best in the stratosphere. CALIOP profile No. 100117.3969729769 (Orbit 2010-01-17T09-30-00Z) was about 25 km away from stratospheric air masses seen by COBALD. This range of uncertainty is expressed by including the range of backscatter values from CALIOP within ± 25 km around the selected profile as a gray shaded area.

The comparison of backscatter profiles between COBALD and the Ny-Ålesund lidar is limited to only few measurements in February 2010 for technical reasons. The period of cold stratospheric temperatures and extensive PSC occurrences was already finished at that time. On the 02 February 2010, a thick cirrus cloud was observed by both instruments. It was persistent in altitude with changing backscatter intensities during the evening. The Ny-Ålesund lidar was operating during the entire balloon flight. Cloud variability seen by the Ny-Ålesund lidar is illustrated by the gray area in Fig. 2.6b with the first 10 min mean profile highlighted in black.

The overall agreement between measurements by COBALD and CALIOP as well as between COBALD and the Ny-Ålesund lidar is convincing and even small-scale structures are represented in both measurements.

2.4   Polar stratospheric cloud classification by means of lidar measurements

Lidar measurements enable the detection of clouds and the determination of their altitude and vertical extent. Measurements at different wavelengths are needed to retrieve information on particle radii and the acquisition of parallel and perpendicular polarized components of backscattered light make a distinction between spherical and aspherical particles possible (see Sect. 2.2). Antarctic lidar measurements comprising information of R and $\delta_{\mathrm{aerosol}}$ stimulated Browell et al. (1990) and Toon et al. (1990) to introduce a first PSC classification scheme. They observed three major PSC types: Type Ia is characterized by a combination of small R and significant $\delta_{\mathrm{aerosol}}$, Type Ib by moderate R without $\delta_{\mathrm{aerosol}}$, and Type II by large R and a significant $\delta_{\mathrm{aerosol}}$. Browell et al. (1990) and Toon et al. (1990) interpreted Type Ia as NAT particles, Type Ib as liquid ternary aerosols and Type II as ice particles (compare Tab. 2.1).

Theoretical calculations of optical properties can be of advantage to interpret lidar data more precisely in terms of particle sizes and number densities. However, optical calculations are not exclusive and a misinterpretation is possible. Figure 2.7 shows plausible PSC compositions of STS, NAT and ice and their position within the optical space defined by inverse R and $\delta_{\mathrm{aerosol}}$. The following parameters are
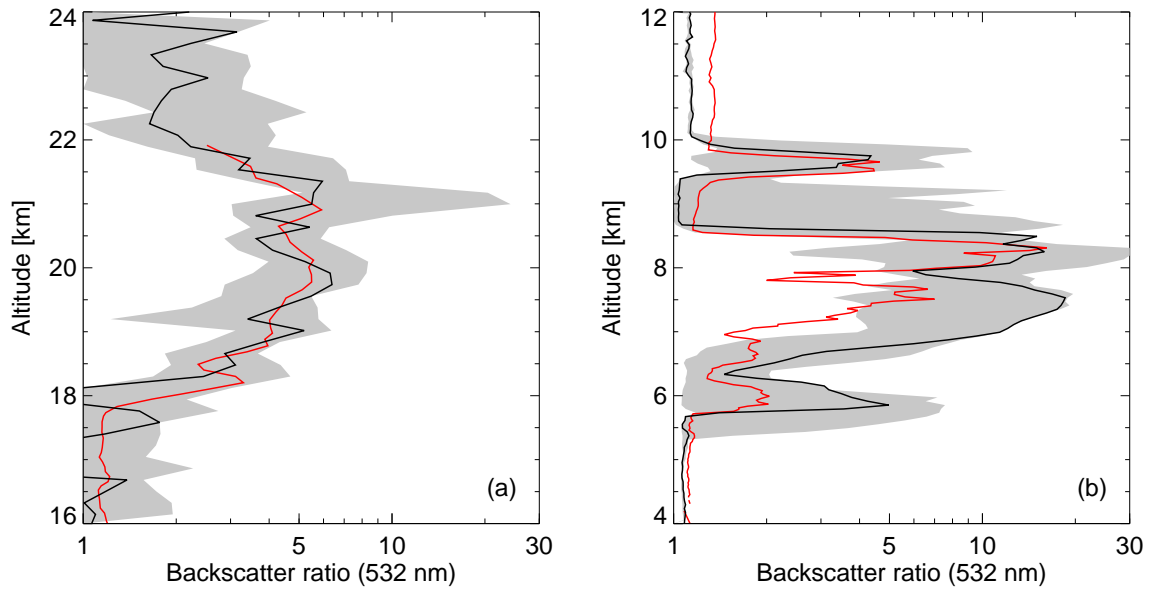
Figure 2.6: Backscatter measurements obtained by COBALD in comparison to (a) CALIOP and (b) the Ny-Ålesund lidar. In both profiles, COBALD backscatter ratios are shown in red calculated for 532 nm. (a) COBALD - CALIOP comparison on 17 January 2010. The gray shaded area comprises maximum and minimum backscatter values from CALIOP within a range of ± 25 km around the CALIOP profile (100117.3969729769) closest to COBALD and emphasized in black. (b) COBALD - Ny-Ålesund lidar comparison on 02 February 2010. Both measurements are taken between 17:25 UTC and 19:15 UTC. The first 10 min interval of the Ny-Ålesund lidar is shown in black and the gray shaded area illustrates the variability of the lidar signal during the period of the balloon flight.

chosen based on common literature (e.g. Dye et al., 1992): Lognormal particle size distribution with a standard deviation (σ) = 1.8 and a total number density = 10 cm^{-3} for STS and with σ = 1.6 and varying number densities for NAT and ice. Mode radii are calculated from condensed volumes depending on temperature. At 50 hPa atmospheric pressure and total mixing ratios of 5 ppmv H_2O and 10 ppbv HNO_3, temperatures were varied from -4 to 6 K relative to T_{frost}. For the optical calculations, indices of refraction are 1.44 (STS), 1.31 (ice) and 1.48 (NAT). The aspect ratio of 0.9 for ice and NAT has been chosen to obtain maximum values of R and depolarization with the T-matrix method (see Fig. 2.3).

Due to different abundances of H_2O and HNO_3 in the stratosphere, ice particles can occur in either higher number densities or with larger radii than NAT particles. Typical number densities for NAT lie in the range from 10^{-4} to 10^{-1} cm^{-3} and those for ice are about two orders of magnitude higher. The effect of increasing number densities and/or radii in the optical calculations can be seen in Fig. 2.7. The larger particle volumes are, the higher values of R and $\delta_{aerosol}$ get. Increasing ensemble number densities are illustrated by a darkening of the color and cause a strengthening of the optical signal. Keeping the number density constant (same color), an increase in R and $\delta_{aerosol}$ can be obtained by increasing particle sizes. The effect of changing temperatures for an ensemble of NAT and STS particles at a constant NAT number density and mode radius is illustrated by the red curves in Fig. 2.7.
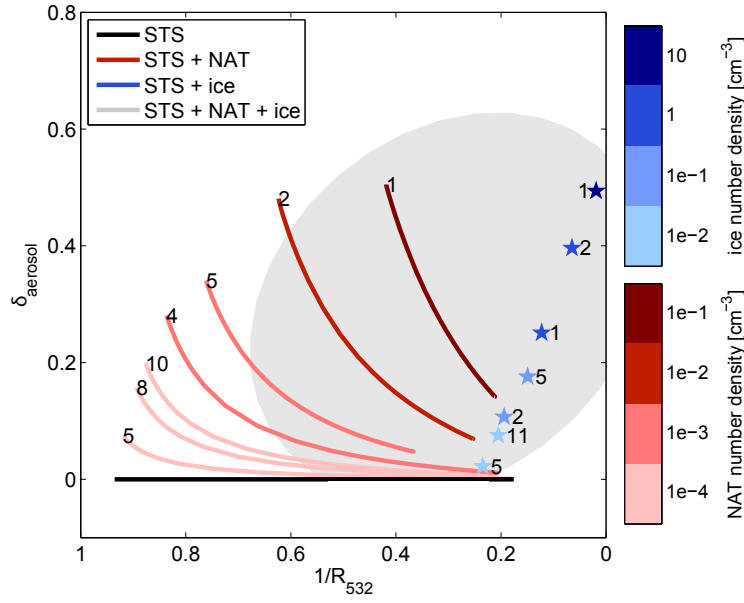
Figure 2.7: Theoretical calculations of backscatter and depolarization characteristics (at λ = 532 nm) by supercooled ternary solution (STS $\equiv$ HNO$_3$-H$_2$SO$_4$-H$_2$O), nitric acid trihydrate (NAT $\equiv$ HNO$_3$· 3 H$_2$O) and ice particles. Black line = pure STS. Red colors = mixtures of STS and NAT. NAT number densities vary from 10^{-4} cm^{-3} (light red) to 10^{-1} cm^{-3} (dark red), in geometric steps of 10. Along individual lines, temperature decreases from the left (6 K > T_{frost}) to the right (4 K < T_{frost}). Blue colors = mixtures of STS and ice. Ice number densities vary from 10^{-2} cm^{-3} (light blue) to 10 cm^{-3} (dark blue), in geometric steps of 10. Particle mode radii [µm] are given as numbers in the plot. Gray area = optical space feasible to fill by mixtures of coexisting STS, NAT and ice particles. More details about the calculations are given in the text.

Along each curve, temperature decreases from the left (6 K > T_{frost}) to the right (4 K < T_{frost}). At warm temperatures, NAT particles are surrounded by small liquid background aerosols and R remains relatively small. With decreasing temperatures, the background aerosol takes up HNO$_3$ and grows to STS droplets as already seen in Fig. 2.1. The curve converges toward the STS line and the δ_{aerosol} signal of NAT particles becomes more and more masked by the growth of STS, responsible for the increase in R. An ensemble of STS and ice has generally higher R than STS and NAT mixtures which provides a possibility to distinguish those PSC types. However, the gray shaded area illustrates an optical region in where the coexistence of STS, NAT and ice particles is possible. For the interpretation of lidar data, additional parameters such as temperature information are useful. If e.g. temperatures are higher than T_{frost}, the presence of ice particles can be excluded.

Today, several different PSC classifications exist (e.g. Santacesaria et al., 2001; Adriani et al., 2004; Blum et al., 2005; Massoli et al., 2006) out of which the classification by Biele et al. (2001) and Pitts et al. (2011) will be discussed in more detail.

The classification defined by Biele et al. (2001) is based upon lidar measurements from Ny-Ålesund comprising data from the Arctic winters 1995 to 1997. Whereas most classifications employ total R and δ_{aerosol} to distinguish particle types, as Browell et al. (1990) and Toon et al. (1990) did, Biele et al. (2001) used parallel R (R_{para}) and perpendicular R (R_{perp}) on the grounds that "this set of observables
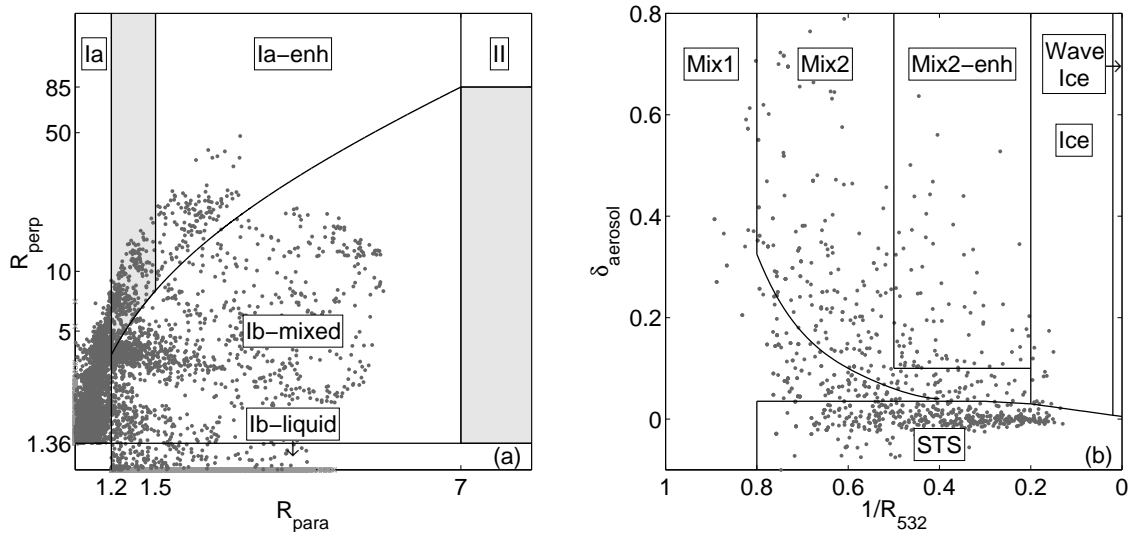
Figure 2.8: Polar stratospheric cloud (PSC) definitions based on (a) Biele et al. (2001) and (b) Pitts et al. (2011). Underlying data points show measurements from (a) the Ny-Ålesund lidar and (b) CALIOP at locations closer than 2.5° to Ny-Ålesund in the Arctic winter 2007/2008. Definitions of particle compositions are given in Tab. 2.1. (a) PSC composition types according to Tab. 1 in Biele et al. (2001). Background aerosols are defined as $R_{\mathrm{para}} < 1 + 2 \cdot \varepsilon$ with a standard deviation $\varepsilon = 0.1$ and $R_{\mathrm{perp}} < 1 + 2 \cdot \varepsilon$ with $\varepsilon = 0.18$. Light gray crosses along both axes show data with calculated $R < 1$. (b) PSC composition classes defined by Pitts et al. (2011). Detailed information about the PSC threshold computations are given in Pitts et al. (2009).

is the better choice for judging the properties of aerosol ensembles" (Biele et al., 2001). A graphical representation of the PSC type definitions is shown in Fig. 2.8. The underlying data set comprises Ny-Ålesund lidar measurements from the Arctic winter 2007/2008. Lidar profiles were averaged to a standard height resolution of 150 m over 10 minutes. Neither in the years 1995 to 1997 nor in the more recent winter 2007/2008, Type II PSCs with $R_{\mathrm{para}} > 7$ were observed in Ny-Ålesund. The majority of measurements are mixtures of NAT and liquid particles. Measurements with $R_{\mathrm{perp}} < 1 + 2 \cdot \varepsilon$ are supposed to consist of purely liquid particles (Ib-liquid). Observations are assigned to Type Ia if $R_{\mathrm{perp}} > 1 + 2 \cdot \varepsilon$ and $R_{\mathrm{para}} < 1 + 2 \cdot \varepsilon$. R measurements exceeding two times the standard deviation (ε) in both polarizations are assumed to be mixtures with higher number densities of NAT particles (Type Ib-mixed and Ia-enh). Table 2.1 summarizes the details of the PSC classification by Biele et al. (2001) amongst others.

One of the newest PSC classifications is based on lidar data from the satellite CALIPSO. The latest improvement of the composition classification algorithm was done by Pitts et al. (2011) based on observations from four Arctic and five Antarctic seasons. Figure 2.8b illustrates the different domains within the 2-D scatter plot of inverse R_{532} ($1/R_{532}$) and $\delta_{\mathrm{aerosol}}$. The SNR is much lower than for ground-based systems. Therefore, the detection of PSCs as statistical outliers of the stratospheric background aerosol signal is already crucial and done in terms of either R_{532} or β_{perp}. Optically thick ice clouds are detectable at the standard resolution of 5 km horizontal and 180 m vertical resolution. For tenuous NAT clouds, a successive averaging up to 135 km in horizontal direction is possible and NAT clouds with number densities as low as $3 \cdot 10^{-4}$ cm^{-3} become detectable. Mixtures of NAT clouds are sorted accord-

Table 2.1: PSC composition classifications presented in the style of Peter and Grooß (2012). The PSC notation of Biele et al. (2001) and Pitts et al. (2011) is listed together with a common interpretation of physical composition, number densities and particle radii. The terminology mixture refers to a coexistence of hydrate particles and binary or ternary droplets. Please note that given values for Type II as defined in Fig. 2.8a are only true for ice number densities > 0.5 cm^{-3} and ice particle radii < 3 μm. Additionally, cloud fractions of CALIOP PSC measurements in the Arctic winter 2009/2010 are shown as percentage of each composition class. The classification by Biele et al. (2001) leaves 21 % unclassified.

Pitts et al. (2011)		Biele et al. (2001)				
Class	Cloud fraction [%]	Type	Cloud fraction [%]	Physical composition	Number density [cm^{-3}]	Mean radius [μm]
STS	25.6	**Ib-liquid**	13.9	ternary droplets	~ 10	~ 0.3
Mix1	27.5	**Ia**	19.1	mixture with few hydrate particles	< 10^{-3}	1 - 10
Mix2	29	**Ib-mixed**	14.6	mixture with some hydrate particles	10^{-3} − 10^{-1}	~ 0.3
Mix2-enh	14	**Ia-enh**	29.9	mixture with many hydrate particles	> 10^{-1}	~ 0.3
Ice	3.7	**II**	1.6	ice particles	10^{-3} − 10^{-1}	> 1.5
WaveIce	0.2				~ 10	1 - 1.5

ing to NAT number densities similar to the classification by Biele et al. (2001). One major difference is a further separation of the ice class into synoptic-scale and wave ice. Ice clouds generated by orographically induced mountain waves experience high cooling rates through which almost the entire background aerosol freeze. With number densities close to 10 cm^{-3}, particle radii remain small. Optical signatures of wave ice clouds differ from synoptic-scale ice by higher R and high δ_{aerosol}. The PSC composition domains are shown in front of CALIOP data in Fig. 2.8b. Within a distance of 2.5° around Ny-Ålesund, CALIOP measurements haven been selected for those days of the winter 2007/2008, on which the Ny-Ålesund lidar was operating.

The majority of both data sets in Fig. 2.8 are liquid/NAT mixtures. The different SNRs of both instruments might explain that weakly backscattering particles are detectable by the ground-based lidar, whereas they are not distinguishable from the background by CALIOP. A comparison between both classifications based on the CALIOP data from the RECONCILE winter 2009/2010 is embedded in Tab. 2.1. Only observations which have already been detected as statistical outliers from the background aerosol were taken into account. Cloud fractions separated into the different classes/types over the season for either classification have been determined. Again, most of the observations are mixtures of NAT and liquid particles. 25 % of all PSCs fall into the STS class according to Pitts et al. (2011), whereas only 14 % are typed as pure liquids using Biele et al. (2001). More differences can be seen focussing on ice particles. 1.6 % of all PSCs belong to Type II with Biele et al. (2001), while almost 4 % are ice PSCs using Pitts et al. (2011). The definition of Biele et al. (2001) leaves 21 % of all observations unclassified, namely those points falling into the gray shaded areas of Figure 2.8a.

Within the work of this thesis, lidar data from the satellite CALIPSO have been used extensively and the classification by Pitts et al. (2011) has been applied for consistency.

Chapter 3

RECONCILE
Arctic field campaign 2009/2010

"Reconciliation of essential process parameters for an enhanced predictability of arctic stratospheric ozone loss and its climate interactions", short RECONCILE, is an European Union (EU) funded project running from 2009 to 2013. RECONCILE aims at a better understanding of the physical and chemical processes controlling stratospheric ozone, with a focus of the future development of the ozone layer taking into account interactions with climate change. To address open questions, the project uses field observations, laboratory experiments, as well as microphysical and chemical modeling studies. Details about the RECONCILE project, the objectives, a complete summary of measurement and modeling activities, and the major outcomes are given in the overview paper by von Hobe et al., 2012. The following chapter is meant to shortly introduce the RECONCILE project to the reader and to put the work of this thesis, presented by the following publications, in the broader perspective.

Within RECONCILE, an extensive Arctic field campaign was carried out comprising two measurement periods in early 2010. The high altitude research aircraft Geophysica was located in Kiruna, Sweden, with a mission of 57 flight hours total. During the first period (17 January - 02 February 2010), eight aircraft flights with focus on PSC characterization and chlorine activation were carried out. The second phase started on 27 February 2010 and comprised additional five flights focusing on measurements related to chlorine deactivation, ozone loss, de- and renitrification. Until 10 March 2010, late winter conditions have been studied and a vortex survey carried out. Geophysica's instrumental payload comprised in situ and remote sensing instruments. Besides meteorological key parameters such as temperature, pressure, and gas phase concentrations of chemical species including O_3, H_2O, NO_y, and ClO were measured. Number densities of condensation nuclei and cloud particle size distributions were determined and impactor samples collected for later offline Environmental Scanning Electron Microscopy and Energy Dispersive X-Ray Analysis. The winter ozone loss was estimated by conducting a simultaneous balloon match campaign with details of the technique described in Rex et al. (1999). The deployment of backscatter and water vapor soundings from Ny-Ålesund and Sodankylä during the first phase of the Arctic field campaign was part of this PhD work and will be described in more detail within Sect. 3.3. Moreover, lidar data from the satellite CALIPSO turned out to contain most valuable information on PSC occurrence, distributions and characteristics. The CALIPSO per-

spective of the Arctic winter 2009/2010 is given in Sect. 3.2. The chapter starts with a short summary
of the meteorological situation in the Arctic stratosphere 2009/2010.

3.1   Meteorological analysis

The meteorology of the Arctic stratospheric winter 2009/2010 is presented at length in Dörnbrack et al.
(2012). A summary of the general meteorological evolution is given with the help of Fig. 3.1, showing
the temporal evolution of the minimum temperatures (T_{min}) at 30 hPa during the RECONCILE winter
in comparison to the climatological mean.

Until November 2009, stratospheric temperatures above the North Pole cooled down as expected. This
downward trend stopped by mid November and T_{min} remained for about a month above climatologi-
cal mean values. The reason for this warming event was found in downward propagating temperature
anomalies. Two vortices evolved as a consequence of this disturbance from which the stronger and
colder vortex survived. The air inside the vortex cooled gradually from mid December on and did
not stop before mid of January. The coherent polar vortex was by then centered near the North Pole.
Values of T_{min} dropped well below T_{NAT} already in December and remained below T_{frost} for several
days in January with minima 7 K lower than the climatological mean at 30 hPa. Orographic gravity
wave activity characterized this period. Unidirectional winds across the east coast of Greenland lifted
stratospheric air up and due to its adiabatic expansion, the actual stratospheric temperatures could
have been even lower than T_{min} values reported by the ECMWF. In late January, the symmetry of the
vortex was disturbed by planetary wave activity which displaced the center towards the European sec-
tor of the Arctic. Followed by a continuous warming, the vortex finally broke up in February. Although
the 2009/2010 winter was overall relatively warm, an exceptional cold six week period from mid De-
cember until end of January made interesting and so far unique PSC studies possible.
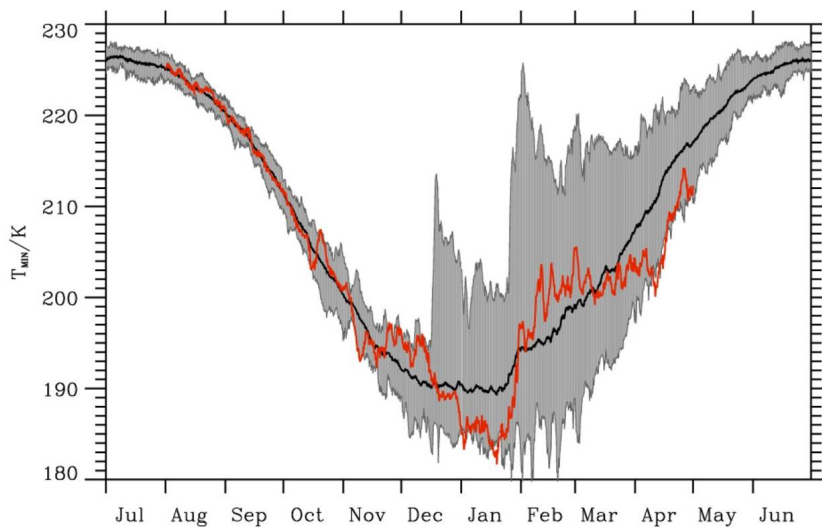

Figure 3.1: Minimum temperatures (T_{min}) between 65°N to 90°N at the 30 hPa pressure surface. Black
line: mean value from 1989–2009; red line: T_{min} evolution from July 2009 through June 2010; shaded
area encompasses the minimum/maximum T_{min} between 1989 and 2009. Source: ECMWF ERA-
interim data provided at 6 hourly temporal resolutions. Courtesy of Andreas Dörnbrack.

3.2 CALIPSO polar stratospheric cloud observations

CALIPSO added to the more focused aircraft and balloon-borne measurements of RECONCILE a vortex wide and season long view on PSCs. Although the Arctic PSC season in 2009/2010 was shorter than in previous years, the overall area covered by PSCs exceeded any other year of the CALIOP lidar data record. The total PSC volume was even as large as the sum of the three previous Arctic winters together. Not only the number of cloud observations was significantly different from other years, also the PSC composition was more similar to Antarctic conditions with widespread ice cloud observations. Pitts et al. (2011) divided the RECONCILE winter into four distinct phases as illustrated in Fig. 3.2. These four phases go along with the meteorological conditions described above.

First, PSCs were detected in the second half of December as patchy, tenuous liquid/NAT mixtures classified predominantly as Mix1 and Mix2 (see Fig. 3.2a). December temperatures remained several
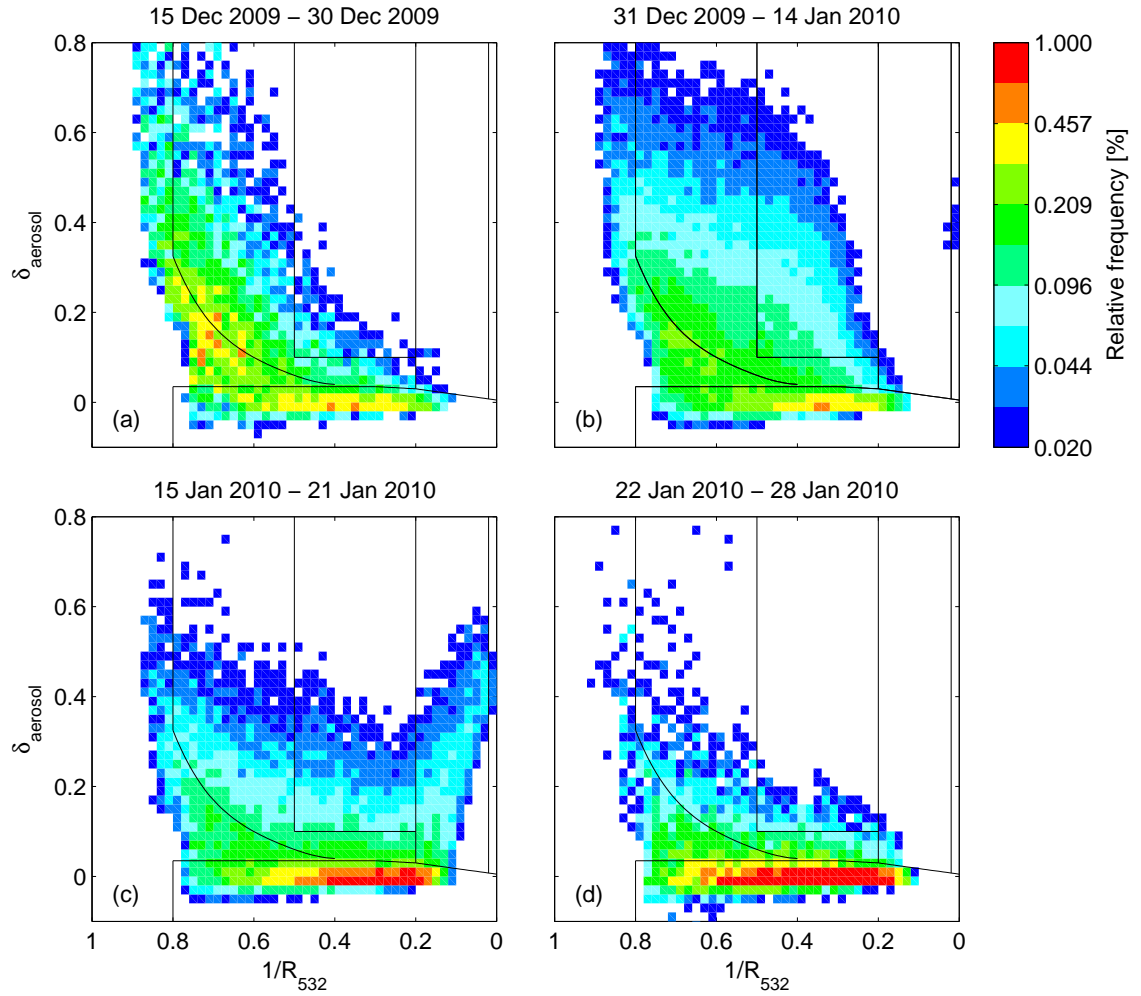

Figure 3.2: Normalized composite 2-D histograms of CALIOP PSC observations from each of four periods during the 2009/2010 Arctic winter over the altitude range from 15-30 km in the $\delta_{\mathrm{aerosol}}$ vs. $1/R_{532}$ coordinate system. Figure adapted from Pitts et al. (2011) with CALIOP data at 25 km horizontal resolution.

K above T_{frost} and no ice cloud was detected by CALIOP before the last day of the year 2009. These observations are at odds with the laboratory understanding of NAT formation subsequent on ice clouds as explained in Sect. 2.1.2. The close meshed CALIOP measurements together with accurate temperature information from high resolved NWP models leave practically no doubt on the existence of an ice independent NAT formation pathway.

The second phase of the winter was characterized by mountain wave ice clouds and lasted from 31 December 2009 until 14 January 2010. Mountain wave ice PSCs have been detected primarily along the east coast of Greenland. This changed the characteristics of existing PSC compositions as seen in Fig. 3.2b. Together with a small cluster of points at R_{532} values > 50, characteristic for wave ice clouds, the area of high number density NAT clouds in the 2-D scatter plot filled up as well. Those Mix2-enh NAT clouds were observed easterly of wave ice occurrences. Wave ice clouds as major source for widespread NAT particles have been suggested earlier by e.g. Carslaw et al. (1998b) and Voigt et al. (2003).

The extremely cold period from 15 to 21 January with synoptic-scale temperatures lower than T_{frost} was characterized by large areas of ice PSCs with signatures similar to ice PSCs usually seen in the Antarctic (see Fig. 3.2c). The relative increase of observations falling into the ice composition class goes along with decreasing NAT observations, in particular those classified as Mix2-enh. Pitts et al. (2011) pointed to heterogeneous ice formation on pre-existing NAT particles as a possible explanation and a potentially important pathway for synoptic-scale ice PSC formation.

The period of exceptional cold temperatures ended after 21 January and vortex temperatures increased to values above T_{frost} as mentioned in Sect. 3.1. Ice PSCs evaporated and the last PSC phase was dominated by STS clouds (see Fig. 3.2d).

Motivated by the quality and the extent of the CALIOP data in combination with the promising findings during the RECONCILE winter, two publications challenging the traditional pathways of PSC formation have been written. Both publications are closely connected to each other. By means of a comprehensive microphysical modeling study, the necessity of heterogeneous PSC formation pathways has been reassessed. Part 1 (Chpt. 4) introduces a new ice independent heterogeneous nucleation pathway for NAT clouds to explain the December 2009 CALIOP observations. Part 2 (Chpt. 5) concentrates on the synoptic-scale ice observations in January 2010 and adapts the approach of the companion paper to conditions suitable for ice formation.

3.3   Balloon-borne backscatter and water vapor measurements

Balloon soundings enable highly resolved in situ measurements at altitudes above common flight levels of research aircrafts. During the first phase of the Arctic field campaign, soundings from Ny-Ålesund and Sodankylä were performed. At both sites, COBALD complemented most of the payloads to discriminate simultaneous measurements of e.g. water vapor into clear and cloudy sky.

In Ny-Ålesund, profiles of particle backscatter were collected. PSCs have been observed by COBALD in every flight within the period from 17 to 25 January 2010. Closely matched measurements between CALIPSO and COBALD and between COBALD and the Ny-Ålesund lidar agree well in their backscatter profiles as presented in Sect. 2.3.3. Water vapor measurements from Ny-Ålesund failed due to instru-

mental problems of the Snow White hygrometer. The instrument turned out to be unable to cope with the extremely cold and dry conditions of the polar winter stratosphere.

The operation of the Cryogenic Frost point Hygrometer (CFH) and the Fluorescent Lyman-Alpha Stratospheric Hygrometer for Balloon (FLASH-B) within the Lapland Atmosphere-Biosphere Facility campaign (LAPBIAT-II) from Sodankylä was successful and revealed unprecedented evidence of water redistribution in the Arctic stratosphere. On 17 January 2010, an active phase of ice PSC formation was captured by the simultaneous balloon measurements of water vapor and aerosol, providing a unique snapshot of repartitioning of water vapor into ice particles. For the first time, concurrent irreversible dehydration by up to 1.6 ppmv within an altitude range of 20 to 24 km were measured, followed by a rehydration in a 2 km thick layer below. Balloon-borne, aircraft and satellite measurements show together a coherent picture which is presented in Chpt. 6. By means of a a microphysical case study, PSC formation and the subsequent redistribution of H_2O by sedimentation of ice particles are simulated and prepared as a companion paper to the observational part in Chpt. 7.

Chapter 4

Heterogeneous formation of polar stratospheric clouds – Part 1: Nucleation of nitric acid trihydrate (NAT)

C. R. Hoyle[1,2]**, I. Engel**[2]**, B. P. Luo**[2]**, M. C. Pitts**[3]**, L. R. Poole**[4]**, J.-U. Grooß**[5]**, and T. Peter**[2]

[1] *Laboratory of Atmospheric Chemistry, Paul Scherrer Institut, Villigen, Switzerland*

[2] *Institute for Atmospheric and Climate Science, ETH Zurich, Zurich, Switzerland*

[3] *NASA Langley Research Center, Hampton, Virginia, USA*

[4] *Science Systems and Applications, Incorporated, Hampton, Virginia, USA*

[5] *Institut für Energie- und Klimaforschung - Stratosphäre (IEK-7), Forschungszentrum Jülich, Jülich, Germany*

Contribution of I. Engel:
Preparation and visualization of model simulations, calculation of CALIOP uncertainties, PSC classification, general discussion of the obtained results.

Abstract

Satellite based observations during the Arctic winter of 2009/2010 provide firm evidence that, in contrast to the current understanding, the nucleation of nitric acid trihydrate (NAT) in the polar stratosphere does not only occur on preexisting ice particles. In order to explain the NAT clouds observed over the Arctic in mid December 2009, a heterogeneous nucleation mechanism is required, occurring via immersion freezing on the surface of solid particles, likely of meteoritic origin. For the first time, a detailed microphysical modeling of this NAT formation pathway has been carried out. Heterogeneous NAT formation was calculated along more than sixty thousand trajectories, ending at Cloud Aerosol Lidar with Orthogonal Polarization (CALIOP) observation points. Comparing the optical properties of the modeled NAT with these observations enabled the thorough validation of a newly developed NAT nucleation parameterization, which has been built into the Zurich Optical and Microphysical box Model (ZOMM). The parameterization is based on active site theory, is simple to implement in models and provides substantial advantages over previous approaches which involved a constant rate of NAT nucleation in a given volume of air. It is shown that the new method is capable of reproducing observed PSCs very well, despite the varied conditions experienced by air parcels traveling along the different trajectories. In a companion paper, ZOMM is applied to a later period of the winter, when ice PSCs are also present, and it is shown that the observed PSCs are also represented extremely well under these conditions.

4.1 Introduction

The discovery of the Antarctic ozone hole (Farman et al., 1985) was rapidly followed by the recognition that polar stratospheric clouds (PSCs), by providing the necessary surface for heterogeneous halogen activation reactions, played a central role in the observed ozone depletion (e.g. Solomon et al., 1986). Solid PSC particles were detected at temperatures well above the frost point, and it was proposed that these particles contained HNO_3 (Toon et al., 1986; Crutzen and Arnold, 1986). Later, experimental work suggested that the composition could be that of nitric acid trihydrate (NAT) (Hanson and Mauersberger, 1988), and more recently, observational work, such as the balloon borne mass spectrometry measurements reported on by Voigt et al. (2000) have shown that solid PSC particles observed above the frost point do indeed have H_2O and HNO_3 stoichiometries consistent with a NAT composition.

The formation of NAT particles sequesters reactive nitrogen compounds from the gas phase, and because these particles can grow to the large sizes necessary for rapid sedimentation (e.g. Salawitch et al., 1988), they cause denitrification of the polar stratosphere. While it is mostly the liquid particles in the polar stratosphere which are responsible for the heterogeneous reactions leading to the activation of the halogens (e.g. Molina et al., 1993; Carslaw et al., 1994; Ravishankara and Hanson, 1996), the observed dimensions of polar ozone loss are only reached because of this denitrification, which prevents deactivation of the halogens.

Despite the importance of NAT particles in determining polar ozone loss, an exact formation mechanism of these particles has remained elusive (e.g. Peter and Grooß, 2012). Initially it was proposed that

NAT could crystallize out homogeneously in liquid stratospheric aerosol droplets (Molina et al., 1993; Beyer et al., 1994; Iraci et al., 1994). Later, however, laboratory experiments, using $1 \, cm^3$ solution volumes, showed that the homogeneous nucleation rates of NAT in liquid ternary ($H_2SO_4/HNO_3/H_2O$) solution droplets were far too low to lead to the observed formation of such PSCs in the ambient polar stratosphere (Koop et al., 1995). The upper bound that Koop et al. (1995) determined for homogeneous NAT nucleation corresponds to an air volume based rate of $J_{NAT^{vol,upper}} = 1.8 \times 10^{-10} \, cm^{-3}$ air h^{-1}, assuming typical stratospheric aerosol particle sizes and number densities. This results in NAT particle number densities lower than $10^{-7} \, cm^{-3}$ when an air mass is cooled below T_{NAT}, the temperature below which NAT is thermodynamically stable, for one week, a period conceivable for the Arctic. Number densities of NAT would still remain below $10^{-6} \, cm^{-3}$, even if air was below T_{NAT} for 4 months, as might occur in the Antarctic. Such low number densities neither result in effective denitrification, nor are they measurable. Subsequent experiments by the same authors (Knopf et al., 2002), using microlitre size solution volumes, determined an upper bound of $J_{NAT^{vol,upper}} = 3 \times 10^{-10} \, cm^{-3}$ air h^{-1}, confirming the results of Koop et al. (1995).

Later, Biermann et al. (1996) showed, based on bulk samples of ternary solution containing solid meteoritic nuclei, that these nuclei could at best have $1/e$ freezing times of around 20 months. While these authors aimed at excluding meteoritic material as responsible for dense ($n > 0.1 \, cm^{-3}$) NAT clouds, their derived upper bound corresponds to an air volume based rate of $J_{NAT^{vol,upper}} = 7 \times 10^{-4} \, cm^{-3}$ air h^{-1} (assuming typical stratospheric aerosol particle sizes and number densities), which is certainly high enough to produce observable NAT clouds.

In contrast, the nucleation of NAT on ice is very certain and has been demonstrated in the laboratory and in the field. Through a combination of observations and microphysical modeling, Carslaw et al. (1998b) and Wirth et al. (1999) showed that NAT can form on ice particles in the atmosphere, suggesting that nucleation of NAT on ice is very efficient and most likely occurs via deposition nucleation on surfaces of ice which are not covered by a liquid coating. Via the so-called "Mother-Cloud/NAT-Rock mechanism", Fueglistaler et al. (2002) developed a potential mechanism by which NAT particles initiated by patchy mountain-wave ice clouds are distributed vortex-wide.

However, a study by Pagan et al. (2004) showed that during early December 1999, while the Arctic stratosphere was too warm for synoptic ice formation, there was also no ice PSC formation in mountain waves, ruling out nucleation on ice as a formation pathway for the NAT clouds observed during this time period. Drdla et al. (2002) presented modeling work which also suggested that a NAT formation mechanism above the frost point is necessary to explain observed denitrification in the 1999/2000 Arctic winter. Several other studies also exist, where constant NAT nucleation rates have been applied to model NAT formation irrespective of the presence or absence of ice. Using balloon based measurements carried out in the Arctic in December 2002, Larsen et al. (2004) found that observed PSC properties can be reproduced by applying the surface nucleation rate of Tabazadeh et al. (2002), reduced by a factor of 10 - 20, to calculate NAD (nitric acid dihydrate) formation from liquid aerosol, followed by instantaneous transformation of NAD to NAT. The rate they determined corresponds to an air volume-based rate of $J_{NAT^{vol}} = 2.5 \times 10^{-5} \, cm^{-3}$ air h^{-1}. The air masses which they observed had not been exposed to synoptic temperatures below the frost point, and there was no mountain wave activity, therefore NAT formation on ice could be ruled out, however heterogeneous nucleation on other types of solid particles could not be excluded.

More recently, Voigt et al. (2005) reported aircraft observations of low number densities of NAT particles in air masses which had been at $T > T_{\mathrm{NAT}} + 10\,\mathrm{K}$ some 24 - 36 h before the measurement and then cooled to $T_{\mathrm{NAT}} > T > T_{\mathrm{ice}} + 3\,\mathrm{K}$ for a period of less than 20 h before the measurement. In order to explain these observations, they suggested that NAT may also nucleate on the surface of meteoritic dust particles. Because the time below T_{NAT} could be well constrained (20 h), they were able to estimate a volume based NAT nucleation rate of $J_{\mathrm{NAT^{vol}}} = 8 \times 10^{-6}\,\mathrm{cm}^{-3}$ air h^{-1}, reproducing their observation of NAT number densities of $1.6 \times 10^{-4}\,\mathrm{cm}^{-3}$. While this rate reproduced the observed number densities, because of the limited measurement data, it was not possible to determine how the NAT nucleation rate increases as temperature decreases below T_{NAT}. It was argued by Voigt et al. (2005) that the heterogeneous NAT nucleation rates on meteoritic material measured by Biermann et al. (1996), while too low to be responsible for dense NAT clouds, might actually be sufficient to produce low NAT number densities within a few hours. Since the nucleation rates published by Biermann et al. (1996) were upper limits and the real rates might be considerably smaller, the suitability of meteoritic dust remains an open issue, which calls for further investigation.

Also for the Arctic winter of 2002/2003, Grooß et al. (2005) found that using a constant volume based rate of $J_{\mathrm{NAT^{vol}}} = 8 \times 10^{-6}\,\mathrm{cm}^{-3}$ air h^{-1} in CLaMS (Chemical Lagrangian Model of the Stratosphere), led to the best agreement between modeled and observed PSC properties and denitrification throughout the winter. A domain filling, Lagrangian particle trajectory model was used by Carslaw et al. (2002) to simulate the characteristics of NAT particles in the Arctic stratosphere in January - March 2000. They also used a simple volume-based NAT nucleation rate, and found that the observed particle sizes were well reproduced when a rate of $2.9 \times 10^{-6}\,\mathrm{cm}^{-3}$ air h^{-1} was used. While the apparent patchiness of wave ice clouds was first taken as an argument against their effectiveness in NAT nucleation, later more detailed vortex-wide simulations by the same authors showed that this mechanism could potentially indeed explain up to 80 % of the observed denitrification (Mann et al., 2005). Davies et al. (2005) simulated Arctic denitrification using a combination of a Lagrangian particle model and the chemistry transport model SLIMCAT. They compared the modeled denitrification with HNO_3 measurements from satellite and aircraft based instruments, and found reasonable agreement for several winters, when using the same NAT nucleation rate as Carslaw et al. (2002). However, for the winter of 1994/1995, they found that in order to reproduce the observed denitrification, this nucleation rate needs to be increased by a factor of 4, highlighting the need for physically based nucleation rates.

During December 2009, space-borne lidar measurements conducted from CALIPSO (Cloud-Aerosol Lidar and Infrared Pathfinder Satellite Observations), showed a situation where thin and patchy liquid-NAT mixed clouds of unprecedented dimensions (typically $1000 \times 2000\,\mathrm{km}^2$) were present in air masses in the Arctic, despite these air masses not having experienced temperatures below the frost point (Pitts et al., 2011). In the present study, this observational data set is utilized to develop a physically based parameterization for NAT nucleation on solid, non-ice particles. The advantage of using such satellite based lidar observations is that they cover a large area of the Arctic vortex, and when back trajectories are calculated starting from the observations, a range of air parcel histories are found, allowing the development of a robust parameterization, which represents NAT formation in air reaching different supersaturations with respect to NAT, for different lengths of time.

In the next section, the observational data set is described, as well as the models which were applied, and the new NAT nucleation parameterization. In Sect. 4.3, the results of modeling NAT formation

with the new parameterization are presented and compared with a constant nucleation rate approach, and in Sect. 4.4 we provide a summary and conclusions of the study. In a companion paper (Part 2, Engel et al., 2013b) the role of heterogeneous nucleation in ice formation is discussed.

4.2 Observational data and model description

4.2.1 The CALIPSO observations

The CALIPSO satellite was launched in April 2006, and includes the Cloud Aerosol Lidar with Orthogonal Polarization (CALIOP) as its principal instrument. CALIOP measures backscatter at two wavelengths, 1064 nm and 532 nm, using the 532 nm signal to measure the depolarization of the backscattered radiation relative to the plane polarized light of the outgoing laser beam. With its high latitude coverage up to 82°, CALIOP has provided extensive observations of PSCs in both hemispheres since its launch.

In order to derive and test the new NAT nucleation parameterization, the CALIOP observations made over the Arctic in December 2009 are used. During the second half of December 2009, stratospheric temperatures were slightly below T_{NAT} and patchy areas of PSCs were detected on a daily basis. Additionally, there were no observations of ice cloud during this period, and due to the meteorological situation, even accounting for small scale temperature fluctuations, the probability of undetected ice clouds having occurred is extremely low. This set of observations therefore supports the existence of a NAT nucleation mechanism which does not require an ice surface. On 31 December, mountain wave ice clouds were first observed, followed by a dramatic increase in observations of NAT containing clouds, marking the end of the period when the NAT PSCs can be considered to have formed without the presence of ice particles.

In the analysis here, we make use of the PSC classification system of Pitts et al. (2009, 2011), which assigns the detected clouds to one of six categories (STS, Mix1, Mix2, Mix2-enh, ice, wave ice), depending on the backscatter and depolarization signals. Though not identical, this classification system is similar to the previously used PSC-types, namely 1b (STS), 1a (Mix1, Mix2), 1a-enh (Mix2-enh), and 2 (ice and wave ice). For the NAT classes, Mix1 includes NAT number densities of less than approximately 10^{-3} cm^{-3}, Mix2 includes NAT number densities between about 10^{-3} cm^{-3} and 0.1 cm^{-3}, while Mix2-enh includes NAT number densities of above 0.1 cm^{-3}.

The PSC detection limit of CALIOP is altitude dependent (Pitts et al., 2009), and we treat the modeled data in a similar way. If the modeled or observed values at a particular point are below the detection limit, then a larger horizontal averaging distance is applied. Thus, for the observations, if no PSC is detected over 5 km, the horizontal resolution is decreased (i.e. the averaging distance is increased) to 15 km, then 45 km and 135 km. The highest resolution for the modeled data is 25 km (the resolution of the grid from which the trajectories used by the model were started) and if no PSCs are detected at a point then the averaging distance is increased to 125 km.

4.2.2   The microphysical box model

The Zurich Optical and Microphysical box Model (ZOMM) used in this study has been applied to simulate PSCs (e.g. Meilinger et al., 1995; Luo et al., 2003b) as well as cirrus clouds (e.g. Hoyle et al., 2005; Brabec et al., 2012). In the latter two studies, a slightly different version of the model was used, however the only significant difference is that the stratospheric version of the model simulates the evolution of a population of ternary solution aerosol droplets (H_2O, H_2SO_4, HNO_3), and their interaction with the gas phase, whereas the tropospheric version accounts for a binary (H_2O, H_2SO_4) solution.

The most prominent feature of the model is that it treats particle sizes in a Lagrangian scheme, i.e. the model follows the radii of growing/shrinking particles and creates a new size class i each time there is new ice or NAT particle nucleation. The model then transports the liquid, NAT and ice particles size class i downstream with time-dependent radius $r_i(t)$ and constant number density, n_i. The Lagrangian size treatment avoids numerical diffusion, which may lead to artificial redistributions of particle number densities on a fixed Eulerian size grid with fixed bins.

The model is initialized with a log-normally distributed population of solution droplets, which represent the background aerosol. This initial distribution is calculated given a user defined mode radius, number density and standard deviation, and in this study consisted of 26 radii. The initial composition of the droplets is calculated assuming thermodynamic equilibrium with the gas phase and accounting for the Kelvin effect of the various species. The total mixing ratios of H_2O, H_2SO_4 and, in the PSC version, HNO_3, are set in the input file and are assumed to remain constant for the whole simulation along a trajectory (i.e. neglecting mixing and particle sedimentation).

The model is run along a trajectory consisting of a time series of temperature and pressure data points, and after the initialization, the aerosol droplet sizes are allowed to evolve freely in radius space, and are no longer restricted to a log-normal form (see Meilinger et al., 1995). As the temperature decreases, growth of the aerosol droplets is calculated, fully kinetically for all species, whereby the Kelvin effect is accounted for in calculating the vapor pressures of the individual species over the droplet surfaces. Latent heat effects of condensation and evaporation (or freezing) are not accounted for in the PSC version of the model, however given the small mixing ratios of matter which condense or evaporate (a few ppmv for H_2O and a few ppbv for HNO_3) in the polar stratospheres, this does not impart any significant uncertainties to the calculations. Accommodation coefficients for the uptake/evaporation of species from/to the gas phase were set to 1.0, for liquid and for solid particles.

A schematic representation of the modeled composition and phase changes of PSCs as a function of temperature is shown in Fig. 4.1. Pathways previously represented in ZOMM are marked with dashed arrows, those which have been added for this study are shown by solid arrows. At temperatures above about 200 K, supercooled aerosol droplets exist as a quasi-binary H_2O/H_2SO_4 solution. Upon further cooling, HNO_3 is taken up to form a supercooled ternary solution (STS). In the absence of solid nuclei, ice may nucleate homogeneously in the STS droplets when temperatures decrease a few degrees below the frost point, and NAT can then form on the surface of the ice particles. Alternatively, if foreign nuclei are present (as indicated by the black triangles), they may lead to ice nucleation at higher temperatures than in the homogeneous case (Engel et al., 2013b), or, as shown here, to the formation of NAT in the absence of ice (thick black line in Fig. 4.1).
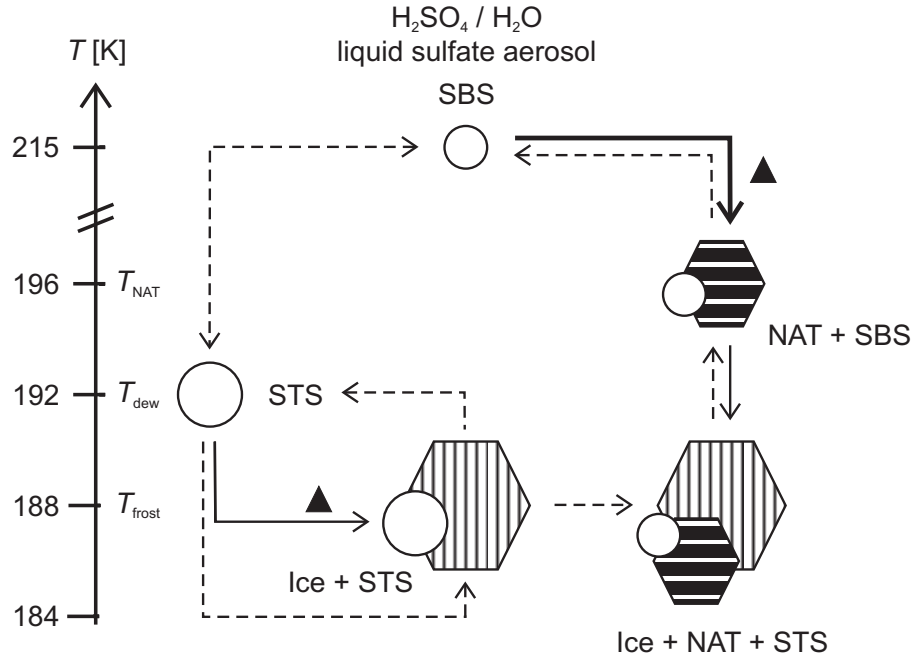
Figure 4.1: A schematic description of the different pathways included in ZOMM. The dashed arrows depict processes which were represented in previous model versions, the solid arrows show those added to the model for this study. Foreign nuclei are indicated by the black triangles. While here, the focus is on the heterogeneous nucleation of NAT (thick black arrow), the heterogeneous nucleation of ice (thin solid black arrows) is discussed in a companion paper (Engel et al., 2013b).

Homogeneous ice nucleation

The homogeneous nucleation rate coefficient, J_{nuc}, for the formation of water ice is calculated based on the temperature and the water activity in the droplet according to

$$J_{nuc} = 10^D \, \mathrm{cm^{-3} \, s^{-1}} \tag{4.1}$$

where

$$D = -906.688 + 8502.28x - 26924.4x^2 + 29179.6x^3 \tag{4.2}$$

and $x = a_{w,liq} - a_{w,ice}$ is the water activity in a droplet ($a_{w,liq}$) minus the water activity in a solution which would be in equilibrium with ice ($a_{w,ice}$) at the particular temperature being considered. $a_{w,ice}$ is defined as the ratio of the H_2O vapor pressures over ice and pure water and its value is given by Zobrist et al. (2011), based on Koop et al. (2000) as:

$$a_{w,ice} = \exp\left(-\frac{-210368 - 131.438\,T + 3.32373 \times 10^6/T + 41729.1 \times \ln(T)}{8.31441 \times T}\right), \tag{4.3}$$

where T is the absolute temperature in Kelvin. The expected number density of ice particles (n_{ice}) nucleated from modeled liquid droplets with number density n_{liq} and volume v_{liq} can be calculated by:

$$n_{ice} = n_{liq}\left(1 - \exp\left(-\int_{t_0}^{t} J_{nuc}\, v_{liq}\, \mathrm{d}t\right)\right). \tag{4.4}$$

Instead of forming a new Lagrangian ice particle size class for every droplet size class, in every time step, which would be computationally impractical, the number of nucleated ice particles in each droplet size class is accumulated until this number exceeds either 1×10^{-5} cm^{-3}, or half the number density of droplets in that size class, or half of the total number density of ice particles in the model, whichever of the three criteria is satisfied first.

After ice is nucleated in a liquid size class, the number of frozen droplets calculated using Eq. (4.4) is transferred from the liquid size class to the new ice size class. All ice particles in a particular size class thus have the same radius, and this radius increases as the ice particles take up water in competition with the remaining liquid droplets. Upon warming, the evaporation/sublimation of species from the solid particles is calculated, until eventually a concentrated solution droplet is released and the number of particles is transferred back from the ice size class to the liquid size class from where it originated.

NAT formation

Until now, NAT formation in ZOMM was only permitted via deposition nucleation on clean (uncoated, dry) surfaces of ice particles. The method used was thoroughly described by Luo et al. (2003b); a summary of this description is provided here.

Ice particles in the atmosphere are generally coated in a layer of liquid solution, however there may be dry patches on the particle, where the ice interacts directly with the gas phase. In rapid cooling events, the supersaturations with respect to NAT in the gas phase can grow to much larger values than in the liquid due to non-equilibrium effects, favoring deposition nucleation on these exposed clean ice surfaces (Luo et al., 2003b). The area of the dry patches was determined by assuming a minimum thickness of the liquid layer of 28.5×10^{-8} cm (approximately 10 monolayers, Luo et al., 2003b), and calculating the resulting surface coverage of the actual volume of liquid available to form the layer on the solid particles. The NAT nucleation rate coefficient on the dry area of the ice particles was calculated based on the classical nucleation theory for the heterogeneous nucleation of water ice, using Eq. (4.5),

$$J_{\text{het}}(T) = \frac{kT}{h} \exp\left[-\frac{\Delta F_{\text{diff}}(T)}{kT} \right] \times n \exp\left[-\frac{\Delta G(T) f_{\text{het}}(\alpha)}{kT} \right] \tag{4.5}$$

where T is the temperature in Kelvin, k and h the Boltzmann and Planck constants, respectively, n is the number density of HNO$_3$ molecules on the ice surface (ca. 2×10^{14} cm^{-2}, at high NAT supersaturations, see Abbatt, 1997), ΔF_{diff} is the temperature dependent diffusion activation energy which has to be surmounted for 2-D diffusion of HNO$_3$ to take place on the surface of a preexisting foreign nucleus (here the ice), and G is the Gibbs free energy for the formation of a critical NAT embryo in the absence of the foreign nucleus, i.e.

$$\Delta G(T) = \frac{16\pi}{3} \frac{m^2 \sigma^3}{[kT\rho \ln(S_{\text{NAT}})]^2}. \tag{4.6}$$

In Eq. (4.6), m is the molecular mass of NAT, σ is the surface energy of NAT, and S_{NAT} is the NAT saturation ratio. The presence of the foreign nucleus reduces ΔG by the compatibility factor f_{het}, defined as

$$f_{\text{het}}(\alpha) = \frac{1}{4}(2 + \cos\alpha)(1 - \cos\alpha)^2, \tag{4.7}$$

where α is the contact angle, a parameterization of the heterogeneous nucleation activity of the foreign nucleus (Seinfeld and Pandis, 2006). The possible values for α range between $0°$ and $180°$, leading to values of f_{het} between 0 and 1, i.e. with a contact angle of $180°$ the foreign nucleus does not cause any enhancement in the nucleation rate.

Now, as ΔF_{diff} is unknown, as is the compatibility factor f_{het}, and the surface energy of NAT, Luo et al. (2003b) defined two new constants (denoted here as b and γ), which they used to tune their nucleation rate coefficient equation, so that the model reproduced the observed NAT distribution:

$$J_{\text{NAT}^{\text{ice}}} = 6.24 \times 10^{24}\,\text{cm}^{-2}\,\text{s}^{-1}\,\text{K}^{-1}\,T\,\exp\left[\frac{-b}{T}\right]\exp\left[-\frac{\gamma(273.15)^3}{T^3(\ln(S_{\text{natice}}))^2}\right], \tag{4.8}$$

where the value 6.24×10^{24} corresponds to kn/h. The values that Luo et al. (2003b) suggested for these two constants were:

$$b = \frac{\Delta F_{\text{diff}}}{k} = 2000\,\text{K} \tag{4.9}$$

and

$$\gamma = \frac{\Delta G(T)\,T^2\ln\left(S_{\text{NAT}}(T)\right)^2 f_{\text{het}}(\alpha)}{273.15^3\,k} = 328\,\text{K}^3 \tag{4.10}$$

Note that in this parameterization, it is implicitly assumed that the nucleation sites on the foreign nuclei are all of the same quality, as the compatibility factor is included in γ and is therefore invariant.

Extension to heterogeneous NAT and ice nucleation on foreign nuclei

The microphysical box model has recently been extended so that in addition to homogeneous nucleation of water ice, and heterogeneous nucleation of NAT on the surface of ice particles, it now includes the heterogeneous nucleation of ice on foreign nuclei as well as NAT formation on foreign nuclei (both in the immersion mode). These two new nucleation pathways are based on the active site parameterization of Marcolli et al. (2007). As foreign nuclei, a monodisperse population of solid particles with radii of 20 nm, and with a number density of 7.5^{-3} is assumed, based on Curtius et al. (2005).

According to the active site theory, freezing cannot be initiated equally well over the entire surface of the foreign nucleus, rather it occurs preferentially at certain active sites. As a proxy for the quality of these sites, the contact angle may be used, which essentially parameterizes the reduction in the nucleation energy barrier associated with a particular active site. In applying Eq. (4.5) to NAT nucleation on nuclei other than clean ice surfaces, the variations in contact angle for active sites of different quality must be accounted for. We therefore define γ', which differs from γ of Luo et al. (2003b) only in that it no longer includes the compatibility factor. The new parameterization for the nucleation rate coefficient of NAT, on foreign nuclei immersed in a ternary $H_2O/HNO_3/H_2SO_4$ solution, is therefore

$$J_{\text{NAT}^{\text{foreign}}}(T) = 6.24 \times 10^{24}\,\text{cm}^{-2}\,\text{s}^{-1}\,(T/K)\,\exp\left[\frac{-b}{T}\right] \times \exp\left[-\frac{\gamma'(273.15)^3 f_{\text{het}}(\alpha)}{T^3(\ln(S_{\text{NAT}}))^2}\right], \tag{4.11}$$

where S_{NAT} is the saturation ratio of the STS with respect to NAT.

In order to adjust the nucleation rate parameterization so that modeled NAT distributions correspond to observations, the value of γ' and the distribution of contact angles α for the available active sites on the foreign nuclei must be determined. Assuming that only the best active site on a particle is

responsible for NAT nucleation, the occurrence probability of an active site with a particular contact angle on a particle can be described as

$$P_{\text{as}}(\alpha) = P_{\text{pre}} \times \exp\left(\frac{-51.0°}{\alpha - \alpha_0}\right) \tag{4.12}$$

similarly to Marcolli et al. (2007). The parameter α_0 represents the lowest contact angle considered, while P_{pre} is a constant (with units of deg^{-1}). In the model, $1°$ contact angle bins were used, for contact angles starting from $\alpha_0 + 1°$. The number density of foreign nuclei, containing at least one active site with a minimum contact angle α (i.e. the number of foreign nuclei in one particular contact angle bin), is then given by

$$n_\alpha = \left(n_{\text{foreign}} - \sum_{\alpha'=\alpha_0+1}^{\alpha-1} n_{\alpha'}\right) P_{\text{as}}(\alpha) \Delta\alpha \frac{4\pi r_{\text{foreign}}^2}{A_1}, \tag{4.13}$$

where $\Delta\alpha = 1°$, r_{foreign} is the radius of the foreign nuclei (20 nm) and A_1 is the area of one active site, which is taken to be $10\,\text{nm}^2$, following Marcolli et al. (2007). The nucleation rate of NAT on a particle is then $J_{\text{NAT}^{\text{foreign}}}$ multiplied by the area of the active site, A_1. This corresponds to a volume based nucleation rate of

$$J_{\text{NAT}^{\text{vol}}}(T) = \sum_{\alpha_i=\alpha_0+1}^{\alpha_{\max}} n_{\alpha_i} \times J_{\text{NAT}^{\text{foreign}}}(T, \alpha) \times A_1. \tag{4.14}$$

The number density of foreign nuclei as a function of the contact angle of their best active site is shown in Fig. 4.2. This figure highlights the contrast between the very few excellent nuclei, characterized by small contact angle active sites, and the large number of mediocre nuclei with larger contact angles. Similar distributions of nuclei quality have previously been observed for populations of volcanic ash particles (Hoyle et al., 2011), and mineral dust particles (Pinti et al., 2012) in ice nucleation experiments. The curve in Fig. 4.2 becomes rather flat beyond $80°$ indicating there are similar numbers of particles having a best active site with a contact angle of, for example, $100°$ or $120°$. With a foreign nuclei number density of $7.5\,\text{cm}^{-3}$, and setting $P_{\text{pre}} = 1 \times 10^{-6}\,\text{deg}^{-1}$ (see below), considering contact angles up to $146°$ accounts for approximately 0.13 particles cm^{-3}, which covers the range of NAT number densities necessary for simulating the PSCs observed during the winter of 2009/2010. Note that Eq. (4.12) is not normalized, which effectively means that the majority of the foreign nuclei have best active sites which are of insufficient quality to decrease the NAT nucleation barrier.

The properties of the PSC modeled with Eq. (4.11) can be adjusted by varying the values of the three fitting parameters γ', α_0 and P_{pre}. A higher value of γ' effectively increases the nucleation barrier represented by the last term of Eq. (4.11), and therefore lowers the temperature at which NAT will first form. The parameter α_0 sets a lower limit on the contact angle associated with the best possible active site. As described above, an active site with a small contact angle has a low value of the compatibility factor (f_{het}), therefore α_0 determines the maximum extent to which the presence of a foreign nucleus can reduce the nucleation barrier. On the other hand, P_{pre} changes the probability of an active site with a particular contact angle occurring, and therefore alters the number density of NAT that can be formed at a particular temperature. As it is assumed that the best active site on a foreign nucleus is responsible for the nucleation event, an increase in P_{pre} shifts the distribution of active sites towards lower contact angles, increasing the number of NAT particles which nucleate at higher temperatures.

While for ice, the nucleation rate is the sum of the heterogeneous and homogeneous rates, in the case of NAT formation, only the heterogeneous nucleation rate on foreign nuclei and on ice is considered.
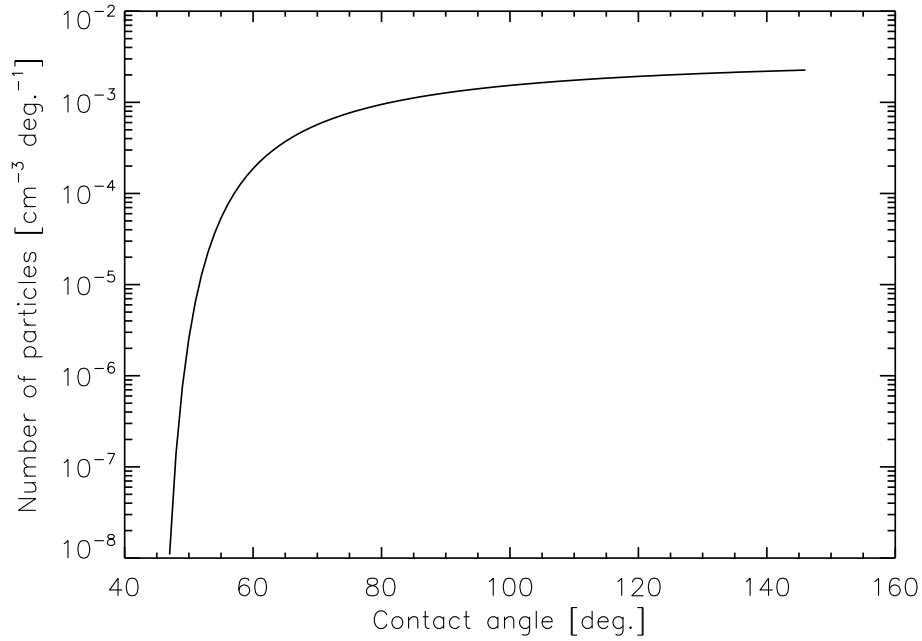
Figure 4.2: The number density of foreign nuclei as a function of the contact angle of the best active site on the particle's surface.

Upon evaporation of the ice or NAT particles, the nuclei are returned to the active site bin from which they originated.

The choice of the fitting variables for NAT nucleation, as well as the other parameters used in this particular study is discussed in Sect. 4.2.3, while the parameters used for heterogeneous ice nucleation are given in Engel et al. (2013b).

The optical properties (backscatter ratio, R_{532} and aerosol depolarization ratio, δ_{aerosol}) of the modeled PSC are calculated from the particle number densities and radii, assuming the particles to be prolate spheroids with aspect ratios (diameter-to-length ratios) of 0.9 (in accordance with Carslaw et al., 1998b) and a refractive index of 1.48 for NAT (Middlebrook et al., 1994). Calculations were then made using a T-matrix light scattering algorithm (Mishchenko, 1991; Carslaw et al., 1998b) for spheroids with a known refractive index.

The CALIOP measurements of parallel and perpendicular backscatter are subject to an uncertainty, and to simulate this in the model results, a normally distributed random instrumental noise component is added to each of these quantities in the model output, before calculating R_{532} and δ_{aerosol}. Subsequently, the modeled PSC is classified according to the same scheme used for the observations. This allows a direct comparison between the modeled and observed PSC properties. The calculation of the uncertainty in the CALIOP measurements is described in detail in Engel et al. (2013b), and an example of the model output without and with the instrumental noise is shown in Fig. 4.3a, b, respectively. Additionally, error bars show the limits of one standard deviation of the normally distributed noise component for a single modeled point. The main effect of the random noise is to increase the variability in the depolarization ratio.
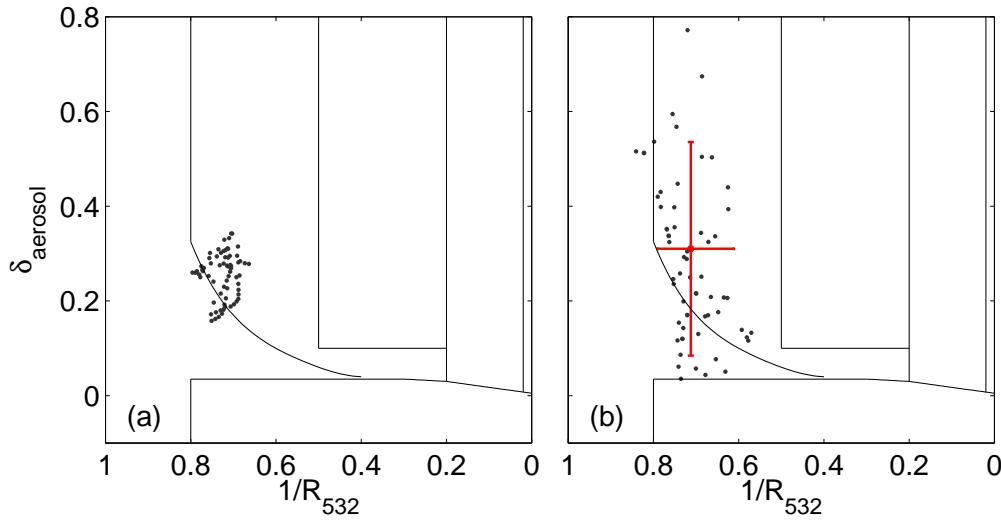
Figure 4.3: Modeled aerosol depolarization ratio (δ_{aerosol}) vs. inverse backscatter ratio ($1/R_{532}$) without (a) and with (b) consideration of instrument noise, for the mixed NAT/liquid cloud observed on the third CALIPSO overpass of the Arctic vortex on December 21 (denoted here as orbit 21_03). The error bars illustrate one standard deviation of the uncertainty for a single point.

4.2.3   Trajectory calculations

The microphysical model was run along trajectories which ended at CALIPSO observation points. For every CALIPSO orbit during December 2009, where PSCs were observed, the following criteria were applied to choose the observation points used in the analysis:

- Latitude north of 50° N;

- Altitude of between 18 km and 26 km;

- The temperature at the observation point was T_{NAT} or less;

- Every 5th vertical profile available in the CALIPSO data set was chosen, to give a 25 km horizontal resolution;

- Every vertical level was used, providing approximately a 180 m vertical resolution;

From all the points fulfilling these criteria, ten-day backward trajectories were calculated, using the trajectory module of CLaMS (McKenna et al., 2002). The trajectories were based on ECMWF ERA-Interim data (Dee et al., 2011) with a resolution of 1° × 1° and 6 h, using potential temperature as the vertical coordinate. The vertical resolution was approximately 1.25 km between the altitudes of 19 km and 30 km at polar latitudes. The internal and output time step for the trajectory calculation was 15 min. To determine the starting point for the model calculation, the trajectories were followed backward in time from their end points, until the temperature rose above T_{NAT}, so as to avoid the complication of having to initialize the PSCs. If no such point was encountered within the ten days preceding

the CALIPSO measurement on which the trajectory ended, the trajectory was not used in the modeling. For each of the valid trajectories, the model was initialized and run forward in time up until the point of the CALIPSO observation. For the days which were investigated in December, there were around 2000 - 5000 valid trajectories per orbit.

In previous work on cirrus nucleation (e.g. Kärcher and Lohmann, 2002; Hoyle et al., 2005), as well as in the analysis of ice PSCs (Engel et al., 2013b) it has been shown that the observed microphysical properties of a cloud can only be properly reproduced by a model if small scale temperature fluctuations (for example with wavelengths of less than 100 km, i.e. below the resolution of CLaMS and the ERA-Interim data) are accounted for. Such fluctuations are expected to be ubiquitous in the atmosphere (e.g. Gary, 2006, 2008). It was demonstrated by Meilinger et al. (1995) that, as the equilibration times for HNO_3 and for H_2O in droplets differs greatly, during the warming phase of a temperature fluctuation, H_2O may partition from a liquid droplet back into the gas phase much more quickly than HNO_3. This can result in an enhanced NAT saturation ratio, and NAT nucleation at higher temperatures than would otherwise be possible in the absence of temperature fluctuations. Several sensitivity runs have been performed to test the effect of small scale temperature fluctuations on NAT nucleation. The time-series of temperature fluctuations which was superimposed on the CLaMS trajectories for this purpose was based on that derived in Hoyle et al. (2005), and had mean amplitudes of ±0.5K, similarly to those used by Engel et al. (2013b), for heterogeneous ice nucleation. The results of these model runs are presented in Sect. 4.3.4.

Model configuration used in this study

For this study, the total number density of liquid aerosol particles was set to $15\,cm^{-3}$. Half of these particles contained no foreign nuclei and the initial radius of these particles followed a log normal distribution, with mode radius of 70 nm, and $\sigma = 1.8$ (e.g. Dye et al., 1992). The number density of foreign nuclei was set to $7.5\,cm^{-3}$, with a radius of 20 nm. The foreign nuclei were immersed in the remaining $7.5\,cm^{-3}$ liquid droplets, which were assigned a radius of 70 nm (equal to the mode radius of the liquid-only droplet distribution). This was done to achieve the computational efficiency necessary to run the large number of trajectories simulated. As all NAT nucleation in the simulations occurred heterogeneously, this simplification had no significant effect on the results. The composition of the liquid solution was initially in equilibrium with the gas phase and the H_2O and HNO_3 mixing ratios were set at the beginning of each trajectory, using daily mean values of Microwave Limb Sounder (MLS) measurements. These daily, vortex average values were calculated from the MLS data by averaging over all cloud free points within the polar vortex on a particular day. By adjusting the model until the CALIOP PSC observations were reproduced as well as possible, the following best values were determined for the fitting parameters: $\alpha_i = 43°$, $\gamma' = 650\,K^3$ and $P_{pre} = 1 \times 10^{-6} deg^{-1}$. In Sect. 4.3, comparisons of the observations and model calculations using the new parameterization with these values are presented, as well as further calculations which illustrate the sensitivity of the results to changes in the fitting parameters.

4.2.4   Constant NAT nucleation rate

Experiments using constant, air volume based nucleation rates were also performed to provide a comparison with the new physically based NAT nucleation parameterization. Similarly to previous studies, the constant nucleation rate was applied at all the trajectory points where the temperature was below T_{NAT}. Rate coefficients of between $J_{\mathrm{NAT^{vol}}} = 7.0 \times 10^{-6}\,\mathrm{cm}^{-3}\,\mathrm{air}\,\mathrm{h}^{-1}$ and $J_{\mathrm{NAT^{vol}}} = 2 \times 10^{-5}\,\mathrm{cm}^{-3}\,\mathrm{air}\,\mathrm{h}^{-1}$ were run along trajectories for the fourth CALIPSO overpass of the Arctic vortex on 24 December 2009, (hereafter 24_04), and the nucleation rate producing the best results, $J_{\mathrm{NAT^{vol}}} = 9 \times 10^{-6}\,\mathrm{cm}^{-3}\,\mathrm{air}\,\mathrm{h}^{-1}$, was then applied to trajectories for the remaining orbits. The results of these model experiments are also shown in Sect. 4.3.

4.3   Results

4.3.1   Constant vs. saturation dependent nucleation rate coefficients

The basic difference between the new parameterization and the constant, volume based nucleation rate can be illustrated by plotting the development of the NAT saturation ratio and the increase in NAT number density as a function of time, for a typical trajectory, as in Fig. 4.4. The model was run once with each nucleation parameterization, along this 60 h trajectory, which was initialized with a temperature of 193.05 K, pressure of 25.5 hPa, HNO_3 mixing ratio of 13.5 ppbv and water vapor mixing ratio of 5.7 ppmv.

The constant nucleation rate is applied as soon as the temperature drops below T_{NAT}, and therefore the number density of NAT particles begins to increase at this point. The new parameterization on the other hand leads to a significant formation of NAT only after the temperature reaches approximately $T_{\mathrm{NAT}} - 4\,\mathrm{K}$. Shortly after this point, the temperature stabilized briefly, therefore only about $1 \times 10^{-4}\,\mathrm{cm}^{-3}$ of NAT is nucleated. Subsequently, the temperature continued to decrease, and the number density of NAT nucleated with the new parameterization climbed rapidly to approximately $1 \times 10^{-3}\,\mathrm{cm}^{-3}$. The step-like nucleation behavior seen from the new parameterization comes about because of the differing active site qualities on the particles. Once all the particles with sufficiently good active sites have nucleated NAT at a particular NAT saturation ratio, the NAT saturation ratio must increase before the particles with the next best active sites may also cause NAT nucleation.

The saturation ratio in both simulations remains fairly similar while the air parcel is cooling, however due to the longer times available for the NAT particles to grow, after approximately 25 h the uptake of HNO_3 by the NAT particles in the constant nucleation case leads to a slightly lower saturation ratio than for the model with the new parameterization. After approximately 40 h, the NAT saturation ratio becomes lower for the simulation with the new parameterization, and continues to decrease faster than in the simulation with the constant nucleation rate.

Three important differences between the constant nucleation rate and the new parameterization are illustrated by Fig. 4.4. The first is that if the temperature is only slightly lower than T_{NAT}, the constant rate will nucleate NAT particles, whereas the new parameterization will not (0 h to 20 h in Fig. 4.4). Secondly, for short periods of time at low temperatures, the new parameterization will nucleate far
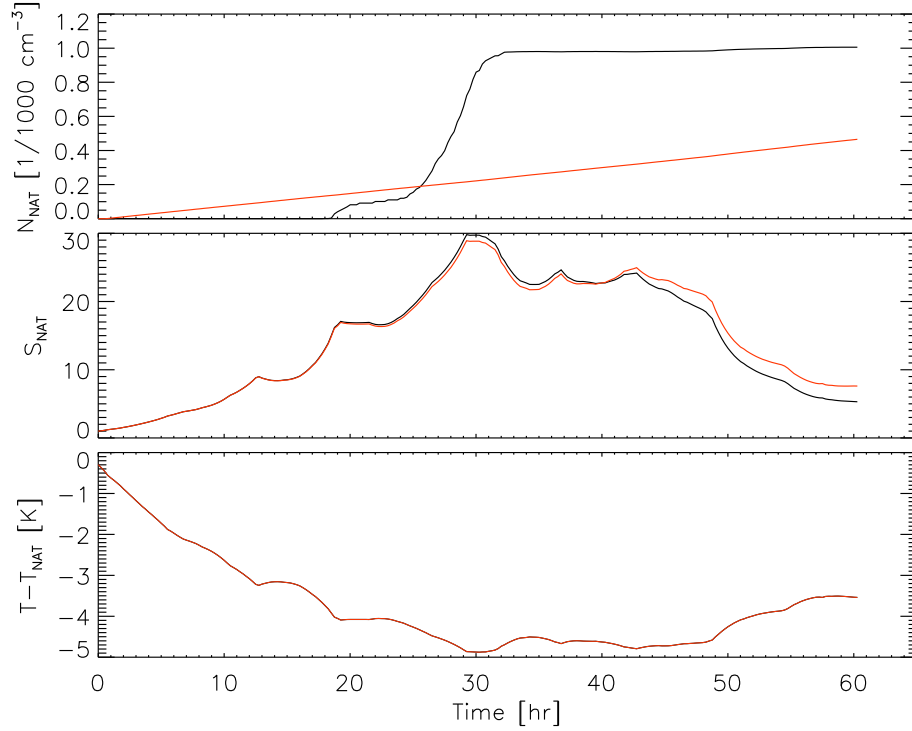
Figure 4.4: A comparison of the volume based nucleation rate parameterization (red), and the new parameterization (black). Both versions of the model were run along the temperature trajectory shown in the bottom panel. The development over time, of NAT number density and saturation with respect to NAT, is shown in the top and middle panels, respectively.

more NAT than the constant rate (e.g. 20 h to 30 h). Finally, if the temperature remains below T_{NAT} for very long periods of time (as can be seen in Fig. 4.6, times below T_{NAT} of 120 h or more are not unusual), the constant rate will eventually nucleate more NAT than the new parameterization. This would happen after approximately 110 h for the trajectory in Fig. 4.4, if it were to continue without further cooling.

4.3.2 Sensitivity of new parameterization to choice of parameters

The values of the model parameters γ', α_0 and P_{pre} were determined by systematically varying each parameter in turn, and comparing the resulting modeled PSC optical properties with the CALIOP observations. For this purpose, the orbit 24_04 was particularly suitable, as a fairly large, coherent area of PSC was observed, and the time that this air mass had experienced temperatures below T_{NAT} was only between about 48 and 72 h, minimizing complications caused by mixing or by the sedimentation of PSC particles. After the match between the modeled results and the observations for orbit 24_04 was optimized, the model was applied to other orbits in a predictive capacity, to evaluate the robustness of the new parameterization.

The PSC classifications of the model runs used to define the model parameters are shown in Fig. 4.5, along with contours indicating the temperature at the observation point relative to T_{NAT}. The upper-

most panel shows the observed PSC classifications. On the top row of the figure, the nucleation barrier parameter γ' is varied from a value of $550\,K^3$ to $750\,K^3$ in steps of $50\,K^3$. As expected, at low values of γ', the PSC area is greater, and with increasing γ', the area of PSC formed gradually decreases until only those trajectories that had experienced the coldest temperatures still nucleate NAT. On the second row of Fig. 4.5, the nucleation strength parameter P_{pre} is varied from $1 \times 10^{-7}\,deg^{-1}$ to $1 \times 10^{-5}\,deg^{-1}$. Here, the situation is reversed, with the larger values leading also to larger areas of PSC formed, and also an enhancement in the NAT number density, as shown by the increasing number of points being classed as Mix1/Mix2 and then as Mix-2enh. On the bottom row of the figure, the compatibility factor α_0 is varied from $41°$ to $45°$ in steps of $1°$. Again, the increasing values of α_0 lead to a decrease in the temperature at which NAT can form, and a reduction of the area of NAT modeled. The three plots in the middle column of Fig. 4.5 are identical, and represent the model results using our chosen set of parameters, ($\alpha_0 = 43°$, $P_{pre} = 1 \times 10^{-6}\,deg^{-1}$ and $\gamma' = 650\,K^3$).

It is evident from this plot, that the same results can be achieved with different combinations of the three factors. For example, an α_0 of $43°$, P_{pre} of $1 \times 10^{-6}\,deg^{-1}$ and γ' of $650\,K^3$ leads to a very similar PSC classification as is found when using an α_0 of $43°$, P_{pre} of $5 \times 10^{-6}\,deg^{-1}$ and γ' of $750\,K^3$. We do not, therefore, claim that the values for the parameters which we have determined are the only values that will result in an accurate modeling of the observed PSC. However, lacking laboratory data on quantities such as the distribution of the quality of the foreign nuclei (i.e. the active site distribution), ΔF_{diff} and the surface energy of NAT, it is not possible to further constrain the choice of parameters, and the set of values which we have chosen are shown, in Figs. 4.6, 4.7 and 4.8, to lead to a very good representation of the observed NAT PSCs. Additionally, it can be seen in Fig. 4.5, that the results are relatively insensitive to small changes in the three parameters, indicating a certain robustness of the parameterization.

In Fig. 4.6, PSC classifications calculated from observational data (top row) and model output from simulations using the new parameterization (middle row) as well as the constant, volume based nucleation rate (third row) are shown. The plots represent a selection of orbits from throughout late December in which the advantage of the saturation dependent nucleation rate parameterization over a constant rate is particularly evident. The bottom two rows of Fig. 4.6 show the time that the air parcel spent at temperatures below T_{NAT} and below $T_{NAT} - 4\,K$, while the contour lines on these two rows of plots show the minimum temperature reached along the trajectory, with respect to T_{NAT}.

Orbit 24_04. The middle column of Fig. 4.6 shows the results for orbit 24_04, which, as described above, was used to fit the model parameterizations. The observed PSC consisted of a compact area of Mix1 and Mix2, with a few spots of Mix2-enh and STS. The new parameterization reproduces the observed area of PSC rather well, however Mix2 is over-represented, and there are only a few areas of Mix1 about the periphery of the cloud. The constant nucleation rate produces considerably less PSCs than observed, and at a lower altitude than the observed PSC. Of course a larger area of PSC could have been formed with a higher constant rate, however other orbits shown in Fig. 4.6 illustrate that a higher rate will not improve the overall agreement between the constant rate simulations and the observed PSCs.

Orbit 19_08. In the first column of Fig. 4.6, results for orbit 19_08 are shown. These were among the first observations of PSC for the 2009/2010 winter, and the observed area of Mix1 and Mix2 PSC is
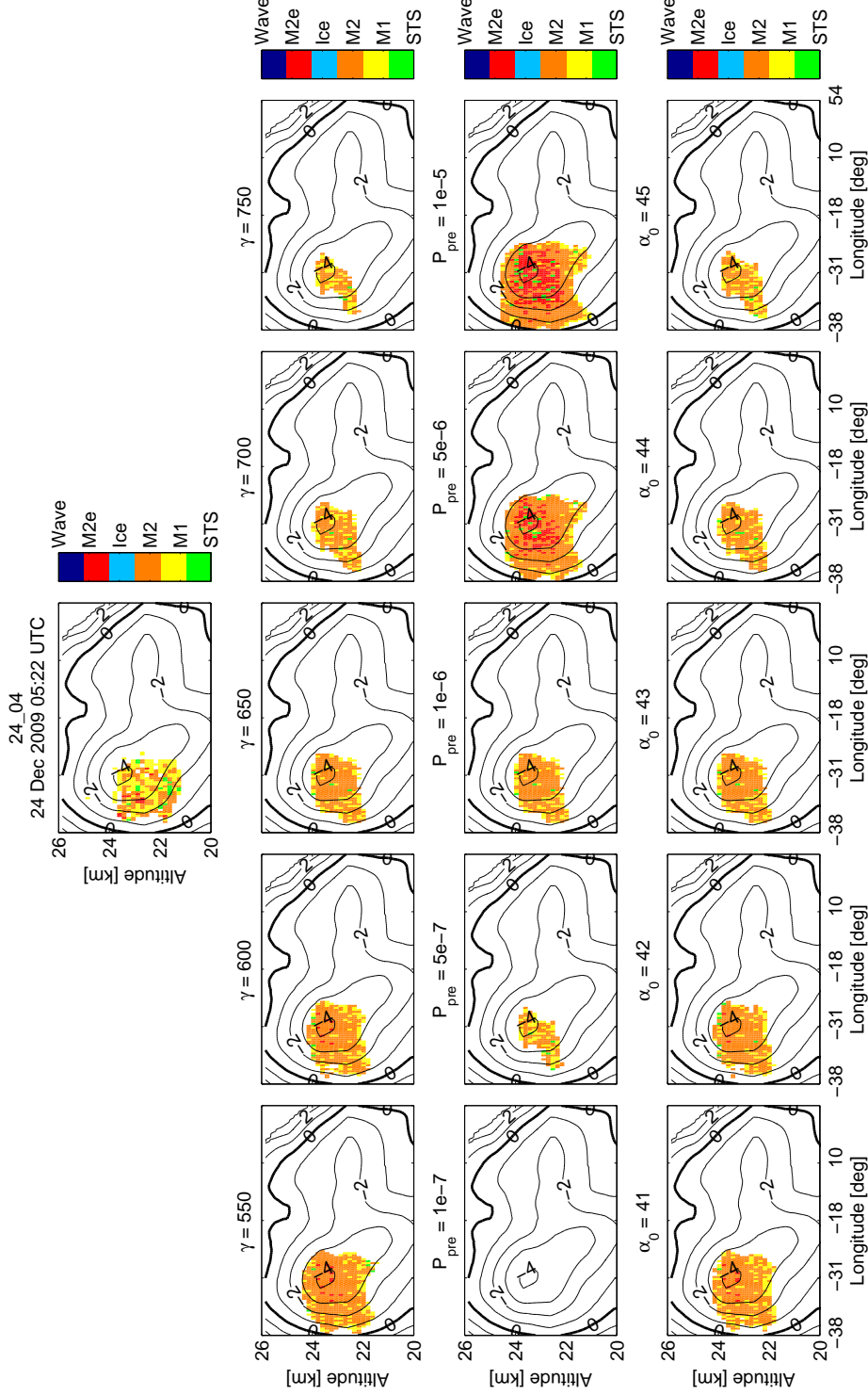
Figure 4.5: An illustration of the sensitivity of the modeled NAT classification to the three fitting parameters used in the new model, applied to CALIPSO orbit 24 December 2009 05:22:08 UTC (denoted orbit 24_04 in the text). The uppermost panel shows the observed PSC. The top row of panels shows how the results change as γ' is varied, while P_{pre} is held constant at 1×10^{-6} deg^{-1}, and α_0 at $43°$. In the second row, P_{pre} is varied while γ' is held constant at $650 K^3$, and α_0 at $43°$, while in the bottom row, P_{pre} and γ' are held constant at 1×10^{-6} and $650 K^3$, respectively, while α_0 is varied.
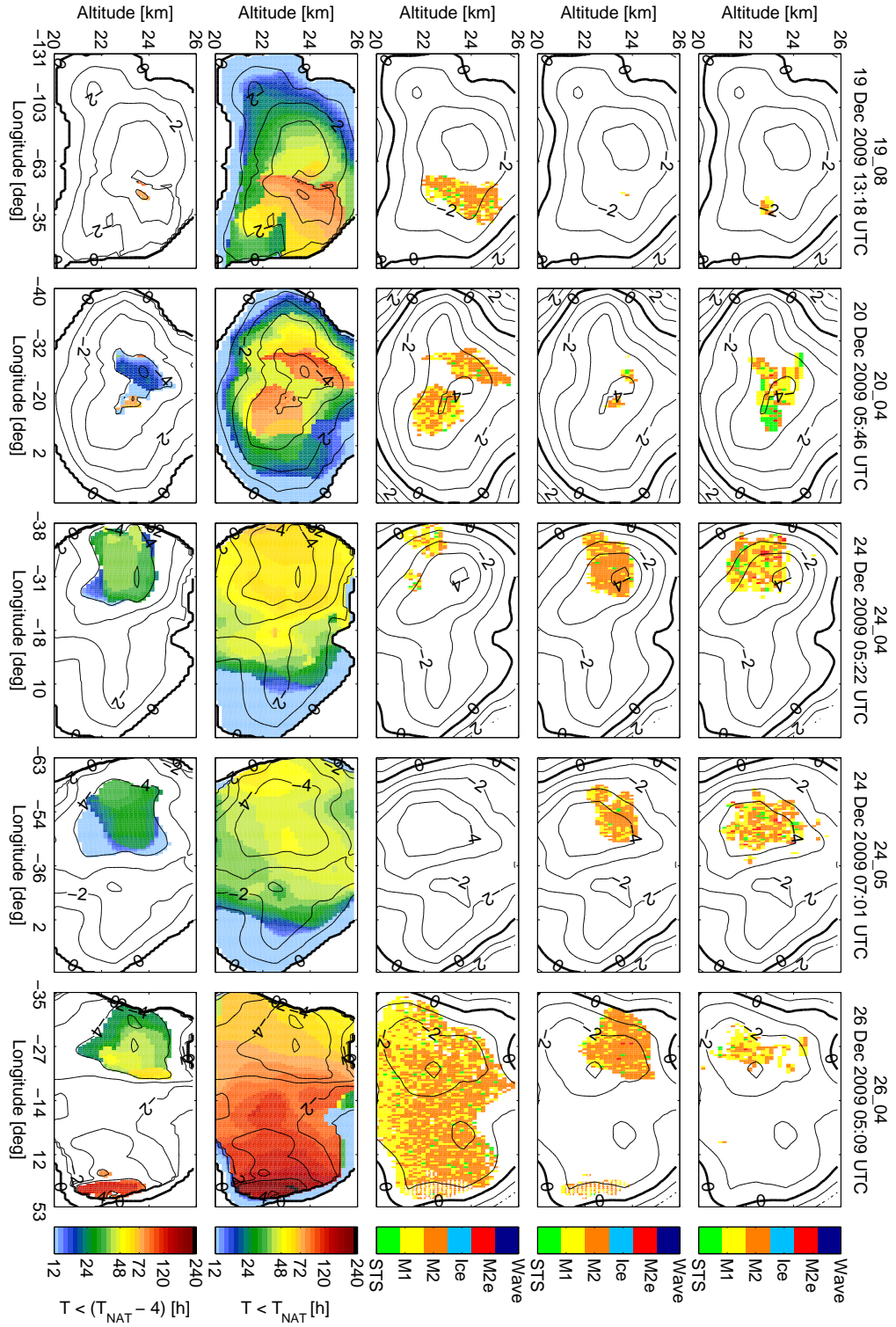
Figure 4.6: A comparison of the PSC classifications calculated from CALIOP observations (top row), from model results using the new nucleation parameterization (second row) and from model results using a constant, volume based nucleation rate (third row). The contour lines in the upper three rows indicate the temperatures (from the ERA-Interim reanalysis) at the time of CALIOP observation. Each column shows the results from one orbit. The bottom two rows of plots show the time spent by the trajectories at temperatures lower than T_{NAT} (fourth row) and $T_{NAT} - 4\,K$ (bottom row). On these two rows, the contour lines show the minimum temperature encountered along the trajectory.
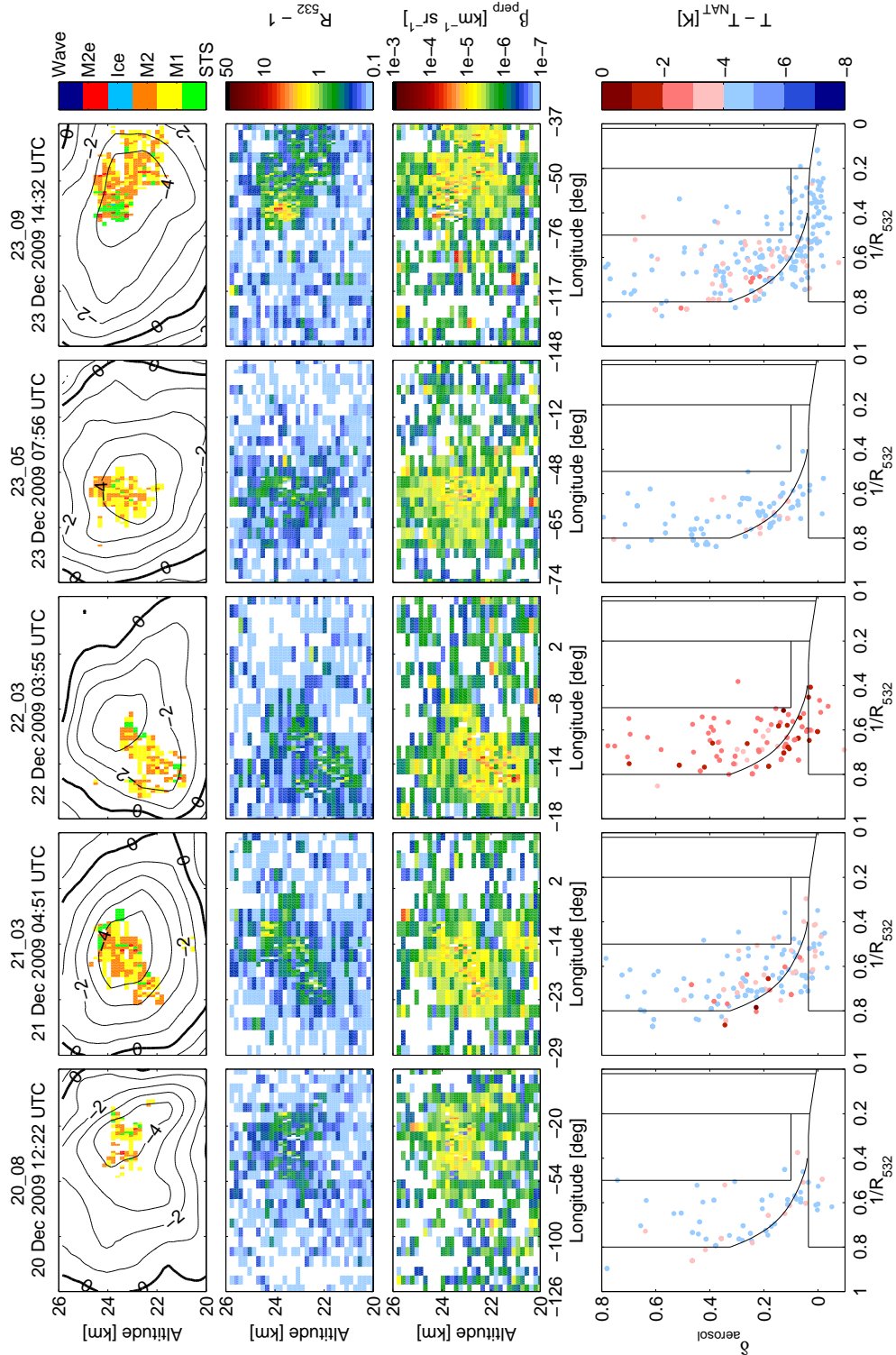
Figure 4.7: PSC classification (upper row) and optical properties obtained by CALIOP along several orbits in December 2009. The second row shows the aerosol backscatter ratio ($R_{532} - 1$) and the third the perpendicular backscatter coefficient (β_{perp}). In the panels on the bottom row, each observation point is represented by a dot, placed according to the observed aerosol depolarization ($\delta_{\mathrm{aerosol}}$), and inverse backscatter ratio, measured at a wavelength of 532 nm ($1/R_{532}$). The points are color coded to indicate the temperature with respect to T_{NAT} at the observation point.

Figure 4.8: As for Fig. 4.7, except in this case the model results are presented.
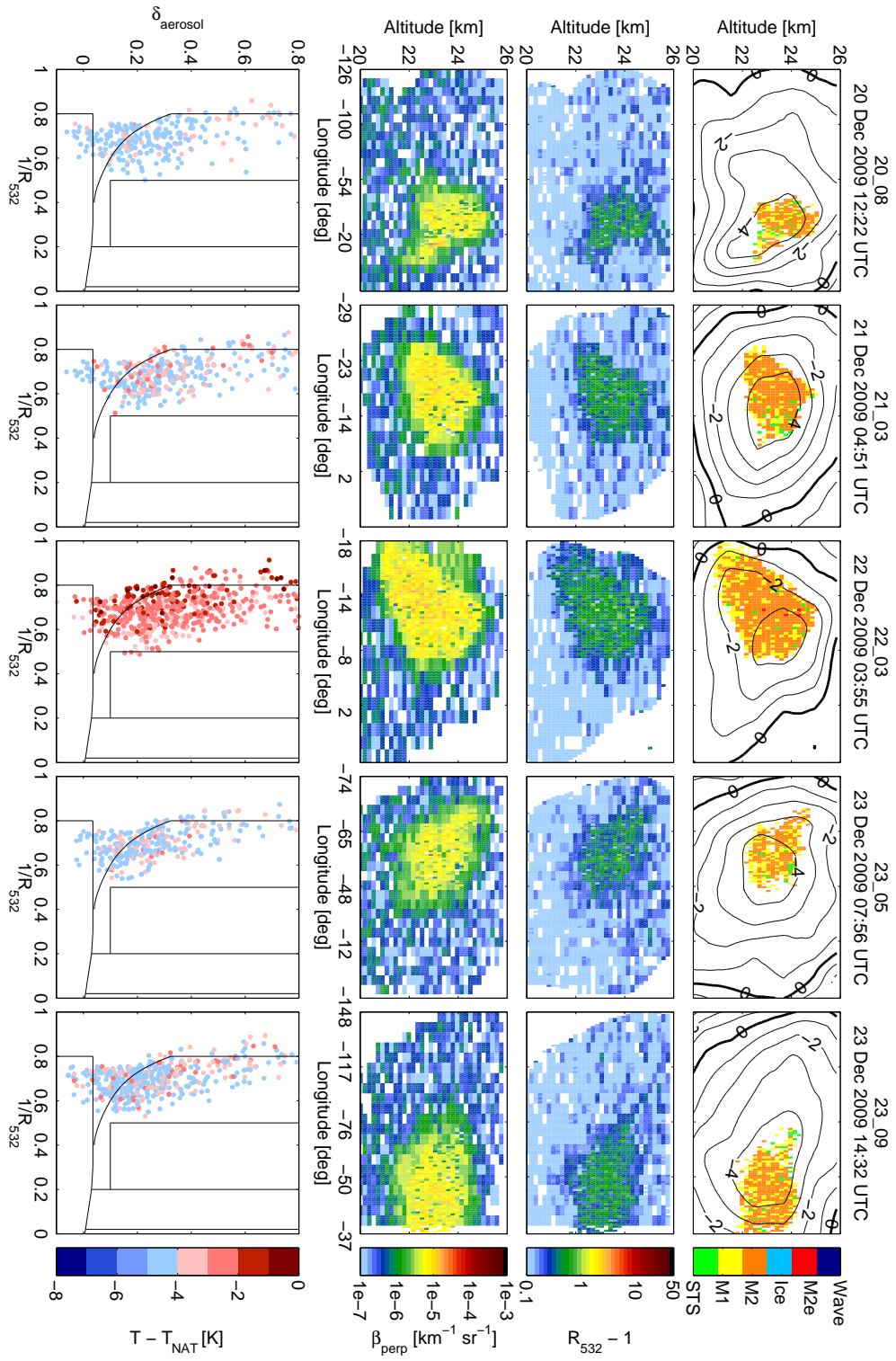
small. The new parameterization captures this well, also producing a small speck of PSC in the correct general area of the plot, while the constant nucleation rate, despite being on the low side for orbit 24_04, produces far to great an area of PSC. The reason for this can be seen by examining the temperature plots for this orbit. While a large number of trajectories spent up to approximately 100 h below T_{NAT}, only a very small fraction reached temperatures below $T_{\mathrm{NAT}} - 4$ K. As seen in Fig. 4.4, while the constant nucleation rate begins to produce NAT at a slow rate as soon as the temperature is below T_{NAT}, the new parameterization requires higher saturations, and once these saturations are reached, produces NAT relatively quickly. Of the studies discussed above, which used an air-volume based nucleation rate, only Grooß et al. (2005) carried out any simulations where a certain NAT saturation ratio had to be exceeded before NAT was nucleated. In their case, a constant nucleation rate was applied as soon as the temperature was below T_{NAT}, to form a low number density mode of large, sedimenting particles, while a mode of higher number density and smaller, non-sedimenting particles was nucleated only once the NAT saturation ratio exceeded 30 (equivalent to approximately $T_{\mathrm{NAT}} - 5$ K). Applying such a nucleation barrier may slightly improve the agreement of a simple volume based nucleation rate with the observations in some situations, however it will not solve the fundamental problem that such a nucleation parameterization cannot reproduce both PSCs formed during short periods at cold temperatures, and PSCs formed during long periods at relatively warm temperatures.

Orbit 20_04. In the next column, results from the orbit 20_04 are shown, where the new parameterization this time does not do as well, underestimating the area of PSC formed. The results from the constant nucleation rate are however again an overestimate of the PSC area. Orbit 20_04 is rather unique, in that the time spent at low temperatures is very short compared to the other orbits. The observed PSCs are mostly STS and Mix1 clouds, an aspect which is missing in the model results, which might also suggest that the ERA-Interim temperatures along this orbit are very likely too warm.

Orbit 24_05. For this orbit, the new parameterization produces PSCs at the correct altitude and longitude in comparison with the observed PSCs, albeit a slightly too small area, while the constant nucleation rate leads to a total absence of detectable PSC, due to the short time the trajectories spent at temperatures below T_{NAT}.

Orbit 26_04. For this orbit, the constant nucleation rate leads again to a far greater area of PSC than that which was observed. The new parameterization simulates a slightly too large area of PSC, again with an overestimation of the fraction of Mix2 with respect to Mix1. While only a few pixels of PSCs were observed at higher longitudes, the new parameterization leads to a significant region of a Mix1/Mix2 cloud. However, these simulated trajectories have spent more than 80 h below $T_{\mathrm{NAT}} - 4$ K before reaching the orbit. As discussed above, these particles will have sedimented, and mixed into air parcels with different saturations ratios, which is not taken into account in the analysis. This area has therefore been marked by shading.

4.3.3 Modeling the NAT formation in December 2009

The ability of the new NAT nucleation parameterization to reproduce the observed PSC characteristics is further illustrated by comparing the results from simulating a range of orbits from mid to late December 2009. In Fig. 4.7, each column shows the classification and observed optical characteris-

tics of PSCs observed along a particular orbit. The corresponding model results are shown in Fig. 4.8. The model reproduces the PSC classes quite well in all orbits, both in terms of the location and the size of the modeled PSC area, and largely also in terms of optical characteristics. However, the model slightly underestimates the observed proportion of STS. This underestimation would be reduced if the temperatures were lower.

In the plots of aerosol backscatter ratio ($R_{532} - 1$), the observations exhibit a larger variability than the modeled results, with the observational data containing some points reaching values of up to about 5 - 6 (i.e. $1/R_{532} > 0.15$), while the modeled values are generally below 1 (i.e. $1/R_{532} > 0.5$).

The observations show perpendicular backscatter coefficients (β_{perp}) up to $1 \times 10^{-5}\,\mathrm{km}^{-1}\,\mathrm{sr}^{-1}$ scattered throughout the observation area, while in the modeled case, such high values are confined to the vicinity of PSCs, and the modeled background signal remains below $1 \times 10^{-6}\,\mathrm{km}^{-1}\,\mathrm{sr}^{-1}$. The cause of this difference is that the instrumental noise spikes in the background observations, particularly those which form the tails of the β_{perp} distribution, are not entirely reproduced by the function used to generate the instrumental noise which was added to the modeled optical values. The noise in the measured backscatter is often caused by variations in radiation from space, to which the satellite based instruments are subjected.

Comparing the bottom panels of Figs. 4.7 and 4.8 shows that while the model generally reproduces the distribution of the points as a function of $\delta_{\mathrm{aerosol}}$ and inverse backscatter ratio, the distribution of the modeled points is more compact with respect to the inverse backscatter ratio than is the case for the observational data. While the points at small backscatter ratios ($1/R_{532} > 0.5$) are well represented, the model misses the observed large backscatter ratios. This concerns mainly STS clouds. Since STS clouds, owing to their large surface area, respond to temperature changes without significant kinetic delay, they act as thermometer, i.e. the only reasonable explanation is that the ERA-Interim reanalysis temperatures are occasionally too high. In the critical temperature regime of maximum HNO_3 uptake by STS, a temperature reduction of just $1\,\mathrm{K}$ can cause STS clouds to grow by up to a factor of 4 in volume (Carslaw et al., 1994), i.e. about a factor 1.6 in radius, which translates into an increase in ($R_{532}-1$) by up to a factor 6 (Biele et al., 2001). Indeed, the uncertainty of the ERA-Interim stratospheric temperatures is of the order of $1\,\mathrm{K}$ during the 2009/2010 Arctic winter, as a detailed comparison with radiosondes launched from Ny Ålesund and Sodankylä reveals (during the RECONCILE and LAPBIAT campaigns, not shown here). This corroborates the notion that the lack of high backscatters is most likely due to uncertainties in the reanalysis data.

4.3.4 The effect of temperature fluctuations

The model runs shown in Fig. 4.8 were repeated, however this time, random phases of the temperature fluctuations described in Sect. 4.2.3 were superimposed on the trajectories along which ZOMM was run. As expected, due to the increased NAT saturation ratios resulting from the temperature fluctuations, the area of the modeled NAT PSCs increased, as did the number density of the NAT particles in the clouds. In order to restore agreement with the observed properties of the PSCs, the value of γ' was increased from $650\,\mathrm{K}^3$ to $700\,\mathrm{K}^3$, increasing the NAT nucleation barrier. The results of these model runs are shown in Fig. 4.9. Comparing Fig. 4.9 with Fig. 4.7, it can be seen that the areas and
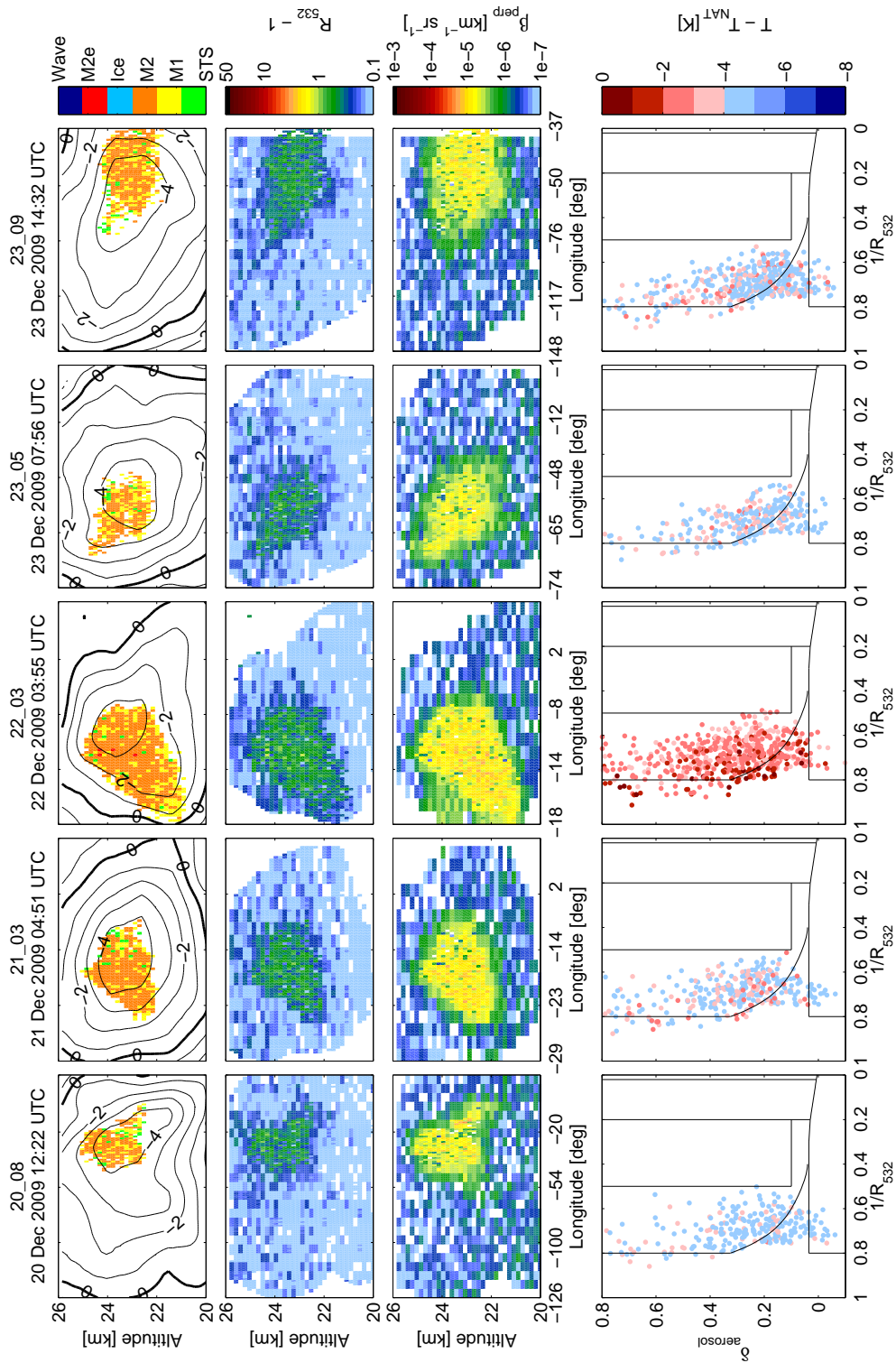
Figure 4.9: As for Fig. 4.8, except in this case the model results were calculated along trajectories with small scale temperature fluctuations included, and γ' was set to 700 K³.

classifications of PSCs modeled when accounting for temperature fluctuations generally agree very well with the observed PSC properties, although for orbits 21_03 and 22_03, the modeled PSC areas in Fig. 4.9 are slightly larger than observed. However, including the fluctuations also leads to a better representation of the observed $R_{532} - 1$ and β_{perp} values, particularly in the case of orbits 20_08 and 23_05.

4.4   Summary and conclusion

The 2009/2010 Arctic winter was unique, in that during the second half of December, the stratospheric temperatures were below T_{NAT}, while having stayed at least 2 K above the frost point and 5 K above the temperature required for homogeneous ice nucleation. Whereas there have been previous studies which have suggested that nucleation on ice is not the only NAT formation pathway in the polar stratosphere, the CALIOP measurements presented by Pitts et al. (2011) and modeled here provide unprecedented evidence for persistent ice-free NAT formation on the synoptic scale. Because of the meteorological situation, the CALIOP observational data set, together with a microphysical model, could be used to perform a detailed modeling of NAT formation in the absence of ice, enabling the derivation of a parameterization of the heterogeneous nucleation process. A new NAT nucleation parameterization was constructed, whereby NAT nucleates on foreign nuclei, such as meteoritic dust particles, immersed in stratospheric aerosol droplets. The parameterization uses active site theory to account for the range of qualities of the nucleation sites on the available nuclei. It extends the parameterization used by Luo et al. (2003b) for NAT formation via deposition nucleation on the uncoated surface of ice particles.

The PSC model ZOMM, containing the new parameterization, was applied to ten orbits between 19 December 2009, when the first pixels of PSC were observed by CALIPSO, and 26 December 2009. Later orbits were excluded as they were getting close to the date when ice was first observed and also because the time that a substantial fraction of the trajectories spent below T_{NAT} was longer than 80 h, increasing the influence of factors other than nucleation on the reproducibility of the observed PSC.

It has been shown that the new NAT nucleation parameterization leads to an accurate modeling of the observed PSC throughout this period, with the extent of the observed NAT PSC being extremely well reproduced. There is one notable exception, orbit 20_04, where the area of PSC was underestimated by the model. In this particular case, there was a relatively small number of trajectories which had spent a short time (less than 24 h) at low temperatures ($T_{NAT} - 4$ K). Under such conditions, small differences between the actual meteorological situation and the ERA-Interim data used by the model along the trajectories may lead to a larger apparent discrepancy between the modeled and observed PSC classifications. An examination of the modeled backscatter shows that it just marginally misses the CALIOP PSC classification criteria.

The classification of the modeled PSCs corresponds very well with the classification of the observed PSCs, however the model has a slight tendency to over represent Mix2, and underestimate Mix1 and STS. Again this could be due to slightly too high temperatures in the trajectories. On the other hand, Engel et al. (2013b) found that using the ECMWF operational analysis to calculate the trajectories,

rather than the ERA-Interim data, would have led to temperatures along the trajectories having a low bias.

The model also reproduces the individual optical quantities such as the backscatter ratio (R_{532}) and the perpendicular backscatter coefficient (β_{perp}) very well, while the variability as well as peak values in these quantities are not quite as high as those observed. The most significant differences are in the β_{perp} outside of the areas where PSC has been detected. In these places the observed β_{perp} exhibits a substantially larger variability than the modeled values. However, as no PSCs were detected in these areas, this has no impact on our results.

Small scale temperature fluctuations, with wavelengths that are not resolved in the ERA-Interim data, are expected to be present in the polar stratospheres. When such fluctuations are added to the trajectories along which ZOMM is run, higher NAT saturation ratios are reached, and thus NAT nucleates at higher temperatures. However, a similar effect can also be achieved to a large extent with a lower NAT nucleation barrier (γ') in the new parameterization. The standard value of $650\,\text{K}^3$ which was determined for γ', can therefore be viewed, to a certain extent, as including the main effects of the temperature fluctuations. On the other hand, if the new parameterization was to be implemented in a model where the small scale temperature fluctuations are resolved, a value of $\gamma' = 700\,\text{K}^3$ should be used instead.

The new parameterization has significant advantages over an approach which applies a single, saturation independent, air volume based nucleation rate per air volume as soon as the temperature drops below T_{NAT}. Such a method cannot accurately model both situations with temperatures remaining slightly below T_{NAT} for an extended period of time as well as situations with temperatures substantially below T_{NAT} prevailing over only short time periods. The new parameterization copes well with both situations (see for example Fig. 4.6, orbits 24_05 and 26_04), while also partially reproducing the observed PSCs in more extreme cases (e.g. orbit 20_04).

The new parameterization is computationally efficient and simple to implement in large scale models. Beyond the application in our microphysical box model without sedimentation, we hope that the application of this parameterization in three dimensional simulations of denitrification and renitrification in the polar stratospheric vortex will provide the opportunity to follow the development of the NAT particles over extended time periods, from nucleation through their growth and subsequent sedimentation, all the way to final evaporation or tropospheric removal.

Acknowledgments

Chapter 5

Heterogeneous formation of polar stratospheric clouds – Part 2: Nucleation of ice on synoptic scales

I. Engel[1], **B. P. Luo**[1], **M. C. Pitts**[2], **L. R. Poole**[3], **C. R. Hoyle**[4,1], **J. U. Grooß**[5], **A. Dörnbrack**[6], **and T. Peter**[1]

[1] *Institute for Atmospheric and Climate Science, ETH Zurich, Zurich, Switzerland*

[2] *NASA Langley Research Center, Hampton, Virginia, USA*

[3] *Science Systems and Applications, Incorporated, Hampton, Virginia, USA*

[4] *Laboratory of Atmospheric Chemistry, Paul Scherrer Institut, Villigen, Switzerland*

[5] *Institut für Energie- und Klimaforschung - Stratosphäre (IEK-7), Forschungszentrum Jülich, Jülich, Germany*

[6] *Institut für Physik der Atmosphäre, DLR Oberpfaffenhofen, Oberpfaffenhofen, Germany*

Abstract

This paper provides unprecedented evidence for the importance of heterogeneous nucleation, likely on solid particles of meteoritic origin, and of small-scale temperature fluctuations, for the formation of ice particles in the Arctic stratosphere. During January 2010, ice PSCs (Polar Stratospheric Clouds) were shown by CALIPSO (Cloud-Aerosol Lidar and Infrared Pathfinder Satellite Observations) to have occurred on a synoptic scale (~ 1000 km dimension). CALIPSO observations also showed widespread PSCs containing nitric acid trihydrate (NAT)particles in December 2009, prior to the occurrence of synoptic-scale regions of ice PSCs during mid-January 2010. We demonstrate by means of detailed microphysical modeling along air parcel trajectories that the formation of these PSCs is not readily reconciled with expectations from the conventional understanding of PSC nucleation mechanisms. The measurements are at odds with the previous laboratory-based understanding of PSC formation, which deemed direct heterogeneous nucleation of NAT and ice on preexisting solid particles unlikely. While a companion paper (Part 1) addresses the heterogeneous nucleation of NAT during December 2009, before the existence of ice PSCs, this paper shows that also the large-scale occurrence of stratospheric ice in January 2010 cannot be explained merely by homogeneous ice nucleation but requires the heterogeneous nucleation of ice, e.g. on meteoritic dust or preexisting NAT particles. The required efficiency of the ice nuclei is surprisingly high, namely comparable to that of known tropospheric ice nuclei such as mineral dust particles. To gain model agreement with the ice number densities inferred from observations, the presence of small-scale temperature fluctuations, with wavelengths unresolved by the numerical weather prediction models, is required. With the derived rate parameterization for heterogeneous ice nucleation we are able to explain and reproduce CALIPSO observations throughout the entire Arctic winter 2009/2010.

5.1   Introduction

The crucial role of polar stratospheric clouds (PSCs) for ozone destruction was identified by Solomon et al. (1986) shortly after the discovery of the Antarctic ozone hole (Farman et al., 1985). At that time, PSCs were thought to consist solely of ice, as other types of PSC particles were still unknown, such as nitric acid trihydrate (NAT) crystals or supercooled ternary solution (STS) droplets. However, little was known about PSC formation conditions. Reports about colorful PSC observations above the Scandinavian mountains go back to the late nineteenth century (Stanford and Davis, 1974; Peter and Grooß, 2012). These so called mother-of-pearl clouds consist of water ice and their existence requires temperatures low enough to nucleate ice particles despite the extreme dry conditions in the stratosphere. Whereas stratospheric temperatures in the Antarctic winter and spring regularly fall below the ice frost point (T_{frost}), mean temperatures within the Arctic vortex are warmer, owing to the larger land-ocean contrasts in the Northern Hemisphere generating atmospheric waves, which weaken the Arctic polar vortex. As a consequence, warm air masses from lower latitudes may mix into the polar vortex and increase the synoptic-scale temperatures (Solomon, 2004). However, on local scales, mountain-induced gravity waves cause air parcels to rise with accompanying high cooling rates reaching record low temperatures from time to time (Dörnbrack et al., 1999). This occasionally results in localized ice PSC

formation above the Arctic mountains with almost monodisperse particle distributions and, hence, their spectacularly colorful appearance (Carslaw et al., 1998b).

Since 2006, the spaceborne lidar CALIOP (Cloud-Aerosol Lidar with Orthogonal Polarization) aboard CALIPSO (Cloud-Aerosol Lidar and Infrared Pathfinder Satellite Observations) has provided a vortex wide view of PSC seasons and has contributed to our understanding of cloud formation processes. The Arctic winter 2009/2010 was of particular interest because of an European Union project with a field campaign aiming at a better understanding and the "Reconciliation of essential process parameters for an enhanced predictability of Arctic stratospheric ozone loss and its climate interactions" (RECON-CILE) (von Hobe et al., 2012). A major finding of Pitts et al. (2011) based on the CALIOP measurements during the Arctic winter 2009/2010 is that widespread PSCs containing NAT particles, albeit in low number densities, were frequently observed in December 2009, some ten days before any ice could have been present in the polar vortex due to the temperatures being well above the T_{frost}. This is in contradiction to our previous laboratory-based understanding of NAT formation, which (1) excluded the possibility of homogeneous NAT formation (Koop et al., 1995; Knopf et al., 2002) and (2) found heterogeneous nucleation rates on meteoritic and other material too slow to be an efficient mechanism (Biermann et al., 1996). The only well characterized pathway to form NAT was downstream of ice clouds through heterogeneous nucleation on ice particles (Luo et al., 2003b). However, the new CALIOP observations leave no doubt that there has to be an ice-independent NAT nucleation mechanism. Therefore, the role of particles, possibly consisting of meteoritic material (Curtius et al., 2005) and acting as NAT nuclei has to be reassessed. This question is addressed in the companion paper by Hoyle et al. (2013), while we show here that there is also evidence for heterogeneous ice nucleation, possibly on the same nuclei.

Dörnbrack et al. (2012) analyzed the meteorological conditions during the Arctic winter 2009/2010. Stratospheric minimum temperatures first fell below the existence temperature of NAT (T_{NAT}) in mid-December. A strong and cold vortex was persistent in January with minimum temperatures below T_{frost} for a week. Synoptic-scale ice clouds were observed during this time period, which is a rare occurrence in the Arctic. Even though 2009/2010 was an Arctic winter with unusually low minimum temperatures, we show here that these temperatures are, in themselves, insufficient to explain the CALIOP ice observations in terms of homogeneous nucleation. Rather, ice nucleates homogeneously only when $T \lesssim T_{\mathrm{frost}} - 3\,\mathrm{K}$, which according to meteorological temperature data was not reached on synoptic scales. Since heterogeneous nucleation of NAT is necessary to explain the CALIOP observations in December (when temperatures stayed more than $10\,\mathrm{K}$ above $T_{\mathrm{frost}} - 3\,\mathrm{K}$), this suggests that a similar pathway for ice formation might exist. For the troposphere, different laboratory as well as theoretical studies suggest that this process could be of importance for cirrus cloud formation (e.g. Zuberi et al., 2002; DeMott et al., 2003; Kärcher and Lohmann, 2003, and references therein). However, little attention has been paid to the implications of heterogeneous ice nucleation for PSC formation, although Bogdan et al. (2003) have shown that fumed silica, possibly representative for meteoritic smoke particles, is suitable to induce heterogeneous freezing of ice under stratospheric conditions. In addition, the possibility of heterogeneous nucleation of ice on preexisting NAT particles needs to be taken into account.

The approach of this paper is as follows: CALIOP PSC observations from the 2009/2010 winter serve as endpoints of air parcel trajectories, which are based on ERA-Interim reanalysis of the European

Centre for Medium-range Weather Forecasts (ECMWF). Microphysical box model runs including new heterogeneous nucleation pathways for PSC formation were performed along these trajectories. We adopt the functional dependence of nucleation on active sites as derived in previous work for Arizona Test Dust (ATD), and show that the assumption of active sites is suitable to describe the behavior of stratospheric ice nuclei. Through model comparisons with CALIOP observational data, we constrain the various parameters controlling the heterogeneous nucleation rate. We then show that the heterogeneous pathway for ice nucleation is in accordance with various time periods of the 2009/2010 Arctic winter and with other Arctic winters. A mountain wave ice cloud has also been studied using wind and temperature fields with different temporal and spatial resolutions. Details of how the heterogeneous nucleation of ice on nanometer-sized particles is implemented in our box model are explained in Sect. 5.2. Model results are shown in Sect. 5.3 including a detailed discussion of the evaluation procedure. Conclusions are provided in Sect. 5.4.

5.2   Observational data and model description

5.2.1   CALIPSO observations

Since April 2006, the CALIPSO satellite has provided a unique platform for near-global cloud observations. With its extensive coverage in particular in the polar regions, CALIOP is well suited for PSC studies. CALIPSO completes 14.5 orbits per day and reaches latitudes up to 82° (Winker et al., 2007). Along orbit tracks, the CALIOP lidar performs backscatter measurements at 532 and 1064 nm and linear depolarization measurements at 532 nm. PSCs are distinguished from the background aerosol as statistical outliers with significant enhancement in the backscatter ratio at 532 nm (R_{532}) or in the perpendicular backscatter coefficient (β_{perp}). Composition classes are discriminated according to Pitts et al. (2009, 2011). Six different composition classes are distinguished from the measured lidar signal, covering supercooled ternary solutions (STS), mixtures of liquids and NAT particles and ice PSCs. Liquid/NAT mixtures are further separated according to varying NAT number densities inferred from optical calculations. Mix1 is limited to NAT particles $< 10^{-3}\,\mathrm{cm}^{-3}$, intermediate number densities of NAT particles are classified as Mix2, high number density NAT clouds with number densities $> 0.1\,\mathrm{cm}^{-3}$ are captured in the Mix2-enh class. In addition to synoptic-scale ice clouds, wave ice with $R_{532} > 50$ are treated separately. We note that the "PSC mixture classes" of Pitts and coworkers are very similar to the previously used "PSC types" (e.g. Table 1 of Biele et al., 2001), but through their name make explicit that PSCs are external particle mixtures.

We evaluate the model results by comparing with the spatial pattern of aerosol R_{532} (or the aerosol backscatter, $R_{532} - 1$, respectively) and β_{perp}, and with the PSC classification of Pitts et al. (2011) as described above. To this end we demand that the model agrees with the spatial patterns of the optical measurements of R_{532}, β_{perp}, and mixture classes along individual orbits, as well as with the 2-D scatter plots of aerosol depolarization ratio ($\delta_{\mathrm{aerosol}}$) versus inverse backscatter ratio ($1/R_{532}$). To our knowledge this is a PSC modeling approach of hitherto unprecedented rigor. This approach is required to enable identification and quantification of the heterogeneous nucleation pathway.

5.2.2 Trajectory calculations

Based on six-hourly wind and temperature fields from the ERA-Interim reanalysis produced by the ECMWF (Dee et al., 2011) with a horizontal resolution of $1° × 1°$, we calculated ten day backward trajectories using the trajectory module of the Chemical Lagrangian Model of the Stratosphere (CLaMS) (McKenna et al., 2002). In the altitude range of 18 to 26 km, we started backward trajectories every 25 km horizontally and every 500 m vertically from CALIPSO orbits. With this mesh of trajectories we cover every 15th CALIOP data point within an orbit curtain, enabling us to reproduce whole orbit scenes within a reasonable computing time. Box model runs were performed forward in time, ending at the point of CALIOP observations. We initialized the model at temperatures above T_{NAT} to start the calculations from the background aerosol and to avoid the preexistence of PSC particles. The box model trajectory is driven by ERA-Interim temperature and pressure data interpolated to time steps of 15 min. Even though the temporal resolution of the underlying meteorological data is on a six hourly basis, the shorter trajectory time steps allow for a more accurate spatial representation of the pathway (see Brabec et al., 2012, for a discussion of this point). Additionally, short-range forecasts were conducted by the Integrated Forecast System of the ECMWF to study the impact of higher temporal and spatial resolutions on the microphysical processes. The forecasts were initialized every 6 h, had a lead time of 5 h, and were run for a period of 24 h. Here, the one hourly output is used for trajectory calculations of a particular event of mountain wave induced PSCs above Greenland. To calculate T_{NAT} and T_{frost} along the trajectories, we used H_2O and HNO_3 mixing ratios for the corresponding days from the Aura Microwave Limb Sounder (MLS) (Waters et al., 2006). Daily values were horizontally averaged over cloud free areas within the vortex and vertically interpolated to starting pressures of the trajectories. In addition, Aura MLS H_2O and HNO_3 mixing ratios served as starting values for the calculations and are transported along the trajectories of air parcels serving as input for PSC formation, which enables a point-by-point comparison of model results and observations. However, particle sedimentation is ignored. To cope with this problem, we focused on orbits where the backward trajectories had only short time periods below T_{NAT}. Cases where temperatures were either as cold as T_{NAT} at thebeginning of the trajectory or stayed below $T_{\text{NAT}} - 4$ K for longer than 80 h, were removed from our analysis and shaded in the graphical representation of the results, see below.

This modeling approach fully relies on temperature information obtained from meteorological data sets. Furthermore, MLS measurements hold uncertainties in the gas phase H_2O and HNO_3 mixing ratios, which affect the calculations of T_{frost} and T_{NAT}, but to a lesser degree. Typical single-profile precisions are 4 to 15 % for H_2O (Read et al., 2007; Lambert et al., 2007) and 0.7 ppbv for HNO_3 (Santee et al., 2007). Microphysical studies of PSCs are highly temperature dependent and inaccuracies of a few Kelvin, especially in situations close to T_{frost} could change the interpretation of results significantly (Manney et al., 2003). For this study, we compared temperatures from ERA-Interim reanalysis with ECMWF operational analysis and the Goddard Earth Observing System Model, Version 5 (GEOS-5) analysis. We found that temperatures from the ECMWF operational analysis were consistently lower (on average by 1 K) during the entire winter than both other temperature data sets. A comparison of both ECMWF data sets with unassimilated measured temperatures from 25 radiosondes, which we launched from Ny-Ålesund (Spitsbergen) and the Finnish Met Service launched from Sodankylä (courtesy of Rigel Kivi), shows the same tendency. ECMWF operational analysis temperatures are colder

than temperatures measured above Ny-Ålesund and Sodankylä during January 2010. Therefore we decided to base our analysis on ERA-Interim reanalysis data. Even though we are confident that we have chosen the best meteorological data available for this study, temperature uncertainties exist and remain difficult to quantify.

5.2.3 Microphysical box model

The Lagrangian Zurich Optical and Microphysical box Model (ZOMM) is used to calculate the formation of PSCs. The kinetics of uptake and release of nitric acid and water in STS droplets is determined using vapor pressures from an ion interaction model (Pitzer, 1991; Luo et al., 1995). As already mentioned, the model is initialized at temperatures where background conditions can be assumed. The total number of supercooled binary solution (SBS) droplets is assumed to be equal to $15\,\mathrm{cm}^{-3}$. Half of them are assumed to be pure SBS, log-normally distributed across 26 radii with a mode radius of 70 nm and a standard deviation of 1.8, as is characteristic for winter polar stratospheric background conditions (Dye et al., 1992). The other half is assumed to contain a solid core of 20 nm of an insoluble material with an additional coating of 50 nm, motivated by observations of Curtius et al. (2005). Along the trajectories, allowing for changing pressure and temperature, droplet radii grow and shrink in a full kinetic treatment and without being restricted to the initial log-normal shape of the distribution (Meilinger et al., 1995). Ice or NAT particle nucleation results in initiation of additional size classes as soon as number densities exceed a critical value of $10^{-6}\,\mathrm{cm}^{-3}$. Evaporated particles, e.g. after a temperature increase, can be relocated to their original droplet radius. Homogeneous ice nucleation in STS droplets is calculated using rates provided by Koop et al. (2000). Details of the new heterogeneous pathway of ice nucleation are specified in Sect. 5.2.3. Section 5.2.3 deals with NAT nucleation within ZOMM. The output includes among several other parameters size-resolved number densities of STS, NAT and ice, which are used in Mie and T-Matrix scattering codes (Mishchenko et al., 2010) to compute optical parameters for comparison with CALIOP observations. Liu and Mishchenko (2001) recommended that ice crystals in PSCs be modeled as prolate spheroids with aspect ratios ⩽ 0.83 (diameter-to-length ratio). Our calculations show a better agreement with CALIOP maximum values of $\delta_{\mathrm{aerosol}}$ for prolate spheroids with aspect ratios of 0.9 (diameter-to-length ratio). This value has been chosen for both ice and NAT. The refractive index is 1.31 for ice and 1.48 for NAT. For more details see the companion publication as well as the listed literature.

Figure 5.1 summarizes the homogeneous and heterogeneous pathways of PSC formation, which are accounted for in this study. In previous modeling studies, ice was only allowed to nucleate homogeneously within liquid STS particles at $T \lesssim T_{\mathrm{frost}} - 3\,\mathrm{K}$, and only then NAT was allowed to form on the preexisting ice particles (dashed arrows). Our companion paper (Hoyle et al., 2013) introduced heterogeneous NAT nucleation on foreign nuclei, while within this publication we discuss the possibility of heterogeneous ice formation. These previously not quantified pathways have been implemented into ZOMM and are indicated by solid arrows. In addition, we allow ice to nucleate heterogeneously on NAT particles, also marked by a solid arrow (see Fig. 5.1).
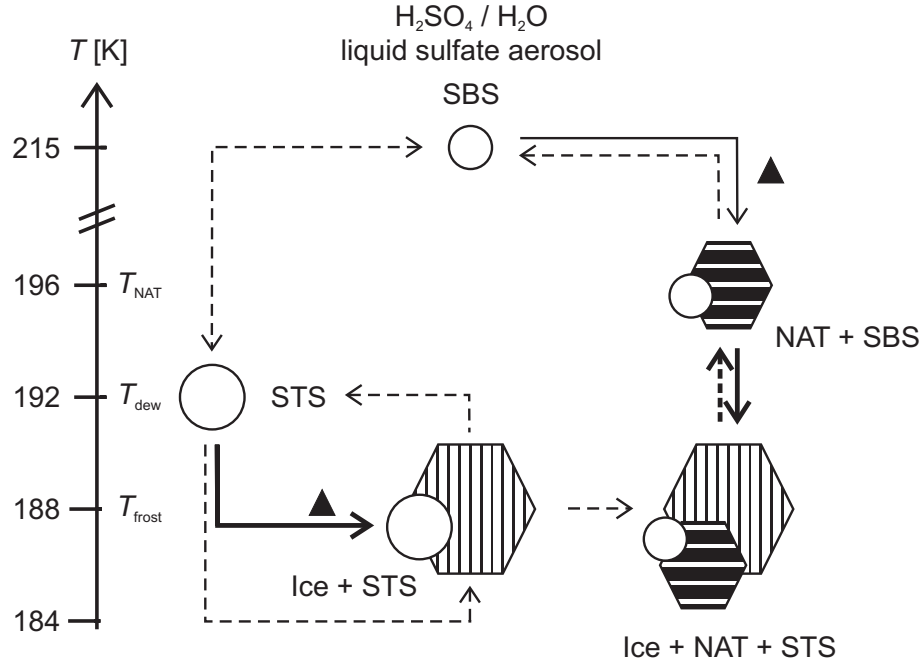
Figure 5.1: PSC formation pathways implemented into ZOMM (Zurich Optical and Microphysical box Model) with SBS = Supercooled Binary Solution (H_2SO_4/H_2O), STS = Supercooled Ternary Solution ($HNO_3/H_2SO_4/H_2O$), NAT = Nitric Acid Trihydrate ($HNO_3 \cdot 3H_2O$), ▲ = foreign nuclei, e.g. meteoritic dust. Dashed arrows denote pathways included in previous schemes (e.g. following Lowe and MacKenzie, 2008; Peter, 1997). Solid arrows show the heterogeneous nucleation pathways of NAT and ice on preexisting solid particles supported by the new field observations. Thick arrows are discussed within this publication; thin solid arrow is discussed in companion paper (Hoyle et al., 2013). Note that some arrows are unidirectional (i.e. the other direction is thermodynamically not possible), while others are bidirectional.

Heterogeneous ice nucleation

According to classical nucleation theory (Pruppacher and Klett, 1996), the heterogeneous rate coefficient J_{het} for ice nucleation with units of $cm^{-2}\,s^{-1}$ is dependent on temperature T and can be formulated as

$$J_{het}(T) = \frac{kT}{h} \exp\left[-\frac{\Delta F_{diff}(T)}{kT}\right] \times n \, \exp\left[-\frac{\Delta G(T) f_{het}}{kT}\right] \tag{5.1}$$

where k is the Boltzmann and h the Planck constant. n is the number density of water molecules at the interface between water and the ice nucleus (IN) and is set to $10^{15}\,cm^{-2}$ (Marcolli et al., 2007). The diffusion activation energy ΔF_{diff} and the Gibbs free energy ΔG are parameterized according to Zobrist et al. (2007) and references therein.

The ice saturation ratio S enters into the calculation of ΔG and is defined for immersion freezing as

$$S(T) = \frac{p_{liq}(T)}{p_{ice}(T)}. \tag{5.2}$$

Vapor pressures of liquid water p_{liq} and ice p_{ice} are calculated following Murphy and Koop (2005). The compatibility function f_{het} discriminates homogeneous and heterogeneous nucleation. f_{het} expresses a reduction of ΔG needed to form a critical ice embryo and can be written as

$$f_{het} = \frac{1}{4}(2 + \cos \alpha)(1 - \cos \alpha)^2. \tag{5.3}$$

The contact angle α between the ice embryo and the IN can vary from 0° to 180°, which for small contact angles results in nucleation starting as soon as the vapor is saturated, whereas for large contact angles heterogeneous nucleation is not favored and is comparable to homogeneous nucleation (Seinfeld and Pandis, 2006).

Subsequently, we will utilize a parameterization for ice nucleation on ATD performed by Marcolli et al. (2007). They performed freezing experiments and observed heterogeneous nucleation over a broad temperature range. They concluded that the ability to nucleate ice varies between different ATD particles and formulated an occurrence probability (P_{as}) of so called active sites:

$$P_{as}(\alpha) = P_{pre} \times \exp\left(\frac{-51°}{\alpha - \alpha_0}\right). \tag{5.4}$$

Active sites are surface inhomogeneities such as steps or cavities, or chemical or electrical inhomogeneities, which are assumed to initiate ice nucleation (Pruppacher and Klett, 1996). Following Marcolli et al. (2007), the mean area of an active site is set to $A_{as} = 10\,nm^2$. Even though a single particle may carry several active sites, only the best active site with the smallest contact angle α is of importance. The occurrence probability of active sites decreases with decreasing α. The best fit for ATD in tropospheric ice formation was achieved by assuming the nucleation to follow the singular hypothesis with $\alpha_0 = 46°$ and $P_{pre} = 10^{-5}$ for a step width of 1° (Marcolli et al., 2007). Here, we implement the singular hypothesis of an active site distribution into ZOMM by treating the prefactor P_{pre} and the most suitable (minimum) contact angle α_0 as free fitting parameters to adjust the formulation of P_{as} to stratospheric conditions, fitted to the CALIOP observations.

Our concept of heterogeneous nucleation cannot discriminate different kinds of dust or other solid cores that might be immersed in the stratospheric background aerosol. However, our choice of number densities and sizes are in general agreement with studies of meteoritic material, transported from the mesosphere down into the polar vortex. With an average extraterrestrial mass influx of 20 to 100 tons per day (Cziczo et al., 2001), which compares with 160 tons per day of sulfur influx (or 650 tons per day of aqueous sulfuric acid) during volcanically quiescent times (SPARC, 2006), meteoritic material constitutes 3 to 15 wt% of the stratospheric aerosol. It is spread all over the globe and funneled into the polar winter stratosphere of both hemispheres by the Brewer-Dobson circulation. For our study, we assume a number density of $7.5\,cm^{-3}$ of meteoritic particles uniformly distributed throughout the Arctic stratosphere, which results in 50 % of the total background aerosol droplets carrying meteoritic particles. These numbers are in agreement with Curtius et al. (2005) and supported by similar measurements performed within RECONCILE (von Hobe et al., 2012). Stratospheric H_2SO_4/H_2O particle concentrations range from 10 to 20 cm^{-3}, and a higher fraction of nonvolatile compounds was measured inside (67 %) the vortex than outside (24 %), supporting the funneling effect mentioned above. The foreign nuclei within ZOMM are represented with a fixed radius of 20 nm following Hunten et al. (1980), who modelled the recondensation of ablated meteoric material into nanometer-sized smoke particles.

Pitts et al. (2011) observed that the increase in synoptic-scale ice PSCs starting on 15 January 2010 goes along with a decrease in high number density NAT mixtures. During the first two weeks of January 2010, wave ice was the major source of observed Mix2-enh. Decreasing number densities in the Mix2-enh class might be an indicator for nucleation of synoptic-scale ice on these preexisting NAT particles. To substantiate such a dependence, vortex wide calculations on longer time scales would be needed, and mixing of air masses and a resolution high enough to represent mountain waves would be additional requirements. Our approach is not capable for simulations lasting over more than a few days. Therefore, we consider heterogeneous nucleation of ice on NAT only in a simplified way with a fixed α of 60°. By using a fixed contact angle, we assume that all NAT particles have an equal efficiency to nucleate ice. This simplification is in agreement with Luo et al. (2003b), who made a similar assumption for the converse nucleation of NAT on ice. Since CALIOP observed extensive fields of Mix2-enh only directly after the occurrence of wave-induced ice clouds (Pitts et al., 2011), whereas NAT number densities of Mix1 and Mix2 clouds are more than two orders of magnitude lower than number densities of foreign nuclei, this simplification seems to be sufficient as shown in Sect. 5.3. Changing α in either direction does not significantly change modeled ice number densities because the result is dominated by either homogeneously nucleated ice (typically in mountain waves) or heterogeneous nucleation of ice on dust particles (on the synoptic-scale).

Heterogeneous NAT nucleation

Our current understanding of PSC formation includes two mechanisms to nucleate NAT. First, the nucleation scheme of NAT particles forming on solid inclusions such as meteoritic dust, is described and discussed in detail in the companion paper by Hoyle et al. (2013). We apply the newly developed NAT nucleation parameterization as defined in the companion paper by using $\gamma' = 650\,\mathrm{K}^3$ in simulations without and $\gamma' = 700\,\mathrm{K}^3$ in simulations with small-scale temperature fluctuations. Second, the original approach, the formation of NAT on preexisting ice particles, follows Luo et al. (2003b). The parameterizations for the nucleation rate for NAT on ice is defined as follows:

$$J_{\mathrm{NAT}}(T) = 6.24 \times 10^{24}\,\mathrm{cm}^{-2}\,\mathrm{s}^{-1} \times (T/\mathrm{K}) \times \exp\left[-\frac{273.15^3}{T^3} \frac{\gamma}{(\ln S_{\mathrm{NAT}}(T))^2} - \frac{2000\,\mathrm{K}}{T} \right]. \qquad (5.5)$$

The parameter γ was constrained by Luo et al. (2003b) to be $\gamma = 328\,\mathrm{K}^3$. We discuss the importance of changing this parameter in Sect. 5.3.

5.2.4 Small-scale temperature fluctuations

Small-scale temperature fluctuations arise from gravity waves, which can be described as an adiabatic displacement of an air parcel (Fritts and Alexander, 2003). Gary (2006) found that fluctuation amplitudes have a strong latitudinal and seasonal dependence and are largest during winter at high latitudes. A comparison between two different sets of aircraft measurements at different flight levels (∼ 11 and 18 km) showed that amplitudes are larger in the stratosphere than in the troposphere. The underlying terrain, e.g. mountains, has an additional influence (Carslaw et al., 1998b). Besides topography, convection and wind shear are further significant sources for gravity waves (Fritts and Alexander, 2003). Several earlier studies investigated the effect of small-scale temperature fluctua-

tions and associated high cooling rates on PSC formation and properties (e.g. Murphy and Gary, 1995; Meilinger et al., 1995; Bacmeister et al., 1999). The effect of different cooling rates on the number density of ice crystals in cirrus clouds was demonstrated by Hoyle et al. (2005) and Kärcher and Lohmann (2003). On synoptic scales with cooling rates of less than one Kelvin per hour, ice number densities remain low and particles can grow to large sizes. In contrast, high cooling rates of several Kelvin per hour result in higher number densities and therefore the ice particles remain smaller. Here we make use of the vertical velocity and temperature time series obtained from the SUCCESS (Subsonic Aircraft: Contrail and Cloud Effects Special Study) data used by Hoyle et al. (2005) to conduct model runs with and without fluctuations to investigate their importance for computed ice cloud properties. The magnitude of the SUCCESS temperature fluctuations is in agreement with the findings by Gary (2006). We prepared a pool of 100 different fluctuation time series with a temporal resolution of 1 min, which we superimposed randomly onto the synoptic-scale trajectories. Only wavelengths $< 100\,\mathrm{km}$ were considered, which are not resolved in the wind fields used in our trajectory calculations. Mean temperature amplitudes were scaled to $\pm 0.5\,\mathrm{K}$. A typical synoptic-scale trajectory with superimposed temperature fluctuations is shown in Fig. 5.2a. The distribution of cooling rates taken from a representative number of trajectories with and without fluctuations is illustrated in Fig. 5.2b. Ice number densities from ZOMM simulations carried out with either homogeneous ice nucleation only or homogeneous and heterogeneous ice nucleation in competition are presented in Fig. 5.2c. Independent of the nucleation mechanism, ice number densities originating from ERA-Interim synoptic-scale cooling rates remain below $\sim 0.1\,\mathrm{cm^{-3}}$. Ice crystal number densities increase with increasing cooling rates. At the same time, because heterogeneous nucleation sets in at higher temperatures compared to homogeneous nucleation, the maximum saturation reached is lower, and therefore the number of ice crystals formed is also lower. In the homogeneous case, cooling rates $> 10\,\mathrm{K\,h^{-1}}$ enable the entire background aerosol of $15\,\mathrm{cm^{-3}}$ to freeze. In the case of heterogeneous and homogeneous nucleation, cooling rates $> 50\,\mathrm{K\,h^{-1}}$ are needed to also activate the remaining $7.5\,\mathrm{cm^{-3}}$, which have no solid inclusion, homogeneously.

Meilinger et al. (1995) demonstrated that the relaxation times for ice and NAT differ greatly due to different partial pressures. While H_2O reaches equilibrium on a timescale of seconds, HNO_3 uptake into micron size particles takes hours. During the warming phase of a temperature fluctuation, H_2O may partition from a liquid droplet back into the gas phase more quickly than HNO_3, which causes an increase in the NAT saturation ratio. Small-scale temperature fluctuations lead to an increase in the modeled area of NAT PSCs, as well as an increase in the number densities of NAT particles within the clouds. Hoyle et al. (2013) accounted for the effect of rapid cooling rates by providing two different parameterizations for NAT nucleation, depending on weather or not small-scale fluctuations are resolved by the trajectories.

5.2.5 CALIOP comparison

We estimated the uncertainty σ with units of $\mathrm{km^{-1}sr^{-1}}$ in the CALIOP measurements individually for the parallel and perpendicular backscatter coefficients β as follows:

$$\sigma(\beta) = \frac{1}{75}\,\beta\,\sqrt{\frac{2.39 \times 10^{-5}\,\mathrm{km^{-1}sr^{-1}}}{\beta} \times \frac{1500\,\mathrm{km}}{\Delta_{\mathrm{horizontal}}} \times \frac{5\,\mathrm{km}}{\Delta_{\mathrm{vertical}}}}. \qquad (5.6)$$
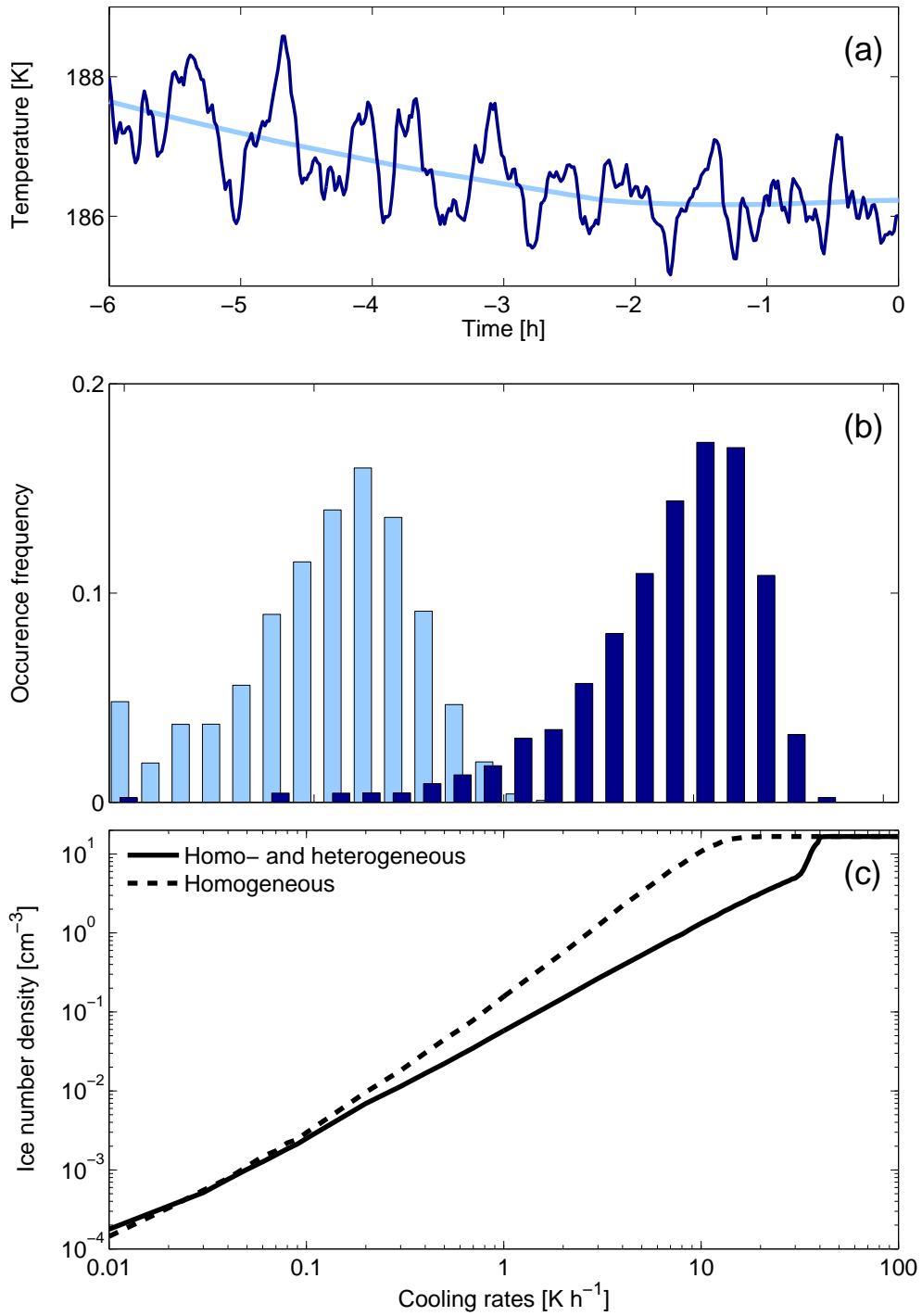
Figure 5.2: (a) A typical synoptic-scale ERA-Interim trajectory (light blue), shown together with the same trajectory, with temperature fluctuations superimposed (dark blue). (b) The occurrence frequency of cooling rates on ERA-Interim synoptic-scale trajectories (light blue) and trajectories with superimposed temperature fluctuations (dark blue). (c) Simulated ice number densities versus cooling rates with only homogeneous ice nucleation (dashed curve) and in addition heterogeneous ice nucleation (solid curve).
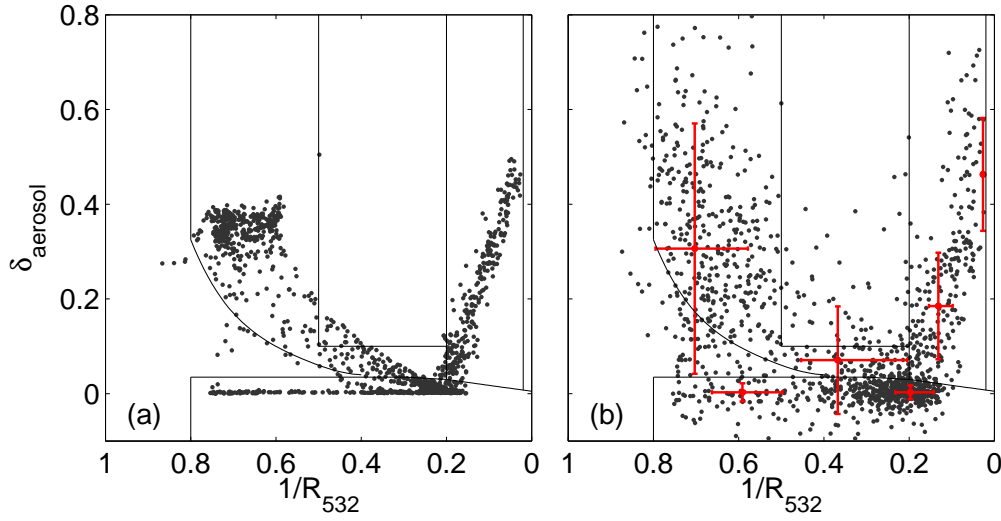
Figure 5.3: Simulated model results for an exemplary CALIPSO orbit. Results are shown within the 2-D scatter plot of aerosol depolarization ratio (δ_aerosol) versus inverse R_{532} ($1/R_{532}$). (a) Unperturbed model results. (b) Model results with applied CALIOP uncertainties (σ). Uncertainties in parallel and perpendicular backscatter are calculated using Eq. (5.6), propagated into δ_aerosol and $1/R_{532}$ and shown as red error bars.

The uncertainty scales as the square root of the signal β, inversely as the square root of the horizontal averaging distance $\Delta_\text{horizontal}$, and inversely as the square root of the vertical averaging distance Δ_vertical. The observed signal-to-noise ratio (SNR = $\beta/\sigma(\beta)$) for molecular backscatter at an altitude of 30 km ($\beta = 2.39 \times 10^{-5}\,\text{km}^{-1}\text{sr}^{-1}$) averaged over 1500 km horizontally and 5 km vertically is 75 (Hunt et al., 2009).

We apply the noise level of the satellite data to our model results by calculating σ for the simulated parallel and perpendicular backscatter coefficients. Before adding the uncertainty to each component, we scaled those values randomly under the assumption of a normal distribution. The noise perturbed coefficients were used to further calculate optical properties such as R_{532} and δ_aerosol for a comparison with CALIOP. Figure 5.3 gives an example for CALIPSO uncertainties in δ_aerosol and $1/R_{532}$. We classified the model output according to Pitts et al. (2011) in the composition classes STS, Mix1, Mix2, Mix2-enh, ice, and wave ice (separated by thin black lines). An altitude dependent PSC detection threshold for R_{532} and β_perp was applied (Pitts et al., 2009) to avoid modeled areas with optical signatures smaller than the noise of the lidar measurement being classified as PSCs.

5.3   Results and Discussion

We use two CALIPSO orbit tracks on 18 January 2010 to constrain the fits and compare later with other time periods in January 2010 and with other seasons. The geographical location of the selected orbit tracks is shown in Fig. 5.4. Orbit 1 (2010-01-18T01-58-53Z) is located upstream of the cold pool of the polar vortex. Temperatures along the associated backward trajectories are lowest at the CALIPSO orbit track. Synoptic-scale areas of ice PSCs were observed during this time of the winter and Orbit 1 was
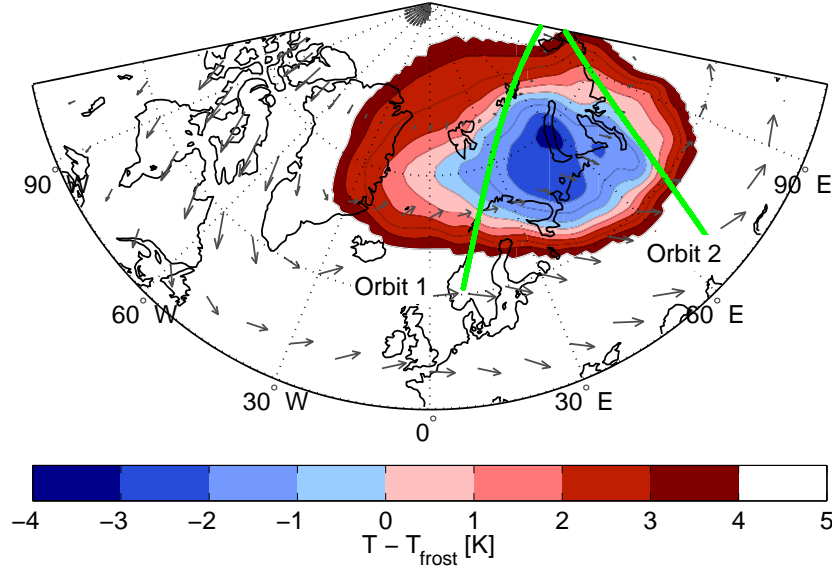
Figure 5.4: Geographical location of two selected CALIPSO orbit tracks on 18 January 2010. Referring to the Supplement of Pitts et al. (2011), Orbit 1 is defined as 2010-01-18T01-58-53Z and Orbit 2 as 2010-01-18T21-45-30Z, respectively. ERA-Interim wind fields (arrows) and temperatures (color-coded relative to T_{frost}) are shown at the 30 hPa pressure level for 12:00 UTC.

chosen as being representative for this period. Orbit 2 (2010-01-18T21-45-30Z) is located downstream of Orbit 1 at the eastern edge of the polar vortex. Trajectories ending at Orbit 2 experienced temperatures below T_{frost} for an extended period of time. The freshly formed ice cloud observed in Orbit 1 has altered while passing through the cold pool of the vortex. At Orbit 2, temperatures are increasing and partly already above T_{frost}. Hence, along Orbit 2, CALIOP observes a mixed-phase PSC dominated by higher number densities of NAT particles (Mix2-enh) formed on the preexisting ice.

We compare model runs with different nucleation mechanisms and temperature treatments with CALIOP observations. Figures 5.5 and 5.6 summarize the results for Orbit 1 and 2, respectively. The CALIOP measurements are shown in the first column, while the other columns show four different model runs: homogeneous (Column 2 and 4) and heterogeneous ice nucleation (Column 3 and 5) in combination with synoptic-scale temperatures (Column 2 and 3) and with superimposed small-scale fluctuations (Column 4 and 5). Heterogeneous nucleation of NAT is included in every model run (Hoyle et al., 2013).

The assumption that ice PSCs formed only via homogeneous nucleation requires temperatures $T \lesssim T_{frost} - 3\,\mathrm{K}$. The Arctic stratospheric winter 2009/2010 offered such meteorological conditions but not to the same spatial extent as ice clouds observed by CALIOP. CALIOP observations along Orbit 1 indicate large areas of ice PSCs, even though temperatures along the backward trajectories remained 1.5 K above the threshold for homogeneous ice nucleation before the point of observation. While the lacking 1.5 K of additional cooling might be due to uncertainties in the underlying meteorological data, we will see below that homogeneous nucleation, in combination with the ubiquitous temperature fluctuations, leads to ice particle number densities too high to explain the observation. Consequently, model results based merely on classical homogeneous ice nucleation (Fig. 5.5, Column 2) fail
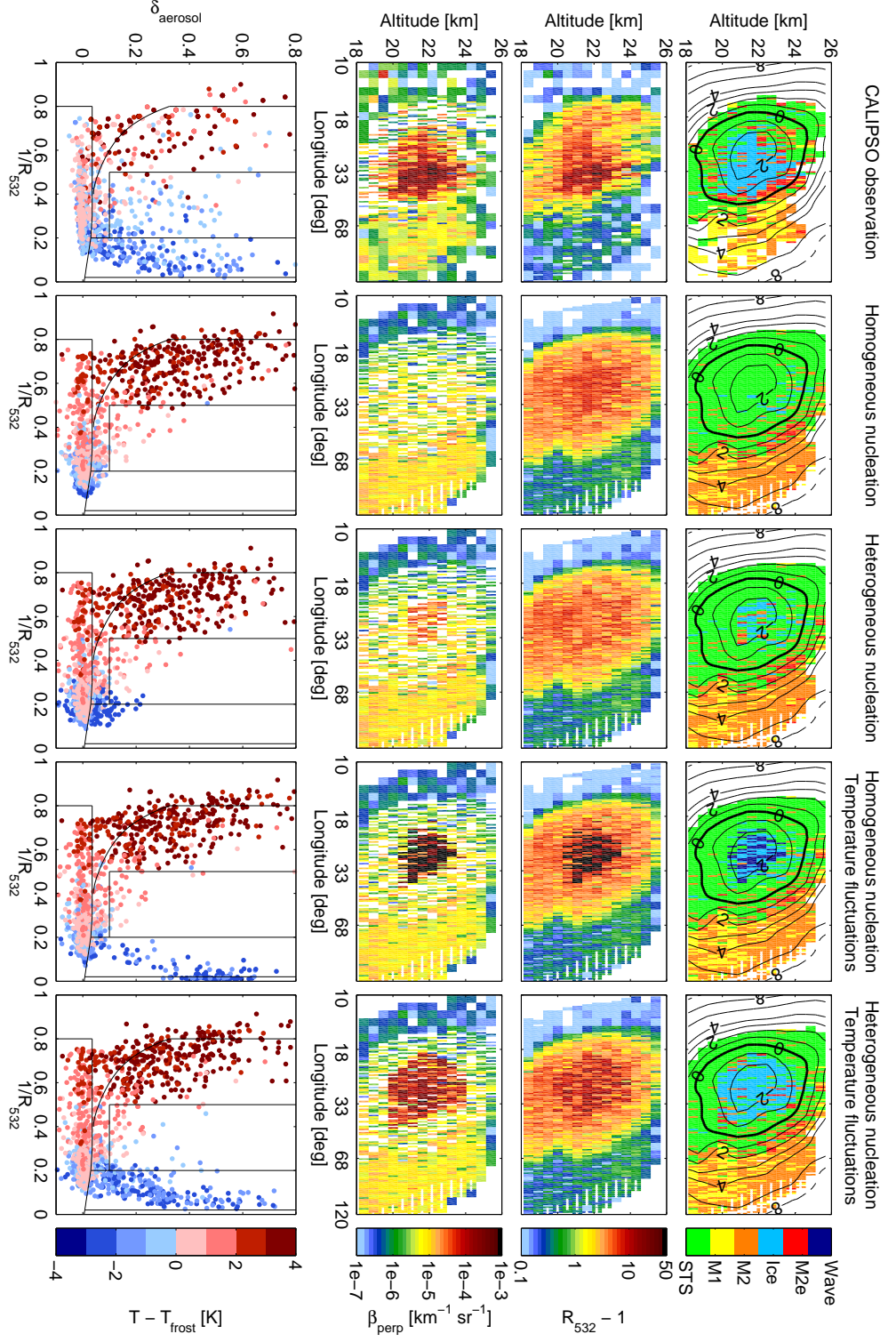
Figure 5.5: Orbit 1 on 18 January 2010: CALIPSO orbit track 2010-01-18T01-58-01-53Z. CALIOP measurements are shown in the first column, model results varying nucleation mechanism and trajectory temperatures in the subsequent columns. White striped areas indicate trajectories with temperatures below $T_{NAT} - 4$ K longer than 80 h or temperatures below T_{NAT} at the trajectory's starting point resulting in an inaccurate initialization. Contour lines display ERA-Interim temperatures relative to T_{frost}.
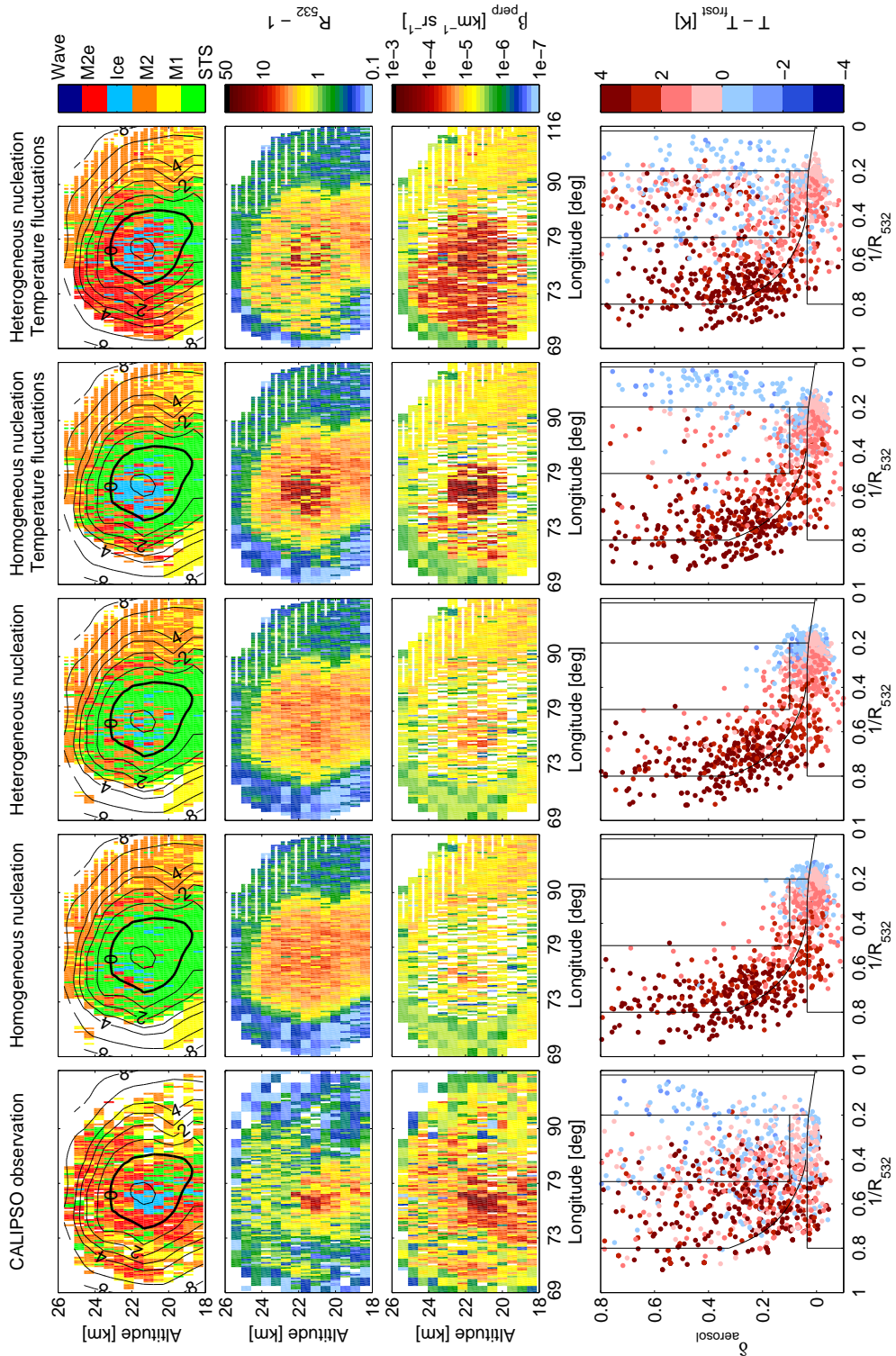
Figure 5.6: Same as Fig. 5.5, but for Orbit 2 on 18 January 2010: CALIPSO orbit track 2010-01-18T21-45-30Z.

to explain the observations. The picture changes by allowing ice to nucleate heterogeneously on foreign nuclei and NAT particles (Fig. 5.5, Column 3). It increases the area of ice coverage by lowering the nucleation barrier. However, calculated aerosol R_{532} and β_{perp} values of the modeled ice particles stay clearly below the maximum values observed (Fig. 5.5, Rows 2-4). The 2-D scatter plot in the bottom row of Fig. 5.5 illustrates the large discrepancy between model calculations and observations in the ice particle class. Whereas CALIPSO ice observations scatter over the entire range of depolarization, modeled ice particles have a maximum depolarization values of 0.24 (and this value already takes the instrumental noise shown in Fig. 5.3 into account). Higher ice crystal number densities are required to get a better agreement in the optical parameters (see also theoretical considerations by Pitts et al., 2009). Higher cooling rates are needed, which can be achieved by adding small-scale temperature fluctuations as described in Sect. 5.2.4. This approach lowers the temperatures along the trajectories occasionally, which causes ice particles to nucleate homogeneously. In the case where homogeneous nucleation is the only pathway for ice formation, high levels of supersaturation build up along the trajectory and clouds with optical parameters comparable to wave ice PSCs are generated by the fluctuations on short time scales (Fig. 5.5, Column 4). Only the combination of heterogeneous nucleation, which takes place at lower supersaturation, and small-scale temperature fluctuations leads to a satisfactory agreement between the model and the CALIOP observations (Fig. 5.5, Column 5).

Figure 5.6 illustrates an identical set of model runs performed for Orbit 2. The CALIOP observations show predominantly high number density NAT clouds (Mix2, Mix2-enh) with some incorporated ice particles. From our analysis, we conclude that the formation of high number density NAT clouds requires preexisting ice PSCs. The low number density ice clouds formed in model runs without fluctuations do not result in cloud particles classified as Mix2-enh once temperatures increase. Therefore Mix2-enh requires ice in sufficient number densities to serve as heterogeneous NAT nuclei, which follows the traditional concept of ice-induced NAT formation (Peter and Grooß, 2012). Dense NAT clouds were only observed within the polar vortex after the first mountain wave ice PSCs formed at the east coast of Greenland (Pitts et al., 2011). The agreement in the Mix2-enh class relies on a proper simulation of ice number densities upstream on the trajectories. In our analysis this means that only the combination of high cooling rates and heterogeneous ice nucleation allows the successful reproduction of the observed large regions of high number density NAT clouds, Mix2-enh, in the 2-D scatter plot (Fig. 5.6, Column 5).

In addition to the four model treatments discussed so far, free model parameters within the equations governing ice nucleation were also varied to test the model's sensitivity and to support our parameterization. We extended the analysis to five days within the period of synoptic-scale ice (16-20 January 2010). The first orbit of each day corresponds to a situation dominated by synoptic-scale ice whereas in the second orbit Mix2-enh prevails. The so called "standard" case in Table 5.1 is highlighted in bold and comprises heterogeneous nucleation of ice on foreign nuclei and NAT as well as superimposed small-scale temperature fluctuations. The standard case is equal to Column 5 in Fig. 5.5 and 5.6 and is our choice of the best set of fitting parameters. For this sensitivity study, we either switched on and off the heterogeneous nucleation pathway for ice, temperature fluctuations, or varied single param-

Table 5.1: Root-mean-square errors (RMSE) of selected ZOMM simulations in comparison to CALIPSO observations (Eq. 5.7, rounded to next integer). See text for a more detailed description. Calculations are performed with a horizontal resolution of 100 km. In each specific case, only one parameter is changed with respect to the so-called standard case with the following set of parameters: fluctuations: with; ice on foreign nuclei prefactor: $P_{\mathrm{pre}} = 5 \times 10^{-4}\,\mathrm{deg}^{-1}$; ice on foreign nuclei minimum contact angle: $\alpha_0 = 43°$; ice on NAT contact angle: $\alpha = 60°$; NAT on ice parameter: $\gamma = 164\,\mathrm{K}^3$. The mean $\bar{x}$ is shown for the parameterization of each specific case averaged over all orbits.

Changed quantity	Case	16/1	16/2	17/1	17/2	18/1	18/2	19/1	19/2	20/1	20/2	$\bar{x}$
Only homogeneous ice nucleation												
fluctuations	without	11	11	9	12	9	11	9	12	5	5	9.4
	with	10	9	8	9	8	8	9	10	4	5	8.0
In addition heterogeneous ice nucleation												
standard	with; 43°; 5×10⁻⁴ deg⁻¹; 60°; 164 K³	**4**	**6**	**4**	**5**	**4**	**6**	**4**	**5**	**3**	**3**	**4.5**
fluctuations	without	10	10	9	13	7	11	8	12	5	5	9.0
	÷ 2	7	8	8	10	5	6	6	9	4	5	6.7
	× 2	8	5	7	12	11	22	8	16	6	6	10.1
ice on dust (α_0)	− 10° (33°)	4	5	4	5	6	7	5	9	4	2	5.2
	+ 10° (53°)	6	7	6	6	4	4	4	6	4	4	5.1
ice on dust (P_{pre})	× 10 (5×10⁻³ deg⁻¹)	6	6	4	3	6	5	4	4	4	3	4.6
	÷ 10 (5×10⁻⁵ deg⁻¹)	6	7	6	5	5	2	4	6	4	3	4.8
ice on NAT (α)	− 20° (40°)	5	8	4	4	3	3	5	5	4	4	4.6
	+ 20° (80°)	4	5	4	4	4	8	5	6	3	4	4.7
NAT on ice (γ)	÷ 2 (82 K³)	5	5	4	6	6	11	4	8	3	3	5.5
	× 2 (328 K³)	5	7	5	10	5	11	4	11	3	4	6.5

eters, which constrain our new heterogeneous nucleation parameterization. The performance of the different model runs at those selected orbits is judged by the root-mean-square error (RMSE):

$$\mathrm{RMSE} = \sqrt{\frac{1}{n} \sum_{i=1}^{n} (M_i - C_i)^2}. \tag{5.7}$$

We distributed the domain defined by Mix2-enh, ice and wave ice in the $\delta_{\mathrm{aerosol}}$ vs. $1/R_{532}$ coordinate system into twelve boxes. Every composition class is divided into three boxes stacked over each other to identify differences in $\delta_{\mathrm{aerosol}}$. i defines a single box with a total number of $n = 12$ such boxes. The difference between the number of hits produced by the model M and the number of measurements by CALIOP C is calculated for each grid box i. The RMSE describes the mean difference of all boxes. A large RMSE expresses a large difference between model results and measurements. We limited this calculation to Mix2-enh, ice and wave ice since those classes are the focus of this study. The relatively large number of STS particles would otherwise cover the effect of changing ice parameters in the RMSE.

As already discussed, exclusive homogeneous nucleation of ice is not able to explain the observations. The largest errors in Table 5.1, not only on 18 January but in almost every other case looked at, are associated with runs excluding the possibility of a heterogeneous ice formation pathway. The combination of temperature fluctuations and homogeneous nucleation improves the model performance somewhat, but not in a satisfactory manner, mainly because it cannot account for the large regions with Mix2-enh and keeps overestimating the amount of STS. In cases with homogeneous ice nucleation only, temperature fluctuations lead to the nucleation of ice, but with properties similar to wave ice. The amplitude of the temperature fluctuations is another fitting parameter and we included simulations with peak to peak fluctuations half and twice as large as in our standard case. Whereas too large temperature amplitudes result in excess wave ice, amplitudes which remain too small underestimate ice number densities. Differences in the RMSE become smaller for changes of the individual fitting parameter defined in Sect. 5.2.3. A decrease or increase of the minimum contact angle (compare α_0 in Eq. (5.4)) results in ice nucleation at higher or lower temperatures, respectively. Both options have a mean RMSE larger than those for $\alpha_0 = 43°$. Furthermore, we do not assume a change in the active site properties throughout the winter. Possibly, vertical redistribution due to particle sedimentation could lower the availability of good active sites, which would then favor changing α_0 to values larger than 43°. The prefactor (P_{pre} in Eq. (5.4)) scales the number density of ice particles. Decreasing (increasing) P_{pre} results in lower (higher) number densities of ice particles. While the error calculation suggests a relatively weak dependence, plots provided in the Supplement demonstrate this effect clearly. Orbit 16/1 is a good example to see how changing P_{pre} moves points within the 2-D scatter plot. As already mentioned in Sect. 5.2.3, the fixed α for ice on NAT originates in the assumption that this parameter is quite insensitive within this study and ice number densities are much more dependent on heterogeneous nucleation on foreign nuclei and homogeneous nucleation rather than on the nucleation on preexisting low number density NAT particles. The numbers in Table 5.1 show no clear trend for changing α in either direction. A change of $\pm 20°$ would be nearly as good as the standard case. The parameter γ for NAT nucleation on ice refers to Eq. (5.5). Whereas Luo et al. (2003b) found $328\,\mathrm{K}^3$ to be the best fit, we show that NAT might nucleate onto ice particles with a nucleation barrier half as large. The value of $\gamma = 164\,\mathrm{K}^3$ is defined by Luo et al. (2003b) as the lower limit, which is still in agreement with the analyzed observations from the winters 1995 and 1997. Whereas Luo et al. (2003b) were limited to four PSC lidar observations, our analysis is based on multiple CALIPSO orbits throughout the 2009/2010 Arctic winter. Orbit 17/2, 18/2 and 19/2 clearly indicate that the original value of $\gamma = 328\,\mathrm{K}^3$ cannot reproduce Mix2-enh observations by CALIPSO.

Overall, our parameterization gives consistently good results. In specific cases, different model parameters might yield better performance than our standard values and it remains difficult to constrain single parameters against background of temperature inaccuracies and unknown nuclei properties. Nevertheless, we clearly demonstrated the necessity of heterogeneous ice nucleation on preexisting solid particles in combination with small-scale temperature fluctuations. The overall model performance and its agreement with the CALIOP measurements in mid-January is summarized in Fig. 5.7. Following Pitts et al. (2011), we created a 2-D histogram of more than 5000 microphysical model results performed with our standard set of parameters for the period of widespread ice cloud observations and compared those to the associated CALIOP measurements. Although the overall agreement
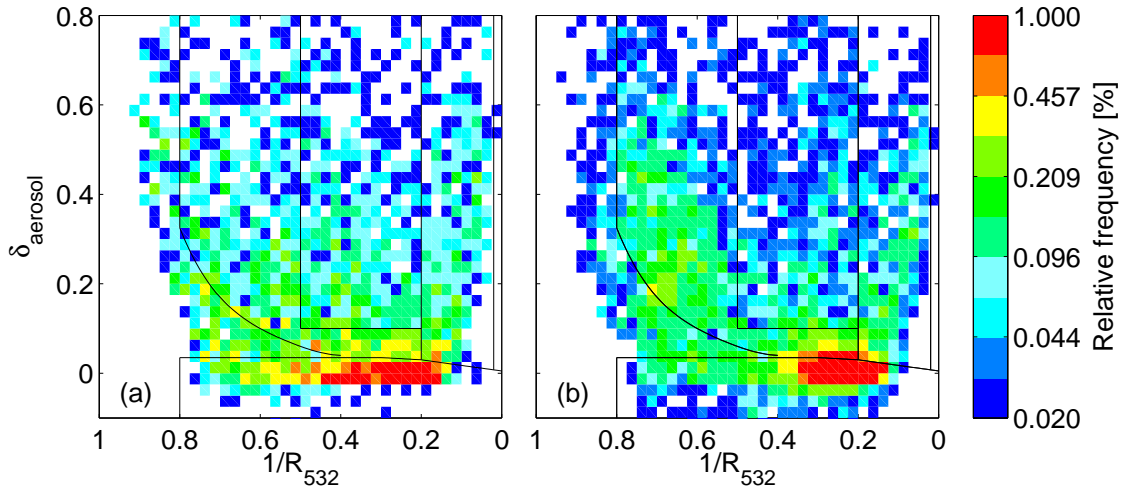
Figure 5.7: Normalized composite 2-D histogram of CALIOP PSC observations (a) and simulated PSCs (b) from selected orbits (standard case shown in Table 5.1) within the period of synoptic-scale ice during the 2009/2010 Arctic winter over the altitude range from 18 to 26 km.

is very good, the model produces more points in the Mix2 class than CALIOP observes. This might be an artifact of missing sedimentation in ZOMM.

We extended our analysis to the remaining time periods of the 2009/2010 Arctic winter to cover, together with the companion paper by Hoyle et al. (2013), each of the four periods defined by Pitts et al. (2011). In mid December, the vortex was located over the Canadian sector of the Arctic and cooled gradually through mid-January 2010 (Dörnbrack et al., 2012). The stability of the vortex allowed air parcels to stay within the cold pool of the vortex and led to long exposure times of temperatures below T_{NAT}. Numerous wave ice PSCs appeared over the east coast of Greenland at the beginning of January 2010. Figure 5.8 compares CALIOP observations on the 4 January 2010 to our model results. Focusing on the wave ice cloud above Greenland (seen in the upper left panel of CALIOP observations), cooling rates $> 10\,\mathrm{K h^{-1}}$ at the onset of ice nucleation are needed for freezing of the entire background aerosol population (Fueglistaler et al., 2003). The ERA-Interim temperature analysis with a horizontal resolution of $1° \times 1°$ misses the wave activity over Greenland entirely and corresponding temperature contour lines in the two upper left panels of Fig. 5.8 do not show any anomalies. Dörnbrack et al. (2012) based their analysis of stratospheric gravity waves on ECMWF operational analysis with a $0.25° \times 0.25°$ grid and derived a correlation between stratospheric temperature anomalies and the magnitude of the horizontal divergence. This result motivated us to redo our analysis with trajectories based on these higher resolution data sets. If the horizontal resolution of the input temperature data is fine enough to capture mountain-induced gravity waves, ZOMM reproduces wave ice clouds satisfactorily (Fig. 5.8, Column 3). Simultaneous to the occurrence of wave ice PSCs, a remarkable increase in Mix2 and Mix2-enh NAT cloud occurrence was detected (Pitts et al., 2011). From our study, we can conclude that ice is a prerequisite for the formation of high number density NAT clouds, though synoptic-scale ice is sufficient to form Mix2-enh and wave ice is not necessary. To model the dependency of NAT from wave ice, vortex wide simulations including processes like mixing and sedimentation on the basis of high resolution meteorological data would be necessary and will be considered in future work.
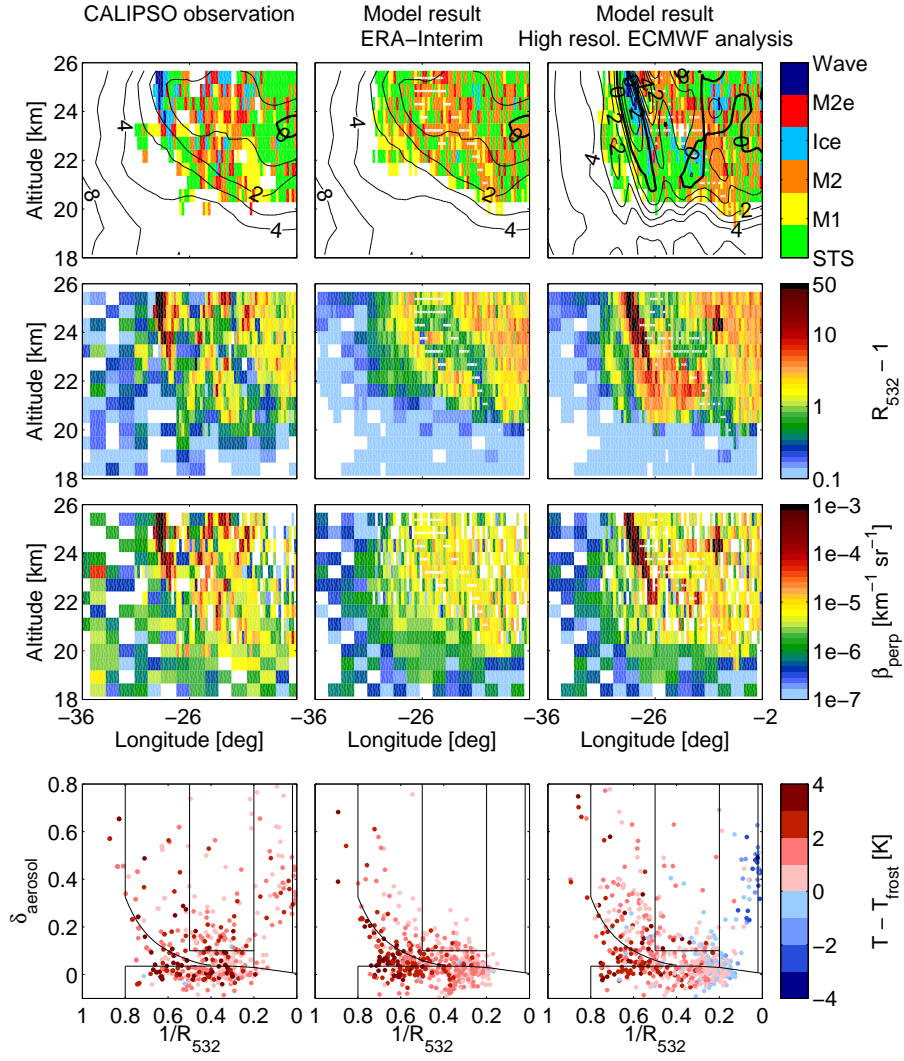
Figure 5.8: 4 January 2010: CALIPSO orbit track 2010-01-04T05-03-43Z. CALIOP measurements are shown in the left column, model results based on ERA-Interim temperature data in the middle column and model results based on high resolution ECWMF analysis temperature data in the right column. White striped areas indicate trajectories with temperatures below $T_{NAT} - 4$ K longer than 80 h or temperatures below T_{NAT} at the trajectory's starting point. Contour lines and the color-coded data presented in the lowermost row display ERA-Interim temperatures relative to T_{frost} in the left and middle column and ECMWF analysis temperatures in the right column.

The PSC season ended in late January 2009/2010, at which time the vortex was dominated by STS clouds. The model is able to reproduce these liquid clouds as illustrated in Fig. 5.9. Even though temperatures were still slightly below T_{frost}, our temperature threshold for heterogeneous ice nucleation seems sufficient to prevent the nucleation of ice. This goes along with the observations of essentially no ice PSCs and less liquid/NAT mixtures than during the earlier period. Near the end of January, the final break down of the vortex finished the PSC season of the winter 2009/2010.
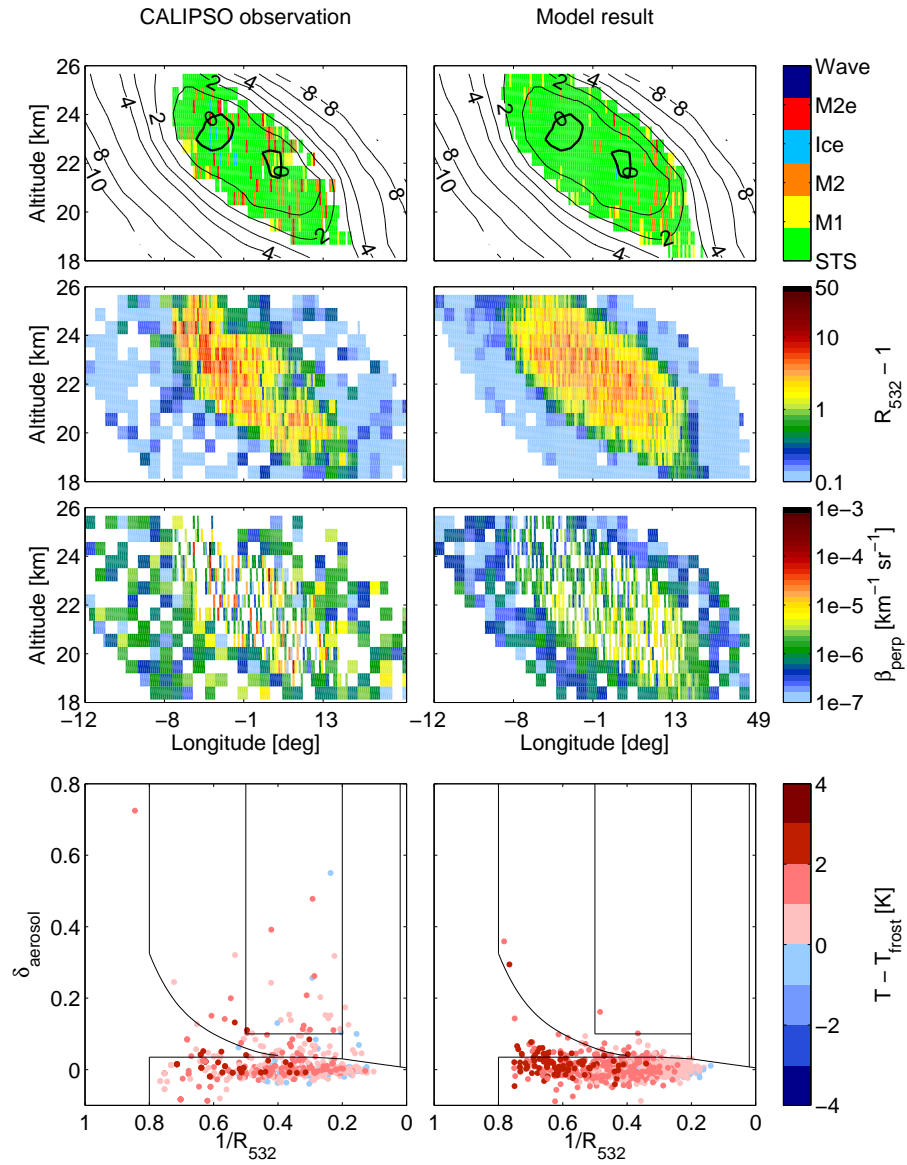
Figure 5.9: 24 January 2010: CALIPSO orbit track 2010-01-24T03-01-02Z. CALIOP measurements are shown in the left column, model results in the right column. Contour lines display ERA-Interim temperatures relative to T_{frost}.

Compared to previous and following winters, the 2009/2010 winter was unusually cold from mid December until end of January. Within this particular winter, CALIPSO observed more PSCs than in the three previous Arctic seasons combined. Moreover, it was one of only few Arctic winters with synoptic-scale temperatures below T_{frost} and the occurrence of ice PSC observations was exceptional in the CALIOP record (Pitts et al., 2011). Looking at Arctic winters other than 2009/2010, the number of similar orbits with ice observations not related to strong mountain wave activity is limited. We performed simulations for selected CALIOP orbits from the Arctic winters 2007/2008 and 2010/2011 and Fig. 5.10 illustrates that the heterogeneous ice nucleation mechanisms are required in other years as well. Attempted simulations performed for the Antarctic reveal that sedimentation cannot be ne-
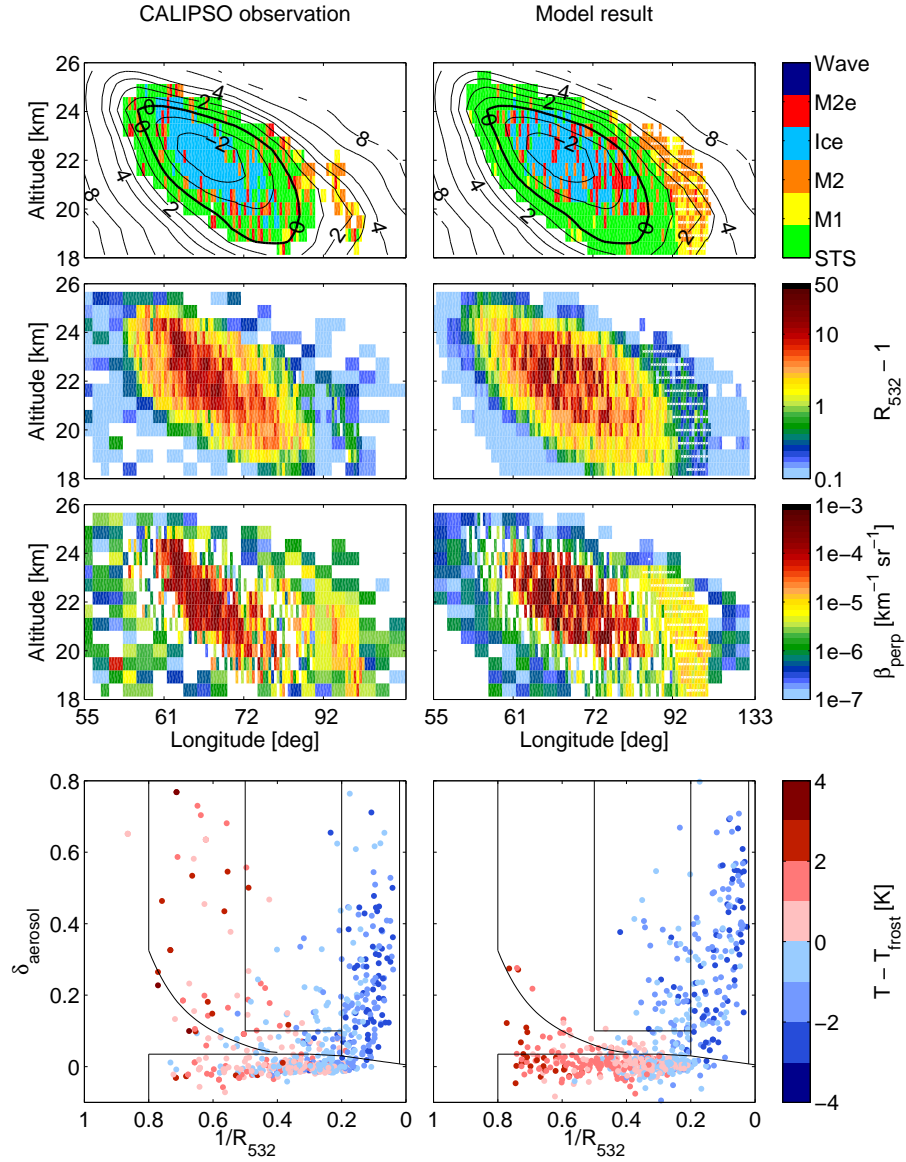
Figure 5.10: 26 February 2011: CALIPSO orbit track 2011-02-26T23-09-10Z. CALIOP measurements are shown in the left column, model results in the right column. White striped areas indicate trajectories with temperatures below $T_{NAT} - 4$ K longer than 80 h or temperatures below T_{NAT} at the trajectory's starting point. Contour lines display ERA-Interim temperatures relative to T_{frost}.

glected, which we will investigate in future research. Moreover, we will concentrate on the question if the Arctic winter 2009/2010 might have been exceptional with regard to the supply of heterogeneous nuclei.

5.4 Conclusions

Spaceborne lidar observations by CALIOP have been analyzed by extensive trajectory and microphysical box model calculations to review PSC ice formation processes. The Arctic winter 2009/2010 was

the focus of the RECONCILE project and the meteorological situation of that winter enabled us to discover inconsistencies in our former understanding of NAT and ice nucleation. Hoyle et al. (2013) showed that NAT particles observed in December 2009 can only be explained by heterogeneous nucleation on preexisting solid particles. Although an ice independent mechanism of NAT nucleation has been discussed earlier, its necessity has never been observed as clearly as in this particular winter. Furthermore, synoptic-scale temperatures dropped below T_{frost} in January 2010 for several days. Despite those low temperatures, which are exceptional for the Arctic, the wide spread synoptic-scale ice clouds seen by CALIOP cannot be explained solely by homogeneous ice nucleation. Rather a pathway of heterogeneous ice nucleation is required in our microphysical model to reconcile the results with observations. The origin of the nuclei can possibly be explained by meteoritic dust but this remains speculative as long as chemical analyses of the dust particles are lacking. Equally important for the reconciliation of model results with observations is the influence of small-scale temperature fluctuations on cloud properties. Sufficiently rapid cooling is required to obtain ice number densities with optical signatures as large as those observed by CALIOP. Furthermore, we conclude that the formation of high number density NAT clouds is related to preexisting ice particles. Spot tests show that the proposed mechanisms are applicable throughout the whole winter. Whereas a meteorological dataset with a horizontal resolution of $1° \times 1°$ is sufficient for simulations of synoptic-scale ice, trajectories calculated from higher spatial resolutions are necessary to reproduce wave ice. However, uncertainties in temperature fields and neglect of sedimentation leave room for interpretation and further research is required with large-scale models applying the nucleation parameterizations developed in the present work.

Acknowledgments

Chapter 6

Arctic stratospheric dehydration - Part 1: Unprecedented observation of vertical redistribution of water

S. M. Khaykin[1,2]**, I. Engel**[3]**, H. Vömel**[4]**, I. M. Formanyuk**[1]**, R. Kivi**[5]**, L. I. Korshunov**[1]**, M. Krämer**[6]**, A. D. Lykov**[1]**, S. Meier**[4]**, T. Naebert**[4]**, M. C. Pitts**[7]**, M. L. Santee**[8]**, N. Spelten**[6]**, F. G. Wienhold**[3]**, V. A. Yushkov**[1]**, and T. Peter**[3]

[1] *Central Aerological Observatory, Dolgoprudny, Moscow Region, Russia*

[2] *LATMOS-IPSL, Université Versailles St. Quentin, CNRS/INSU, Guyancourt, France*

[3] *Institute for Atmospheric and Climate Science, ETH Zurich, Zurich, Switzerland*

[4] *Deutscher Wetterdienst, Meteorological Observatory Lindenberg - Richard Aßmann Observatory, Lindenberg, Germany*

[5] *Finnish Meteorological Institute, Arctic Research, Sodankylä, Finland*

[6] *Institut für Energie- und Klimaforschung - Stratosphäre (IEK-7), Forschungszentrum Jülich, Jülich, Germany*

[7] *NASA Langley Research Center, Hampton, Virginia, USA*

[8] *JPL/NASA, California Institute of Technology, Pasadena, California, USA*

Contribution of I. Engel:
Analysis of COBALD data, visualization of MLS and CALIOP data, general discussion of the obtained results.

Abstract

We present high-resolution measurements of water vapor, aerosols and clouds in the Arctic stratosphere in January and February 2010 carried out by in situ instrumentation on balloon-sondes and high-altitude aircraft combined with satellite observations. The measurements provide unparalleled evidence of dehydration and rehydration due to gravitational settling of ice particles. An extreme cooling of the Arctic stratospheric vortex during the second half of January 2010 resulted in a rare synoptic-scale outbreak of ice PSCs (polar stratospheric clouds) detected remotely by the lidar aboard the CALIPSO satellite. The widespread occurrence of ice clouds was followed by sedimentation and consequent sublimation of ice particles, leading to vertical redistribution of water inside the vortex. A sequence of balloon and aircraft soundings with chilled mirror and Lyman-α hygrometers (CFH, FISH, FLASH) and backscatter sondes (COBALD) conducted in January 2010 within the LAPBIAT and RECONCILE campaigns captured various phases of this phenomenon: ice formation, irreversible dehydration and rehydration. Consistent observations of water vapor by these independent measurement techniques show clear signatures of irreversible dehydration of the vortex air by up to 1.6 ppmv in the 20–24 km altitude range and rehydration by up to 0.9 ppmv in a 1 km-thick layer below. Comparison with space-borne Aura MLS water vapor observations allow the spatiotemporal evolution of dehydrated air masses within the Arctic vortex to be derived and upscaled.

6.1 Introduction

Water vapor in the polar stratosphere plays a significant role in ozone chemistry and is an important indicator of polar vortex dynamics. Water vapor within the stratospheric vortex is generally characterized by a gradual increase of mixing ratio with height due to subsidence of air masses from higher altitudes, where water is produced by methane oxidation. Conversely, in the cold and stable Antarctic vortex, the water mixing ratio can be reduced to 1.5 ppmv (Vömel et al., 1995) as the water freezes into ice particles, sedimenting and sublimating at lower altitudes, thus causing an irreversible dehydration, i.e. removal of water from a certain air mass. The same may apply to the other components in the particle phase, such as HNO_3, which results in denitrification, an effect prolonging the time of ozone destruction via chlorine-induced catalytic cycles (Salawitch et al., 1993). Hence the gravitational settling of solid PSC particles may cause a dramatic change in the chemical composition of the polar vortex, and subsequently also of the mid-latitude stratosphere due to release of chemically perturbed air from the vortex after its breakup.

Due to the persistent low temperature, formation of ice PSC and dehydration are large-scale climatological features in the Antarctic winter (e.g. Nedoluha et al., 2000; Stone et al., 2001). In contrast, the occurrence of ice clouds in the Arctic vortex is much less frequent or severe. In fact, local reductions of water mixing ratios associated with ice formation have only been documented for sporadic events during the coldest winters in the Arctic stratosphere, namely 1988/89 (Fahey et al., 1990), 1994/95 (Ovarlez and Ovarlez, 1994), 1995/96 (Vömel et al., 1997; Hintsa et al., 1998), 1996/97 (Pan et al., 2002), 1999/2000 (Schiller et al., 2002) and 2004/05 (Jimenez et al., 2006; Maturilli and Dörnbrack, 2006). The most severe episode of water depletion in the presence of ice PSCs in the Arctic has been reported by Vömel et al. (1997), whose balloon-borne water vapor measurements revealed a reduction in mixing

ratio of 2 ppmv. Except the pioneering work of Fahey et al. (1990) and Vömel et al. (1997), all other above mentioned authors link the observed dehydration episodes in the Arctic to mesoscale cooling events induced by orographic perturbations above mountains. Indeed, the majority of Arctic ice PSC observations are documented for Scandinavia (e.g. Kivi et al., 2001), where gravity waves with amplitudes large enough to reduce the temperature by several degrees below the ice frost point (T_{frost}) are frequently excited (e.g. Dörnbrack et al., 1999). The wave-induced ice clouds are characterized by high number densities ($n_{\text{ice}} > 1\,\text{cm}^{-3}$) of small ($r_{\text{ice}} \sim 1\text{–}1.5\,\mu\text{m}$) ice particles with a short lifetime and very slow sedimentation rate (e.g. Fueglistaler et al., 2003). Although it has been hypothesized that the sublimation of ice particles formed after a rapid cooling might be deferred by a coating of nitric acid trihydrate (NAT) (Peter et al., 1994), laboratory work lent only little support to this hypothesis (Biermann et al., 1998), so that the dehydration potential of the short exposure of the air to highly localized mountain wave ice clouds might be small. Indeed, the signatures of irreversible dehydration and rehydration as a consequence of growth and evaporation of sedimenting particles have so far not been documented for the Arctic.

While homogeneous freezing of supercooled ternary solution (STS) particles has been the generally accepted formation pathway of ice PSCs, new results – mainly triggered by space-borne observations using the CALIPSO satellite – suggest that heterogeneous nucleation plays a major role (Pitts et al., 2011; Engel et al., 2013b). Homogeneous nucleation of ice requires temperatures about 3 K below the frost point, T_{frost} (Koop et al., 1995). Heterogeneous formation pathways of ice have been discussed in the past, for example the original three-stage model proposed by Drdla and Turco (1991), suggested homogeneous nucleation of solid sulphuric acid hydrates in the stratospheric aerosol droplets, which then serve as heterogeneous nuclei for NAT particles, which in turn serve as heterogeneous nuclei for ice. Still there is little support from field or laboratory studies favoring the formation of sulphuric acid hydrates. However, the idea of ice particles nucleating heterogeneously on pre-existing NAT particles was brought up again by Pitts et al. (2011), who observed the increase in synoptic-scale ice PSCs concomitant with a decrease of NAT mixture clouds in January 2010. This process would imply that sedimenting ice particles not only dehydrate but also denitrify the stratosphere due to the enclosed HNO_3, a possibility discussed by most of the above mentioned work. Also Khosrawi et al. (2011) offered this as a possible explanation for the low HNO_3 observations by ODIN/SMR during the 2009/2010 Arctic winter. Non-volatile particles, observed in up to 80 % of the detected sub-micron particles in the Arctic vortex (Curtius et al., 2005), could be another source of heterogeneous nuclei of NAT and ice, facilitating their formation. Their origin is still unclear and might be, for example, meteoritic or anthropogenic. Recent studies by Hoyle et al. (2013) and Engel et al. (2013b) highlight the importance of this pathway for NAT and ice nucleation. The companion paper by Engel et al. (2013a) relates the question of these ice formation pathways and the concurrent dehydration to the measurements of de- and rehydration described here.

The Arctic winter 2009/2010 was characterized by extremely low temperatures encountered in the vortex during the second half of January 2010. These conditions, unusual for the Arctic stratosphere, led to a major outbreak of ice PSCs detected by the CALIPSO space-borne lidar (Pitts et al., 2011). Extreme temperatures and ice clouds persisted on a synoptic scale from 15 through 21 January, causing significant vertical redistribution of water within the stratospheric vortex as concluded in this study. The extensive aircraft and balloon measurements conducted across Northern Scandinavia from January to

March 2010 were accompanied by space-borne observations, lending themselves to a detailed investigation of the rare phenomenon. The evolution of dehydration and rehydration, its amplitude and vertical extent are inferred from a sequence of balloon and satellite water vapor observations. The source region of dehydration and its spatial development are identified using satellite water vapor maps.

The paper is organized as follows: Section 6.2 gives a detailed description of experimental set-up and instrumentation used. Section 6.3 discusses the meteorological conditions in the stratosphere during January 2010, presents the observational results, and identifies the source region and spatiotemporal evolution of dehydration. Section 6.4 concludes the paper. A comprehensive trajectory-based microphysical modeling study connects the individual balloon-borne observations and is provided in the companion paper by Engel et al. (2013a).

6.2 Experimental setup and instrumentation

During the winter 2009/2010 a number of extensive measurement activities was carried out in the Arctic stratosphere. Our study makes use of a series of balloon, aircraft, and satellite observations of water vapor and aerosol backscatter obtained using various measurement platforms and techniques. The water vapor measurements are provided by the balloon-borne CFH and FLASH-B sondes, aircraft-borne FISH and FLASH-A hygrometers and space-borne Aura MLS instrument, while backscatter measurements are provided by balloon-borne COBALD aerosol sondes and the CALIPSO lidar. The balloon and aircraft measurements are courtesy of LAPBIAT-II and RECONCILE field campaigns, respectively, both carried out in the Arctic during January - March 2010 period.

6.2.1 Balloon soundings

The balloon-borne measurements of water vapor, temperature and particles were obtained within the LAPBIAT-II (Lapland Atmosphere-Biosphere Facility) atmospheric sounding campaign carried out in Sodankylä, Finland (67.4° N, 26.6° E) under the auspices of the Finnish Meteorological Institute's Arctic Research Centre (FMI-ARC). The majority of the balloon flights was conducted in close timing with deployments of the stratospheric research aircraft M55-Geophysica, operating from Kiruna, Sweden, 360 km west of Sodankylä. The balloon soundings were implemented in two phases, with 18 launches during 17 January - 6 February 2010 (see Tab. 6.1) and 15 launches during 10 - 24 March 2010. Altogether 172 individual balloon instruments were flown during the campaign (Kivi et al., 2010). The analysis of this study is restricted to the data obtained within the first deployment phase, corresponding to the period of coldest stratospheric temperatures.

Table 6.1 provides an overview of the balloon-borne measurements of stratospheric water vapor and backscatter conducted during LAPBIAT-II. Two types of hygrometers were used: the Cryogenic Frost-point Hygrometer (CFH) and the Fluorescence Lyman-Alpha Stratospheric Hygrometer for Balloons (FLASH-B). For aerosol and cloud measurements, the balloons were equipped with a Compact Optical Backscatter Aerosol Detector (COBALD). During the first phase of LAPBIAT-II, the CFH instrument was part of 15 payloads, of which 11 included also the COBALD backscatter sonde; 4 payloads in-

Table 6.1: Listing of water vapor and aerosol soundings conducted during the first phase of the LAPBIAT-II campaign, Jan/Feb 2010, Sodankylä, Finland. The soundings, which did not provide useful data in the stratosphere due to technical issues are not listed. From left to right: date and time of the balloon launch; hygrometer type used (FLB = FLASH-B); backscatter sonde used (BKS = Wyoming backscatter sonde); indicator of ice occurrence (I), STS or NAT/liquid mixture clouds (M), dehydration (D) or rehydration (R) signatures (identified as deviation of the vertical profiles from the 10 yr January-mean profile); maximum amplitude of dehydration or rehydration signal, negative or positive, respectively (in ppmv). All soundings included ECC ozone sondes.

Date	Time (UTC)	Hygrometer	Backscatter sonde	Indicator	Amplitude (ppmv)
17 Jan 2010	19:47	CFH, FLB	COBALD	I, D	−1.3
20 Jan 2010	15:25	CFH	COBALD	M	–
21 Jan 2010	09:26	CFH	–	D, R	−0.7 /+0.6
22 Jan 2010	04:18	CFH	COBALD	D, M	−0.6
22 Jan 2010	19:08	CFH	COBALD	D, M	−1.0
23 Jan 2010	17:30	CFH	COBALD, BKS	D, R, M	−1.6/+0.9
25 Jan 2010	00:00	CFH, FLB	COBALD, BKS	D, R	−0.8/+0.6
25 Jan 2010	18:13	CFH	COBALD	D, M	−0.8
28 Jan 2010	16:44	CFH, FLB	COBALD	D, R	−0.7/+0.5
29 Jan 2010	17:12	CFH, FLB	COBALD	D	−0.8
02 Feb 2010	12:27	CFH	–	–	–
03 Feb 2010	20:11	CFH	COBALD	D, R	−0.5 /+0.4
06 Feb 2010	17:15	CFH	COBALD	D	−0.3

cluded FLASH-B sondes and 2 payloads included in addition to COBALD the backscatter sonde of the University of Wyoming (Rosen and Kjome, 1991), denoted by "BKS" in Tab. 6.1. All payloads were suspended 50 m below the balloon using an unwinder device in order to minimize the balloon outgassing effect. Temperature and pressure in all flights were measured using the Vaisala RS-92 radiosonde. The altitude used in this study is that of the GPS and the potential temperature is that calculated from pressure and temperature provided by the Vaisala RS-92 radiosonde.

Cryogenic Frostpoint Hygrometer (CFH)

CFH has been developed at the University of Colorado (Vömel et al., 2007a). It is a small lightweight balloon-borne hygrometer, based on the chilled mirror technique. Like many chilled mirror instruments, CFH is not calibrated for water vapor, but is considered an absolute reference for water vapor measurements. It measures the temperature at which an ice layer is in equilibrium with the gas phase of water passing over this ice layer. The largest source of uncertainty in CFH water vapor measurements is the stability of the feedback controller, which maintains the constant frost layer on the mirror. In most cases the feedback controller will lead to slight oscillations around the true frost point, which may have an amplitude of somewhere between 0.1 °C for well behaved instruments to 1.0 °C for slightly unstable instruments. The total uncertainty in frost point is better than 0.5 K throughout the entire profile (Vömel et al., 2007a), which translates to a mixing ratio uncertainty of about 10 %

in the lower and middle stratosphere. The only limitations are measurements inside liquid clouds, which may disable the instrument due to wetting of the detector lens, and contamination at altitudes above 26 - 27 km during the ascent leg due to outgassing from the balloon or any other surface of the flight train. The data processing includes a step with the aim of screening out these artifacts and, if necessary, applying running average over 40 s interval. The quality of descent measurements by CFH can deteriorate because of the controller's inability to properly respond to the changes in water vapor at high vertical speed reaching $60\,\mathrm{m\,s^{-1}}$ in the stratosphere. Therefore only ascent measurements are used in this study.

Fluorescence Lyman-Alpha Stratospheric Hygrometer for Balloon (FLASH-B)

The balloon version of FLASH is a compact lightweight sonde developed at the Central Aerological Observatory, Russia, for balloon-borne water vapor measurements in the upper troposphere and stratosphere (Yushkov et al., 1998). The instrument is based on the fluorescent method (Kley and Stone, 1978; Bertaux and Delannoy, 1978), which uses the photodissociation of H_2O molecules exposed to vacuum ultraviolet radiation ($\lambda < 137\,\mathrm{nm}$) followed by the measurement of the fluorescence of excited OH radicals using a Hamamatsu photomultiplier. The intensity of the fluorescent light sensed by the photomultiplier is directly proportional to the water vapor mixing ratio under stratospheric conditions (10 - 150 hPa). The H_2O measurement range is limited to pressures lower than 300 - 400 hPa due to strong Lyman-alpha absorption in the lower troposphere. The instrument uses an open optical layout design, where the analyzed volume is located outside the instrument, which allows a reduction in the size of the instrument to a small sonde with a total weight of about 1 kg including batteries. This arrangement restricts the use of the instrument to night-time only.

Each FLASH-B instrument is calibrated in the laboratory against a reference dew point hygrometer MBW 373 L. A description of the procedure can be found in Vömel et al. (2007b). The detection limit for a 4 s integration time at stratospheric conditions is of the order of 0.1 ppmv, while the accuracy is limited by the calibration error amounting to 4 %. The typical precision in the stratosphere is 5 - 6 %, whereas the total uncertainty is less than 10 % throughout the stratosphere. While the minimum response time of the FLASH-B is 0.2 s, here we use the data averaged over 4 s, resulting in a vertical resolution of 20 m during ascent and 100 m during the fast descent ($15\,\mathrm{m\,s^{-1}}$ around the tropopause) in the stratosphere. The flight configuration of FLASH-B, in which the analyzed volume is located beneath the downward looking optics 2 - 3 cm away from the lens, caused noticeable self-contamination due to water outgassing from the instrument and possibly also from other equipment and the balloon above about 70 hPa during the ascent. In contrast, the FLASH-B measurements during the fast descent at the bottom of the flight train in undisturbed air are contamination free as shown by the drop of water vapor readings immediately after the burst of balloon. Accordingly, only descent data are used in this study.

Intercomparison of stratospheric water vapor measurements by FLASH-B and CFH used in this study (Tab. 6.1) show mean difference between the profiles above 14 km of 0.78 % (with 1σ standard deviation of 4 % and good consistency in reproducing vertical structures. Additional information on the intercomparison is provided in Appendix B. Excellent agreement between the water vapor profiles ob-

tained using two different techniques suggests high quality of the measurements and allows for using FLASH-B and CFH measurements as coherent data series.

Compact Optical Backscatter Aerosol Detector (COBALD)

COBALD was developed at ETH Zurich as a successor to the Wyoming backscatter sonde of Rosen and Kjome (1991). With a total weight of approximately 550 g including batteries, the instrument can be flown on operational weather balloons and thus facilitates practical application. COBALD measures molecular, aerosol and cloud particle backscatter in the atmosphere from the ground to the level of balloon burst. Two LEDs with 250 mW optical power each emit light at wavelengths of 455 and 870 nm. To register the backscattered light, a photodiode is placed between the LEDs, and the associated optics establishes an overlap region at distances larger than 0.5 m in front of the instrument. So far, the instrument is designed for applications during night-time only as solar radiation saturates the detector.

Backscatter by molecules and aerosols contribute to the measured signal, whose separation is achieved following Rosen and Kjome (1991). The molecular number density is determined from temperature and pressure recorded simultaneously by the hosting radiosonde. Together with certain conservative assumptions on aerosol loading in regions of clean air, the normalization of the backscatter signal yields the backscatter ratio (*BSR*) defined as the ratio of the total – aerosol and molecular – to molecular signal. Analogously to the *BSR* the aerosol backscatter ratio is *ABSR = BSR* - 1. The two different wavelengths allow definition of the colour index (*CI*) as the ratio of the *ABSR* at 870 nm divided by the *ABSR* at 455 nm. Information on particle size can be obtained from the *CI* subject to certain assumption on particle size distribution, shape and refractive index. For the COBALD wavelengths the range of *CI* varies from 1 for very small particles (Rayleigh limit) up to approximately 14 for large particles in the geometric limit around 2 μm radius. It should be noted that it is possible for the *CI* to significantly exceed 14 before reaching large particle values, because scattering functions oscillate about the asymptotic limit. These Mie oscillations cause ambiguity and thus inhibit distinct radius information for certain sizes. Stratospheric background aerosols are known to be characterized by a *CI* of 5 (Rosen and Kjome, 1991).

Usage of the Wyoming backscatter sonde has ranged from observations of volcanic aerosol (Rosen et al., 1992) over cirrus (e.g. Beyerle et al., 2001) to polar stratospheric clouds (e.g. Larsen et al., 2004). The new COBALD sonde has started to be applied in various field studies (e.g. Bukowiecki et al., 2011; Brabec et al., 2012). The COBALD *BSR* profiles used here are binned to 1 hPa pressure intervals to reduce measurement noise, which typically increases in the stratosphere.

6.2.2   M55-Geophysica aircraft measurements

In the frame of the European research project RECONCILE (Reconciliation of essential process parameters for an enhanced predictability of Arctic stratospheric ozone loss and its climate interactions) an intensive field campaign of coordinated aircraft, balloon and ground-based measurements related to ozone chemistry and PSCs was conducted during January - March 2010 (von Hobe et al., 2012). The Russian high-altitude aircraft M55-Geophysica was deployed in Kiruna, Sweden and conducted 12

research flights carrying over 20 in situ and remote instruments for measurements of gaseous and particle constituents. In accordance with the balloon soundings in Sodankylä, the aircraft campaign was implemented in two phases.

The in situ water vapor instruments operating onboard the M55-Geophysica aircraft are FISH and FLASH-A, both closed-cell hygrometers, making use of the fluorescent method for measuring water vapor in the upper troposphere and lower stratosphere with 1 Hz sampling frequency. The Fast In-situ Stratospheric Hygrometer (FISH) is equipped with a forward-facing inlet and thus measures total water, i.e. the sum of gas-phase water and ice particles. The description and calibration procedure of FISH instrument have been documented by Zöger et al. (1999) and Schiller et al. (2008). Mixing ratios of H_2O between 0.5 and 1000 ppmv can be detected by FISH with a time resolution of 1 s and an overall accuracy of 6 %. FISH was calibrated regularly before and after every flight during the aircraft campaign using a calibration bench including a frost point hygrometer (MBW DP30) as a reference.

FLASH-A (Fluorescent Lyman-Alpha Stratospheric Hygrometer for Aircraft) is a recent modification of the FLASH instrument (Sitnikov et al., 2007) previously utilized onboard the M55-Geophysica aircraft. FLASH-A has a rear facing inlet for measurement of gas-phase water vapor in the altitude range between 7 - 20 km, with the latter being the aircraft ceiling altitude. Its total measurement uncertainty amounts to 10 % for a 6 s integration time with a detection limit of 0.2 ppmv. During the RECON-CILE campaign FLASH-A was calibrated after every third flight using the FISH calibration bench. The signal-to-noise ratio of the FLASH-A instrument is lower than that of FISH for 1 s resolution data, therefore we use 6 s averaged data in this study. The point-by-point comparison between FLASH-A and FISH stratospheric cloud-free data acquired during the RECONCILE flights showed a mean relative difference of 2.7 % (with 1σ standard deviation of 3 %), which is well within the uncertainty limits of both hygrometers. The details of airborne hygrometers intercomparison are provided in Appendix B.

6.2.3   Microwave Limb Sounder (MLS)

The MLS instrument operating onboard Aura satellite was launched in July 2004 as a part of the NASA/ESA "A-Train" satellite constellation. MLS is a limb sounding instrument that measures the thermal emission at millimeter and sub millimeter wavelengths using seven radiometers to cover five broad spectral regions (Waters et al., 2006). Measurements are performed from the surface to 90 km with global latitude coverage from 82° S to 82° N each day. Here we use the version v3.3 described by Livesey et al. (2013), reporting for the middle stratosphere the vertical resolution of 3.1 - 3.3 km, horizontal resolution of 220 - 300 km, accuracy of 7 - 9 % and precision of 6 %. The data screening criteria specified by Livesey et al. (2013) have been applied to the data.

The MLS instrument operating onboard Aura satellite was launched in July 2004 as a part of the NASA/ESA "A-Train" satellite constellation. MLS is a limb sounding instrument that measures the thermal emission at millimeter and sub millimeter wavelengths using seven radiometers to cover five broad spectral regions (Waters et al., 2006). Measurements are performed from the surface to 90 km with global latitude coverage from 82°S to 82°N each day. Here we use the version v3.3 described by Livesey et al. (2013), reporting for the middle stratosphere the vertical resolution of 3.1 - 3.3 km, hori-

zontal resolution of 220 - 300 km, accuracy of 7 - 9 % and precision of 6 %. The data screening criteria specified by Livesey et al. (2013) have been applied to the data.

6.2.4 Cloud-Aerosol Lidar with Orthogonal Polarization (CALIOP)

CALIPSO (Cloud-Aerosol Lidar and Infrared Pathfinder Satellite Observations) is a part of the "A-Train" satellite constellation and has been in operation since June 2006 (Winker et al., 2009). CALIPSO is in a 98.2° inclination orbit which provides extensive measurements over the polar regions of both hemispheres up to 82° in latitude. Measurements of PSCs are provided by CALIOP, the primary instrument onboard CALIPSO, which is a two wavelength, polarization sensitive lidar. High vertical resolution profiles of the backscatter coefficient at 532 and 1064 nm as well as two orthogonal (parallel and perpendicular) polarization components at 532 nm are provided (Pitts et al., 2007). The lidar pulse rate is 20.25 Hz, corresponding to one profile every 333 m. The vertical resolution of CALIOP varies with altitude from 30 m in the lower troposphere to 180 m in the stratosphere. For the PSC analyses, the CALIOP profile data are averaged to a spatial resolution of 180 m vertical and 5 km horizontal.

6.3 Observations and discussion

6.3.1 Meteorological situation

The 2009/2010 Arctic winter lower stratosphere was unusually cold during the six-week period from mid-December 2009 until the end of January 2010. Among the Arctic winters of the past half century, the 2009/2010 Arctic winter was one of the few winters with synoptic-scale temperatures below the frost point, T_{frost} (Pitts et al., 2011). During a seven-day period ending on 21 January the vortex cooled below T_{frost} over a large region between roughly 70- 80° N and 10° W - 80° E. The vortex formed in early December and a warming over Canada in mid-December caused a splitting of the vortex into two parts. The colder part of the vortex survived and cooled down through mid-January reaching temperatures below T_{frost}. During this time period, orographic waves were frequently excited by the flow over Greenland, but even synoptic-scale temperatures were colder than T_{frost}, which is quite unusual for the Arctic and resulted in the formation of ice PSCs on large scales. A major warming around 24 January caused a displacement of the vortex to the European Arctic and also initiated the breakup of the vortex. A detailed description of the Arctic winter 2009/2010 is provided by Dörnbrack et al. (2012) and Pitts et al. (2011).

6.3.2 Ice PSC formation and water depletion

The first balloon sounding from Sodankylä within the LAPBIAT-II campaign was carried out on 17 January. By that time a large area north of Sodankylä had cooled below T_{frost} at and above the 490 K potential temperature level, i.e. above ~ 22 km altitude. The balloon payload included both FLASH-B and CFH hygrometers as well as the COBALD backscatter sonde. Figure 6.1 displays the vertical profiles of *BSR*, water mixing ratio, and relative humidity with respect to ice (RH$_{ice}$ calculated from the measured mixing ratio and temperature). All profiles in Fig. 6.1 were taken during the descent
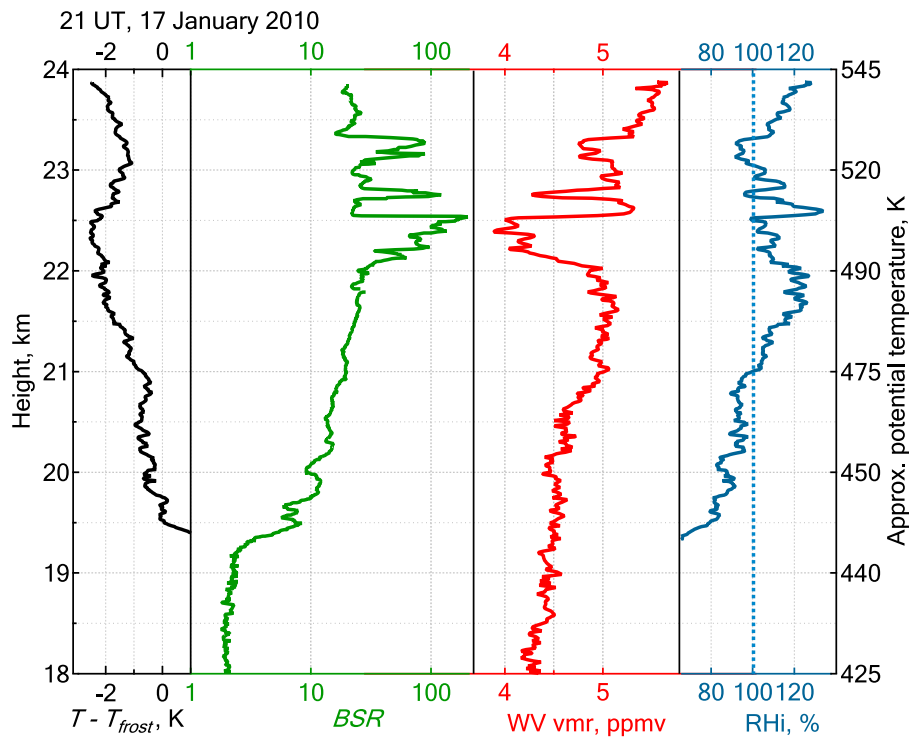
Figure 6.1: Vertical profiles obtained during balloon descent on 17 January 2010. From left to right: difference between the observed temperature and the "climatological" frost point (based on January mean water vapor from FPH and CFH soundings in 2002 - 2010, black line); backscatter ratio at 870 nm (COBALD, green line); water vapor volume mixing ratio (FLASH-B, red line); relative humidity with respect to ice (based on water vapor from FLASH-B and temperature from the RS92 Vaisala radiosonde). The time stamp in the upper-left corner refers to the time of stratospheric measurements.

under parachute with a rather low vertical speed of about $5 \, \mathrm{m\,s^{-1}}$ due to incomplete burst of the balloon. Owing to the slow descent, the actual vertical resolution of the water vapor profile is about 20 m. To provide a comparison with the climatological situation, the leftmost panel further shows the difference between the observed temperature and the "climatological" frost point, calculated using the January-mean water vertical profile, obtained from the NOAA frost point hygrometer (FPH) and CFH soundings at Sodankylä since 2002 in the absence of ice clouds (see Appendix A for details).

The *BSR* profile displays three remarkable enhancements between 22 and 23.5 km (potential temperature 490 - 535 K). A layer between 22 and 22.5 km is characterized by a gradual increase of *BSR* from 20 to nearly 200 followed by a sharp drop back to the value of 20. Two additional enhancements of smaller vertical extent and with maximum *BSR* values of about 50 were measured, centered at 22.7 km and 23.3 km. The colour index in the 22 - 23.5 km layer (not shown), ranges from 7 to 14, pointing to supermicron particles. Most likely, the three layers of large *BSR* and *CI* contain ice particles with radii larger than ~ 2 μm. The ice layers are superimposed onto a broad layer of elevated backscatter values above 19.5 km, most likely composed of liquid PSC particles or mixtures of liquid and NAT (termed "STS" or "Mix-1", respectively, in the classification of Pitts et al., 2011).

The presence of ice clouds is strongly supported by the measured profile of water mixing ratios, showing a clear anti-correlation with *BSR*, with considerable reductions in mixing ratio (by up to 1.3 ppmv) inside the ice PSC layers, which results from repartitioning of gas-phase water into the solid phase. The precise altitude match of these layers in *BSR* and mixing ratio, including fine details, is remarkable. Above 21 km (~ 475 K) the air is mostly supersaturated, as shown by the profile of RH_{ice}. The maximum values of RH_{ice} are observed outside the ice layers with a peak value of 134 % at 22.6 km, just between the two layers of ice PSCs, whereas inside the ice clouds the RH_{ice} is in the range 90 - 110 %. This is probably due to equilibration between the gas and condensed phase. Indeed, equilibration times for the water vapor condensing onto the ice particles is in the order of $\tau \sim 10^3$ s × $(1 \, \mu m / r_{ice}) \times (1 \, cm^{-3} / n_{ice})$ for monodisperse ice particles with radius r_{ice} and number density n_{ice}. As we show in the companion paper (Engel et al., 2013a), microphysical modeling suggests $r_{ice} \sim 10 \, \mu m$ and $n_{ice} \sim 10^{-2} \, cm^{-3}$, i.e. $\tau \sim 3$ h at the time it was measured in Sodankylä.

Important information is provided by the difference between the frost point temperature and the observed temperature ($T - T_{frost}^{climatol}$). Temperatures 2 K below the climatological frost point are observed in a 1 km thick layer between 21.6 and 22.6 km with the maximum absolute value reaching 2.5 K inside the thickest ice cloud between 22 and 22.5 km. Trajectories backward and forward in time show that the air masses were in a continuing cooling phase. Details of trajectory calculations, the temperature evolution, and possible formation pathways of the observed PSC are provided by Engel et al. (2013a)

The balloon measurements on 17 January capture freshly formed layers of ice PSCs and concurrent uptake of water from the gas phase. In the following section we will describe the evolution of the perturbed air masses based on the subsequent balloon soundings.

6.3.3 Irreversible dehydration and rehydration

Evidence of irreversible dehydration is provided by the subsequent water vapor profiles, shown in Fig. 6.2 (see also Fig. 6.6 in Appendix A for supplementary information on selected soundings, including the backscatter profiles, and Tab. 6.1 for the summary of all soundings). While all the backscatter profiles obtained after 17 January suggested an absence of ice particles (as inferred from the values of *BSR* not exceeding 20), the water vapor profiles reveal a persistent reduction in mixing ratio at different levels above 19.5 km (450 K).

The sounding performed on 21 January, exhibits a broad layer between 470 - 570 K (21 - 24.5 km), where water vapor is depleted by up to 0.7 ppmv and a narrower layer of enhanced vapor mixing ratio by 0.6 ppmv below, between 450 - 470 K (20 - -21 km). The observed vertical structure suggests a removal of water from the upper layer through gravitational settling of ice particles, followed by their sublimation below at higher temperatures (rehydration). Note that advection of extra-vortex air as a reason for local reductions in water mixing ratios, as reported by e.g. Müller et al. (2003), can be ruled out given the strength of the vortex at that time. Another indication of the inner-vortex origin of the water-depleted air masses is provided by the trajectory analysis performed using Lagranto model (Wernli and Davies, 1997) initialized by ECMWF (European Centre of Medium-Range Weather Forecasts) reanalysis. The 7-days backward trajectories showed that the air masses sampled on 21 January were following the vortex rotation and passing an area of sub frost point temperatures between Scandi-
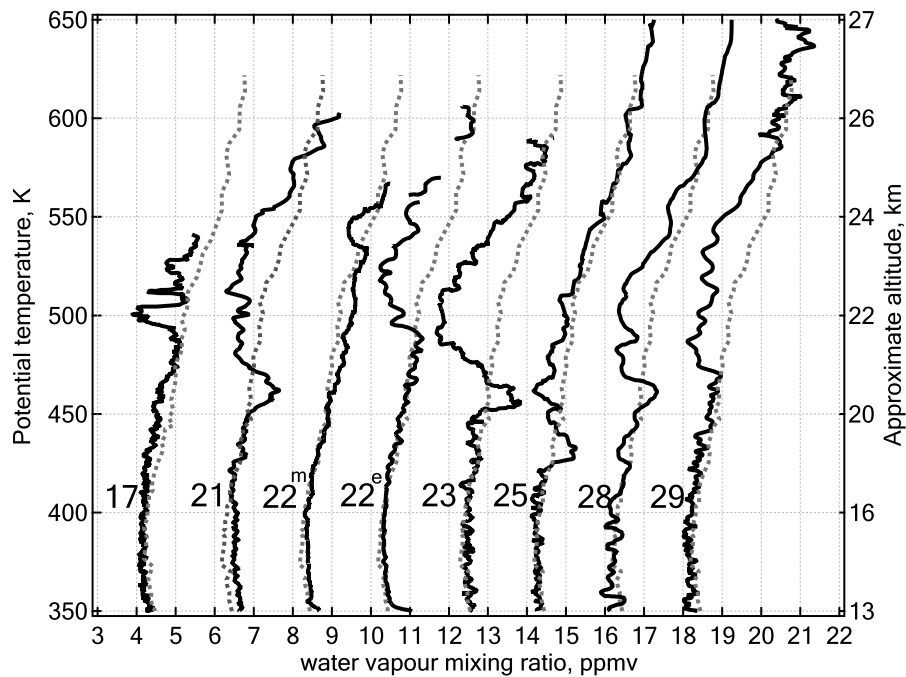
Figure 6.2: Vertical profiles of water vapor obtained during January 2010 (solid black lines) compared against the "climatological" water vapor profile (based on January mean water vapor from FPH and CFH soundings at Sodankylä in 2002 - 2010, gray dashed lines). Successive profiles are shifted by 2 ppmv. The dates of the soundings are given on the left of each profile. The superscript indices "m" and "e" indicate respectively morning and evening soundings on 22 January. The profiles of 17, 25, 28 and 29 January were obtained using FLASH-B, the remaining profiles were obtained using CFH.

navia and Spitsbergen on 16 January. The respective observations by CALIOP indicated a widespread occurrence of ice PSCs in this region, extending between 20 and 25 km altitude (Pitts et al., 2011, suppl. material), which is consistent with the vertical range of the dehydrated layer.

The next sounding performed 19 h later in the early morning on 22 January (marked 22[m] in Fig. 6.2) revealed a remarkable change in water vertical distribution with a narrow dehydrated layer between 540 - 555 K (23.5 - 24 km) and absence of rehydration signatures, indicating arrival of a new patch of perturbed air masses. A significant vertical enlargement of the water-depleted layer is revealed by the profile obtained 15 h later (22[e] in Fig. 6.2), showing the lower boundary of dehydration signal at 490 K (22 km). Remarkably, neither sounding of 22 January shows rehydration signatures similar to that observed on 21 January. This can be explained by the positive vertical wind shear (reported by the radiosondes), making the lower levels travel around the vortex more slowly (see also Engel et al., 2013a).

The effect of wind shear is clearly demonstrated by the sequence of successive 22[m], 22[e] and 23 January profiles, showing the dehydrated layer broadening and spreading towards the lower levels. The rehydrated air masses traveling at the lower levels and thus arriving at the sounding location later appear only in the 23 January profile, the one providing the most prominent evidence of the water vertical redistribution. Figure 6.3 shows the details of this sounding, represented by the vertical profiles of frost point difference, BSR, water mixing ratio and RH_{ice}. The excursion of temperature below the "clima-
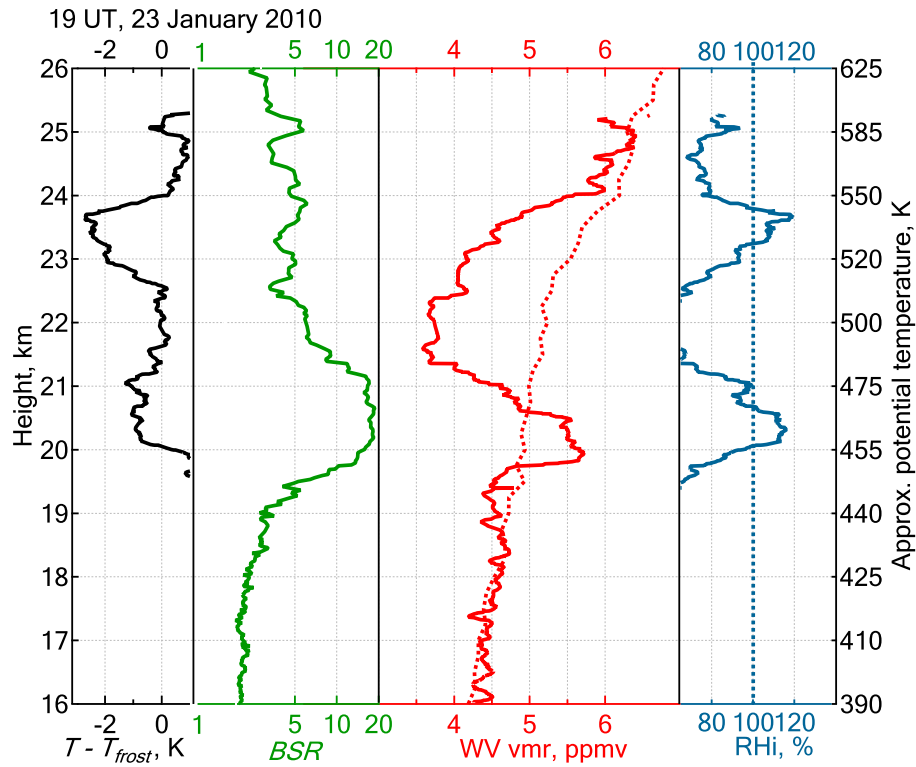
Figure 6.3: Vertical profiles obtained during balloon ascent on 23 January 2010. From left to right: difference between the observed temperature and the "climatological" frost point (based on January mean water vapor from FPH and CFH soundings in 2002 - 2010, black line); backscatter ratio at 870 nm (green); water mixing ratio (CFH), with climatological mean shown as dotted line (red); relative humidity with respect to ice (blue). Note the different vertical and horizontal scaling compared to Fig. 6.1. The time stamp in the upper-left corner refers to the time of stratospheric measurements.

tological" frost point is still visible in a layer between 20 and 24 km, where the frost point difference reaches 2.8 K. These conditions would likely cause formation of ice in an unperturbed stratosphere. However, as shown by the water mixing ratio profile, the stratospheric layer between 21 and 24 km is already dehydrated by 1.6 ppmv. Hence, RH_{ice} does not exceed 120 % (at the coldest point of 183 K). Importantly, despite the extremely low temperatures, the *BSR* profiles indicate only moderate concentration of particles, approaching the background state above 22 km (500 K), which suggests that these layers are also denitrified. This is consistent with Khosrawi et al. (2011), reporting the onset of denitrification in early January and a fast decrease of HNO_3 from 12 ppbv down to 5 ppbv at 480 K level during the first half of January as inferred from Aura MLS observations.

A totally different regime is represented by the layer below, between 450 - 460 K (19.7 - 20.6 km), showing an enhancement in water mixing ratios of about 1 ppmv, that can be unambiguously associated with rehydration. This layer is also characterized by enhanced *BSR* with values reaching 20, indicative of a cloud and a local maximum of RH_{ice}, reaching 116 %. The *BSR* values are an order of magnitude smaller than those observed on 17 January and, although it is not possible to draw a definitive conclusion on the type of this cloud from the COBALD data alone, this is most likely an STS PSC, possibly

externally mixed with NAT particles at low number densities (classes "STS" or "Mix-1" in the terminology of Pitts et al. (2011), previously also called "type I PSCs"). Indeed, the CALIOP observations suggest widespread occurrence of STS clouds (Pitts et al., 2011, Fig. 16 and suppl. material) without any indications of ice.

The vortex breakup followed by a major warming began around the 24 January (Dörnbrack et al., 2012). The sounding carried out 30 h later on 25 January (see Fig. 6.1 and Fig. 6.7) showed a further descent of dehydration and rehydration signatures, occurring at 460 K (20 km) and 430 K (18.3 km), respectively, lower *BSR* values reaching 10, and a warmer temperature minimum of 187 K at 22 km (515 K). The minimum temperature increased further to 191 K by the time of the subsequent sounding on 28 January, showing no indications of PSCs. The water vapor profile, however, still displays a remarkable dehydration signal between 470 - 550 K (20 - 22.5 km) of 1 ppmv amplitude and a subtle rehydration signature at 460 K (19.5 km). The next sounding performed 24 h later on 29 January revealed further warming, absence of clouds and a very similar dehydration signal in the same layer but without a rehydration signature at lower levels. An enhancement of water mixing ratios above 24 km might be indicative of the strong downwelling of moist air masses from the middle and upper stratosphere, which is a characteristic feature of major warmings. The three subsequent soundings conducted in early February indicated an absence of PSCs and a further gradual warming and descent of the temperature minimum amounting to 202 K at 19 km (463 K) on 06 February. The signatures of water redistribution could still be detected on 03 and 06 February, but with decreasing amplitude of perturbations, likely due to a dispersion of the perturbed air masses in the vortex.

The summary of the water vapor and aerosol soundings conducted during the first phase of the LAPBIAT-II campaign is provided in Tab. 6.1, including the information on the observed PSCs, de- and rehydration signatures and their amplitudes. The table shows that the dehydration signal was observed in all soundings except 20 January and 02 February, whereas the rehydration signal appears in 5 out of 13 soundings only, namely on 21, 23, 25 and 28 January as well as on 06 February. Although the very first sounding on 17 January showed a reduction of water vapor in the presence of ice, the evidence of permanent removal of water is demonstrated by the subsequent soundings only, showing depleted water in the absence of ice clouds. The maximum amplitude of water depletion amounts to 1.6 ppmv, which is comparable to the few previous observations of dehydration in the Arctic (quoted above), except the historical observation in the Arctic by Vömel et al. (1997), reporting the reduction in water mixing ratio of up to 2.5 ppmv. In contrast, signatures of rehydration and the coherent relationship between de- and rehydration in the winter Arctic stratosphere have been observed for the first time.

6.3.4   Spatiotemporal evolution of dehydration

The balloon soundings represent high-resolution snapshots of the water vertical redistribution measured above a single location. We will further examine the global spatiotemporal evolution of ice PSCs and concurrent dehydration using space-borne observations of scattering ratios and water mixing ratios provided by CALIOP and Aura MLS, respectively.

Figure 6.4 displays a series of polar projection maps of daily averaged water mixing ratios on the 490 K potential temperature measured by Aura MLS during the second half of January 2010. Superimposed

on these maps are the observations of ice PSCs by CALIOP; vortex boundary (defined as potential vorticity (PV) contour of $35 \times 10^{-6}\,\mathrm{K\,m^2\,kg^{-1}\,s^{-1}}$), and 187 K temperature contour, corresponding to the frost point at 30 hPa (corresponding roughly to 490 K potential temperature). The map of 15 January shows an area of mixing ratio reduced below 4.5 ppmv north-west from Scandinavia inside the frost point contour. As expected, the occurrence of ice is confined to the area colder than T_{frost}. The area of sub-frost point temperatures and ice clouds expands and moves eastward, approaching Sodankylä on 17 January. The daily-averaged water vapor field on 17 January from MLS does not yet show the signature of water depletion directly above Sodankylä, but further North, whereas the balloon measurements acquired late on the same day (at 21:00 UT) revealed the onset of dehydration, as discussed above. The situation on 18 January indicates a further expansion of the cold pool of $T < T_{\mathrm{frost}}$ reaching the sounding location and comprising a large area of depleted water mixing ratios as low as 3.5 ppmv northeast from Scandinavia, centered above the island of Novaya Zemlya. An occurrence of synoptic-scale ice PSCs, covering several millions of square kilometers within the cold pool is observed by CALIOP. Remarkably, the area of water depletion extends outside the area of temperatures below the frost point, unambiguously demonstrating irreversible dehydration. The observations of 19 January exhibit essentially the same picture as on the previous day but with less extensive ice PSC occurrence as well as a smaller extent of the cold and dehydrated pools. In contrast, the dehydrated air masses that have been advected outside the cold area gain a larger spatial extent.

Over the next few days the dehydrated pool elongated and traveled around the center of vortex, passing across the pole (beyond MLS coverage) during 21 - 22 January and reappearing above northern Scandinavia by 23 January. The balloon sounding conducted in the late afternoon on 23 January displayed the largest amplitude of dehydration, which is consistent with the MLS observations showing the dry pool approaching the sounding location on 23 January and fully covering Sodankylä on 24 January.

On 24 January, due to a planetary wave event, the vortex began to lose its symmetry and the cold region progressively shifted away from the vortex center (Dörnbrack et al., 2012). Meanwhile, the trace of dehydrated air masses becomes less discernible on the satellite images due to mixing with non-dehydrated air inside the vortex. The pool of mixing ratios below 4.5 ppmv passed across northwest Russia on 25 January, further elongating and dissipating along the southeast boundary of the vortex. The final indications of the air patches dehydrated below 4.5 ppmv appear during 28 - 29 January, after their second circuit within the vortex. On 28 January the dry pool is partly obscured by the MLS polar "blind spot", and on 29 January it emerges above Scandinavia. Consistent with that, the balloon soundings of 28 and 29 January show the dehydration signal of 0.7 - 0.8 ppmv maximum amplitude.

Whereas the spatial evolution of the dehydrated pool observed by MLS is consistent with the picture provided by the balloon soundings, one should consider the limited sampling density of MLS measurements and their broad vertical resolution, which may impede the observation of weaker dehydration signals. Thus, the movement of the largest dehydrated pool, arisen during 17 - 19 January is easily discernible on the polar projections, whereas the smaller patches of dehydrated air, processed by the sub-frost point temperatures during the preceding days (as detected in the 21 January sounding) are far less obvious. The 3 km vertical resolution of MLS does not allow tracking the rehydration signatures of ~ 1 km thickness as shown by the balloon soundings. In addition, the rehydration signal could be smeared out with the dehydration signal immediately above, thereby weakening one another.
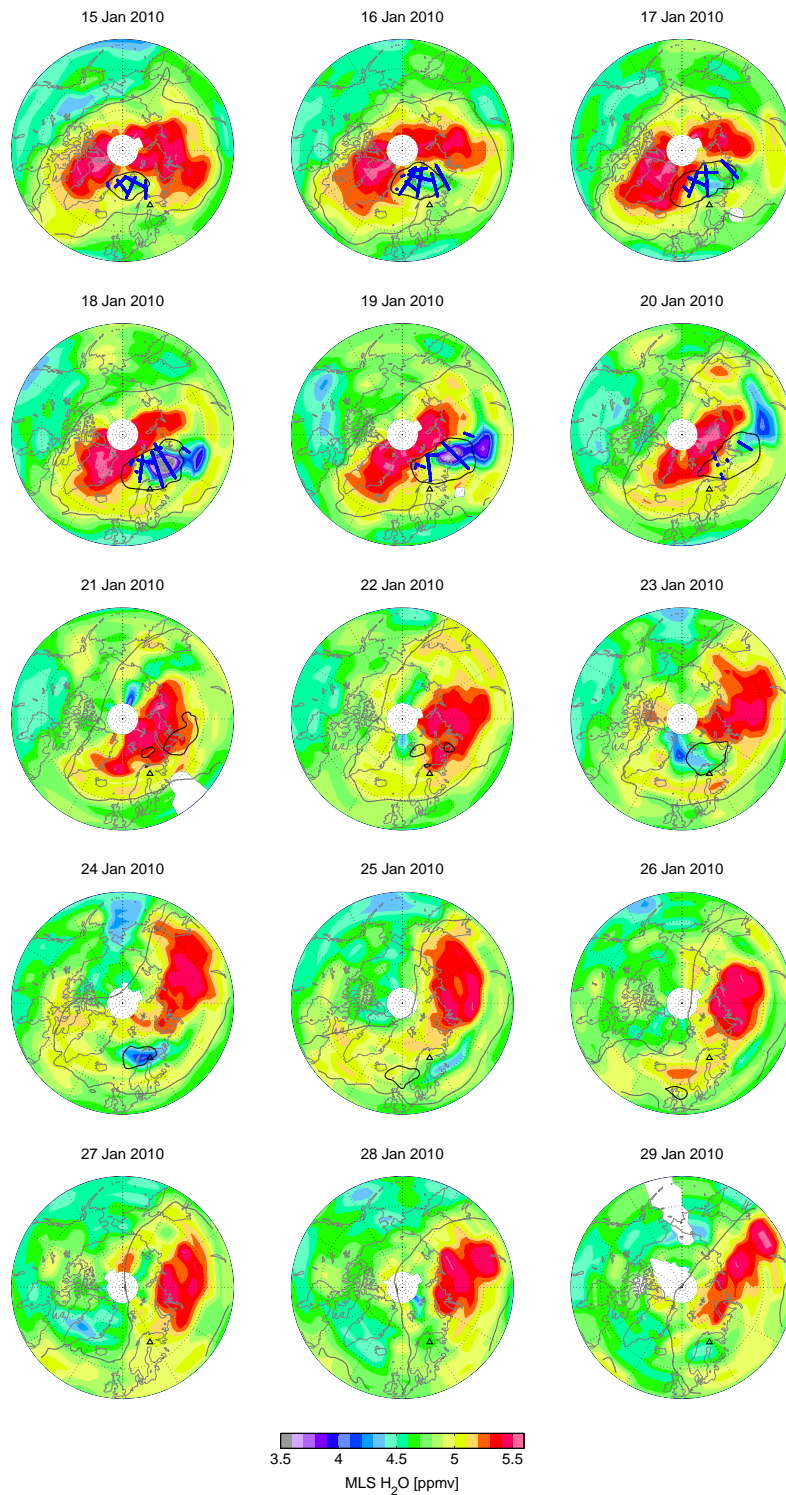
Figure 6.4: Aura MLS polar projection maps of water vapor mixing ratio for 15 - 29 January 2010, interpolated onto the 490 K potential temperature surface. Grey contour denotes the vortex boundary given as potential vorticity value of $35 \times 10^{-6}\,\mathrm{K\,m^2\,kg^{-1}\,s^{-1}}$. Black contour: 187 K at 00:00 UTC (T_{frost} at 30 hPa assuming 5 ppmv water vapor). Blue markers: CALIOP observations of ice clouds thicker than 540 m in the 20 - 24 km altitude range. Balloon sounding location is marked with a black triangle.

Table 6.2: Listing of aircraft flights during January - February 2010 (RECONCILE first phase). From left to right: date and time of the aircraft takeoff; hygrometer type used (FLA=FLASH-A); indicator of rehydration signatures; maximum amplitude of rehydration signal (ppmv).

Date	Time, UTC	Hygrometer	Indicator	Amplitude
17 Jan 2010	11:17	FISH, FLA	–	–
20 Jan 2010	08:13	FISH	–	–
22 Jan 2010	10:01	FISH, FLA	–	–
24 Jan 2010	13:30	FISH, FLA	–	–
25 Jan 2010	05:50	FISH, FLA	R	+(0.3–0.7)
28 Jan 2010	09:00	FISH, FLA	R	+0.6
30 Jan 2010	06:36	FISH, FLA	–	–
02 Feb 2010	10:01	FISH, FLA	–	–

6.3.5 Evidence of dehydration and rehydration from aircraft measurements

The 20 km ceiling altitude of the M55-Geophysica aircraft carrying the RECONCILE payload did not allow for sampling the dehydrated air masses, which, according to the balloon soundings, were mostly restricted to the altitudes above 20 km (475 K). However, the rehydrated plumes, detected in the balloon soundings as low as 18 km, were within reach of the aircraft. A summary of the aircraft flights and the rehydration signatures detected therein is provided in Tab. 6.2.

Enhancements in water vapor mixing ratio by 0.3 - 0.9 ppmv were detected in the aircraft flights on 25 and 28 January, consistent with the balloon profiles obtained on the same day and showing the rehydrated layers. Figure 6.5 displays the time series of water vapor measured by FISH and FLASH-A instruments on the flight of 25 January, climatological January-mean water vapor for the given altitude (based on balloon soundings at Sodankylä in 2002 - 2010), potential temperature and altitude flight profile. The time series of water vapor provided by the two aircraft hygrometers are in good agreement (see Appendix B for details), although both FISH and FLASH-A water vapor time series are 5 - 8 % drier than the climatological mean.

During the horizontal flight leg conducted at constant altitude of 19 km, water vapor enhancements of 0.5, 0.3 and 0.7 ppmv are observed within the time intervals 24 900 - 25 200, 25 680 - 25 900 and 28 000 - 28 470 s, corresponding respectively to 58, 42 and 81 km horizontal crosscut distances (marked by 3 black arrows). The water enhancements coincide with local maxima in potential temperature, suggesting that the aircraft was flying just at the lower edge of a rehydrated layer, crossing three troughs of it, which were bulging down and intersecting the aircraft flight level. This is confirmed by a larger enhancement of water mixing ratio by 1 ppmv detected once the aircraft started climbing to its ceiling altitude of 20 km. An increase of 1 ppmv within a 1 km layer significantly exceeds the expected vertical gradient of mixing ratio inside the vortex, as seen from the climatological mean water vapor (dashed black curve), displaying a difference of only 0.3 ppmv between 19 and 20 km. Furthermore, at the highest part of the flight, the water vapor series show a small drop of 0.3 ppmv, which could be due to the aircraft approaching the top of the rehydrated layer. Such a vertical structure is consistent with the balloon profile of 25 January, taken 7 h prior to the aircraft flight and displaying the rehydrated layer
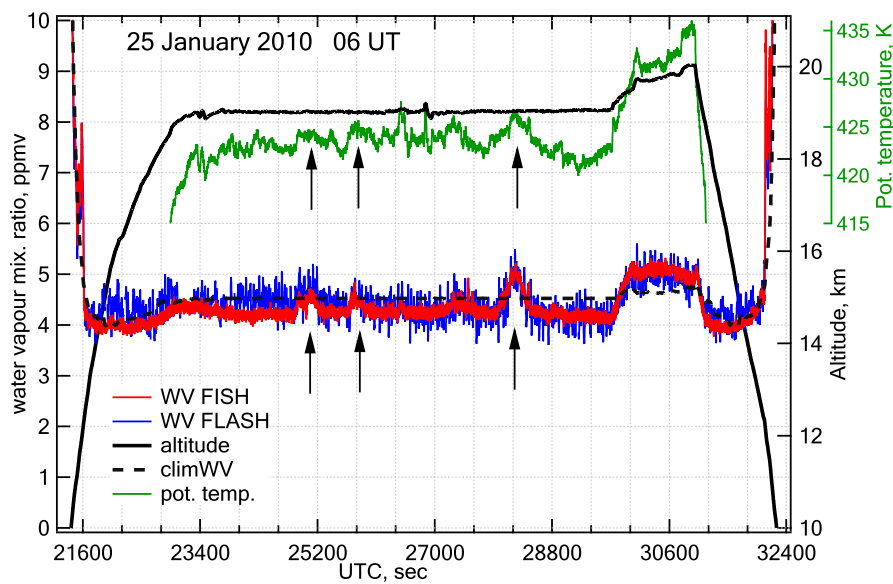
Figure 6.5: Results of the aircraft flight on 25 January 2010 showing the rehydration signatures: time series of water mixing ratio measured by FISH and FLASH-A (left axis); potential temperature (upper right axis); altitude flight profile (right axis) and climatological mean water vapor for the given altitude (based on January mean water vapor from FPH and CFH soundings in 2002 - 2010, dashed black line, left axis). Tick marks on the horizontal axis correspond to 10 min interval. Three black arrows point to regions with positive water vapor anomalies, associated with rehydration.

between 18.2 km (430 K) and 19 km (440 K). Similar features were observed in the aircraft flight on 28 January (not shown), when both hygrometers detected an increase of 0.5 - 0.6 ppmv at 19 km during the final climb of the aircraft to 20 km altitude, followed by a drop of water vapor to its background level at the aircraft ceiling point. This observation is consistent with the balloon profile obtained 6 h later from Sodankylä, showing a rehydrated layer with 0.5 ppmv water enhancement between 19 and 19.5 km altitude.

6.4 Summary and conclusions

By 15 January 2010 the coldest regions of the Arctic stratospheric vortex reached temperatures as low as T_{frost}. This was accompanied by a major outbreak of ice PSCs observed by CALIOP on a synoptic scale lasting from 15 to 21 January (Pitts et al., 2011). Owing to the extensive sounding program implemented within the LAPBIAT-II and EU RECONCILE campaigns, the composition of the Arctic stratosphere during this period was accurately monitored using stratospheric balloons and the high-altitude M55-Geophysica aircraft.

13 balloon soundings were conducted from Sodankylä during 17 January - 06 February, involving CFH and FLASH-B hygrometers flown together with the COBALD backscatter sonde. The measurements of water vapor, obtained using two independent techniques, are in excellent agreement, which allows using FLASH-B and CFH profiles as consistent and interchangeable data sets. The balloon measurements on 17 January capture freshly formed layers of ice PSC and concurrent uptake of water from the

gas phase in great detail, providing an unprecedented high-resolution "snapshot" of the process of ice PSC formation. Possible formation pathways of the observed PSC are discussed in the companion paper by Engel et al. (2013a). Furthermore, balloon soundings provided evidence of irreversible dehydration by showing a permanent layer of reduced water mixing ratio between 19.5 and 24 km altitude in the absence of ice PSCs as well as an underlying 1 km thick layer of enhanced water mixing ratio, attributed to rehydration through evaporation of the falling ice particles. The vertical redistribution of water vapor is observed for the first time in the Arctic stratosphere. The signatures of dehydration and rehydration in the vertical profiles could be detected until 06 February, although the amplitude of perturbations was decreasing over time due to continuing dispersal of the air masses in the vortex. Additional evidence of the existence of rehydrated layers is provided by the aircraft-borne FISH and FLASH-A hygrometers in two out of eight aircraft flights carried out during the given period by the stratospheric research aircraft M55-Geophysica. The airborne hygrometers, being in good agreement with each other, show enhancements in mixing ratio of 0.3 - 0.7 ppmv between 19 and 20 km altitude, which is consistent with the corresponding balloon flights. In contrast, the dehydrated layers, residing above the aircraft ceiling altitude could not be sampled by the airborne instruments.

The source region of dehydration and its spatiotemporal evolution was examined using space-borne Aura MLS water vapor observations. A sequence of polar projection water vapor maps shows the onset of dehydration on 15 January and its maximum development on 18 - 19 January, when the dehydrated pool extends outside the area below the frost point. The dehydrated air masses travel around the center of the vortex, reappearing above Scandinavia on 22 January. The final indications of patches of air dehydrated below 4.5 ppmv appear on 28 - 29 January, after their second circuit within the vortex. The spatial evolution of the dehydrated pool observed by MLS is consistent with the picture provided by the balloon soundings, although due to ~ 3 km vertical resolution of MLS measurements the dehydration signal could be smeared out with the rehydration signal immediately below, resulting in a weakening of both. In particular, the evolution of the 1 km-thick rehydration layer could not be followed by MLS.

Overall, the consistent observations of water vapor from balloon, aircraft and satellite platforms together with the aerosol observations by COBALD and CALIOP provide a comprehensive view of the consequences of the widespread ice PSC occurrence, that is:

1. formation of a dehydrated layer at 19.5 - 24 km (450 - 550 K) with a reduction in water mixing ratios of up to 1.6 ppmv;

2. formation of a rehydrated layer at 18 - 20.5 km (430 - 460 K) with mixing ratio enhancements up to 0.9 ppmv;

3. redistribution of water within 18 - 24 km due to gravitational settling and subsequent evaporation of ice particles.

Such exceptional conditions in the Arctic stratosphere have been observed for the first time. These observations represent the most accurate and detailed data set on water vapor redistribution in the stratospheric vortex ever recorded.

6.5   Appendix A

The present study is based on extensive experimental material comprising various data sets. In order to avoid overloading the main part of the manuscript with numerous figures, we provide here additional information in the form of sequences of plots.

Figure 6.6 displays the results of selected balloon soundings carried out at FMI-ARC, Sodankylä during the first phase of the LAPBIAT-II field campaign. The plots of 17, 25 and 29 January are constructed using descent profiles with water vapor measured by FLASH-B. The remaining plots are constructed using ascent profiles with water vapor measured by CFH (see Appendix B for justification of this approach). The climatological mean water vapor profile shown in the plots is a January-mean profile from all soundings with frost point hygrometers (NOAA FPH and CFH) conducted in Sodankylä from 2002 to 2010, excluding the single historical sounding of 23 January 1996, which showed a strong dehydration signature, reported by Vömel et al. (1997). There is a remarkable match between the measured water vapor profiles and climatological profile in the unperturbed stratosphere below the dehydration and rehydration signatures. Local deviations from the mean profile are also observed below 14 km, where the water vapor vertical distribution may be affected by cross-tropopause exchange.

The vertical profiles of temperature and backscatter ratio in the plots for 17, 25, 28 and 29 January (where FLASH-B profiles are used) were measured during balloon descent. The remaining plots (where CFH profiles are used) contain the ascent profiles. The highest *BSR* value of 200 corresponding to ice PSC observation was detected on 17 January. The last indication of PSC was obtained on 25 January with *BSR* values below 10. The minimum temperature observed in each sounding was varying between 183 K (23 January) and 202 K (06 February). The minimum saturation mixing ratio of 4 ppmv was observed on 17 January.

6.6   Appendix B

6.6.1   Intercomparison of hygrometers

Since the main message of this study is delivered by the observations of water vapor by different hygrometers, it is of relevance to report the degree of agreement between these data sets. First, we compare the data from the instruments flown on the same platform (i.e. CFH - FLASH-B for balloon and FISH - FLASH-A for aircraft), then provide the results of intercomparison between all data sets.

Intercomparison of balloon hygrometers

Among the 13 soundings with CFH conducted during the first phase of the LAPBIAT-II campaign, four of them included FLASH-B flown on the same balloon. The description of CFH and FLASH-B instruments is given in Sect. 6.2.1 and 6.2.1, respectively. As discussed therein, the performance of CFH is better during balloon ascent, although above 26 - 27 km the measurements may be affected by the water outgassing. Occasionally the descent measurements of CFH, whose quality strongly depends on the payload vertical velocity, can be of equal quality. In contrast, FLASH-B performs better during de-
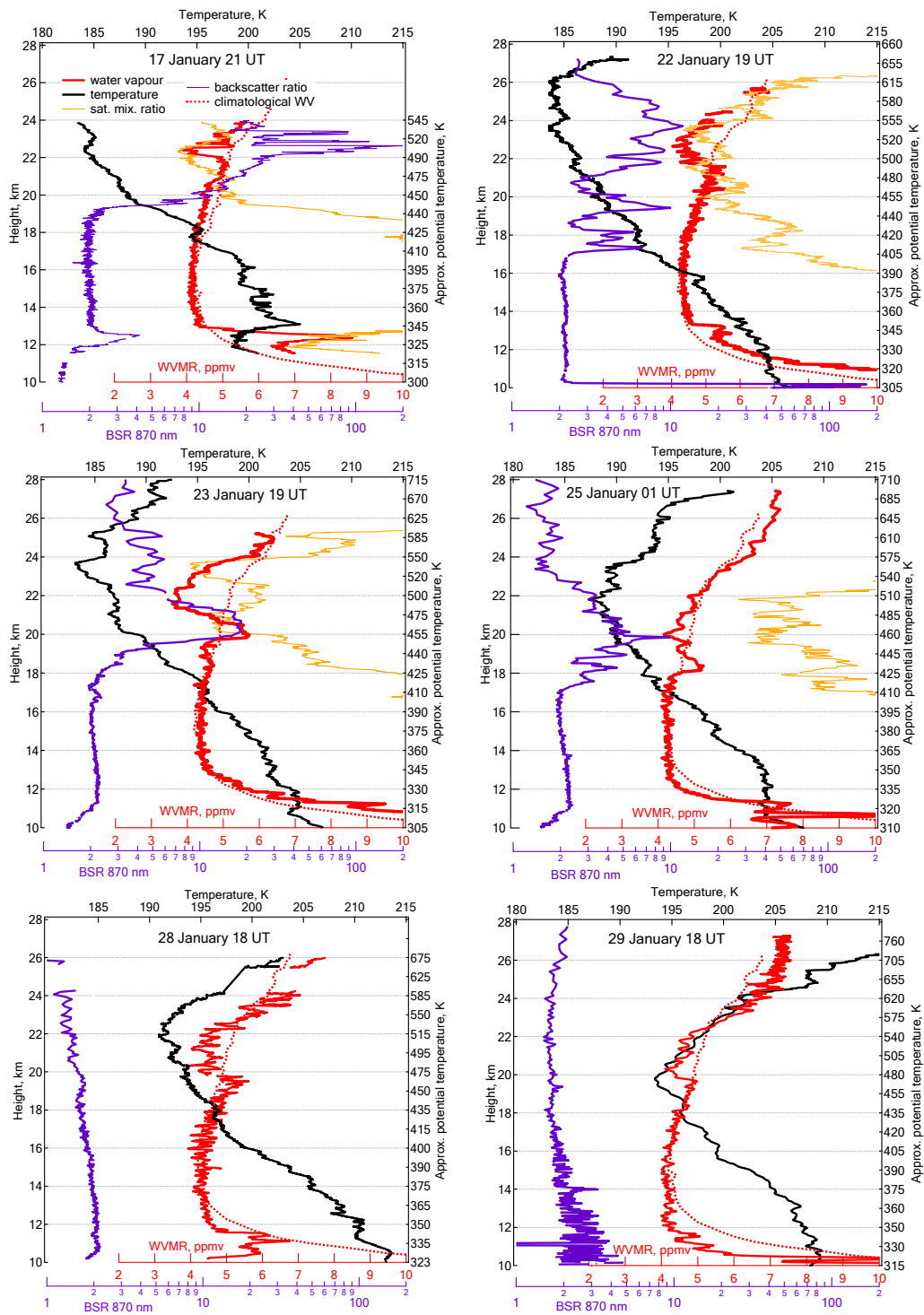
Figure 6.6: Results of selected balloon soundings carried out from Sodankylä during January 2010: water mixing ratio, climatological mean water and saturation mixing ratio (lower axis); backscatter ratio at 870 nm (lowermost axis); temperature (upper axis). The legend is given in the upper left panel. Date and UT time of the measurement are given in each panel. The time stamp refers to the time of stratospheric measurements.
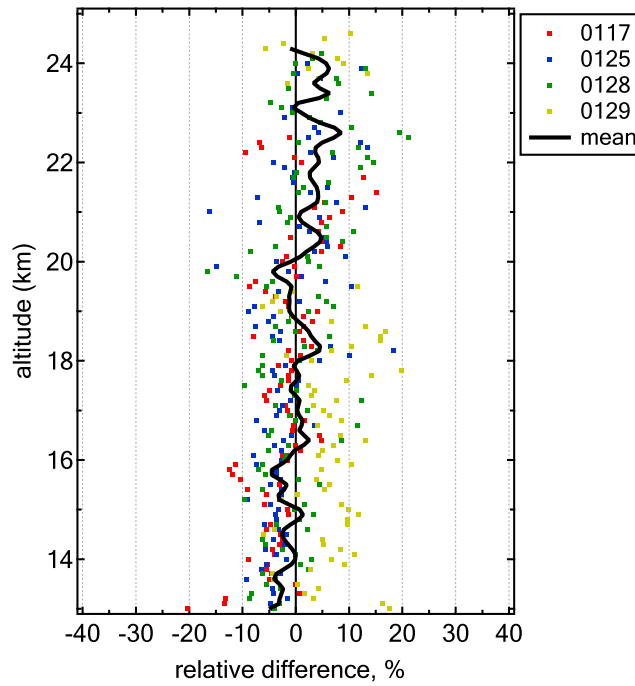
Figure 6.7: Mixing ratio relative difference between CFH ascent profiles and FLASH-B descent profiles: $100\% \, (\mu_{\mathrm{FLB}} - \mu_{\mathrm{CFH}})/\mu_{\mathrm{CFH}}$.

scent, whereas the ascent measurements above about 90 hPa are strongly affected by water outgassing due to the instrument's measurement layout. The statistical intercomparison is thus done using four pairs of CFH ascent and FLASH-B descent profiles in the 13 - 25 km altitude range. The validity of such approach is justified by the negligible temporal variability of water vapor at the stratospheric levels above 14 km. Although vertical distribution of water vapor during the sounding campaign was characterized by a noticeable variability between 18 and 24 km on a scale of tens of hours, the lag between ascent and descent sampling at 20 km altitude was always less than 30 min. Note also that since the balloon is following the wind motion, the ascent and descent legs would sample nearly the same air mass given a moderate wind shear in the mid stratosphere.

Figure 6.7 displays the results of intercomparison given as relative mixing ratio difference: 100% $(\mu_{\mathrm{FLB}} - \mu_{\mathrm{CFH}})/\mu_{\mathrm{CFH}}$, where μ denotes water vapor mixing ratio. The mean relative difference (solid line) based on four pairs of profiles does not indicate any systematic bias or altitude dependence and remains within 10 % limits throughout the range of intercomparison and within 5 % for the major part of the range. The vertically-averaged mean difference is as small as 0.78 %, whereas the standard deviation of the difference (1-σ level) amounts to 4 %.

While the vertically-averaged difference between CFH and FLASH-B data indicates very high degree of statistical agreement, the next step is to examine the relative capabilities of the hygrometers in reproducing vertical structures in stratospheric water vapor, which are of particular importance for this study.

Figure 6.8 displays both ascent and descent water vapor profiles of the four simultaneous CFH - FLASH-B soundings. As expected, the ascent profiles of FLASH-B are wet-biased due to the water
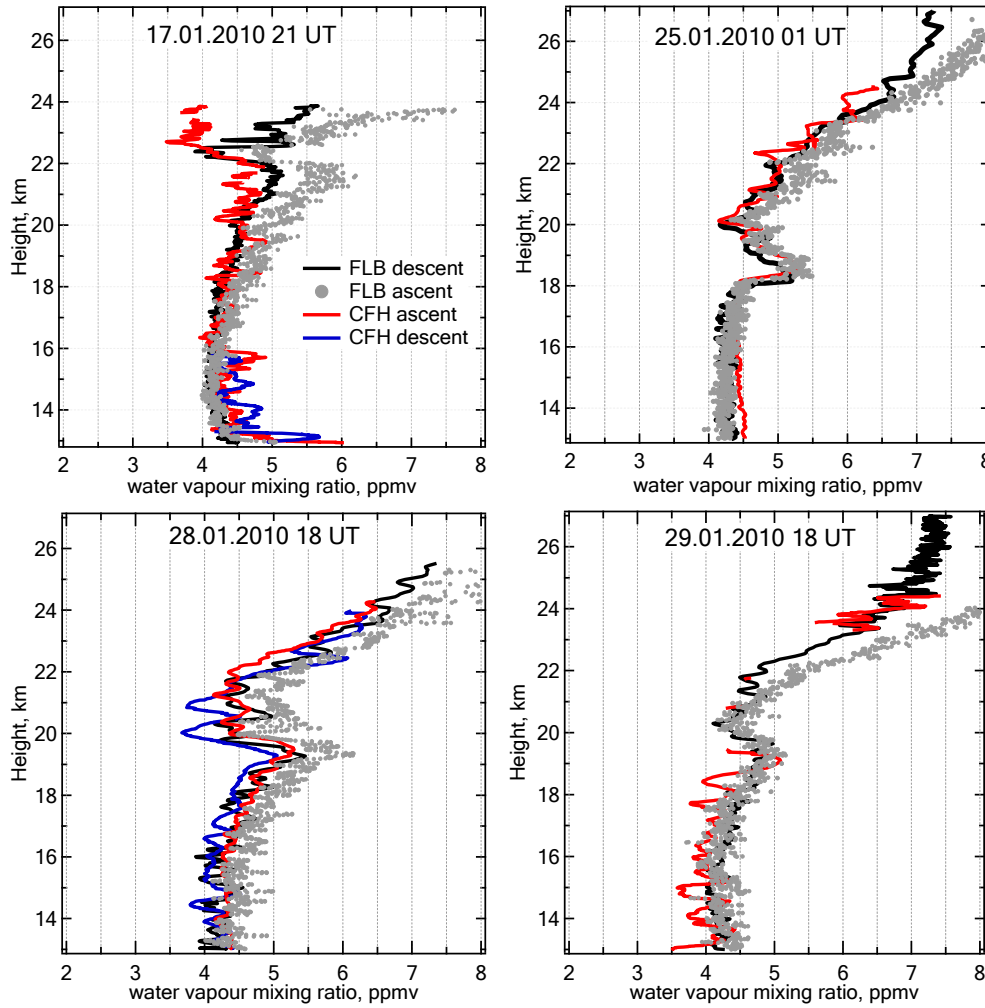
Figure 6.8: Comparison of ascent and descent profiles of water vapor mixing ratio measured by CFH and FLASH-B. The ascent CFH profiles of 25.01 and 28.01 soundings are averaged over 40 s to reduce the controller oscillations. The descent CFH profiles of 25 and 29 January, which were screened out during the initial quality check are not shown. The legend is given in the upper-left panel. The date and time of the sounding is given in each panel. The time stamps refer to stratospheric descent measurements time.

outgassing effect and the amplitude of the bias increases with altitude. The onset of the contamination effect, defined as departure of the ascent profile from the non-contaminated descent profile, is observed at altitudes between 17 km (17 Jan) and 21 km (29 Jan) depending on the amount of moisture crossed by the payload during the tropospheric ascent leg. Note that the lower non-contaminated portion of the ascent profile is in a precise match with the descent profile, indicating a stable performance of FLASH-B.

The vertical structures in water vapor, associated with de- and rehydration and the amplitudes of the perturbations are reproduced nearly identically by FLASH-B and CFH in all soundings except the case of 17 January, which requires a special consideration. Since the sounding on 17 January sampled an

active phase of ice formation and concurrent vapor uptake, rapidly alternating its vertical distribution, the ascent and descent measurements may not be directly compared. However, the reduction of water vapor above 22 km is clearly visible in CFH ascent and both FLASH-B wet-biased ascent and clean descent profiles. Due to somewhat unstable performance of the CFH feedback controller producing oscillations in the data, the uppermost part of the ascent profile and the major part of the stratospheric descent profile had to be screened out.

Overall, the measurements of water vapor by the two balloon-borne hygrometers are in excellent agreement suggesting high quality of the data and allowing FLASH-B and CFH vertical profiles to be used as coherent and interchangeable data series.

Intercomparison of aircraft hygrometers

The intercomparison of the aircraft-borne hygrometers FISH and FLASH-A was based on the simultaneous measurements from eleven aircraft flights carried out during both phases of the RECONCILE campaign. As described in Sect. 6.2.2, the fundamental difference between these hygrometers, both making use of the fluorescence method, is that FISH is equipped with a forward facing inlet and therefore measures total water, while FLASH-A uses a rear-facing inlet and is thus sensitive to gas-phase water only. This difference limits the stratospheric intercomparison to the ice-free measurements, which is the case for all aircraft flights performed during RECONCILE (von Hobe et al., 2012).

Analogous to Fig. 6.7, Fig. 6.9 shows the results of intercomparison based on all data above 200 hPa and given as relative mixing ratio difference: $100\% \, (\mu_{\mathrm{FLA}} - \mu_{\mathrm{FISH}})/\mu_{\mathrm{FLA}}$. While the deviation in the individual flights can exceed 15 %, the mean relative difference based on 11 flights remains below 6 % with FLASH-A showing slightly higher values compared to FISH virtually at all levels but without any altitude dependence. The vertically-averaged difference amounts to 2.7 %, which is higher than that for balloon hygrometers but is based on a far larger amount of data and is therefore of higher significance. The standard deviation of the difference (1σ level) is estimated to 3 %. Good agreement between FISH and FLASH-A in reproducing small-scale horizontal structures is demonstrated in Fig. 6.5. Note that since both FISH and FLASH-A were calibrated during the campaign using the same calibration facility, the small statistical discrepancies identified in this intercomparison originate from random measurements errors only.

General intercomparison

In order to estimate the agreement between the observations by aircraft and balloon hygrometers we provide in Tab. 6.3 mean mixing ratios measured by each of the 4 hygrometers during January at 14 - 16 km altitude range – the layer of smallest water variability inside the vortex, as shown by the balloon soundings. Also listed in the table is the standard deviation of the respective data, providing information on the precision of the measurements. The highest value of water vapor is that of CFH and the lowest is that of FISH. The maximum deviation between the data sets amounts to 11 %, which is comparable to the uncertainty limits of all hygrometers. The precision of the measurements varies between 0.09 and 0.21 ppmv.
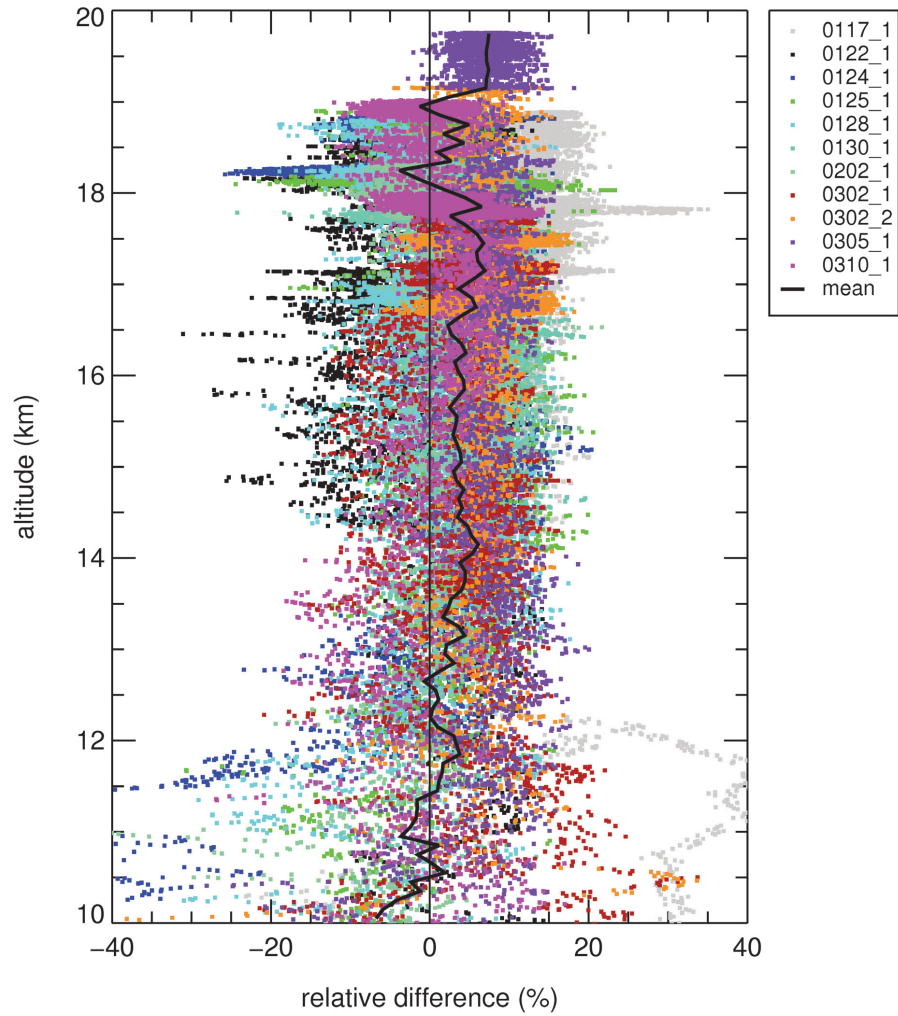
Figure 6.9: Comparison between FLASH-A and FISH based on the measurements of 11 flights, carried out during the RECONCILE campaign: relative mixing ratio difference (100 % (μ_{FLA} - μ_{FISH})/μ_{FLA}) in each flight (markers are colour coded by the flight date as shown in the legend), and mean difference (black line).

Table 6.3: Mean water vapor mixing ratio measured by in situ balloon-borne and aircraft-borne hygrometers during January at 14 - 16 km altitude range.

Hygrometer	Mean H_2O @ 14 - 16 km, ppmv	Standard deviation (1σ), ppmv
CFH	4.40	0.12
FLASH-B	4.20	0.09
FLASH-A	4.14	0.21
FISH	3.93	0.09

Acknowledgments

Chapter 7

Arctic stratospheric cehydration – Part 2: Microphysical modeling

I. Engel[1]**, B. P. Luo**[1]**, S. M. Khaykin**[2,3]**, F. G. Wienhold**[1]**, H. Vömel**[4]**, R. Kivi**[5]**, C. R. Hoyle**[1,6]**, J.-U. Grooß**[7]**, M. C. Pitts**[8] **and T. Peter**[1]

[1] *Institute for Atmospheric and Climate Science, ETH Zurich, Zurich, Switzerland*

[2] *Central Aerological Observatory, Dolgoprudny, Moscow Region, Russia*

[2] *LATMOS-IPSL, Université Versailles St. Quentin, CNRS/INSU, Guyancourt, France*

[4] *Deutscher Wetterdienst, Meteorological Observatory Lindenberg - Richard Aßmann Observatory, Lindenberg, Germany*

[5] *Finnish Meteorological Institute, Arctic Research, Sodankylä, Finland*

[6] *Laboratory of Atmospheric Chemistry, Paul Scherrer Institut, Villigen, Switzerland*

[7] *Institut für Energie- und Klimaforschung - Stratosphäre (IEK-7), Forschungszentrum Jülich, Jülich, Germany*

[8] *NASA Langley Research Center, Hampton, Virginia, USA*

Abstract

Large areas of synoptic-scale ice PSCs distinguished the Arctic winter 2009/2010 from other years and revealed unprecedented evidence of water redistribution in the stratosphere. A unique snapshot of water vapor repartitioning into ice particles was observed under extremely cold Arctic conditions with temperatures around 183 K. Balloon-borne, aircraft and satellite-based measurements suggest that synoptic-scale ice PSCs and concurrent reductions and enhancements in water vapor are tightly linked with the observed de- and rehydration signatures, respectively. In a companion paper (Part 1), water vapor and aerosol backscatter measurements from the RECONCILE and LAPBIAT-II field campaigns have been analyzed in detail. This paper uses a column version of the Zurich Optical and Microphysical box Model (ZOMM) including newly developed NAT and ice nucleation parameterizations. Particle sedimentation is calculated in order to simulate the vertical redistribution of chemical species such as water and nitric acid. Accounting for small-scale temperature fluctuations along the trajectory is essential to reach agreement between simulated optical cloud properties and observations. Whereas modeling only homogeneous nucleation causes the formation of ice clouds with particle radii too small to explain the measured vertical redistribution of water, we show that the use of recently developed heterogeneous ice nucleation parameterizations allows the model to quantitatively reproduce the observed signatures of de- and rehydration.

7.1   Introduction

Polar stratospheric clouds (PSCs) may form in the lower stratosphere above the winter poles at sufficiently low temperatures. Ice PSCs require the coldest conditions, with temperatures about 3 K below the frost point (T_{frost}) to nucleate ice particles homogeneously (Koop et al., 2000). When the particles grow to sizes large enough to sediment, dehydration may occur, i.e. the irreversible redistribution of water vapor, as frequently observed above the Antarctic (e.g. Kelly et al., 1989; Vömel et al., 1995; Nedoluha et al., 2000). Temperatures in the Arctic stratosphere are generally warmer than in the Antarctic stratosphere and therefore the formation of ice PSCs and the occurrence of dehydration events is relatively infrequent. Some observations of ice PSCs and water vapor depleted regions from the coldest Arctic winters are published in the literature (e.g. Fahey et al., 1990; Vömel et al., 1997; Jimenez et al., 2006; Maturilli and Dörnbrack, 2006), however, these studies did not observe such a clear case of vertical redistribution of water vapor as that, which occurred above Sodankylä during the Arctic winter 2009/2010.

This paper presents vertical profiles of water vapor and aerosol backscatter obtained within the framework of the LAPBIAT-II (Lapland Atmosphere-Biosphere Facility) balloon campaign in January 2010 from Sodankylä, Finland. Whereas the majority of Arctic PSC studies describe wave ice cloud observations above Scandinavia (e.g. Carslaw et al., 1998b; Fueglistaler et al., 2003), we present model simulations based on observations of rare synoptic-scale ice clouds. A week-long period (15 January until 21 January) of unusually cold temperatures at stratospheric levels led to the formation of synoptic-scale ice PSCs (Pitts et al., 2011). Balloon-borne measurements of particle backscatter and water vapor on 17 January captured an ice PSC and the concurrent uptake of water from the gas phase in fine detail, providing a high-resolution snapshot of the process of ice PSC formation. A vertical re-

distribution of water inside the vortex, which was tracked remotely and could be quantified again by in situ measurements some five days later, was observed in the Arctic stratosphere for the first time. A companion paper (Khaykin et al., 2013) presents the series of in situ observations in January 2010 above Sodankylä, which coincide with vortex-wide satellite measurements. This study connects two individual balloon soundings by trajectories and simulates the formation, growth and sedimentation of the ice particles.

Very recently, the commonly accepted theories describing the formation mechanisms of PSCs have been revised. Homogeneous freezing of supercooled ternary solution (STS) particles is the generally accepted formation pathway for ice PSCs, requiring a supercooling of $T \lesssim T_{\text{frost}}$ - 3 K (e.g. Koop et al., 1995). The importance of heterogeneous ice nucleation for PSC formation was shown by Engel et al. (2013b), together with a study by Hoyle et al. (2013), which reconciled the current theory of nitric acid trihydrate (NAT) nucleation with observed PSC characteristics.

This paper uses a column version of the Zurich Optical and Microphysical box Model (ZOMM) including the newly developed NAT and ice nucleation parameterizations. Similar to the one dimensional version of ZOMM, the new column version allows the simulation of the nucleation and growth of PSC particles and the associated reduction in water vapor. Additionally, because sedimentation is included, the column version can be used to follow trajectories over longer periods of time and thus allows the simulation of the observed dehydration of the Arctic stratosphere.

In this study, we examine the effect of different nucleation mechanisms, in particular homogeneous vs. heterogeneous ice formation, as well as temperature fluctuations, on PSC properties. The overall goal of this work is to compare the modeled microphysics with the observations and thus test the newly proposed heterogeneous ice nucleation parameterizations. We show that in order to successfully reproduce the observed dehydration and rehydration, heterogeneous nucleation and temperature fluctuations must be accounted for in the model.

7.2 Methods

The following section provides a short overview of the measurement techniques used to obtain the data for this study. Furthermore, the trajectory calculation tool and the microphysical column model are characterized. A more comprehensive description of the different instruments is given in the companion paper by Khaykin et al. (2013).

7.2.1 Backscatter measurements

Backscatter measurements from balloon- and spaceborne instruments are utilized in this work. The Compact Optical Backscatter Detector (COBALD) is a backscatter sonde, engineered at ETH Zurich, complementing operational weather balloon payloads. The sonde is a follow up development of the backscatter sonde designed by Rosen and Kjome (1991). Two LEDs emitting at wavelengths of 455 nm and 870 nm are aligned in parallel and located to the left and right of a silicon detector. The light scattered back by air molecules, aerosols, and cloud particles is recorded with a typical frequency of 1 Hz. The data analysis follows Rosen and Kjome (1991) to separate the individual contributions

from molecules and aerosols to the measured backscatter signal. The molecular air number density is derived from temperature and pressure recorded simultaneously by the radiosonde hosting COBALD. A direct indicator for the presence of aerosols is the backscatter ratio (*BSR*): it is defined as the ratio of the total (aerosol and molecular) to the molecular backscattered light intensity (at ∼ 180back to the detector). Accordingly, the aerosol backscatter ratio is equal to *BSR* - 1. COBALD has already been applied in several different field studies, e.g. measuring the volcanic aerosol plume after the eruption of the Eyjafjallajökull (Bukowiecki et al., 2011) and cirrus clouds (Brabec et al., 2012; Cirisan et al., 2013).

The Cloud-Aerosol Lidar and Infrared Pathfinder Satellite Observations (CALIPSO) satellite provides profiling measurements of cloud and aerosol distribution and properties obtained by the Cloud-Aerosol Lidar with Orthogonal Polarization (CALIOP). The satellite completes 14.5 orbits per day and has a near-global coverage, ranging from 82 to 82 S (Winker et al., 2007). CALIPSO's orbit inclination and its associated extensive polar coverage make the satellite an ideal platform for PSC observations. For this purpose, Pitts et al. (2007) introduced a detection algorithm to identify and further classify PSCs. Their composition classification is based on *BSR* at a wavelength of 532 nm and aerosol depolarization ($\delta_{\mathrm{aerosol}}$) obtained from the CALIOP Level 1B Data Product. The data is averaged to a uniform grid with a horizontal resolution of 5 km and a vertical resolution of 180 m. Pitts et al. (2011) distinguish six different PSC composition classes with varying number densities of liquid, NAT, and ice particles.

7.2.2 Water vapor and nitric acid measurements

Balloon-borne water vapor measurements are obtained by two different techniques. The Fluorescence Lyman-Alpha Stratospheric Hygrometer for Balloons (FLASH-B) is a Russian water vapor instrument developed at the Central Aerological Observatory (Yushkov et al., 1998). The fluorescence method uses the photodissociation of H_2O molecules exposed to Lyman-alpha radiation followed by the measurement of the fluorescence of the resulting excited OH radicals (Kley and Stone, 1978). The intensity of the fluorescent light sensed by the photomultiplier is directly proportional to the water vapor mixing ratio under stratospheric conditions (10 hPa to 150 hPa). The second instrument used within this study is the Cryogenic Frost point Hygrometer (CFH), which was developed at the University of Colorado (Vömel et al., 2007a). The instrument's principle is based on a chilled mirror. The temperature of the mirror can be regulated such that a thin but constant layer of frozen condensate covers the surface. The thickness of the frozen layer is controlled by a photodiode connected to an LED. The photodiode measures variations of the reflected light caused by changes in the thickness of the condensate, which feeds back into the regulation of the mirror temperature. Under these conditions, T_{frost} of the surrounding air is equal to the mirror temperature. The reported overall uncertainty for both instruments in the middle stratosphere is less than 10 % (Vömel et al., 2007b).

Water vapor and nitric acid were measured using the Microwave Limb Sounder (MLS) aboard the Aura satellite. MLS provides atmospheric profiles of temperature and composition (including H_2O and HNO_3) via passive measurement of microwave thermal emission from the limb of the Earth's atmosphere (Waters et al., 2006). Vertical scans are performed every 25 seconds, corresponding to a distance of 165 km along the orbit track. Vertical and horizontal along-track resolutions are 3.1 km to 3.5 km and 180 km to 290 km, respectively, for H_2O, and 3.5 km to 5.5 km and 400 km to 550 km for

HNO_3. Aura flies in formation with CALIPSO in the A-train satellite constellation and CALIOP and MLS measurement tracks are closely aligned. The spatial and temporal differences are less than 10 km and 30 s after a repositioning of the Aura satellite in April 2008 (Lambert et al., 2012). MLS water vapor profiles presented in this study are interpolated to the CALIOP PSC grid using a weighted average of the two nearest MLS profiles (Pitts et al., 2013). Typical single-profile precisions of the MLS version 3.3 measurements (Livesey et al., 2013) are 4 % to 15 % for H_2O (Read et al., 2007; Lambert et al., 2007) and 0.7 ppbv for HNO_3 (Santee et al., 2007).

7.2.3 Trajectory calculation

The trajectories used within this study are calculated from six-hourly wind and temperature fields of the ERA-Interim reanalysis produced by the ECMWF (Dee et al., 2011), with a horizontal resolution of 1×1 We used the trajectory module of the Chemical Lagrangian Model of the Stratosphere (CLaMS) (McKenna et al., 2002) to calculate trajectories for the microphysical study. Vertical velocities are derived from ERA-Interim total diabatic heating rates (Ploeger et al., 2010). Starting at 19:47 UTC on 17 January 2010, a balloon sounding was performed from Sodankylä (hereafter referred to as S1). Individual balloon positions along its pathway at pressure levels < 100 hPa served as start points for the first set of trajectory calculations. With a vertical distance of 100 m between two trajectories, two-day backward and three-day forward trajectories with time steps of 15 minutes were computed. A second sonde was launched on 23 January 2010 at 17:30 UTC (hereafter referred to as S2), for which three-day backward and two-day forward trajectories in the same altitude range as for the first sounding have been calculated. Figure 7.1 illustrates the pathways of two exemplary trajectories for each sounding within the Arctic vortex. It is apparent that Sodankylä was located in the cold pool, while upstream the air had been by more than 10 K warmer. On 17 January Sodankylä was at the edge of a larger area of synoptic-scale ice clouds seen by CALIOP.

As the sedimentation scheme in the microphysical column model (described in detail in Sect. 7.2.4) cannot account for wind shear, changes in wind velocity with altitude lead to errors in the location of the sedimentation events. The 440-K and 520-K trajectories are about 3 km apart in altitude. At a point 12 hours downstream of S1, the distance between these trajectories started at potential temperatures of 520 K (cloud top) and 440 K (cloud base) is about 350 km. This distance is within the area of ice PSC with consistent cold temperatures, and as the modeled sedimentation takes place within these first 12 hours, the wind shear has only a moderate effect on the results.

Pressure and temperature from the joined backward and forward trajectories constitute the meteorological input for the microphysical model. Additionally, information about total water and nitric acid mixing ratios is needed at the upstream end of the trajectories. For S1, HNO_3 values were taken from MLS, averaged for the corresponding day over cloud-free areas within the vortex and vertically interpolated to the starting pressure of the trajectories. Vertically resolved climatological mean values for January were used as H_2O input. The H_2O profile is calculated from ice cloud free measurements conducted above Sodankylä, between 1996 and 2013, using the NOAA frost point hygrometer and the CFH (see Khaykin et al. (2013) for more details). The climatological mean, which excludes the single dehydration measurement from 23 January 1996 (Vömel et al., 1997), is shown below. Simulations of S2 were initialized with the H_2O profile from S1 at $t = 21$ days. Even though a horizontal displacement
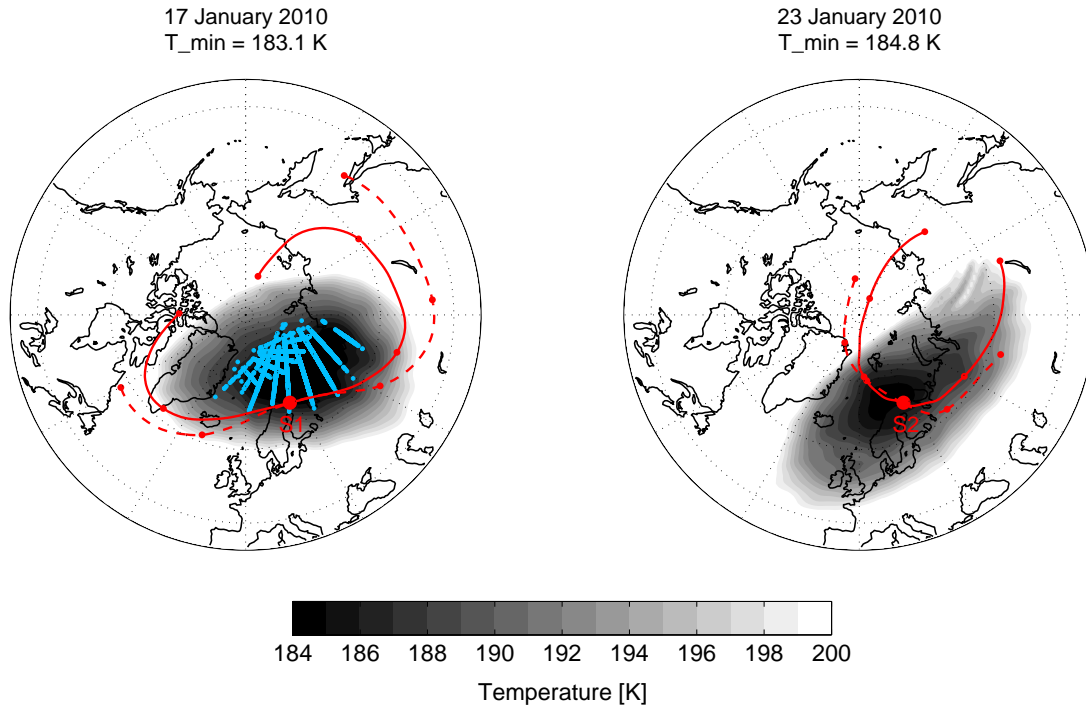
Figure 7.1: Polar maps with ERA-Interim temperatures at 30 hPa (grayscale) on 17 January 2010 (left) and 23 January 2010 (right). Red curves: CLaMS trajectories starting on the corresponding day above Sodankylä at 520 K (solid) and 440 K (dashed) potential temperature. Trajectories are two days backward and three days forward in time for 17 January 2010 (S1) and three days backward and two days forward in time for 23 January 2010 (S2). Red dots: 24-h time periods along the trajectories. Cyan points: ice clouds observed by CALIOP on 17 and 18 January 2010 between 16 km and 30 km altitude. No ice clouds have been observed by CALIOP on 23 January 2010.

exists between the individual trajectory end and start points of S1 and S2, respectively, the approach is justified given the temperature distribution on vortex scale: at points, where trajectories are matched, temperatures were above 200 K, ensuring cloud-free air and thus no change in the H_2O distribution.

Trajectory temperatures were corrected according to Fig. 7.2, showing temperature deviations between ERA-Interim reanalysis data and measurements, taken by the Vaisala RS-92 on S1. The total measurement uncertainty for the temperature sensor is 0.5 K with an accuracy of 0.3 K between 100 hPa and 20 hPa as specified by Vaisala. Between 32 hPa and 25 hPa, ERA-Interim temperatures were more than 1.5 K too warm compared to the measured temperatures. The temperature deviation coincides with the observed ice cloud, which cannot be reproduced using original ERA-Interim temperatures, as shown below. Assuming that the temperature difference is caused by a local cold pool not resolved in the ERA-Interim data, temperatures along the trajectories were changed only within a short time window around the observation. The amplitude of the applied temperature correction is assumed to decrease (using a sine curve) with increasing distance from the observation (vertical red line in Fig. 7.2c) and equals zero 12 hours before and after the observation. Figure 7.2c illustrates an exemplary trajectory without (black dashed line) and with (red solid line) applied temperature correction. In the absence of better knowledge, the maximum amplitude is assumed to occur at the sonde flight path and is assumed to be altitude dependent as shown in Fig. 7.2b (red line).
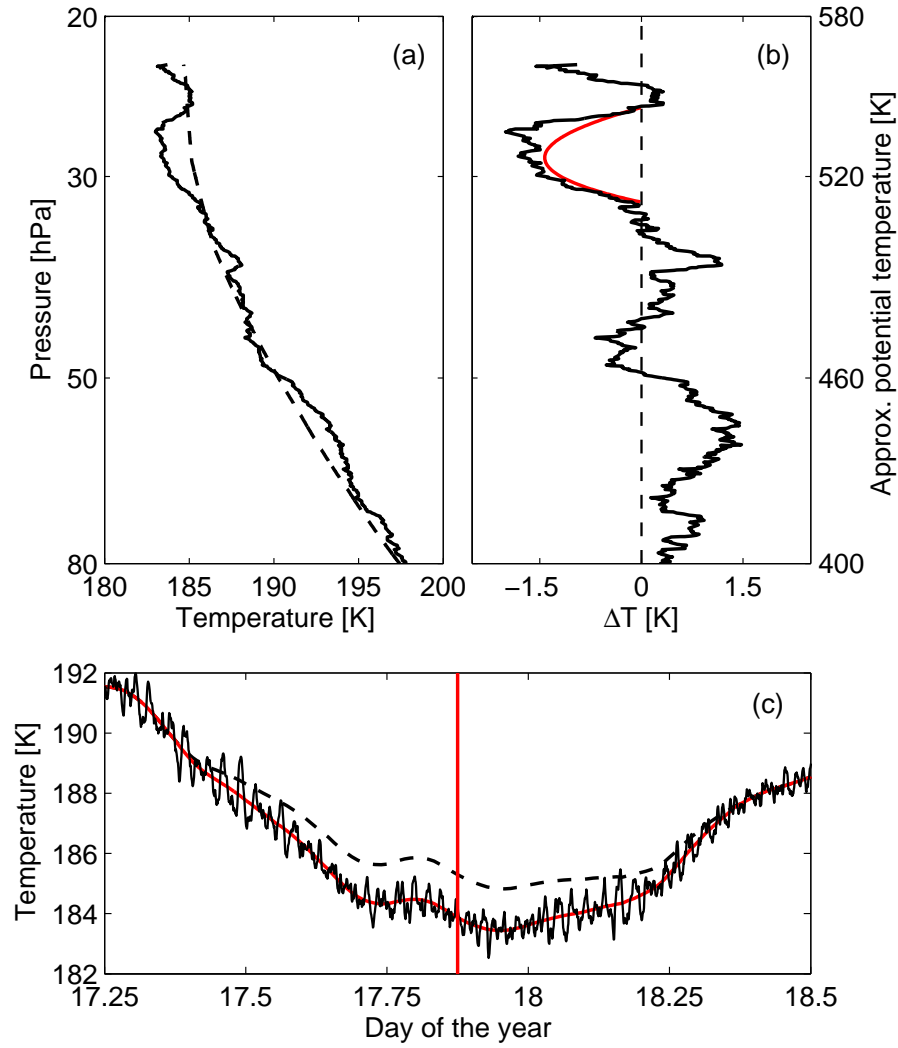
Figure 7.2: (a) Solid line: Temperatures measured with the Vaisala RS-92 radiosonde on 17 January 2010 above Sodankylä. Dashed line: ERA-Interim reanalysis temperatures interpolated in time and space to the position of the balloon. (b) Difference between measurement and ERA-Interim as shown in panel (a). Red line: temperature correction applied to the trajectories between 32 hPa and 25 hPa. (c) Black dashed line: Exemplary ERA-Interim trajectory at 29 hPa. Red solid line: ERA-Interim trajectory with temperature correction. Black solid line: ERA-Interim trajectory with temperature correction and superimposed small-scale fluctuations. See text for details.

Small-scale temperature fluctuations

Early studies (e.g. Murphy and Gary, 1995; Kärcher and Lohmann, 2003; Hoyle et al., 2005) have investigated the effect of rapid temperature fluctuations and associated high cooling rates on ice cloud formation and properties. Cooling rates of less than one Kelvin per hour favor the growth of preexisting ice particles and total number densities of ice particles remain low. In contrast, high cooling rates of several Kelvin per hour can produce supersaturations high enough to nucleate a major fraction of the stratospheric background aerosol. Gary (2006) found that a significant component of the short-term vertical displacements of isentropic surfaces remains unresolved also by current numerical weather

prediction models. Recent microphysical modeling studies confirmed the importance of an adequate representation of cooling rates for cirrus (Brabec et al., 2012; Cirisan et al., 2013) and polar stratospheric clouds (Engel et al., 2013b). We follow the same approach chosen in these studies and make use of the vertical velocity and temperature time series obtained from the SUCCESS (Subsonic Aircraft: Contrail and Cloud Effects Special Study) data analyzed by Hoyle et al. (2005) to conduct model runs along trajectories with superimposed temperature fluctuations. Only wavelengths < 400 km were considered, which are not resolved in the ERA-Interim wind fields used in our trajectory calculations. The temperature fluctuations are assumed to have a mean amplitude of about ± 0.5 K and were superimposed onto the synoptic-scale trajectories with random frequencies and a temporal resolution of 1 second as seen in Fig. 7.2c (black solid line). A more detailed description of the method can be found in Engel et al. (2013b).

7.2.4   Microphysical column model

The new column version of the Zurich Optical and Microphysical box Model (ZOMM) with implemented heterogeneous ice and NAT nucleation rates is used to simulate the formation, evolution and sedimentation of ice particles along trajectories. The underlying model, utilized for PSC simulations, has been described by Meilinger et al. (1995) and Luo et al. (2003b) and recently extended by Hoyle et al. (2013) and Engel et al. (2013b). The following section provides an overview and the details of the modifications made to ZOMM for the purposes of this study.

ZOMM can be initialized with a log-normally distributed population of supercooled binary solution (SBS) droplets, described by a mode radius, number density and distribution width, typical for winter polar stratospheric background conditions (Dye et al., 1992). Driven by temperature and pressure data along trajectories, the uptake and release of nitric acid and water in ternary solution droplets is determined. The total amounts of H_2O, H_2SO_4 and HNO_3 contained in the air parcel are set at the beginning of the trajectory and subsequently remain constant. Distributed across 26 radius bins when the model is initialized, droplets are henceforward allowed to grow and shrink in a fully kinetic treatment and without being restricted to the initial log-normal shape of the distribution (Meilinger et al., 1995). The formation of solid particles results in an initiation of additional size bins. Homogeneous ice nucleation in STS droplets is calculated as well as heterogeneous nucleation of ice on foreign nuclei and NAT surfaces. NAT nucleation is implemented as deposition nucleation on ice particles and as immersion freezing on foreign nuclei (e.g. meteoritic dust). Whereas homogeneous ice nucleation, following Koop et al. (2000), and NAT nucleation on uncoated ice surfaces, described in detail in Luo et al. (2003b), have been accepted pathways of PSC formation for many years now, the possibility of PSC formation via heterogeneous ice and NAT nucleation on foreign nuclei (e.g. Tolbert and Toon, 2001; Drdla et al., 2002; Voigt et al., 2005) had until previously only a narrow observational data basis so that definitive conclusions about nucleation rates were not possible, and also any clear support from laboratory measurements was lacking (see detailed discussion by Peter and Grooß, 2012). The observational impasse has been overcome recently by the wealth of CALIOP PSC observations on NAT and ice PSCs obtained in the winter 2009/2010 (Pitts et al., 2011), which unmistakably suggests that both particle types must have nucleated heterogeneously. A heterogeneous nucleation mechanism, occurring on preexisting particle surfaces, e.g. on meteoritic particles, has been developed to explain

CALIOP PSC observations over the Arctic in December 2009 and January 2010. The parameterizations, based on active site theory (Marcolli et al., 2007), for NAT and ice are given in Hoyle et al. (2013) and Engel et al. (2013b), respectively. These studies used ZOMM in a pure box model configuration and limitations caused by neglecting sedimentation of NAT and ice particles in the winter polar stratosphere were already pointed out by these authors.

For the present study, we developed the stratospheric version of ZOMM further into a column model similar to the existing cirrus column version of ZOMM (e.g. Luo et al., 2003a; Brabec et al., 2012; Cirisan et al., 2013). Sedimentation of ice and NAT particles is realized in a Eulerian scheme, allowing particles to sediment within the advected column from one box to the next lower one. For the present study the column consists of a stack of 100-m thick boxes and the timestep for sedimentation is 15 minutes. Once ice or NAT particles grow to sizes large enough to sediment, the appropriate fraction of particles is removed from its current box and, according to its size-dependent sedimentation speed, injected into the next lower box. This is done in a way that the number and mass of the particles are conserved. Strictly speaking, such an approach is only possible in situations without horizontal or vertical wind shear. The case investigated in this study is sufficiently close to meeting these criteria, as the column of air parcels rotates with the polar vortex (compare Fig. 7.1).

The optical properties of the simulated PSCs are calculated using Mie and T-Matrix scattering codes (Mishchenko et al., 2010) to compute optical parameters for size-resolved number densities of STS, NAT and ice. The refractive index is 1.31 for ice and 1.48 for NAT. Following Engel et al. (2013b), both crystals are treated as prolate spheroids with aspect ratios of 0.9 (diameter-to-length ratio).

7.3 Observations

The Arctic winter 2009/2010 was characterized by a week-long period of unusually cold temperatures in the lower stratosphere. From 15 to 21 January, temperatures below T_{frost} led to widespread synoptic-scale ice PSCs, which were observed by CALIOP (Pitts et al., 2011). The balloon sonde S1 equipped with COBALD and FLASH-B (besides ozone, meteorological parameters and GPS) was launched from Sodanklyä on 17 January 2010 at 19:47 UTC (Khaykin et al., 2013). At about 21 UTC the balloon reached its point of burst and the payload began its descent. COBALD and FLASH-B profiles measured during the descent are shown in Figs. 7.3 and 7.4, respectively. Particle backscatter ratios and the simultaneously captured reduction in water vapor reveal three distinct layers of ice particles. Maximum backscatter ratios at 870 nm reach 200 at a potential temperature of 510 K and mark the clearly defined upper edge of the lowest ice layer. The ice layers are embedded in a cloud of supercooled ternary solution (STS) droplets extending from 440 K upwards and identified by the backscatter increase from the background level below.

A vortex wide change in PSC composition occurred on 22 January together with the onset of a major warming, and CALIOP measurements after this time showed predominantly liquid PSCs (Pitts et al., 2011). An unprecedented measurement of vertical redistribution of water followed on 23 January 2010. Sonde S2 with COBALD and CFH was launched at 17:30 UTC (Khaykin et al., 2013). A stratospheric layer of irreversibly dehydrated air was measured at potential temperatures above 470 K. The reduction in water vapor of 1.6 ppmv was observed in essentially cloud free air with backscatter ratios

below 5 at 870 nm. Even though temperatures at this level were as cold as on the 17 January, no ice cloud formed due to the reduced amount of H_2O and hence a depression of T_{frost}. A clear signal of re-hydration was detected below this layer (between 450 K and 470 K). The enhancement in water vapor of about 1 ppmv above climatological mean conditions coincided with COBALD backscatter measurements of up to 20. Backscatter values from COBALD suggest the existence of liquid particles and NAT in this layer, which is consistent with the CALIOP observations.

7.4   Microphysical analysis

To analyze differences in PSC properties resulting from homogeneous or heterogeneous ice nucle-ation as well as from changes in temperatures and cooling rates, we performed various simulations with different initial conditions. The results with the best agreement between simulated and observed PSC properties are shown in Figs. 7.3 and 7.4. This simulation accounted for homogeneous ice nucle-ation, heterogeneous nucleation of NAT and ice on foreign nuclei as well as the nucleation of ice on preexisting NAT particles and the nucleation of NAT on preexisting ice particles. Small-scale temper-ature fluctuations needed to be superimposed onto the trajectories in order to reproduce the obser-vations.

7.4.1   Direct measurement-model comparison

The comparison of measured and simulated optical properties, namely BSR and $\delta_{aerosol}$, is presented in Fig. 7.3. Here, the modeled temporal evolution of BSR at 532 nm along the trajectories is shown in Panels a and d as a function of potential temperature. We started trajectories backward and forward in time as described in Sec. 7.2.3 along the descent of S1 (FLASH-B and COBALD) and the ascent of S2 (CFH and COBALD). A discussion about the availability of FLASH-B and CFH and about the data quality during ascent and descent can be found in our companion paper (Khaykin et al., 2013). Both vertical profiles have been compared to balloon and satellite-borne measurements. Their approxi-mate observation time is indicated by vertical red lines in the upper panels. Their exact position is equal to the position of S1 and S2, respectively. Panel b shows modeled and observed backscatter for the initial sounding S1 on 17 January and Panel e for S2, the sounding which took place on 23 Jan-uary 2010. Panel c and f show satellite measurements, a 25 km mean around the profile closest in time and space to the corresponding balloon sounding from Sodankylä. Whereas CALIPSO and Aura were ~ 500 km far from Sodankylä with a time difference of 3 hours between the individual measurements on 17 January, measurements on the 23 January have a horizontal displacement of only ~ 100 km but a 6 hour time lag. All measurements are shown in black, simulations in red. Figure 7.4 presents the corresponding results for water vapor. Simulated NAT and ice number densities as well as their mean radii are presented in Fig. 7.5, which shows various scenarios with respect to nucleation mechanisms and will be explained in detail below. (The rightmost column of Fig. 7.5 depicts the scenario from which Figs. 7.3 and 7.4 were derived.)

Temperatures above the existence temperature of NAT (T_{NAT}) ensure sub-saturated conditions (i.e. no PSCs) at the beginning of the simulation. Within the first 48 hours after the start of the simulation, a significant enhancement in BSR indicates the formation of a cloud. At $t \sim 17.5$ days, temperatures
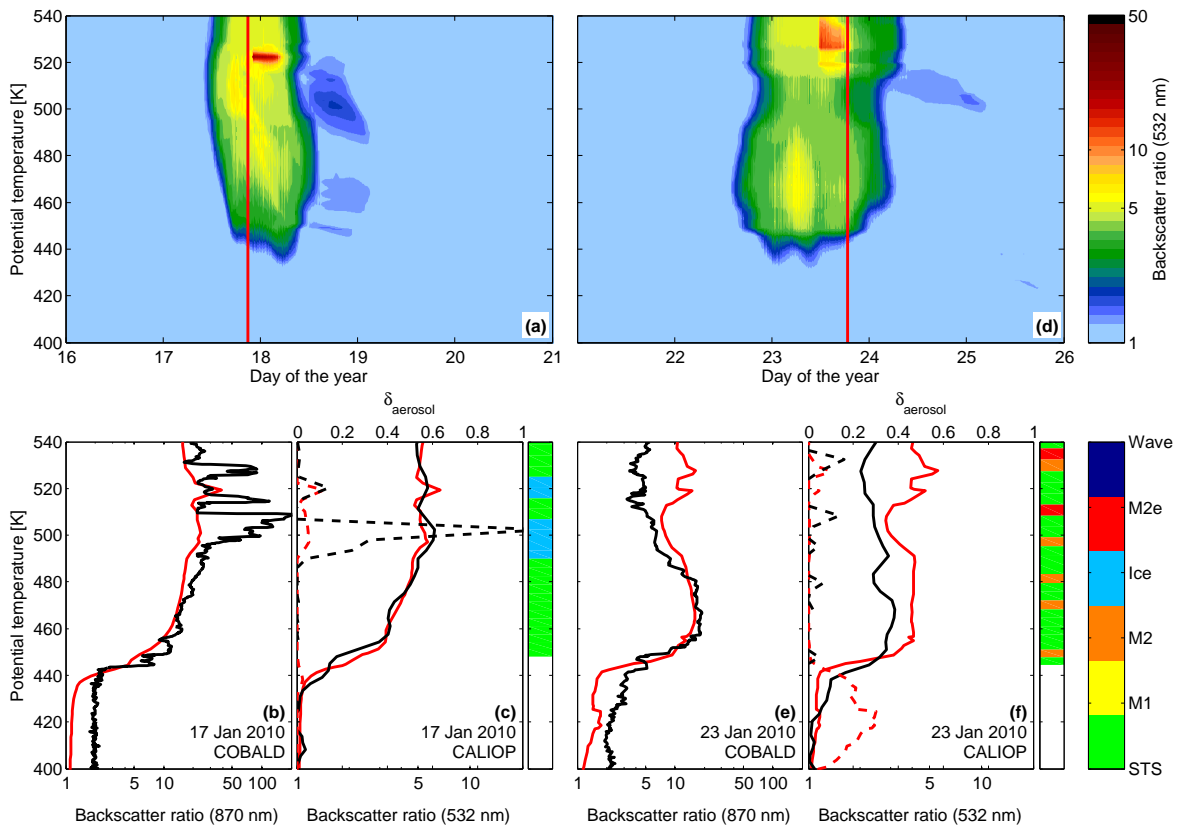
Figure 7.3: Results from the microphysical column model ZOMM driven by ERA-Interim based CLaMS trajectories with superimposed small-scale temperature fluctuations. Upper panels (a,d): Time series of backscatter ratios *BSR* at 532 nm (color coded). Vertical red lines: S1 and S2. Lower panels: Comparison between simulations (red) and measurements (black), namely COBALD *BSR* at 870 nm (b,e) and CALIOP *BSR* (solid) and depolarization (dashed) at 532 nm (c,f). Color bars: PSC classification scheme according to Pitts et al. (2011) for CALIOP observations. CALIOP data are from orbits 2010-01-18T00-19-57Z (c) and 2010-01-24T01-22-07Z (f) closest to Sodankylä.

become low enough to permit first NAT nucleation on preexisting particle surfaces. NAT number densities of 10^{-3} cm^{-3} lead to a small but visible increase in *BSR*. With decreasing temperatures, STS particles grow through uptake of HNO$_3$ from the gas phase and contribute significantly to a continuous increase of *BSR*. The onset of reduced water vapor mixing ratios shortly before the point of observation is shown in Fig. 7.4 and marks the formation of ice particles. The comparison between simulated vertical backscatter profiles (red) with those measured by COBALD (black line in Fig. 7.3b) shows a reasonable agreement. However, small-scale structures of enhanced *BSR* seen by COBALD are only partly reflected and *BSR* values stay below the maximum detected by COBALD. *BSR* values as large as 200 (at 870 nm) are possible to simulate by choosing a slightly different phase of a fluctuation as seen in the presentation of the ensemble runs below. As Fig. 7.3c shows, CALIOP measurements (black line) are represented extremely well. Simulated $\delta_{aerosol}$ values are enhanced in the same altitude region as in the CALIOP observations, but values of $\delta_{aerosol}$ measured by CALIOP fluctuate more strongly producing "jumps" between the ice and STS class (compare dashed lines in Fig. 7.3c). Even though
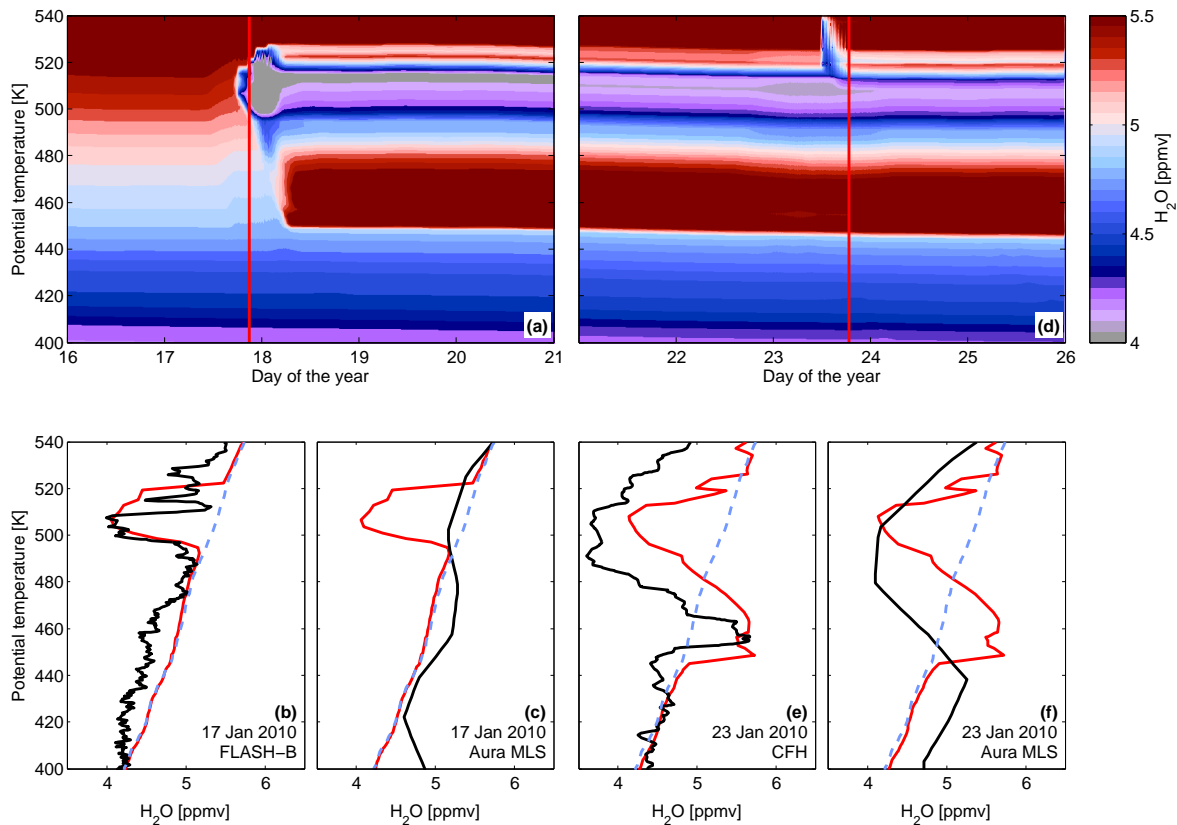
Figure 7.4: Results from the microphysical column model ZOMM driven by ERA-Interim based CLaMS trajectories with superimposed small-scale temperature fluctuations. Upper panels (a,d): Time series of water vapor mixing ratios (color coded). Vertical red lines: S1 and S2. Lower panels: Comparison between simulations (red) and measurements (black), namely FLASH-B (b), CFH (e) and MLS (c,f). Dashed line in lower panels (b,c,e,f): Climatological mean water vapor profile. MLS data are interpolated to orbits 2010-01-18T00-19-57Z (c) and 2010-01-24T01-22-07Z (f) closest to Sodankylä.

instrumental noise and the lower resolution might be an explanation for this behavior, the COBALD measurements suggest that fluctuations in the cloud composition profile are possible. A perfect anti-correlation between the profiles of *BSR* and H_2O (black lines in Fig. 7.3b and Fig. 7.4b) suggests an ice cloud and the corresponding depletion in the vapor phase, both strongly layered. The small color bar next to the vertical profiles denotes the results from the CALIOP particle classification scheme, suggesting clear layers of ice embedded in a broader liquid PSC. Simulated ice number densities in the core of the cloud lie between $10^{-3}\,\mathrm{cm}^{-3}$ and $10^{-2}\,\mathrm{cm}^{-3}$, leading to a maximum *BSR* at 532 nm of almost 7. In Fig. 7.3a, downwind of S1, homogeneous ice nucleation sets in and higher ice number densities between $0.1\,\mathrm{cm}^{-3}$ and $1\,\mathrm{cm}^{-3}$ are simulated. Those high number densities cause an increase in *BSR* by a factor of 3.5. The part of the ice cloud with the highest *BSR* values is followed by a tail of moderate *BSR* upon warming, whereas elsewhere *BSR* values are much smaller. This tail consists of NAT particles (see Fig. 7.5) that nucleated on the ice cloud, forming a NAT cloud of class "Mix2" and "Mix2-enh", as first described by Carslaw et al. (1998a).
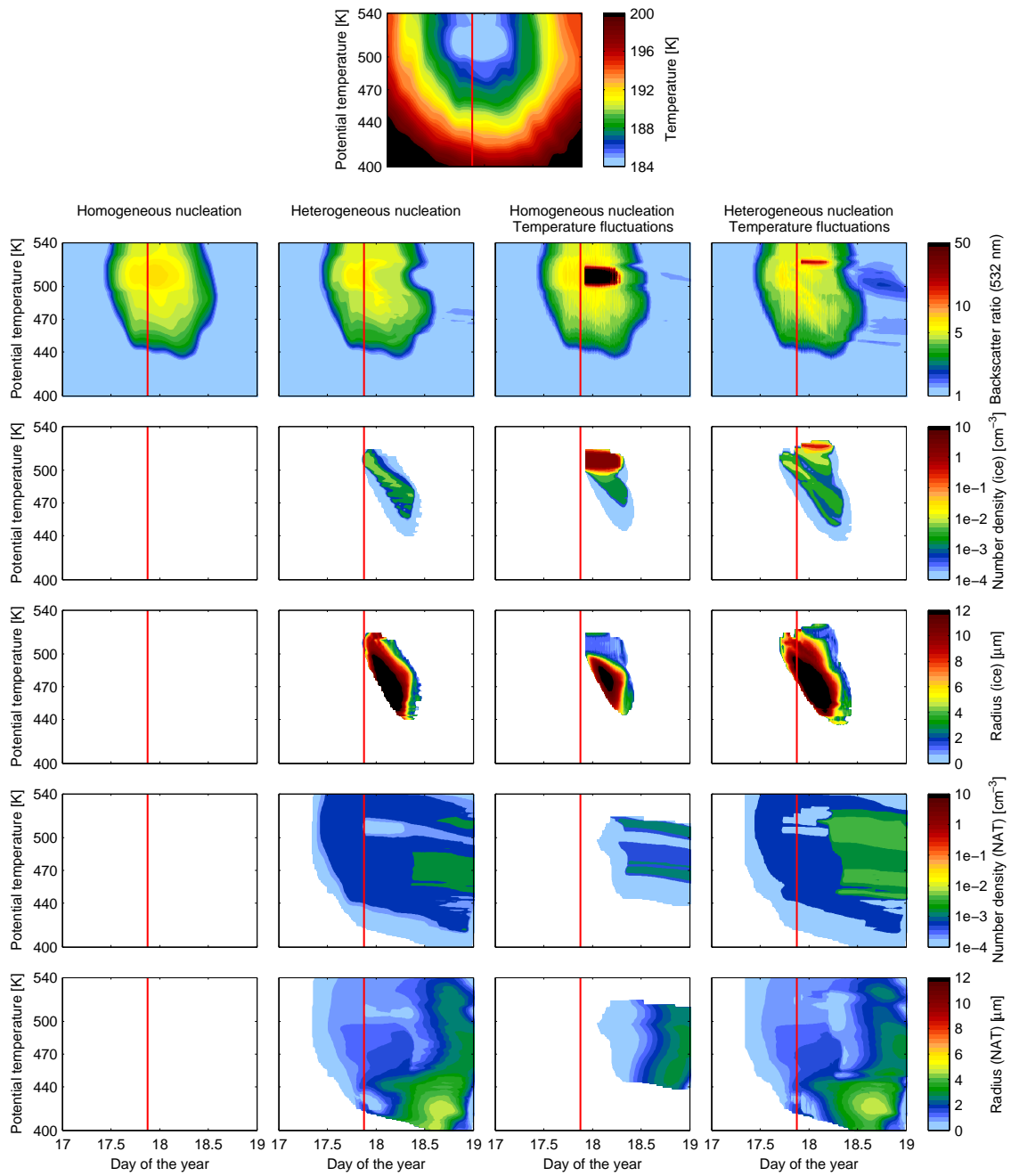
Figure 7.5: Results from the microphysical column model ZOMM driven by ERA-Interim based CLaMS trajectories (17 - 19 January 2010). Vertical red line: S1. Top panel: ERA-Interim temperatures (temperature correction applied). Rows: Backscatter ratios at 532 nm, ice and NAT number densities and radii. Columns: four different scenarios. Column 1: only homogeneous nucleation of ice; no superimposed temperature fluctuations. Column 2: same, but in addition allow for heterogeneous nucleation. Column 3: only heterogeneous nucleation of ice, but with superimposed small-scale temperature fluctuations. Column 4: with both. Homogeneous simulations include homogeneous ice nucleation and NAT nucleation on preexisting ice particles only. Heterogeneous model runs include in addition heterogeneous ice and NAT nucleation on foreign nuclei.

The magnitude of the H_2O reduction in the gas phase observed by FLASH-B is roughly captured by the simulations. Again, fine-scale structures are not reproduced by the model (Fig. 7.4b). The resolution of MLS is too coarse to capture the local reduction in H_2O at this time (Fig. 7.4c). Ice particles evaporate already 12 hours after the FLASH-B observation and a clear and permanent redistribution of H_2O becomes visible at $t \sim 18.5$ days in Fig. 7.4a, which remains visible until the end of the simulation.

Close to the second observation, temperatures drop again and reach values almost as cold as on the 17 January. However, the reduction in H_2O prevents the formation of ice clouds in the model, except at levels above 520 K. Also the magnitude of *BSR* from COBALD and CALIOP would not suggest an ice cloud. Values of *BSR* remain smaller than they were on 17 January and CALIOP observations suggest a predominantly liquid cloud with few embedded NAT particles. The NAT signal is partially obscured by the strong STS signal (Fig. 7.3f). The comparison between modeled and observed H_2O reveals that even though the model captures signatures of de- and rehydration, the vertical extent of the dehydrated air remains too small in the simulation. The simulated maximum reduction in water vapor of -1.4 ppm at 514 K is almost as large as observed by CFH. However, the dehydrated region is smaller and ranges only from 485 K to 525 K. A possibility for the underestimated vertical extend of dehydrated air in the simulation might again be the temperature profile. Figure 7.2b shows that ERA-Interim temperatures are too warm compared to the observation also at the top of the sounding, which prevents the formation of ice particles above 525 K. The resulting availability of H_2O at high altitudes offers the possibility for ice formation on the 23 January 2010 in our simulation, whereas CALIOP observations documented the last ice clouds in the vortex on 21 January (Pitts et al., 2011). Finally, clear signatures of de- and rehydration are also visible in the MLS profile (Fig. 7.4f), which reveal that the redistribution of water is a large-scale phenomenon.

Figure 7.5 compares simulations using four different scenarios. The top panel shows ERA-Interim temperatures, which were corrected according to the measured temperature profile of S1 (compare Sec. 7.2.3 and Fig. 7.2) and provide the basis for all four simulations. The first scenario (Fig. 7.5, 1st column), which accounts only for homogeneous ice nucleation, cannot explain the observations at all. Supersaturations with respect to ice remain too small and since no ice particles form, NAT particles cannot form either. The second scenario (Fig. 7.5, 2nd column), which includes heterogeneous nucleation of ice and NAT particles according to Engel et al. (2013b) and Hoyle et al. (2013), changes the model results completely. Ice supersaturations are sufficient for heterogeneous nucleation of 10^{-3} cm^{-3} ice particles. Within a short time, these particles grow to sizes $> 12\,\mu$m in radius. With a settling velocity between $100\,\text{m}\,\text{h}^{-1}$ and $200\,\text{m}\,\text{h}^{-1}$, ice particles can sediment up to 2 km before evaporation. The third scenario (Fig. 7.5, 3rd column) shows that the superposition of small-scale temperature fluctuations on the synoptic trajectories leads to ice formation even in the homogeneous freezing case. However, this result does not agree with the observations, because the nucleation of high ice number densities (between $1\,\text{cm}^{-3}$ and $10\,\text{cm}^{-3}$) prevents the growth of ice particles to sizes which could sediment fast enough to achieve a satisfying agreement with the observations (maximum sedimentation distances of only a few hundred meters). The final scenario (Fig. 7.5, 4th column) includes both, heterogeneous nucleation and superimposed small-scale temperature fluctuations. The inclusion of heterogeneous nucleation in this simulation causes NAT to form prior to ice. Consequently, those NAT particles are assumed to be enclosed by ice and redistributed by the subsequent growth and sedimentation of the ice particles. We will discuss this point further below. Additionally,

the nucleation of ice particles starts earlier than in all other cases and the fluctuations enable a larger ice cloud area to be generated.

7.4.2   Ensemble calculations for stochastic impact of temperature fluctuations

Figures 7.3 - 7.5 showed the comparison between the measurements and the ZOMM calculations for one particular set of small-scale temperature fluctuations. The properties of the NAT and ice clouds depends on the exact cooling rates in the moment of the nucleation of the NAT and ice particles, because this dictates the nucleation rates. This happens at the place of cloud formation somewhere upstream of the measurements and is principally unknown to us. At the best we have an idea of the statistical nature of the small-scale temperature fluctuations, which determine the cooling rates and thus the resulting cloud morphology. Therefore, ensemble calculations applying different sets of small-scale temperature fluctuations need to be performed, in order to retrieve the dependence of PSC properties on the stochastic effects caused by the fluctuations. Cirisan et al. (2013) have performed similar calculations for cirrus clouds.

Figure 7.6 presents a comparison of profiles of *BSR* and ΔH_2O for various scenarios with and without heterogeneous nucleation and with 10 different sets of small-scale temperature fluctuations. *BSR* profiles for 17 January are presented in the upper four panels, ΔH_2O profiles for 23 January are shown in the lower four panels. The model results, which have already been described above and shown in Figs. 7.3 - 7.5, correspond to the red curves while the other nine members are shown as gray area. The red curves also represent the particular member which produced the best agreement with the measurements in terms of dehydration.

As expected, no signatures of de- or rehydration are visible if only homogeneous ice nucleation and synoptic-scale temperatures are applied. The lower row shows that an improved agreement between CFH and the simulation can only be achieved if heterogeneous ice nucleation or small-scale temperature fluctuations are included, or both. However, when heterogeneous nucleation is included but not the small-scale temperature fluctuations (2nd column), modeled values of *BSR* remain too small in comparison with COBALD *BSR* values. Conversely, combining homogeneous nucleation and the superposition of small-scale temperature fluctuations improves the modeled backscatter, but generates an irregular signature of two layers of dehydration (red curve in 3rd column). The combination of both, heterogeneous ice nucleation and superimposed small-scale temperature fluctuations, combines the improvement in terms of *BSR* values with clear signatures of de- and rehydration, which agree well with the measurements (red curve in 4th column). Particular choices of fluctuations can generate *BSR* values as large as the spikes observed by COBALD during sounding S1. This demonstrates that different fluctuations generate different ice number densities, and this in turn leads to different backscatter ratios and dehydration strengths. In passing we note, that the spikes in *BSR* observed during S1 represent onsets of wave ice embedded in a synoptic ice cloud. The spikes contain ice crystals in high number density, which cannot grow to large sizes and thus cannot explain the vertical redistribution of water observed about a week later. Therefore, those ensemble members, which represent the highest BSR measurements best, lead only to shallow denitrification. Rather, it is the synoptic scale ice clouds with moderate ice concentrations which cause the most efficient dehydration.
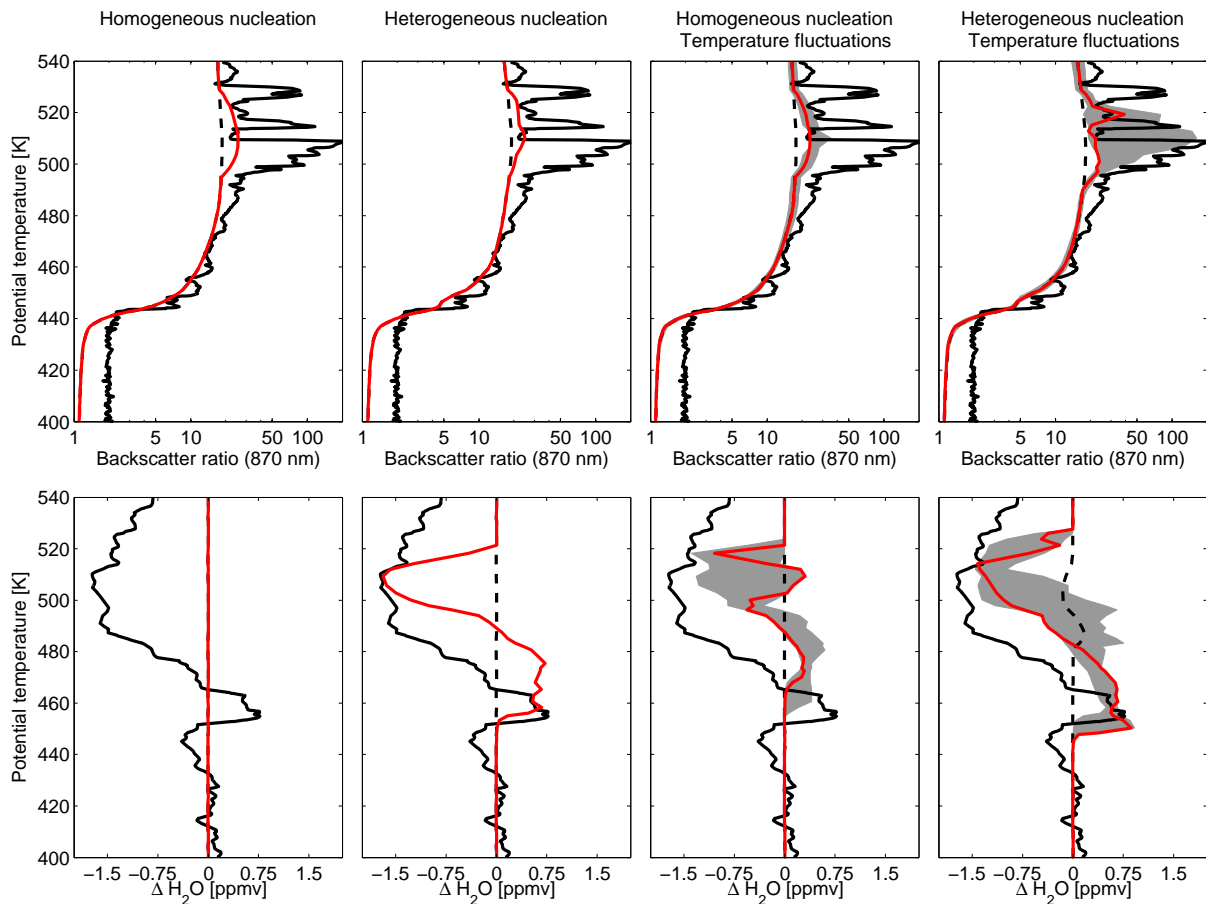
Figure 7.6: Comparison between measured and simulated profiles of backscatter ratios (*BSR*) for S1 (upper row) and water vapor mixing ratios for S2 (lower row). Mixing ratios are expressed as deviation from the climatological mean water vapor profile. The four different model scenarios are the same as in Fig. 7.5. Black line: COBALD (upper row) and CFH (lower row) measurements. Gray shaded area: Variations caused by different small-scale temperature fluctuations modeled by an ensemble with 10 members. Red line: Model results for the best fluctuation member shown in Figs. 7.3 - 7.5. Dashed line: Model results obtained without temperature correction (as shown in Fig. 7.2).

Finally, to demonstrate the need for the temperature correction depicted in Fig. 7.2b/c, we included model results based on the original ERA-Interim trajectories with and without superimposed small-scale temperature fluctuations as dashed black lines in Fig. 7.6. The only simulation which produced any dehydration signal is the one combining heterogeneous nucleation with temperature fluctuations. However, the modeled dehydration is much smaller than that observed.

7.4.3   Relevance for denitrification

Denitrification plays an important role by slowing the conversion of chlorine radicals back into reservoir species. This process may effect an enhancement of ozone destruction and can lead to increased accumulated ozone losses over the course of the winter (Müller et al., 1994). Denitrification is particularly important in the Arctic with its warmer temperatures (Chipperfield and Pyle, 1998) and severe
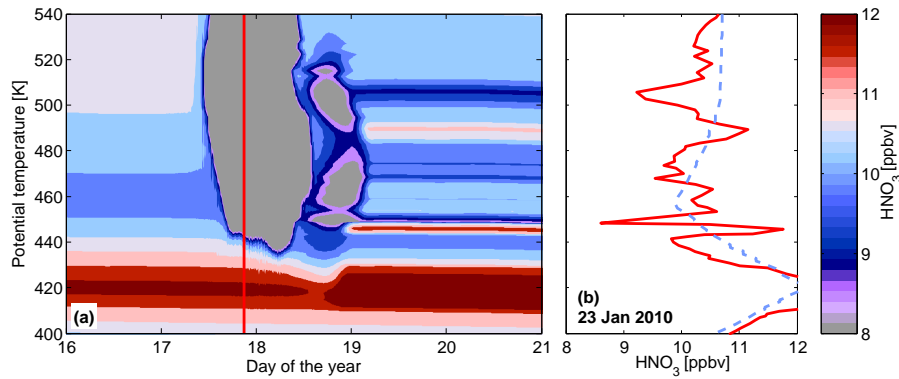
Figure 7.7: Results from the microphysical column model ZOMM driven by ERA-Interim based CLaMS trajectories with superimposed small-scale temperature fluctuations. (a) Time series of gas phase nitric acid mixing ratios (color coded). Vertical red line: S1. (b) Simulated HNO_3 profile (red) at S2 compared to the initial HNO_3 profile (dashed).

denitrification has been a major factor in bringing about the record ozone loss in the Arctic winter 2010/2011 (Manney et al., 2011).

Recent observations suggest the possibility of heterogeneous ice nucleation on preexisting NAT particles. Pitts et al. (2011) observed an increase in synoptic-scale ice PSCs concomitant with decreasing number densities of NAT mixtures in January 2010. Such a process would imply that the sedimentation of ice particles not only dehydrates but also denitrifies the stratosphere due to the removal of HNO_3. Khosrawi et al. (2011) investigated this hypothesis and offered ice nucleation on NAT particles as a possible explanation for the low HNO_3 observations by ODIN during the same winter. However, the observed dehydration event does not contribute to the overall denitrification. This is for the following reasons: In the beginning of the simulations, before ice formation, the nucleation of NAT on foreign nuclei accounts for NAT number densities of 10^{-3} cm^{-3}, but the effective radius of NAT particles formed along the trajectories does not exceed 2 μm before the onset of ice nucleation. The amount of HNO_3 condensing on these NAT particles is negligible. The major fraction of HNO_3 resides in the liquid droplets due to temperatures below the dew point of STS for most of the time; this results in an HNO_3 depletion in the gas phase (see denoxification in Fig. 7.7a) and decelerates the growth of the NAT particles (see Fig. 4 in Voigt et al., 2005). Next, ice nucleates, which happens partly on the preexisting NAT, and HNO_3 also co-condenses on the growing ice particles, which sediment and dehydrate efficiently. However, the resulting denitrification is minor, as most of the mass of the falling particles is composed of water molecules, not HNO_3 molecules. After the ice evaporated, NAT particles are released and would have the chance to denitrify the air, if they could live long enough. However, the air warms rapidly from $T < T_{\text{frost}}$ to $T > T_{\text{NAT}}$ (see Fig. 7.1) and does not stay for sufficient time in the interval T_{NAT} - 5 K $< T < T_{\text{NAT}}$ - 2 K, which is most efficient for denitrification (Voigt et al., 2005). The resulting denitrification signal in Fig. 7.7b shows redistributions of HNO_3 over small height differences, but no strong, coherent denitrification. Instead, the strong dentrification of the Arctic winter 2009/2010 occurred during the first half of January, i.e. before the onset of synoptic scale ice clouds, and was likely caused by NAT clouds downwind of mountain wave ice PSCs, which can act as mother clouds for so called NAT rocks (Fueglistaler et al., 2002). This interpretation is in accordance with the

Odin/SMR and Aura/MLS satellite measurements of HNO_3 shown in Fig. 3 of Khosrawi et al. (2011), but contradicts their explanation that the denitrification was linked to ice particle formation on NAT during the synoptic cooling event in mid-January. In the case investigated within our study, denitrification is not linked to dehydration, as it is most efficient at temperatures below T_{NAT}, but above the HNO_3 dew point and, thus, clearly above T_{frost}.

7.5   Discussion and Conclusions

Unprecedented de- and rehydration has been observed above Sodankylä during the Arctic winter 2009/2010. Using a microphysical column model, we were able to relate two unique balloon soundings by means of trajectories, one showing the redistribution of water from the gas phase into the ice phase without sedimentation, the second 6 days later showing the effects of gravitational settling and irreversible dehydration. To corroborate this interpretation we simulated the formation and sedimentation of the ice particles. Simulated water vapor profiles agree reasonably with CFH and FLASH-B onboard the balloon sondes, and with MLS satellite measurements. Optical T-Matrix calculations enabled the direct comparison of the simulations with COBALD and CALIOP backscatter measurements. To this end, we examined the effect of small-scale temperature fluctuations and compared homogeneous vs. heterogeneous formation of ice particles.

It was demonstrated that heterogeneous nucleation of ice is essential to reproduce the observed de- and rehydration signatures. Even though ERA-Interim temperatures along the trajectories had to be lowered by up to -1.5 K in order to obtain agreement with the temperatures measured by the sondes, temperatures stayed clearly above T_{frost} - 3 K, which is the temperature required for homogeneous nucleation of ice in ternary solution droplets. Small-scale temperature fluctuations additionally lowered the temperature, caused higher supersaturations and therefore enabled the formation of ice clouds, even when homogeneous ice nucleation was the only allowed ice formation pathway. However, homogeneous nucleation at high supersaturations resulted in ice formation with the characteristics of wave clouds: High number densities of particles remain too small to sediment and cannot explain the observed vertical redistribution of water. In contrast, heterogeneous ice nucleation takes place at lower supersaturations, causing a selective freezing of only a few ice crystals. Those particles can grow to sizes large enough ($r \gtrsim 10\,\mu m$) to settle fast and reproduce the signatures of de- and rehydration.

Even though small-scale temperature fluctuations are not indispensable to achieve de- and renitrification in the present case, the resulting PSC backscatter is too low without small-scale temperature fluctuations and rapid cooling rates help to improve the agreement with the COBALD measurements. However, the two balloon soundings provide only snapshots of the atmosphere, which depend on the precise temperature variations not only at the point of observation, but also upstream along the air parcel trajectories. Discrepancies between ERA-Interim temperature fields and measured temperatures were found, which we needed to correct. Whereas Sodankylä, located at the edge of the cold pool, is characterized by temperatures just below T_{frost} and is therefore very sensitive to smallest temperature changes, the CALIOP measurements show large areas deeper in the vortex with persistent synoptic-scale ice clouds. The observed dehydration above Sodankylä, not only on 23 January but also a few days earlier and later (as shown by Khaykin et al., 2013), is most likely caused by such large-

scale fields of persistent ice clouds and not by the observed small-scale structures above Sodankylä. The fact that the reduction in H_2O measured by CFH is not balanced by the rehydration layer below suggests that wind shear and subsequent mixing of air masses have affected the observed profile. An accurate estimate of these effects can only be made using a three-dimensional modeling approach.

Acknowledgments

Chapter 8

Conclusions and outlook

A detailed microphysical modeling study has been performed, questioning the conventional understanding of PSC formation, namely that ice would be the first solid, nucleating homogeneously within liquid aerosol particles, and that NAT would nucleate only subsequently on the ice. Within this thesis, we developed heterogeneous nucleation parameterizations for NAT and ice, which have been implemented in the Zurich Optical and Microphysical box Model (ZOMM) and thoroughly validated against vortex wide PSC observations by the spaceborne lidar CALIOP. The main conclusions can be summarized as follows:

- Heterogeneous NAT nucleation

  In December 2009, CALIOP frequently observed PSCs consisting of mixtures of liquid particles and low number densities of hydrate particles - most likely NAT -, clearly before temperatures were low enough to permit the first ice clouds to form in the polar vortex. Previous studies, based on aircraft (Voigt et al., 2005) and balloon-borne (Larsen et al., 2004) measurements, suggested already the need for an ice independent NAT nucleation mechanism. The vortex wide spatial and high temporal coverage of the satellite brings the probability of undetected ice clouds down to a minimum and at the same time shows the widespread occurrence of NAT particles. We introduced NAT nucleation in ZOMM by immersion freezing on heterogeneous nuclei, such as nanometer sized dust particles, possibly of meteoritic origin. Their nucleation efficiency is characterized by active sites, which implies that only a minor fraction of the dust particles are effective nuclei. Advantages compared to constant, saturation independent rates of NAT nucleation (e.g. Drdla et al., 2002; Grooß et al., 2005) are the ability to cope with situations, in which temperatures drop only slightly below T_{NAT} for an extended period of time, yielding only a moderate degree of nucleation, as well as with situations, in which temperatures drop substantially below T_{NAT}, but for only short time periods, possibly resulting in massive NAT nucleation. It was shown that the new NAT nucleation parameterization leads to an accurate modeling of CALIOP observations of low number density NAT clouds and we unambiguously demonstrated the importance of heterogeneous NAT nucleation for PSC formation.

  Besides heterogeneous nucleation on dust surfaces, this study supports the well established ice assisted pathway of NAT formation. Early on, airborne lidar observations suggested that NAT formation occurs downstream of mountain wave induced ice clouds (e.g. Carslaw et al., 1998b;

Fueglistaler et al., 2003). We could show that the occurrence of high number density NAT clouds require preexisting ice particles. However, ice number densities of synoptic-scale ice clouds are sufficient to achieve agreement with observations, whereas the occurrence of wave ice clouds is not a sine qua non.

- Heterogeneous ice nucleation

Little attention has been paid so far to heterogeneous ice nucleation in the context of PSC formation, even though laboratory as well as theoretical studies suggest that this process might well be of importance for tropospheric cirrus cloud formation (see (Hoose and Möhler, 2012), for a recent review, and references therein). A week-long occurrence of ice PSCs in January 2010, unusual for the Arctic winter stratosphere, reveals that the large-scale occurrence of ice cannot be explained merely by homogeneous ice nucleation, because temperatures fell only marginally below the frost point and unresolved, small-scale orographic cold pools could be excluded. Thus, also the existence of this ice appears to require heterogeneous nucleation mechanisms as for NAT. The efficiency of the ice nuclei is surprisingly high, namely comparable to that of the best tropospheric ice nuclei such as mineral dust particles.

The importance of heterogeneous ice nucleation on preexisting NAT particles could not be quantified until now, because there is a certain trade-off between ice nucleation directly on dust or on NAT that nucleated on dust. However, such a process could possibly increase denitrification and thus enhance halogen-catalyzed chemical reactions leading to intensified ozone depletion. NAT particles, occurring in higher number densities, are typically too small to exhibit observable sedimentation velocities. Enclosed into larger ice particles, HNO_3 might efficiently be removed and thus can contribute to denitrification. This potential pathway will be followed up in future work.

- Small-scale temperature fluctuations

Temperature profiles in the middle atmosphere show a highly irregular small-scale structure associated with gravity waves and/or decaying turbulence (Gary, 2006; Fritts and Alexander, 2003, and references therein). Within this work, we made use of the vertical velocity and temperature time series obtained from the SUCCESS (Subsonic Aircraft: Contrail and Cloud Effects Special Study) data used by Hoyle et al. (2005) to include realistic mesoscale effects in our trajectory based modeling studies. While temperature fluctuations do not affect the results for NAT formation, they are essential for ice formation. Meilinger et al. (1995) demonstrated that the relaxation times for ice and NAT differ greatly due to different partial pressures. While H_2O is in equilibrium on a timescale of seconds, HNO_3 uptake into micron size particles needs hours. Therefore, with respect to rapid small-scale temperature fluctuations the composition of the droplets are quasistatic, and the nucleation rate does not change significantly. However, the reconciliation of model results with ice observations requires sufficient rapid cooling to obtain ice number densities with optical signatures as large as those observed by CALIOP. The present work shows that including the influence of small-scale temperature fluctuations on ice cloud properties is equally important as the provision for heterogeneous nucleation mechanisms.

- Dehydration and rehydration

  Water vapor measurements from balloon, aircraft and satellite platforms were presented. They provide, in combination with aerosol observations by COBALD and CALIOP, a comprehensive view of the consequences of widespread ice PSC occurrence. Vertical redistribution of Arctic stratospheric water vapor has never been presented as detailed and clear as within this study. The requirement for both, potent heterogeneous nuclei and small-scale temperature fluctuations are unambiguously demonstrated by model calculations accompanying these unique observations.

The future evolution of stratospheric temperatures depends on the recovery of the ozone layer, increasing concentrations of greenhouse gases and resultant changes in the Brewer-Dobson circulation. While the middle and upper stratosphere is expected to cool by several degrees, temperature changes in the high-latitude lower stratosphere are believed to be much smaller and of undetermined sign (WMO, 2011). These findings are contradictory to the observed tendency towards higher extreme values in the potential PSC volume, associated with a cooling of Arctic winters (Rex et al., 2004, Fig. 2-16 in WMO, 2011). How climate change will alter PSCs and their occurrence frequency remains an open question. In this context, accurate knowledge of their formation processes and of their representation in global models becomes even more important. The subsequent section gives attention to a few questions, which remained unresolved in this work, and research tasks, which ought to be addressed in the near future.

Outlook

A pressing issue is the apparent contradiction that previous laboratory experiments have in the past been used to help excluding heterogeneous nucleation as an important pathway for NAT formation, whereas now the results of the very experiments are used to argue that extremely low NAT number density could actually be explained as upper limits of the measured nucleation rate coefficients. We presently perform laboratory experiments to investigate heterogeneous NAT nucleation rates on meteoritic material. These experiments are based on earlier studies by Biermann et al. (1996). Back then, upper bounds had been reported for NAT freezing rates under stratospheric conditions in ternary $HNO_3/H_2SO_4/H_2O$ solutions of different concentrations characteristic for the polar winter stratosphere. The new bulk experiments are carried out on fragments of meteorites using a Differential Scanning Calorimeter (DSC). Preliminary results suggest that the heterogeneous nucleation rates of NAT might indeed reach the upper limits specified by Biermann et al. (1996). Supported by in situ measurements of non-volatile residues in stratospheric aerosol particles during RECONCILE and today's insights into low number density NAT clouds, meteoritic particles become favorable candidates to explain CALIOP observations in December 2009.

Chemistry transport models like CLaMS often comprise only idealized, constant NAT nucleation rates for all locations with temperatures below T_{NAT}. Simulations of the Arctic winter 2009/2010 failed so far in reproducing the extent of vertical HNO_3 redistribution by using constant volume-proportional nucleation rates, which showed agreement in earlier winters. Therefore, we tabulated NAT number densities as a function of temperature and supersaturation based on the results of the present work, in

order to easily implement the newly developed heterogeneous NAT nucleation rates into CLaMS, or in fact into any other 3-dimensional model of the atmosphere. First comparisons of ClaMS particle size distributions and denitrification signatures with measurements indicate good agreement. This work is still in progress. The long-term goal is to provide a fast parameterization of NAT and ice formation for implementation in chemistry transport and chemistry climate models enabling reliable modeling of present and prediction of future polar ozone loss.

List of abbreviations

ATD	Arizona Test Dust
CALIOP	Cloud-Aerosol Lidar with Orthogonal Polarization
CALIPSO	Cloud-Aerosol Lidar and Infrared Pathfinder Satellite Observations
CFH	Cryogenic Frost point Hygrometer
CLaMS	Chemical Lagrangian Model of the Stratosphere
COBALD	Compact Optical Backscatter Aerosol Detector
CFC	Chlorofluorocarbon
DU	Dobson units
EU	European Union
ECMWF	European Centre for Medium-range Weather Forecasts
FISH	Fast In-situ Stratospheric Hygrometer
FLASH-A	Fluorescent Lyman-Alpha Stratospheric Hygrometer for Aircraft
FLASH-B	Fluorescent Lyman-Alpha Stratospheric Hygrometer for Balloon
FMI-ARC	Finnish Meteorological Institute's Arctic Research Center
FPH	Frost Point Hygrometer
GEOS-5	Goddard Earth Observing System Model, Version 5
IN	Ice Nucleus
IPCC	Intergovernmental Panel on Climate Change
LAPBIAT	Lapland Atmosphere-Biosphere Facility
LED	Light-Emitting Diode
LIDAR	LIght Detection And Ranging
MLS	Microwave Limb Sounder
NAD	Nitric Acid Dihydrate
NAT	Nitric Acid Trihydrate
NWP	Numerical Weather Prediction
ODS	Ozone depleting substance
OMI	Ozone Monitoring Instrument
PSC	Polar Stratospheric Cloud
PV	Potential vorticity
RECONCILE	Reconciliation of essential process parameters for an enhanced predictability of arctic stratospheric ozone loss and its climate interactions
RMSE	Root-Mean-Square Error
SAT	Sulfuric Acid Tetrahydrate

SBS	Supercooled Binary Solution
SNR	Signal-to-Noise Ratio
STS	Supercooled Ternary Solution
SUCCESS	Subsonic Aircraft: Contrail and Cloud Effects Special Study
UV	Ultraviolet
WMO	World Meteorological Organization
ZOMM	Zurich Optical and Microphysical box Model

References

Abbatt, J. P. D.: Interaction of HNO_3 with water-ice surfaces at temperatures of the free troposphere, Geophys. Res. Lett., 24, 1479–1482, 1997.

Adriani, A., Massoli, P., Di Donfrancesco, G., Cairo, F., Moriconi, M. L., and Snels, M.: Climatology of polar stratospheric clouds based on lidar observations from 1993 to 2001 over McMurdo Station, Antarctica, J. Geophys. Res., 109, 2004.

Bacmeister, J. T., Eckermann, S. D., Tsias, A., Carslaw, K. S., and Peter, T.: Mesoscale temperature fluctuations induced by a spectrum of gravity waves: A comparison of parameterizations and their impact on stratospheric microphysics, J. Atmos. Sci., 56, 1999.

Bertaux, J. L. and Delannoy, A.: Premieres measures stratospheriques par un hygrometre a fluorescence ultraviolette, C. R. Acad. Sc. Paris, 286, 191–194, 1978.

Beyer, K., Seago, S., Chang, H., and Molina, M.: Composition and freezing of aqueous H_2SO_4/HNO_3 solutions under polar stratosopheric conditions, Geophys. Res. Lett., 21, 871–874, 1994.

Beyerle, G., Gross, M. R., Haner, D. A., Kjome, N. T., McDermid, I. S., McGee, T. J., Rosen, J. M., Schafer, H. J., and Schrems, O.: A lidar and backscatter sonde measurement campaign at Table Mountain during February-March 1997: Observations of cirrus clouds, J. Atmos. Sci., 58, 1275–1287, 2001.

Biele, J., Tsias, A., Luo, B. P., Carslaw, K. S., Neuber, R., Beyerle, G., and Peter, T.: Nonequilibrium coexistence of solid and liquid particles in Arctic stratospheric clouds, J. Geophys. Res., 106, 22 991–23 007, 2001.

Biermann, U. M., Presper, T., Koop, T., Mossinger, J., Crutzen, P. J., and Peter, T.: The unsuitability of meteoritic and other nuclei for polar stratospheric cloud freezing, Geophys. Res. Lett., 23, 1693–1696, 1996.

Biermann, U. M., Crowley, J. N., Huthwelker, T., Moortgat, G. K., Crutzen, P. J., and Peter, T.: FTIR studies on lifetime prolongation of stratospheric ice particles due to NAT coating, Geophys. Res. Lett., 25, 3939–3942, 1998.

Blum, U., Fricke, K. H., Müller, K. P., Siebert, J., and Baumgarten, G.: Long-term lidar observations of polar stratospheric clouds at Esrange in northern Sweden, Tellus B, 57, 412–422, 2005.

Bogdan, A., Molina, M. J., Kulmala, M., MacKenzie, A. R., and Laaksonen, A.: Study of finely divided aqueous systems as an aid to understanding the formation mechanism of polar stratospheric clouds: Case of HNO_3/H_2O and H_2SO_4/H_2O systems, J. Geophys. Res., 108, 2003.

Bohren, C. F. and Huffman, D. R.: Absorption and scattering of light by small particles, Wiley-VCH, 2004.

Brabec, M.: Backscatter and humidity measurements in cirrus and dust clouds using balloon sondes, Ph.D. thesis, ETH Zurich, 2011.

Brabec, M., Wienhold, F. G., Luo, B. P., Vömel, H., Immler, F., Steiner, P., Hausammann, E., Weers, U., and Peter, T.: Particle backscatter and relative humidity measured across cirrus clouds and comparison with microphysical cirrus modelling, Atmos. Chem. Phys., 12, 9135–9148, 2012.

Browell, E. V., Butler, C. F., Ismail, S., Robinette, P. A., Carter, A. F., Higdon, N. S., Toon, O. B., Schoeberl, M. R., and Tuck, A. F.: Airborne lidar observations in the wintertime Arctic stratosphere - polar stratospheric clouds, Geophys. Res. Lett., 17, 385–388, 1990.

Brühl, C., Lelieveld, J., Crutzen, P. J., and Tost, H.: The role of carbonyl sulphide as a source of stratospheric sulphate aerosol and its impact on climate, Atmos. Chem. Phys., 12, 1239–1253, 2012.

Bukowiecki, N., Zieger, P., Weingartner, E., Jurányi, Z., Gysel, M., Neininger, B., Schneider, B., Hueglin, C., Ulrich, A., Wichser, A., Henne, S., Brunner, D., Kaegi, R., Schwikowski, M., Tobler, L., Wienhold, F. G., Engel, I., Buchmann, B., Peter, T., and Baltensperger, U.: Ground-based and airborne in-situ measurements of the Eyjafjallajökull volcanic aerosol plume in Switzerland in spring 2010, Atmos. Chem. Phys., 11, 10 011–10 030, 2011.

Cairo, F., Di Donfrancesco, G., Adriani, A., Pulvirenti, L., and Fierli, F.: Comparison of various linear depolarization parameters measured by lidar, Appl. Opt., 38, 4425–4432, 1999.

Carslaw, K., Kettleborough, J., Northway, M., Davies, S., Gao, R., Fahey, D., Baumgardner, D., Chipperfield, M., and Kleinbohl, A.: A vortex-scale simulation of the growth and sedimentation of large nitric acid hydrate particles, J. Geophys. Res., 107, 2002.

Carslaw, K. S., Wirth, M., Tsias, A., Luo, B. P., Dörnbrack, A., Leutbecher, M., Volkert, H., Renger, W., Bacmeister, J. T., and Peter, T.: Particle microphysics and chemistry in remotely observed mountain polar stratospheric clouds, J. Geophys. Res., 103, 5785–5796, 1998a.

Carslaw, K. S., Wirth, M., Tsias, A., Luo, B. P., Dörnbrack, A., Leutbecher, M., Volkert, H., Renger, W., Bacmeister, J. T., Reimer, E., and Peter, T.: Increased stratospheric ozone depletion due to mountain-induced atmospheric waves, Nature, 391, 675–678, 1998b.

Carslaw, K. S., Luo, B. P., Clegg, S. L., Peter, T., Brimblecombe, P., and Crutzen, P. J.: Stratospheric aerosol growth and HNO_3 gas phase depletion from coupled HNO_3 and water uptake by liquid particles, Geophys. Res. Lett., 21, 2479–2482, 1994.

Chapman, S.: Theory of upper atmospheric ozone, Memoirs of the Royal Meteorological Society, 3, 103–125, 1930.

Chipperfield, M. P. and Pyle, J. A.: Model sensitivity studies of Arctic ozone depletion, J. Geophys. Res., 103, 28 389–28 403, 1998.

Cirisan, A., Luo, B. P., Engel, I., Wienhold, F. G., Krieger, U. K., Weers, U., Romanens, G., Levrat, G., Jeannet, P., Ruffieux, D., Philipona, R., Calpini, B., Spichtinger, P., and Peter, T.: Balloon-borne match measurements of mid-latitude cirrus clouds, submitted to Atmos. Chem. Phys. Discuss., 2013.

Crutzen, P. and Arnold, F.: Nitric-acid cloud formation in the cold Antarctic stratosphere - a major cause for the springtime ozone hole, Nature, 324, 651–655, 1986.

Crutzen, P. J.: The influence of nitrogen oxides on the atmospheric ozone content, Quart. J. Roy. Meteorol. Soc., 96, 320–325, 1970.

Curtius, J., Weigel, R., Vossing, H. J., Wernli, H., Werner, A., Volk, C. M., Konopka, P., Krebsbach, M., Schiller, C., Roiger, A., Schlager, H., Dreiling, V., and Borrmann, S.: Observations of meteoric material and implications for aerosol nucleation in the winter Arctic lower stratosphere derived from in situ particle measurements, Atmos. Chem. Phys., 5, 3053–3069, 2005.

Cziczo, D. J., Thomson, D. S., and Murphy, D. M.: Ablation, flux, and atmospheric implications of meteors inferred from stratospheric aerosol, Science, 291, 1772–1775, 2001.

Davies, T., Cullen, M. J. P., Malcolm, A. J., Mawson, M. H., Staniforth, A., White, A. A., and Wood, N.: A new dynamical core for the Met Office's global and regional modelling of the atmosphere, Quart. J. Roy. Meteorol. Soc., 131, 1759–1782, 2005.

Dee, D. P., Uppala, S. M., Simmons, A. J., Berrisford, P., Poli, P., Kobayashi, S., Andrae, U., Balmaseda, M. A., Balsamo, G., Bauer, P., Bechtold, P., Beljaars, A. C. M., van de Berg, L., Bidlot, J., Bormann, N., Delsol, C., Dragani, R., Fuentes, M., Geer, A. J., Haimberger, L., Healy, S. B., Hersbach, H., Hólm, E. V., Isaksen, L., Kållberg, P., Köhler, M., Matricardi, M., McNally, A. P., Monge-Sanz, B. M., Morcrette, J.-J., Park, B.-K., Peubey, C., de Rosnay, P., Tavolato, C., Thépaut, J.-N., and Vitart, F.: The ERA-Interim reanalysis: configuration and performance of the data assimilation system, Quart. J. Roy. Meteorol. Soc., 137, 553–597, 2011.

DeMott, P. J., Cziczo, D. J., Prenni, A. J., Murphy, D. M., Kreidenweis, S. M., Thomson, D. S., Borys, R., and Rogers, D. C.: Measurements of the concentration and composition of nuclei for cirrus formation, Proc. Nat. Acad. Sci. USA, 100, 14 655–14 660, 2003.

Dieterichs, H.: Mother-of-pearl clouds and their problems, Pure Appl. Geophys, 16, 128–132, 1950.

Dörnbrack, A., Leutbecher, M., Kivi, R., and Kyro, E.: Mountain-wave-induced record low stratospheric temperatures above northern Scandinavia, Tellus Ser. A-Dyn. Meteorol. Oceanol., 51, 951–963, 1999.

Dörnbrack, A., Pitts, M. C., Poole, L. R., Orsolini, Y. J., Nishii, K., and Nakamura, H.: The 2009-2010 arctic stratospheric winter - general evolution, mountain waves and predictability of an operational weather forecast model, Atmos. Chem. Phys., 12, 3659–3675, 2012.

Drdla, K. and Turco, R. P.: Denitrification through PSC formation: A 1-D model incorporating temperature oscillations, J. Atmos Chem., 12, 319–366, 1991.

Drdla, K., Schoeberl, M. R., and Browell, E. V.: Microphysical modeling of the 1999-2000 Arctic winter: 1. Polar stratospheric clouds, denitrification, and dehydration, J. Geophys. Res., 107, SOL 55–1–SOL 55–21, 2002.

Dye, J. E., Baumgardner, D., Gandrud, B. W., Kawa, S. R., Kelly, K. K., Loewenstein, M., Ferry, G. V., Chan, K. R., and Gary, B. L.: Particle size distributions in Arctic polar stratospheric clouds, growth and freezing of sulfuric acid droplets, and implications for cloud formation, J. Geophys. Res., 97, 8015–8034, 1992.

Engel, I., Luo, B. P., Khaykin, S. M., Wienhold, F. G., Vömel, H., Kivi, R., Hoyle, C. R., Grooß, J.-U., Pitts, M. C., and Peter, T.: Arctic stratospheric dehydration – Part 2: Microphysical modeling, submitted to Atmos. Chem. Phys. Discuss., 2013a.

Engel, I., Luo, B. P., Pitts, M. C., Poole, L. R., Hoyle, C. R., Grooß, J.-U., Dörnbrack, A., and Peter, T.: Heterogeneous formation of polar stratospheric clouds – Part 2: Nucleation of ice on synoptic scales, Atmos. Chem. Phys. Discuss., 13, 8831–8872, doi:10.5194/acpd-13-8831-2013, 2013b.

Eyring, V., Cionni, I., Bodeker, G. E., Charlton-Perez, A. J., Kinnison, D. E., Scinocca, J. F., Waugh, D. W., Akiyoshi, H., Bekki, S., Chipperfield, M. P., Dameris, M., Dhomse, S., Frith, S. M., Garny, H., Gettelman, A., Kubin, A., Langematz, U., Mancini, E., Marchand, M., Nakamura, T., Oman, L. D., Pawson, S., Pitari, G., Plummer, D. A., Rozanov, E., Shepherd, T. G., Shibata, K., Tian, W., Braesicke, P., Hardiman, S. C., Lamarque, J. F., Morgenstern, O., Pyle, J. A., Smale, D., and Yamashita, Y.: Multi-model assessment of stratospheric ozone return dates and ozone recovery in CCMVal-2 models, Atmos. Chem. Phys., 10, 9451–9472, 2010.

Fahey, D. W., Kelly, K. K., Kawa, S. R., Tuck, A. F., Loewenstein, M., Chan, K. R., and Heidt, L. E.: Observations of denitrification and dehydration in the winter polar stratospheres, Nature, 344, 321–324, 1990.

Farman, J. C., Gardiner, B. G., and Shanklin, J. D.: Large losses of total ozone in Antarctica reveal seasonal ClO_X/NO_X interaction, Nature, 315, 207–210, 1985.

Fritts, D. C. and Alexander, M. J.: Gravity wave dynamics and effects in the middle atmosphere, Rev. Geophys., 41, 2003.

Fueglistaler, S., Luo, B. P., Voigt, C., Carslaw, K. S., and Peter, T.: NAT-rock formation by mother clouds: a microphysical model study, Atmos. Chem. Phys., 2, 93–98, 2002.

Fueglistaler, S., Buss, S., Luo, B. P., Wernli, H., Flentje, H., Hostetler, C. A., Poole, L. R., Carslaw, K. S., and Peter, T.: Detailed modeling of mountain wave PSCs, Atmos. Chem. Phys., 3, 697–712, 2003.

Gary, B. L.: Mesoscale temperature fluctuations in the stratosphere, Atmos. Chem. Phys., 6, 4577–4589, 2006.

Gary, B. L.: Mesoscale temperature fluctuations in the Southern Hemisphere stratosphere, Atmos. Chem. Phys., 8, 4677–4681, 2008.

Grooß, J.-U., Günther, G., Müller, R., Konopka, P., Bausch, S., Schlager, H., Voigt, C., Volk, C. M., and Toon, G. C.: Simulation of denitrification and ozone loss for the Arctic winter 2002/2003, Atmos. Chem. Phys., 5, 1437–1448, 2005.

Hanson, D. and Mauersberger, K.: Laboratory studies of the nitric acid trihydrate: Implications for the south polar stratosphere, Geophys. Res. Lett., 15, 855–858, 1988.

Hesstvedt, E.: A two-dimensional model of mother-of-pearl clouds, Tellus B, 14, 1962.

Hintsa, E. J., Newman, P. A., Jonsson, H. H., Webster, C. R., May, R. D., Herman, R. L., Lait, L. R., Schoeberl, M. R., Elkins, J. W., Wamsley, P. R., Dutton, G. S., Bui, T. P., Kohn, D. W., and Anderson, J. G.: Dehydration and denitrification in the Arctic polar vortex during the 1995-1996 winter, Geophys. Res. Lett., 25, 501–504, 1998.

Hoose, C. and Möhler, O.: Heterogeneous ice nucleation on atmospheric aerosols: a review of results from laboratory experiments, Atmos. Chem. Phys., 12, 9817–9854, 2012.

Hoyle, C. R., Pinti, V., Welti, A., Zobrist, B., Marcolli, C., Luo, B., Höskuldsson, A., Mattsson, H. B., Stetzer, O., Thorsteinsson, T., Larsen, G., and Peter, T.: Ice nucleation properties of volcanic ash from Eyjafjallajökull, Atmos. Chem. Phys., 11, 9911–9926, 2011.

Hoyle, C. R., Engel, I., Luo, B. P., Pitts, M. C., Poole, L. R., Grooß, J.-U., and Peter, T.: Heterogeneous formation of polar stratospheric clouds - Part 1: Nucleation of nitric acid trihydrate (NAT), Atmos. Chem. Phys. Discuss., 13, 7979–8021, doi:10.5194/acpd-13-7979-2013, 2013.

Hoyle, C. R., Luo, B. P., and Peter, T.: The origin of high ice crystal number densities in cirrus clouds, J. Atmos. Sci., 62, 2568–2579, 2005.

Hunt, W. H., Winker, D. M., Vaughan, M. A., Powell, K. A., Lucker, P. L., and Weimer, C.: CALIPSO lidar description and performance assessment, J. Atmos. Ocean. Technol., 26, 1214–1228, 2009.

Hunten, D., Turco, R., and Toon, O.: Smoke and dust particles of meteoric origin in the mesosphere and stratosphere, J. Atmos. Sci., 37, 1342–1357, 1980.

IPCC: The Physical Science Basis. Contribution of Working Group I to the Fourth Assessment Report of the Intergovernmental Panel on Climate Change [Solomon, S., D. Qin, M. Manning, Z. Chen, M. Marquis, K.B. Averyt, M. Tignor and H.L. Miller (eds.)], Cambridge University Press, Cambridge, United Kingdom and New York, NY, USA, 996 pp., 2007.

Iraci, L., Middlebrook, A., Wilson, M., and Tolbert, M.: Growth of nitric-acid hydrates on thin sulfuric-acid films, Geophys. Res. Lett., 21, 867–870, 1994.

Jimenez, C., Pumphrey, H. C., MacKenzie, I. A., Manney, G. L., Santee, M. L., Schwartz, M. J., Harwood, R. S., and Waters, J. W.: EOS MLS observations of dehydration in the 2004-2005 polar winters, Geophys. Res. Lett., 33, 2006.

Junge, C., Chagnon, C., and Manson, J.: Stratospheric aerosols, J. Meteor., 18, 81–108, 1961.

Kärcher, B. and Lohmann, U.: A parameterization of cirrus cloud formation: Homogeneous freezing including effects of aerosol size, J. Geophys. Res., 107, 2002.

Kärcher, B. and Lohmann, U.: A parameterization of cirrus cloud formation: Heterogeneous freezing, J. Geophys. Res., 108, 2003.

Kelly, K. K., Tuck, A. F., Murphy, D. M., Proffitt, M. H., Fahey, D. W., Jones, R. L., McKenna, D. S., Loewenstein, M., Podolske, J. R., Strahan, S. E., Ferry, G. V., Chan, K. R., Vedder, J. F., Gregory, G. L., Hypes, W. D., McCormick, M. P., Browell, E. V., and Heidt, L. E.: Dehydration in the lower Antarctic stratosphere during late winter and early spring, 1987, J. Geophys. Res., 94, 11 317–11 357, 1989.

Khaykin, S. M., Engel, I., Vömel, H., Formanyuk, I. M., Kivi, R., Korshunov, L. I., Krämer, M., Lykov, A. D., Meier, S., Naebert, T., Pitts, M. C., Santee, M. L., Spelten, N., Wienhold, F. G., Yushkov, V. A., and Peter, T.: Arctic stratospheric dehydration - Part 1: Unprecedented observation of vertical redistribution of water, Atmos. Chem. Phys. Discuss., 13, 14 249–14 295, doi:10.5194/acpd-13-14249-2013, 2013.

Khosrawi, F., Urban, J., Pitts, M. C., Voelger, P., Achtert, P., Kaphlanov, M., Santee, M. L., Manney, G. L., Murtagh, D., and Fricke, K.-H.: Denitrification and polar stratospheric cloud formation during the Arctic winter 2009/2010, Atmos. Chem. Phys., 11, 8471–8487, 2011.

Kivi, R., Kyrö, E., Dörnbrack, A., and Birner, T.: Observations of vertically thick polar stratospheric clouds and record low temperature in the Arctic Vortex, Geophys. Res. Lett., 28, 3661–3664, 2001.

Kivi, R., Vömel, H., Immler, F., Lehtola, T., Kämpfer, N., Straub, C., Yushkov, V., Khaykin, S., Christensen, T., and Wienhold, F. G.: LAPBIAT Atmospheric Sounding Campaign in 2010: Upper-air and remote sensing observations of water vapour, in: WMO Technical Conference on Meteorological and Environmental Instruments and Methods of Observation (TECO-2010), Helsinki, Finland, 30 August - 1 September 2010, 2010.

Kley, D. and Stone, E. J.: Measurement of water vapor in the stratosphere by photo dissociation with Ly-Alpha (1216 A) light, Rev. Sci. Instrum., 49, 691–697, 1978.

Knopf, D. A., Koop, T., Luo, B. P., Weers, U. G., and Peter, T.: Homogeneous nucleation of NAD and NAT in liquid stratospheric aerosols: insufficient to explain denitrification, Atmos. Chem. Phys., 2, 207–214, 2002.

Koop, T., Ng, H. P., Molina, L. T., and Molina, M. J.: A new optical technique to study aerosol phase transitions: I The nucleation of ice from H_2SO_4 aerosols, J. Phys. Chem., 102, 8924–8931, 1998.

Koop, T., Biermann, U. M., Raber, W., Luo, B. P., Crutzen, P. J., and Peter, T.: Do stratospheric aerosol droplets freeze above the ice frost point?, Geophys. Res. Lett., 22, 917–920, 1995.

Koop, T., Carslaw, K. S., and Peter, T.: Thermodynamic stability and phase transitions of PSC particles, Geophys. Res. Lett., 24, 2199–2202, 1997.

Koop, T., Luo, B. P., Tsias, A., and Peter, T.: Water activity as the determinant for homogeneous ice nucleation in aqueous solutions, Nature, 406, 611–614, 2000.

Lambert, A., Read, W. G., Livesey, N. J., Santee, M. L., Manney, G. L., Froidevaux, L., Wu, D. L., Schwartz, M. J., Pumphrey, H. C., Jimenez, C., Nedoluha, G. E., Cofield, R. E., Cuddy, D. T., Daffer, W. H., Drouin, B. J., Fuller, R. A., Jarnot, R. F., Knosp, B. W., Pickett, H. M., Perun, V. S., Snyder, W. V., Stek, P. C., Thurstans, R. P., Wagner, P. A., Waters, J. W., Jucks, K. W., Toon, G. C., Stachnik, R. A., Bernath, P. F., Boone, C. D., Walker, K. A., Urban, J., Murtagh, D., Elkins, J. W., and Atlas, E.: Validation of the Aura Microwave Limb Sounder middle atmosphere water vapor and nitrous oxide measurements, J. Geophys. Res., 112, 2007.

Lambert, A., Santee, M. L., Wu, D. L., and Chae, J. H.: A-train CALIOP and MLS observations of early winter Antarctic polar stratospheric clouds and nitric acid in 2008, Atmos. Chem. Phys., 12, 2899–2931, 2012.

Larsen, N., Knudsen, B. M., Svendsen, S. H., Deshler, T., Rosen, J. M., Kivi, R., Weisser, C., Schreiner, J., Mauerberger, K., Cairo, F., Ovarlez, J., Oelhaf, H., and Spang, R.: Formation of solid particles in synoptic-scale Arctic PSCs in early winter 2002/2003, Atmos. Chem. Phys., 4, 2001–2013, 2004.

Liu, L. and Mishchenko, M.: Constraints on PSC particle microphysics derived from lidar observations, J. Quant. Spectrosc. Radiat. Transf., 70, 817–831, 2001.

Livesey, N. J., Read, W. G., Froidevaux, L., Lambert, A., Manney, G. L., Pumphrey, H. C., Santee, M. L., Schwartz, M. J., Wang, S., Cofield, R. E., Cuddy, D. T., Fuller, R. A., Jarnot, R. F., Jiang, J. H., Knosp, B. W., Stek, P. C., Wagner, P. A., and Wu, D. L.: Version 3.3 Level 3 data quality and description document, Tech. Rep. JPL D-33509, Jet Propulsion Laboratory, URL `http://mls.jpl.nasa.gov`, last access: January 2013, 2013.

Lowe, D. and MacKenzie, A. R.: Polar stratospheric cloud microphysics and chemistry, J. Atmos. Solar-Terr. Phys., 70, 13–40, 2008.

Luo, B. P., Peter, T., Fueglistaler, S., Wernli, H., Wirth, M., Kiemle, C., Flentje, H., Yushkov, V. A., Khattatov, V., Rudakov, V., Thomas, A., Borrmann, S., Toci, G., Mazzinghi, P., Beuermann, J., Schiller, C., Cairo, F., Di Donfrancesco, G., Adriani, A., Volk, C. M., Strom, J., Noone, K., Mitev, V., MacKenzie, R. A., Carslaw, K. S., Trautmann, T., Santacesaria, V., and Stefanutti, L.: Dehydration potential of ultrathin clouds at the tropical tropopause, Geophys. Res. Lett., 30, 2003a.

Luo, B. P., Voigt, C., Fueglistaler, S., and Peter, T.: Extreme NAT supersaturations in mountain wave ice PSCs: A clue to NAT formation, J. Geophys. Res., 108, 2003b.

Luo, B. P., Carslaw, K. S., Peter, T., and Clegg, S. L.: Vapour pressures of $H_2SO_4/HNO_3/HCl/HBr/H_2O$ solutions to low stratospheric temperatures, Geophys. Res. Lett., 22, 247–250, 1995.

Mann, G., Carslaw, K., Chipperfield, M., Davies, S., and Eckermann, S.: Large nitric acid trihydrate particles and denitrification caused by mountain waves in the Arctic stratosphere, J. Geophys. Res., 110, 2005.

Manney, G. L., Sabutis, J. L., Pawson, S., Santee, M. L., Naujokat, B., Swinbank, R., Gelman, M. E., and Ebisuzaki, W.: Lower stratospheric temperature differences between meteorological analyses in two cold Arctic winters and their impact on polar processing studies, J. Geophys. Res., 108, 2003.

Manney, G. L., Santee, M. L., Rex, M., Livesey, N. J., Pitts, M. C., Veefkind, P., Nash, E. R., Wohltmann, I., Lehmann, R., Froidevaux, L., Poole, L. R., Schoeberl, M. R., Haffner, D. P., Davies, J., Dorokhov, V., Gernandt, H., Johnson, B., Kivi, R., Kyro, E., Larsen, N., Levelt, P. F., Makshtas, A., McElroy, C. T., Nakajima, H., Concepcion Parrondo, M., Tarasick, D. W., von der Gathen, P., Walker, K. A., and Zinoviev, N. S.: Unprecedented Arctic ozone loss in 2011, Nature, 478, 469–U65, 2011.

Marcolli, C., Gedamke, S., Peter, T., and Zobrist, B.: Efficiency of immersion mode ice nucleation on surrogates of mineral dust, Atmos. Chem. Phys., 7, 5081–5091, 2007.

Marshall, S. F., Covert, D. S., and Charlson, R. J.: Relationship between asymmetry parameter and hemispheric backscatter ratio: implications for climate forcing by aerosols, Appl. Opt., 34, 6306–6311, 1995.

Massoli, P., Maturilli, M., and Neuber, R.: Climatology of Arctic polar stratospheric clouds as measured by lidar in Ny-Ålesund, Spitsbergen (79°N, 12°E), J. Geophys. Res., 111, 2006.

Maturilli, M. and Dörnbrack, A.: Polar stratospheric ice cloud above Spitsbergen, J. Geophys. Res., 111, 2006.

McCormick, M. P., Steele, H. M., Hamill, P., Chu, W. P., and Swissler, T. J.: Polar Stratospheric Cloud Sightings by SAM-II, J. Atmos. Sci., 39, 1387–1397, 1982.

McKenna, D., Konopka, P., Grooß, J.-U., Günther, G., Müller, R., Spang, R., Offermann, D., and Orsolini, Y.: A new Chemical Lagrangian Model of the Stratosphere (CLaMS) - 1. Formulation of advection and mixing, J. Geophys. Res., 107, 2002.

Meilinger, S. K., Koop, T., Luo, B. P., Huthwelker, T., Carslaw, K. S., Krieger, U., Crutzen, P. J., and Peter, T.: Size-dependent stratospheric droplet composition in lee wave temperature fluctuations and their potential role in PSC freezing, Geophys. Res. Lett., 22, 3031–3034, 1995.

Middlebrook, A. M., Berland, B. S., George, S. M., Tolbert, M. A., and Toon, O. B.: Real refractive indices of infrared-characterized nitric-acid/ice films: Implications for optical measurements of polar stratospheric clouds, J. Geophys. Res., 99, 25 655–25 666, 1994.

Middlebrook, A. M., Tolbert, M. A., and Drdla, K.: Evaporation studies of model polar stratospheric cloud films, Geophys. Res. Lett., 23, 2145–2148, 1996.

Mie, G.: Beiträge zur Optik trüber Medien, speziell kolloidaler Metallösungen, Annalen der Physik, 330, 377–445, 1908.

Mishchenko, M. I.: Light scattering by randomly oriented axially symmetric particles, J. Opt. Soc. Am. A, 8, 871–882, 1991.

Mishchenko, M. I., Travis, L. D., and Mackowski, D. W.: T-Matrix Computations of Light Scattering by Nonspherical Particles: A Review (Reprinted from vol 55, pg 535-575, 1996), J. Quant. Spectrosc. Radiat. Transf., 111, 1704–1744, 2010.

Molina, L. T. and Molina, M. J.: Production of Cl_2O_2 from the Self-Reaction of the ClO Radical, J. Phys. Chem., 91, 433–436, 1987.

Molina, M. J. and Rowland, F. S.: Stratospheric sink for chlorofluoromethanes: chlorine atomc-atalysed destruction of ozone, Nature, 249, 810–812, 1974.

Molina, M. J., Zhang, R., Wooldridge, P. J., McMahon, J. R., Kim, J. E., Chang, H. Y., and Beyer, K. D.: Physical Chemistry of the $H_2SO_4/HNO_3/H_2O$ System: Implications for Polar Stratospheric Clouds, Science, 261, 1418–1423, 1993.

Müller, M., Neuber, R., Fierli, F., Hauchecorne, A., Vömel, H., and Oltmans, S. J.: Stratospheric water vapour as tracer for Vortex filamentation in the Arctic winter 2002/2003, Atmos. Chem. Phys., 3, 1991–1997, 2003.

Müller, R.: Chapter 1: Introduction, in: Stratospheric ozone depletion and climate change, pp. 1–32, The Royal Society of Chemistry, 2012.

Müller, R., Peter, T., Crutzen, P. J., Oelhaf, H., Adrian, G. P., Clarmann, T., Wegner, A., Schmidt, U., and Lary, D.: Chlorine chemistry and the potential for ozone depletion in the Arctic stratosphere in the winter of 1991/92, Geophys. Res. Lett., 21, 1427–1430, 1994.

Murphy, D. M. and Gary, B. L.: Mesosclae temperature fluctuations and polar stratospheric clouds, J. Atmos. Sci., 52, 1753–1760, 1995.

Murphy, D. M. and Koop, T.: Review of the vapour pressures of ice and supercooled water for atmospheric applications, Quart. J. Roy. Meteorol. Soc., 131, 1539–1565, 2005.

Nedoluha, G. E., Bevilacqua, R. M., Hoppel, K. W., Daehler, M., Shettle, E. P., Hornstein, J. H., Fromm, M. D., Lumpe, J. D., and Rosenfield, J. E.: POAM III measurements of dehydration in the Antarctic lower stratosphere, Geophys. Res. Lett., 27, 1683–1686, 2000.

Newman, P. A., Oman, L. D., Douglass, A. R., Fleming, E. L., Frith, S. M., Hurwitz, M. M., Kawa, S. R., Jackman, C. H., Krotkov, N. A., Nash, E. R., Nielsen, J. E., Pawson, S., Stolarski, R. S., and Velders, G. J. M.: What would have happened to the ozone layer if chlorofluorocarbons (CFCs) had not been regulated?, Atmos. Chem. Phys., 9, 2113–2128, 2009.

Ovarlez, J. and Ovarlez, H.: Stratospheric water vapor content evolution during EASOE, Geophys. Res. Lett., 21, 1235–1238, 1994.

Pagan, K. L., Tabazadeh, A., Drdla, K., Hervig, M. E., Eckermann, S. D., Browell, E. V., Legg, M. J., and Foschi, P. G.: Observational evidence against mountain-wave generation of ice nuclei as a prerequisite for the formation of three solid nitric acid polar stratospheric clouds observed in the Arctic in early December 1999, J. Geophys. Res., 109, 2004.

Pan, L. L., Randel, W. J., Nakajima, H., Massie, S. T., Kanzawa, H., Sasano, Y., Yokota, T., Sugita, T., Hayashida, S., and Oshchepkov, S.: Satellite observation of dehydration in the Arctic Polar stratosphere, Geophys. Res. Lett., 29, 2002.

Peter, T.: Microphysics and heterogeneous chemistry of polar stratospheric clouds, Annu. Rev. Phys. Chem., 48, 785–822, 1997.

Peter, T. and Grooß, J.-U.: Chapter 4: Polar Stratospheric Clouds and Sulfate Aerosol Particles: Microphysics, Denitrification and Heterogeneous Chemistry, in: Stratospheric Ozone Depletion and Climate Change, pp. 108–144, The Royal Society of Chemistry, 2012.

Peter, T., Müller, R., Crutzen, P. J., and Deshler, T.: The lifetime of leewave-induced ice particles in the Arctic stratosphere: II. Stabilization due to NAT-coating, Geophys. Res. Lett., 21, 1331–1334, 1994.

Pinti, V., Marcolli, C., Zobrist, B., Hoyle, C. R., and Peter, T.: Ice nucleation efficiency of clay minerals in the immersion mode, Atmos. Chem. Phys., 12, 5859–5878, 2012.

Pitts, M. C., Poole, L. R., Dörnbrack, A., and Thomason, L. W.: The 2009-2010 Arctic polar stratospheric cloud season: a CALIPSO perspective, Atmos. Chem. Phys., 11, 2161–2177, 2011.

Pitts, M. C., Poole, L. R., Lambert, A., and Thomason, L. W.: An assessment of CALIOP polar stratospheric cloud composition classification, Atmos. Chem. Phys., 13, 2975–2988, 2013.

Pitts, M. C., Thomason, L. W., Poole, L. R., and Winker, D. M.: Characterization of Polar Stratospheric Clouds with spaceborne lidar: CALIPSO and the 2006 Antarctic season, Atmos. Chem. Phys., 7, 5207–5228, 2007.

Pitts, M. C., Poole, L. R., and Thomason, L. W.: CALIPSO polar stratospheric cloud observations: second-generation detection algorithm and composition discrimination, Atmos. Chem. Phys., 9, 7577–7589, 2009.

Pitzer, K.: Activity coefficients in electrolyte solutions, CRC Press, 1991.

Ploeger, F., Konopka, P., Günther, G., Grooß, J.-U., and Müller, R.: Impact of the vertical velocity scheme on modeling transport in the tropical tropopause layer, J. Geophys. Res., 115, 2010.

Pruppacher, H. R. and Klett, J. D.: Microphysics of clouds and precipitation, Atmospheric and oceanographic sciences library, Kluwer Academic Publishers, 1996.

Ravishankara, A. and Hanson, D.: Differences in the reactivity of Type I polar stratospheric clouds depending on their phase, J. Geophys. Res., 101, 3885–3890, 1996.

Read, W. G., Lambert, A., Bacmeister, J., Cofield, R. E., Christensen, L. E., Cuddy, D. T., Daffer, W. H., Drouin, B. J., Fetzer, E., Froidevaux, L., Fuller, R., Herman, R., Jarnot, R. F., Jiang, J. H., Jiang, Y. B., Kelly, K., Knosp, B. W., Kovalenko, L. J., Livesey, N. J., Liu, H.-C., Manney, G. L., Pickett, H. M., Pumphrey, H. C., Rosenlof, K. H., Sabounchi, X., Santee, M. L., Schwartz, M. J., Snyder, W. V., Stek, P. C., Su, H., Takacs, L. L., Thurstans, R. P., Vömel, H., Wagner, P. A., Waters, J. W., Webster, C. R., Weinstock, E. M., and Wu, D. L.: Aura Microwave Limb Sounder upper tropospheric and lower stratospheric H_2O and relative humidity with respect to ice validation, J. Geophys. Res., 112, 2007.

Rex, M., Salawitch, R. J., von der Gathen, P., Harris, N. R. P., Chipperfield, M. P., and Naujokat, B.: Arctic ozone loss and climate change, Geophys. Res. Lett., 31, 2004.

Rex, M., von der Gathen, P., Braathen, G. O., Harris, N. R. P., Reimer, E., Beck, A., Alfier, R., Kruger-Carstensen, R., Chipperfield, M., de Backer, H., Balis, D., O'Connor, F., Dier, H., Dorokhov, V., Fast,

H., Gamma, A., Gil, M., Kyro, E., Litynska, Z., Mikkelsen, S., Molyneux, M., Murphy, G., Reid, S. J., Rummukainen, M., and Zerefos, C.: Chemical ozone loss in the Arctic winter 1994/95 as determined by the Match technique, J. Atmos Chem., 32, 35–59, 1999.

Rex, M., Salawitch, R. J., Santee, M. L., Waters, J. W., Hoppel, K., and Bevilacqua, R.: On the unexplained stratospheric ozone losses during cold Arctic Januaries, Geophys. Res. Lett., 30, 2003.

Rosen, J. M. and Kjome, N. T.: Backscattersonde - a new insturment for atmospheric aerosol research, Appl. Opt., 30, 1552–1561, 1991.

Rosen, J. M., Kjome, N. T., Fast, H., Khattatov, V. U., and Rudakov, V. V.: Penetration of Mt. Pinatubo Aerosols into the North Polar Vortex, Geophys. Res. Lett., 19, 1751–1754, 1992.

Salawitch, R., Wofsy, S., and Mcelroy, M.: Influence of polar stratospheric clouds on the depletion of Antarctic ozone, Geophys. Res. Lett., 15, 871–874, 1988.

Salawitch, R. J., Wofsy, S. C., Gottlieb, E. W., Lait, L. R., Newman, P. A., Schoeberl, M. R., Loewenstein, M., Podolske, J. R., Strahan, S. E., Proffitt, M. H., Webster, C. R., May, R. D., Fahey, D. W., Baumgardner, D., Dye, J. E., Wilson, J. C., Kelly, K. K., Elkins, J. W., Chan, K. R., and Anderson, J. G.: Chemical Loss of Ozone in the Arctic Polar Vortex in the Winter of 1991-1992, Science, 261, 1146–1149, 1993.

Santacesaria, V., MacKenzie, A. R., and Stefanutti, L.: A climatological study of polar stratospheric clouds (1989-1997) from LIDAR measurements over Dumont d'Urville (Antarctica), Tellus B, 53, 306–321, 2001.

Santee, M. L., Lambert, A., Read, W. G., Livesey, N. J., Cofield, R. E., Cuddy, D. T., Daffer, W. H., Drouin, B. J., Froidevaux, L., Fuller, R. A., Jarnot, R. F., Knosp, B. W., Manney, G. L., Perun, V. S., Snyder, W. V., Stek, P. C., Thurstans, R. P., Wagner, P. A., Waters, J. W., Muscari, G., de Zafra, R. L., Dibb, J. E., Fahey, D. W., Popp, P. J., Marcy, T. P., Jucks, K. W., Toon, G. C., Stachnik, R. A., Bernath, P. F., Boone, C. D., Walker, K. A., Urban, J., and Murtagh, D.: Validation of the Aura Microwave Limb Sounder HNO_3 measurements, J. Geophys. Res., 112, 2007.

Schiller, C., Bauer, R., Cairo, F., Deshler, T., Dörnbrack, A., Elkins, J., Engel, A., Flentje, H., Larsen, N., Levin, I., Müller, M., Oltmans, S., Ovarlez, H., Ovarlez, J., Schreiner, J., Stroh, F., Voigt, C., and Vömel, H.: Dehydration in the Arctic stratosphere during the SOLVE/THESEO-2000 campaigns, J. Geophys. Res., 107, 2002.

Schiller, C., Krämer, M., Afchine, A., Spelten, N., and Sitnikov, N.: Ice water content of Arctic, midlatitude, and tropical cirrus, J. Geophys. Res., 113, 2008.

Seinfeld, J. H. and Pandis, S. N.: Atmospheric chemistry and physics: from air pollution to climate change, A Wiley-Intersciencie publications, Wiley, 2006.

Sitnikov, N., Yushkov, V., Afchine, A., Korshunov, L., Astakhov, V., Ulanovskii, A., Kraemer, M., Mangold, A., Schiller, C., and Ravegnani, F.: The FLASH instrument for water vapor measurements on board the high-altitude airplane, Instruments and Experimental Techniques, 50, 113–121, 2007.

Solomon, S.: The hole truth - What's news (and what's not) about the ozone hole., Nature, 427, 289–291, 2004.

Solomon, S., Garcia, R. R., Rowland, F. S., and Wuebbles, D. J.: On the depletion of Antarctic ozone, Nature, 321, 755–758, 1986.

SPARC (Stratospheric Processes And their Role in Climate): SPARC Assessment of Stratospheric Aerosol Properties, edited by L. W. Thomason and T. Peter, WCRP-124, SPARC Report 4, WMO/TD-No.1295, 346 pp., 2006.

Stanford, J. L. and Davis, J. S.: A century of stratospheric cloud reports: 1870-1972, Bull. Amer. Meteorol. Soc., 55, 213–219, 1974.

Stephens, G. L., Vane, D. G., Boain, R. J., Mace, G. G., Sassen, K., Wang, Z. E., Illingworth, A. J., O'Connor, E. J., Rossow, W. B., Durden, S. L., Miller, S. D., Austin, R. T., Benedetti, A., Mitrescu, C., and Team, C. S.: The cloudsat mission and the a-train - A new dimension of space-based observations of clouds and precipitation, Bull. Amer. Meteorol. Soc., 83, 1771–1790, 2002.

Stolarski, R. S., Krueger, A. J., Schoeberl, M. R., McPeters, R. D., Newman, P. A., and Alpert, J. C.: Nimbus 7 satellite measurements of the springtime Antarctic ozone decrease, Nature, 322, 808–811, 1986.

Stone, E. M., Tabazadeh, A., Jensen, E., Pumphrey, H. C., Santee, M. L., and Mergenthaler, J. L.: Onset, extent, and duration of dehydration in the southern hemisphere polar vortex, J. Geophys. Res., 106, 22 979–22 989, 2001.

Tabazadeh, A., Djikaev, Y., Hamill, P., and Reiss, H.: Laboratory evidence for surface nucleation of solid polar stratospheric cloud particles, J. Phys. Chem., 106, 10 238–10 246, 2002.

Tolbert, M. A. and Toon, O. B.: Solving the PSC Mystery, Science, 292, 61–63, 2001.

Toon, O., Hamill, P., Turco, R., and Pinto, J.: Condensation of HNO_3 and HCl in the winter polar stratospheres, Geophys. Res. Lett., 13, 1284–1287, 1986.

Toon, O., Browell, E., Kinne, S., and Jordan, J.: An Analysis of Lidar Observations of Polar Stratospheric Clouds, Geophys. Res. Lett., 17, 393–396, 1990.

Voigt, C., Schreiner, J., Kohlmann, A., Zink, P., Mauersberger, K., Larsen, N., Deshler, T., Kröger, C., Rosen, J., Adriani, A., Cairo, F., Donfrancesco, G. D., Viterbini, M., Ovarlez, J., Ovarlez, H., David, C., and Dörnbrack, A.: Nitric acid trihydrate (NAT) in polar stratospheric clouds, Science, 290, 1756–1758, 2000.

Voigt, C., Larsen, N., Deshler, T., Kroger, C., Schreiner, J., Mauersberger, K., Luo, B. P., Adriani, A., Cairo, F., Di Donfrancesco, G., Ovarlez, J., Ovarlez, H., Dörnbrack, A., Knudsen, B., and Rosen, J.: In situ mountain-wave polar stratospheric cloud measurements: Implications for nitric acid trihydrate formation, J. Geophys. Res., 108, 2003.

Voigt, C., Schlager, H., Luo, B. P., Dörnbrack, A., Roiger, A., Stock, P., Curtius, J., Vossing, H., Borrmann, S., Davies, S., Konopka, P., Schiller, C., Shur, G., and Peter, T.: Nitric Acid Trihydrate (NAT) formation at low NAT supersaturation in Polar Stratospheric Clouds (PSCs), Atmos. Chem. Phys., 5, 1371–1380, 2005.

Vömel, H., Oltmans, S. J., Hofmann, D. J., Deshler, T., and Rosen, J. M.: The evolution of the dehydration in the Antarctic stratospheric vortex, J. Geophys. Res., 100, 13 919–13 926, 1995.

Vömel, H., Rummukainen, M., Kivi, R., Karhu, J., Turunen, T., Kyro, E., Rosen, J., Kjome, N., and Oltmans, S.: Dehydration and sedimentation of ice particles in the Arctic stratospheric vortex, Geophys. Res. Lett., 24, 795–798, 1997.

Vömel, H., David, D. E., and Smith, K.: Accuracy of tropospheric and stratospheric water vapor measurements by the cryogenic frost point hygrometer: Instrumental details and observations, J. Geophys. Res., 112, 2007a.

Vömel, H., Yushkov, V., Khaykin, S., Korshunov, L., Kyrö, E., and Kivi, R.: Intercomparisons of stratospheric water vapor sensors: FLASH-B and NOAA/CMDL frost-point hygrometer, J. Atmos. Ocean. Technol., 24, 941–952, 2007b.

von Hobe, M. et al.: Reconciliation of essential process parameters for an enhanced predictability of Arctic stratospheric ozone loss and its climate interactions, Atmos. Chem. Phys. Discuss., 12, 30 661–30 754, 2012.

Waterman, P. C.: Symmetry, Unitarity, and Geometry in Electromagnetic Scattering, Phys. Rev. D, 3, 825–839, 1971.

Waters, J. W. et al.: The Earth Observing System Microwave Limb Sounder (EOS MLS) on the Aura satellite, IEEE Trans. Geosci. Remote Sensing, 44, 1075–1092, 2006.

Wernli, H. and Davies, H. C.: A Lagrangian-based analysis of extratropical cyclones .1. The method and some applications, Quart. J. Roy. Meteorol. Soc., 123, 467–489, 1997.

Winker, D. M., Pelon, J., and McCormick, M. P.: The CALIPSO mission: Spaceborne lidar for observation of aerosols and clouds, in: Lidar Remote Sensing for Industry and Environment Monitoring III, vol. 4893 of *Proceedings of SPIE*, pp. 1–11, SPIE-INT SOC OPTICAL ENGINEERING, 2003.

Winker, D. M., Hunt, W. H., and McGill, M. J.: Initial performance assessment of CALIOP, Geophys. Res. Lett., 34, 2007.

Wirth, M., Tsias, A., Dörnbrack, A., Weiss, V., Carslaw, K., Leutbecher, M., Renger, W., Volkert, H., and Peter, T.: Model-guided Lagrangian observation and simulation of mountain polar stratospheric clouds, J. Geophys. Res., 104, 23 971–23 981, 1999.

WMO (World Meteorological Organization): Scientific Assessment of Ozone Depletion: 2010, Global Ozone Research and Monitoring Project-Report No. 52, 516 pp., Geneva, Switzerland, 2011.

Yushkov, V., Astakhov, V., and Merkulov, S.: Optical balloon hygrometer for upper-troposphere and stratosphere water vapor measurements, in: Society of Photo-Optical Instrumentation Engineers (SPIE) Conference Series, vol. 3501 of *Society of Photo-Optical Instrumentation Engineers (SPIE) Conference Series*, pp. 439–445, 1998.

Zhang, R., Wooldridge, P. J., and Molina, M. J.: Vapor pressure measurements for the $H_2SO_4/HNO_3/H_2O$ and $H_2SO_4/HCl/H_2O$ systems: Incorporation of stratospheric acids into background sulfate aerosols, J. Phys. Chem., 97, 8541–8548, 1993.

Zobrist, B., Koop, T., Luo, B. P., Marcolli, C., and Peter, T.: Heterogeneous ice nucleation rate coefficient of water droplets coated by a nonadecanol monolayer, J. Phys. Chem., 111, 2149–2155, 2007.

Zobrist, B., Soonsin, V., Luo, B. P., Kreiger, K., Marcolli, C., Peter, T., and Koop, T.: Ultra-slow water diffusion in aqueous sucrose glasses, Phys. Chem. Chem. Phys., 13, 3514–3526, 2011.

Zöger, M., Afchine, A., Eicke, N., Gerhards, M.-T., Klein, E., McKenna, D. S., Mörschel, U., Schmidt, U., Tan, V., Tuitjer, F., Woyke, T., and Schiller, C.: Fast in situ stratospheric hygrometers: A new family of balloon-borne and airborne Lyman α photofragment fluorescence hygrometers, J. Geophys. Res., 104, 1807–1816, 1999.

Zuberi, B., Bertram, A. K., Cassa, C. A., Molina, L. T., and Molina, M. J.: Heterogeneous nucleation of ice in $(NH_4)_2SO_4-H_2O$ particles with mineral dust immersions, Geophys. Res. Lett., 29, 2002.

Acknowledgments

This work would not have been possible without the help and support of many people, to whom I express my gratitude.

I especially thank …

... Thomas Peter for being my doctoral father and for the good time we had together. I enjoyed long discussions with you which always motivated me to continue and rekindled my ambition. I am thankful that you introduced me to your friends and colleagues at the RECONCILE meeting in Kiruna and I still like to look back upon our trip to Narvik. You sent me to visit Mike and Lamont at NASA Langley which was a great experience for me. Stay the way you are!

... Michael Pitts who became more and more involved in my PhD and finally took over a big part of supervision. I would like to thank you for three great months in Virginia and incredible support beyond that. Despite 6 hours of time difference, you were always a great help for me, you answered every single question I had, provided me data and instructions, and read my first publication multiple times.

... Marc von Hobe for agreeing to be my co-examiner. I thank you, the best RECONCILE coordinator, for interesting and fruitful discussions and lots of opportunities to present my work at several different meetings.

... Beiping Luo for being a microphysical wizard with an incredible gut feeling. I enjoyed working with you and I am thankful for all your modeling support during the last years.

... Frank Wienhold for his manifold support before, during, and after my stay in Ny-Ålesund. Thanks for all your help related to COBALD and balloon soundings in general.

... Chris Hoyle for accompanying me to Ny-Ålesund and later on sharing offices together. You introduced me to shell scripts and answered all my nasty questions varying from temperature fluctuations to the theory of contact angles. Although you changed jobs in between, you never lost your interest in PSCs and we will finally publish our common publications. Good things come to those who wait.

... Lamont Poole for his warm, friendly, and hospitable nature. Torsten and I will always remember your invitation to Thanksgiving. Moreover, I enjoyed working together with you and gained a lot from your scientific advice. We finally found the pony!